

ASSESSMENT OF LIQUEFACTION CHARACTERISTICS OF SAND UNDER COUPLED ACTION OF COMPRESSION AND SHEAR WAVES

by

Prasanna Rousseau

M.S., Indian Institute of Technology Madras. 2015
B.E., Thiagarajar College of Engineering, Anna University. 2012

A thesis submitted to the Faculty of Graduate and Postdoctoral
Affairs in partial fulfillment of the requirements for the degree of

Doctor of Philosophy

in

Civil Engineering

Department of Civil and Environmental Engineering
Carleton University
Ottawa, Ontario

© 2020, Prasanna Rousseau

The Doctor of Philosophy in Civil Engineering Program is a joint program with University
of Ottawa, administrated by the Ottawa-Carleton Institute of Civil Engineering

ABSTRACT

A comprehensive experimental study focusing on the influence of coupled action of cyclic compression and shear waves (or Rayleigh waves) on the liquefaction resistance of granular soil is presented. The nature and degree of principal stress rotation caused by this coupled action of compression and shear waves are significantly influenced by the initial consolidation stress state and shearing parameters such as the ratio between shear stress and normal stress increments (S/N), and the phase shift (δ) between the waves. The representative S/N ratios were estimated from the numerical simulations and used as an input for the hollow cylinder torsional shear tests that were used to investigate the cyclic response of water deposited Fraser River sand under coupled loading. The implications of assessing liquefaction resistance in terms of the intensity of the overall cyclic shear stress ratio ($CSR = \sigma_{d,cy}/2\sigma'_{mc}$) and the horizontal shear stress ratio ($HSR = \tau_{h,cy}/\sigma'_{mc}$) are highlighted.

Tests results demonstrate that the liquefaction resistance of sand decreases with the increase in initial effective confining stress regardless of the nature of the cyclic shear and indicate that a K_σ factor can be considered even under generalized coupled loading conditions. For a given CSR and initial σ'_{mc} , the number of cycles to liquefaction decreases with an increase in the S/N upto a limiting value of about 1.6 beyond which increasing S/N does not significantly influences the cyclic resistance. The finding that cyclic resistance ratio CRR decreases with increasing S/N is consistent with understanding that the cyclic resistance is higher under triaxial loading mode compared to simple shear. The dissipated energy ratio (W_{liq}/σ'_{mc}), is not significantly affected by CSR , S/N , σ'_{mc} , initial inclination of principal stress axes and magnitude of stress rotation.

Coupled cyclic loading under out-of-phase compression and shear waves will lead to elliptical loading paths. It is shown that loading under such non-conventional stress paths, could be initiated along different pathways, and soil response is dependent on the overall path including the initial stress state. In an elliptical path initialized with drained preshearing, changing the phase shift between compression and shear waves does not significantly influence the cyclic resistance of sand if the cyclic loading is carried out at a fixed HSR and S/N . At a fixed CSR , increasing the phase shift between the waves reduces the cyclic resistance of sand. At coupled cyclic loading with a fixed CSR , S/N and $\delta = 0$, the liquefaction susceptibility decreases with increasing in consolidation stress ratio K_c in the tested sand. The rate of increase in cyclic resistance with initial static shear stress α_{st} decreases with the increase in S/N which indicates that the triaxial loading mode yields higher K_α than the simple shear loading mode. The liquefaction resistance of sand is also highly influenced by the type of the shear loading imposed on the soil samples. Sand specimens tested with one-way coupled loading exhibit higher cyclic strength compared to the sand specimens tested with two-way coupled loading.

The influence of non-linear strain path representing the simultaneous change in pore pressure and pore volume on the monotonic response of Fraser river sand sheared along different inclination of principal stress axes was assessed. The behaviour of sand systematically transformed from dilative response to softening response as the imposed volumetric strain path changed from contractive to expansive volumetric strain. At a given volumetric strain path, the strain softening tendency of the water deposited sand specimens systematically increases as the direction of major principal stress changes from direction of deposition ($\alpha_\sigma = 0^\circ$) to the direction of bedding ($\alpha_\sigma = 90^\circ$). The friction angle

ϕ_{PeakPP} or ϕ_{PT} mobilized at the instant of peak excess pore water pressure state is a unique property of the sand and it is not influenced by the imposed volumetric strain path and principal stress rotation.

ACKNOWLEDGEMENTS

Foremost, with profound gratitude and great humility, I would like to express my sincere thanks to my supervisor and mentor, Prof. Siva Sivathayalan for his unflinching support, encouragement, and patient guidance throughout my research program. I am so blessed to have a supervisor like him, who genuinely care for the wellbeing and prosperity of his students.

I would like to thank Prof. Peijun Guo, Prof. Sai Vanapalli, Prof. Mehdi Pouragha, Prof. Dariush Motazedian, Prof. David Lau, and Prof. Mohammad Rayhani for being members in my examination committee and for providing valuable suggestions. My sincere thanks to Prof. Paul Simms, Prof. Heng Khoo, and Prof. Ning Guo for their useful inputs during my course of study. The technical assistance rendered by Stanley Conley, Pierre Trudel, Jason Arnott, Kenneth Akhiwu, Stephen Vickers, and Dr. Marie Tudoret in troubleshooting the laboratory equipment is gratefully acknowledged. The financial support provided by Ontario Trillium Scholarship and Faculty of Graduate and Postdoctoral affairs at Carleton University is acknowledged with great appreciation. The counselling support rendered by Carleton health and counselling services is greatly appreciated.

I am deeply indebted to Sentheepan Thiru, Thavakumaran Shanmugarajah and Perry Natchieppan for their never-ending love and support. When I came to Canada without knowing anyone here, they took me under their wing and cared for me like my brothers. I would like to thank my colleagues and friends; Lambo, Manmatharajan, Senthooan, Theena, Chaitanya, Sudhi, Sidharth, Kishore, and Nanthinee for their warm company and support over the years.

I am very grateful to my best buddies back home Sabareesh, Hariharan, Sandeep, Mukunthan, Vijayan, Manoj and our little Saksha Sabareesh for their unconditional friendship and support.

Lastly, and most importantly, I wish to thank my dad Rousseau, mom Mariammal, and loving brother Karthikeyan for their unconditional love, encouragement, and sacrifices in every step of my life. I am thankful to god for blessing me with wonderful parents and brother.

TABLE OF CONTENTS

Abstract	ii
Acknowledgments	v
Table of Contents	vii
List of Figures	xii
List of Tables	xxiii
List of Symbols	xxiv
1 Introduction	1
1.1 Background	1
1.2 Objective of the thesis	5
1.3 Layout of thesis	6
2 Literature review	8
2.1 Introduction	8
2.2 Anisotropy of soils	8
2.2.1 Inherent anisotropy	9
2.2.2 Induced anisotropy	11
2.3 Undrained behaviour of soil	12
2.3.1 Static undrained response of granular soils	13
2.3.2 Cyclic response of granular soils	14
2.4 Stress path dependent behaviour of soil	22
2.4.1 Behaviour of granular soil under monotonic shearing	23
2.4.2 Behaviour of cohesive soil under monotonic shearing	28
2.5 Seismic wave propagation	30

2.5.1	Body waves	30
2.5.2	Surface waves	32
2.5.3	Reflection and refraction of seismic waves at interface	34
2.5.3.1	Normal incidence of seismic waves	34
2.5.3.2	Non-normal incidence of seismic waves	36
2.6	Cyclic behaviour of soil under different stress paths	38
2.7	Partially drained or strain path dependent behaviour of soil	47
2.8	Summary	49
3	Description of the CU-HCT apparatus and its working principles	53
3.1	Introduction	53
3.2	CU Hollow cylinder torsional shear apparatus	54
3.2.1	HCT loading and measurement system	56
3.2.2	Data acquisition of CU-HCT	62
3.3	Formulation of stresses and strains	64
3.3.1	Stress analysis	64
3.3.2	Strain analysis	67
3.3.3	Principal stresses and strains	69
3.3.4	Stress and strain non-uniformities in HCT specimen	70
3.4	Membrane strength correction	71
3.5	Membrane penetration correction	73
4	Test material and procedures	76
4.1	Introduction	76
4.2	Test materials	76
4.2.1	Fraser River sand	76

4.3	Reconstitution of Fraser River sand	76
4.3.1	Preliminary preparation steps	77
4.3.2	Specimen preparation steps	78
4.3.3	Test preparation steps	80
4.4	Determination of void ratio	82
4.5	Preliminary tests	83
4.5.1	Undrained response of Fraser River sand under generalized stress states	83
4.5.2	Undrained behavior of Fraser River sand under generalized strain paths	84
4.5.2.1	Undrained behavior under shearing along different α_ε	92
4.5.3	Cyclic response of Fraser River sand under smooth principal stress rotation	105
5	Cyclic behaviour of sand under simultaneous action of P-wave and S-wave	111
5.1	Introduction	111
5.2	Numerical simulation of the simultaneous propagation of compression and shear waves using FLAC 2D	112
5.3	Simulation of coupled loading condition in a hollow cylinder torsional shear apparatus	128
5.4	Nature and degree of stress rotation under coupled loading	131
5.5	HCT studies on the liquefaction characteristics of sand under coupled loading	136
5.5.1	Repeatability tests	141

5.6	Coupled action of normal and shear stresses at different stress ratios and confining pressure	144
5.7	Influence of S/N ratios on the liquefaction characteristics of Fraser River sand	159
5.8	Energy based method of evaluating the liquefaction potential of soil	176
5.8.1	Background	176
5.8.2	Energy dissipated during cyclic shearing	179
5.8.3	Effects of initial conditions and loading parameters on dissipated energy	181
5.8.4	Pore pressure models	188
5.9	Summary and conclusions	191
6	Behaviour of sand under complex cyclic stress paths	195
6.1	Introduction	195
6.2	Definition of cyclic stress ratio	198
6.3	Phase shift between compression and shear waves on the cyclic response	206
6.3.1	Influence of phase angle at constant HSR and S/N	210
6.3.2	Influence of phase angle at constant CSR and S/N	217
6.4	Effect of coupled loading on anisotropically consolidated loose sand specimens	227
6.5	Simulation of coupled loading with shear wave and one-way compressional wave	235
6.5.1	Influence of S/N and δ_{SN} on the liquefaction characteristics of Fraser River sand	243
6.6	Summary and conclusions	252

7	Monotonic response of sand under partially drained condition	255
7.1	Introduction	255
7.2	Partially drained behaviour of sand under non-linear strain paths	260
7.2.1	Response under fixed α_σ , b_σ but along strain paths with different ε_{vL}	269
7.2.2	Response under fixed ε_{vL} and different α_σ	277
7.4	Summary and conclusions	290
8	Summary and conclusions	292
8.1	Recommendations for future research	299
	References	301

LIST OF FIGURES

Fig 2.1	Effect of reconstitution methods on the undrained simple shear response of Syncrude sand (after Vaid et al. 1999)	11
Fig 2.2	Typical undrained monotonic response of saturated sand (a) stress-strain responses (b) stress paths	17
Fig 2.3	True liquefaction response of sand under cyclic loading (after Vaid and Chern 1985)	18
Fig 2.4	Limited liquefaction of sand under cyclic loading (after Vaid and Chern 1985)	19
Fig 2.5	Cyclic mobility with transient zero effective stress state (after Vaid and Chern 1985)	20
Fig 2.6	Cyclic mobility without transient zero effective stress state (after Vaid and Chern 1985)	21
Fig 2.7	Direction-dependent monotonic behavior of water-deposited Fraser River sands (after Sivathayalan and Vaid 2002)	25
Fig 2.8	Particle motion induced by P-wave (after Shaw et al. 2018)	31
Fig 2.9	Particle motion induced by S-wave (after Shaw et al. 2018)	32
Fig 2.10	Particle motion induced by Rayleigh wave (after Shaw et al. 2018)	33
Fig 2.11	Particle motion induced by Love wave (after Shaw et al. 2018)	34
Fig 2.12	Reflected and refracted waves from normally incident harmonic wave	36
Fig 2.13	Reflected and refracted waves from non-normal incident body waves	37
Fig 2.14	Stress paths due to three typical dynamic loading conditions	40

Fig 2.15	Influence of the degree of principal stress rotation on the measured CRR_{15} on otherwise identical specimens (modified after Sivathayalan et al. 2015)	45
Fig 3.1	Schematic diagram of CU hollow cylinder torsional shear apparatus (Logeswaran 2010)	55
Fig 3.2	End platen with porous stones and radial ribs (Logeswaran 2010)	56
Fig 3.3	Cell pressure control of CU-HCT (Logeswaran 2010)	58
Fig 3.4	Inner chamber volume and pressure control (Logeswaran 2010)	58
Fig 3.5	Schematic arrangement of vertical load control (Logeswaran 2010)	59
Fig 3.6	Schematic arrangement of torsional load control (Logeswaran 2010)	59
Fig 3.7	Back pressure and sample volume control of CU-HCT (Logeswaran 2010)	60
Fig 3.8	Schematic arrangement of torsional displacement measuring system (Logeswaran 2010)	62
Fig 3.9	Schematic representation of data acquisition procedure in CU-HCT (Logeswaran 2010)	63
Fig 3.10	Stress state in a hollow cylindrical specimen	65
Fig 3.11	Strains in horizontal plane on a soil element	68
Fig 3.12	Mohr's circle of stresses in $z-\theta$ plane	70
Fig 4.1	Particle size distribution of Fraser River sand	77
Fig 4.2	Specimen preparation by water pluviation method (after Logeswaran 2010)	79
Fig 4.3	HCT specimen setup (after Logeswaran 2010)	81
Fig 4.4	Monotonic response of sand tested under different stress paths	84
Fig 4.5	Variation of S_{PT} with α_{σ}	84

Fig 4.6	Typical response of Fraser River Sand under shearing with $\alpha_\varepsilon = 30^\circ$	88
Fig 4.7	Comparison of actual and targeted parameters for shearing with $\alpha_\varepsilon = 30^\circ$	89
Fig 4.8	Variation of inner pressure and pore pressure at different DPVC frequencies	90
Fig 4.9	Repeatability of HCT undrained tests at $\alpha_\varepsilon = 30^\circ$ and $b_\varepsilon = 0.4$	91
Fig 4.10	Variation of radial, tangential, and torsional shear strain with vertical strain during shearing with different fixed α_ε	94
Fig 4.11	Variation of surface tractions during shearing with different fixed α_ε .	95
Fig 4.12	Variation of principal strains during shearing with different fixed α_ε	96
Fig 4.13	Variation of principal stresses and effective stress ratio during shearing with different fixed α_ε .	97
Fig 4.14	Variation of imposed α_ε and b_ε under shearing with different fixed α_ε .	98
Fig 4.15	Variation of induced α_σ and b_σ under shearing with different fixed α_ε .	99
Fig 4.16	Undrained monotonic response of sand sheared along different α_ε .	101
Fig 4.17	Total stress path response of sand sheared along different α_ε .	102
Fig 4.18	Pore pressure generated by normal stress increment and shear stress increment at different α_ε	103
Fig 4.19	Variation of shear strength at phase transformation with α_ε .	104
Fig 4.20	Effective stress state at the instant of peak pore pressure at different α_ε .	105

Fig 4.21	Cyclic response of sand subjected to a principal stress rotation of $\pm 45^\circ$	107
Fig 4.22	(a) Excess pore pressure and (b) shear stress development under different loading paths	108
Fig 4.23	Variation of number of cycles to liquefaction with $\alpha_{\sigma, max}$	110
Fig 5.1	Schematic representation of the developed numerical model	114
Fig 5.2	Modulus reduction and damping curves used in the numerical simulation	115
Fig 5.3	Finite difference model of horizontal and inclined bedrock soil strata with similar numerical grid	116
Fig 5.4	Acceleration time history (a) AM sine wave (b) Loma Prieta EQ (Seismosignal 2016)	117
Fig 5.5	Comparison between FLAC and ProShake (a) Time history (b) Response spectra for AM sine wave	119
Fig 5.6	Comparison between FLAC and ProShake (a) Time history (b) Response spectra for 1989 Loma Prieta ground motion	120
Fig 5.7	Comparison of response spectra between FLAC and ProShake for AM sine wave with different frequencies (a) Response spectra of input, (b) Response spectra of output	121
Fig 5.8	Horizontal and vertical surface acceleration at midpoint of (a) horizontal layer model (b) inclined bedrock model for AM sine wave	122
Fig 5.9	Horizontal and vertical surface acceleration at midpoint of (a) horizontal layer model (b) inclined bedrock model for 1989 Loma Prieta ground motion	123
Fig 5.10	Variation of normal and shear stresses for AM sine wave	125

Fig 5.11	Variation of normal and shear stresses for Loma Prieta ground motion	126
Fig 5.12	Variation of S/N at the centerline of inclined bedrock model	127
Fig 5.13	S/N contour for AM sine wave ground motion	127
Fig 5.14	S/N contour for Loma Prieta EQ ground motion	128
Fig 5.15	Variation of stress increments and maximum shear stress for $S/N = 0.25$	130
Fig 5.16	Variation of stress increments and α_σ for $K_c = 1$ under various S/N	133
Fig 5.17	Variation of stress increments and α_σ for $K_c = 1$ under various phase shifts	134
Fig 5.18	Variation of α_σ under different initial stress states and shearing conditions	135
Fig 5.19	Variation of $\alpha_{\sigma,range}$ for different K_c under various S/N and phase shifts	136
Fig 5.20	Variation of applied surface tractions and α_σ for $S/N = 0.5$	139
Fig 5.21	Targeted and achieved stress paths	140
Fig 5.22	Typical response of sand subjected to coupled loading with $S/N = 0.5$	142
Fig 5.23	Repeatability test at $CSR = 0.2$ and $S/N = 0.5$	143
Fig 5.24	Repeatability test at $CSR = 0.225$ and $S/N = 1$	144
Fig 5.25	HSR variation with CSR for $S/N = 0.25$	145
Fig 5.26	Effective stress path response at $\sigma'_{mc} = 200 \text{ kPa}$; $CSR = 0.2$ & $S/N = 0.25$	147
Fig 5.27	Effective stress path response at $\sigma'_{mc} = 200 \text{ kPa}$; $CSR = 0.225$ & $S/N = 0.25$	148

Fig 5.28	Effective stress path response at $\sigma'_{mc} = 200 \text{ kPa}$; $CSR = 0.25$ & $S/N = 0.25$	148
Fig 5.29	Effective stress path response at $\sigma'_{mc} = 100 \text{ kPa}$; $CSR = 0.20$ & $S/N = 0.25$	149
Fig 5.30	Effective stress path response at $\sigma'_{mc} = 100 \text{ kPa}$; $CSR =$ 0.225 & $S/N = 0.25$	149
Fig 5.31	Effective stress path response at $\sigma'_{mc} = 100 \text{ kPa}$; $CSR = 0.25$ & $S/N = 0.25$	150
Fig 5.32	Effective stress path response at $\sigma'_{mc} = 50 \text{ kPa}$; $CSR = 0.2$ & $S/N = 0.25$	150
Fig 5.33	Effective stress path response at $\sigma'_{mc} = 50 \text{ kPa}$; $CSR = 0.225$ & $S/N = 0.25$	151
Fig 5.34	Effective stress path response at $\sigma'_{mc} = 50 \text{ kPa}$; $CSR = 0.25$ & $S/N = 0.25$	151
Fig 5.35	Excess pore pressure and shear strain development for different CSR_s	154
Fig 5.36	Cyclic resistance curves from different investigations on Fraser River sand	155
Fig 5.37	Excess pore pressure and shear strain development at different σ'_{mc}	156
Fig 5.38	Cyclic resistance curve at different initial stress states	157
Fig 5.39	Variation of CRR with initial σ'_{mc}	158
Fig 5.40	Variation of K_σ with effective overburden stress ratio	159
Fig 5.41	HSR variation with H/V for different CSR_s	160
Fig 5.42	Cyclic response of loose Fraser River sand at $CSR = 0.20$ & $S/N = 0.25$	162
Fig 5.43	Cyclic response of loose Fraser River sand at $CSR = 0.20$ & $S/N = 0.5$	163

Fig 5.44	Cyclic response of loose Fraser River sand at $CSR = 0.20$ & $S/N = 1$	164
Fig 5.45	Cyclic response of loose Fraser River sand at $CSR = 0.20$ & $S/N = 2$	165
Fig 5.46	Excess pore pressure and shear strain development at various S/N for $\sigma'_{mc} = 100 \text{ kPa}$	166
Fig 5.47	Excess pore pressure and shear strain development at various S/N for $\sigma'_{mc} = 200 \text{ kPa}$	167
Fig 5.48	Normal and shear strain development at various S/N for $\sigma'_{mc} =$ 100 kPa	168
Fig 5.49	Normal and shear strain development at various S/N for $\sigma'_{mc} =$ 200 kPa .	169
Fig 5.50	Variation of number of cycles to liquefaction with S/N for $\sigma'_{mc} = 100 \text{ kPa}$	170
Fig 5.51	Variation of number of cycles to liquefaction with S/N for $\sigma'_{mc} = 200 \text{ kPa}$	171
Fig 5.52	Variation of CRR with S/N	172
Fig 5.53	Variation of K_{σ} at different S/N	173
Fig 5.54	Comparison of HSR variation with S/N	175
Fig 5.55	Comparison of cyclic resistance variation with S/N	176
Fig 5.56	Typical variation of dissipated energy per unit volume (W) in a coupled loading test with $CSR = 0.2$ and $S/N = 0.5$	180
Fig 5.57	Variation of dissipated energy at liquefaction with confining pressure	182
Fig 5.58	Gradation curves of Fraser River sand and Reid Bedford sand	183
Fig 5.59	Variation of dissipated energy at $r_u = 1$ with CSR	184
Fig 5.60	Variation of dissipated energy at $\gamma_{max} = 3.75\%$ with CSR	184
Fig 5.61	Variation of dissipated energy at $\gamma_{max} = 3.75\%$ with S/N	187

Fig 5.62	Variation of dissipated energy ratio at $\gamma_{max} = 3.75\%$ with S/N	187
Fig 5.63	Variation of dissipated energy ratio at $\gamma_{max} = 3.75\%$ with different degree of stress rotation.	188
Fig 5.64	Variation of pore pressure ratio with cycle ratio	189
Fig 5.65	Fitted quintic curve to predict r_u	190
Fig 5.66	Variation of pore pressure ratio with dissipation energy ratio	191
Fig 6.1	Direction of τ_{max} for both triaxial and simple shear test conditions	199
Fig 6.2	Typical variation of cyclic stress ratio in Triaxial and simple shear tests under initial (a) isotropic stress state and (b) anisotropic stress state	200
Fig 6.3	Direction of τ_{max} under different stress states	203
Fig 6.4	Definition of cyclic stress ration (CSR)	204
Fig 6.5	Variation of applied shear stress and normal stress increments for $\delta = 30^\circ$	207
Fig 6.6	Response of sand under elliptical stress path with $\delta = 30^\circ$	209
Fig 6.7	Response of sand sheared with different δ under fully undrained condition.	212
Fig 6.8	Response of sand sheared with different δ under drained preshear condition.	213
Fig 6.9	Variation of deviatoric stress at $\delta = 90^\circ$ under drained preshear condition	214
Fig 6.10	Pore pressure and shear strain response of sand at different δ	215
Fig 6.11	Influence of phase angle δ on number of cycles to liquefaction	216
Fig 6.12	Variation of HSR with δ for CSR of 0.2	217
Fig 6.13	Variation of τ_{max} for different δ and CSR of 0.2	218
Fig 6.14	Variation of preshear stress and shear strain	219

Fig 6.15	Applied stress path and effective stress path response of sand sheared with CSR of 0.2, S/N of 0.25	221
Fig 6.16	Applied stress path and effective stress path response of sand sheared with CSR of 0.2, S/N of 0.5	222
Fig 6.17	Pore pressure and shear strain response of sand at different δ & $CSR = 0.2$	223
Fig 6.18	Influence of phase angle δ on number of cycles to liquefaction at a fixed $CSR = 0.2$	225
Fig 6.19	Rotation of α_σ for different δ and S/N	226
Fig 6.20	Influence of $\Delta\sigma_d/\Delta\alpha_\sigma$ on number of cycles to liquefaction	227
Fig 6.21	Typical response of anisotropically consolidated Fraser River sand specimen subjected to coupled loading.	229
Fig 6.22	Pore pressure and shear strain response of sand different S/N	231
Fig 6.23	Effect of K_c on pore pressure and shear strain response of sand	231
Fig 6.24	Influence of K_c on number of cycles to liquefaction	233
Fig 6.25	Variation of N_L with respect to initial static shear stress ratio	234
Fig 6.26	K_α under simple shear and triaxial loading mode for Fraser River sand (after Sivathayalan and Ha (2011)).	234
Fig 6.27	Coupled loading with one-way compression wave and its corresponding stress rotation at various S/N .	237
Fig 6.28	Coupled loading with one-way compression wave at different δ_{SN}	238
Fig 6.29	Typical response of sand subjected to coupled loading with one-way compression wave	241
Fig 6.30	Comparison of pore pressure and shear strain response at different CSR	242
Fig 6.31	Cyclic resistance curves from different loading conditions	243
Fig 6.32	Variation of HSR with S/N	244

Fig 6.33	Variation of applied stress increments and principal stresses for $S/N = 0.269$ & 1.17	245
Fig 6.34	Effective stress path responses at various S/N	247
Fig 6.35	Pore pressure and maximum shear strain development at various S/N	248
Fig 6.36	Number of cycles to liquefaction with S/N for one-way cyclic P-wave.	249
Fig 6.37	Applied stress path and effective stress path response of sand sheared with different δ_{SN}	251
Fig 6.38	Variation of applied stress increments, stress rotation and principal stresses at different δ_{SN} .	252
Fig 7.1	Vertical, pore and effective stress in level ground before and after shaking	257
Fig 7.2	Instability due to seepage and void redistribution	257
Fig 7.3	Application of isotropic consolidation stresses using CU-HCT: (a) directional stresses; (b) effective mean normal stress; (c) volumetric strain and normal strains	262
Fig 7.4	Axial, radial and tangential strain increments under hydrostatic stress increment	263
Fig 7.5	Nonlinear strain path imposed on loose Fraser River sand specimens	265
Fig 7.6	Typical response of Fraser River Sand to non-linear volumetric strain path with $\epsilon_{vL} = -0.60\%$	267
Fig 7.7	Comparison of actual and targeted parameters	268
Fig 7.8	Variation of surface tractions for shearing under different non-linear strain paths	270
Fig 7.9	Variation of principal strains under different non-linear strain paths	271

Fig 7.10	Response of Fraser River sand under nonlinear strain paths leading to different limiting volumetric strain	273
Fig 7.11	Variation of shear strength at phase transformation with magnitude of limiting volumetric strain	275
Fig 7.12	Variation of peak excess pore water pressure with magnitude of limiting volumetric strain.	276
Fig 7.13	Effective stress state at the instant of peak pore water pressure.	276
Fig 7.14	Variation of surface tractions during shearing with different fixed α_σ	279
Fig 7.15	Variation of radial, tangential, and torsional shear strain with vertical strain during shearing with different fixed α_σ	280
Fig 7.16	Variation of principal stresses and effective stress ratio during shearing with different fixed α_σ	281
Fig 7.17	Variation of principal strains during shearing with different fixed α_σ	282
Fig 7.18	Response of Fraser River sand under nonlinear strain path with different fixed α_σ	285
Fig 7.19	Variation of brittleness index with α_σ	286
Fig 7.20	Variation of peak shear strength with α_σ	286
Fig 7.21	Variation of friction angle mobilized at peak shear strength with α_σ	287
Fig 7.22	Variation of peak excess pore water pressure ratio with α_σ	288
Fig 7.23	Variation of shear strength at phase transformation with α_σ	289
Fig 7.24	Effective stress state at the instant of peak pore water pressure at different loading modes.	289

LIST OF TABLES

Table 4.1	Initial and shearing parameters for generalized strain path tests	85
Table 4.2	Details of preliminary cyclic tests	106
Table 5.1	Details of initial and cyclic loading parameters	137
Table 6.1	Details of cyclic loading tests with different δ and K_c	205
Table 6.2	Initial and cyclic loading parameters for tests with one-way compression wave	239
Table 7.1	Initial and shearing parameters for nonlinear volumetric strain path tests	265

LIST OF SYMBOLS

<i>AC</i>	Anisotropically consolidated
<i>ADC</i>	Analog to digital converter
<i>AM</i>	Amplitude modulator
<i>AP</i>	Air pluviation
<i>ASTM</i>	American society of testing materials
<i>HCT</i>	Hollow cylinder torsional
<i>CPU</i>	Central processing unit
<i>CSR</i>	Critical stress ratio (or) Cyclic stress ratio
<i>CRR</i>	Cyclic resistance ratio
<i>DAC</i>	Digital to analog converter
<i>DAQ</i>	Data acquisition
<i>DEM</i>	Discrete element method
<i>DPVC</i>	Digital Pressure/Volume controllers
<i>DSC</i>	Directional shear cell
<i>DPT</i>	Differential pressure transducer
<i>EPT</i>	Electro-Pneumatic transducer
<i>FD</i>	Finite difference
<i>FE</i>	Finite element
<i>FLAC</i>	Fast lagrangian analysis of continuum
<i>IC</i>	Isotropically consolidated
<i>LVDT</i>	Linear variable differential transducer
<i>MSC</i>	Multichannel signal conditioner
<i>MT</i>	Moist tamping
<i>NI</i>	National instruments
<i>NRC</i>	National research council
<i>OCR</i>	Over consolidation ratio
<i>OD</i>	Outer diameter
<i>QSS</i>	Quasi steady state

<i>PGA</i>	Peak ground acceleration
<i>PI</i>	Plasticity index
<i>PSA</i>	Peak spectral acceleration
<i>PSR</i>	Principal stress rotation
<i>PT</i>	Phase transformation
<i>P-wave</i>	Primary wave
<i>S-wave</i>	Shear wave
<i>SBS</i>	State boundary surface
<i>SH</i>	Shear wave with horizontally transverse motion
<i>SV</i>	Shear wave with vertical transverse motion
<i>SMD</i>	Stepper motor drives
<i>WP</i>	Water pluviation
A_i	Displacement amplitude of the incident wave
A_r	Displacement amplitude of the reflected wave
A_t	Displacement amplitude of the transmitted wave
A_m	Surface area of the membrane
B	Skempton's pore pressure parameter
b_σ	$(\sigma_2 - \sigma_3)/(\sigma_1 - \sigma_3)$, Intermediate principal stress parameter
$b_{\sigma c}$	Intermediate principal stress parameter at the end of consolidation
b_ε	$(\varepsilon_2 - \varepsilon_3)/(\varepsilon_1 - \varepsilon_3)$, Intermediate principal strain parameter
C_c	Co-efficient of curvature
C_u	Uniformity coefficient
D_{50}	Mean particle size
$d\varepsilon_z, d\varepsilon_\theta, d\varepsilon_r$ & $d\gamma_{z\theta}$	Incremental vertical, circumferential, radial and shear strain
D_{rc}	Density at the end of consolidation
e_c	Void ratio at the end of consolidation
e_{max}	Maximum void ratio
e_{min}	Minimum void ratio
E	Young's modulus
E_h	Young's modulus in the horizontal direction

E_v	Young's modulus in the vertical direction
E_m	Young's modulus of the membrane
F_z	Vertical load
f	Frequency
G_s	Specific gravity of solids
G	Shear modulus
G_{max}	Maximum shear modulus
G_{vh}, G_{hv}	Shear modulus in vertical plane
H	Height of the specimen
HSR	Horizontal stress ratio
S/N	ratio of horizontal shear stress increment to the normal stress increment
i	Hydraulic gradient
I_B	Brittleness index
$I_{\bar{B}}$	Modified brittleness index
K_c	$\sigma'_{1c}/\sigma'_{3c}$, Effective stress ratio at the end of consolidation
K_σ	Correction factor for confining stress
K_0	At-rest earth pressure coefficient
K_α	Correction for initial static shear stress
M_s	Mass of dry soil
N_{eq}	Equivalent number of uniform stress cycles
N_L	Number of cycles to liquefaction
P_e	External cell pressure
P_i	Internal cell pressure
R	σ'_1/σ'_3 , Principal stress ratio
R_e	External radius of the soil specimen
R_i	Internal radius of the soil specimen
r_N	Cycle ratio
r_u	Pore pressure ratio
S_a	Spectral acceleration

S_{PT}	Shear strength at phase transformation
S_{peak}	Peak shear strength
S_{min}	Minimum shear strength
S_{QSS}	Shear strength at quasi steady state
T_h	Torque
T_{hc}	Torque corrected for the membrane forces
T_m	Torque acting on the membrane
t_m	Thickness of the membrane
v_P	P-wave velocity
v_S	S-wave velocity
v_L	Love wave velocity
v_R	Rayleigh wave velocity
W	Cumulative energy dissipated per unit volume
W_N	Normalized energy ratio
W_{liq}	Dissipated strain energy per unit volume required to liquefy
α	Calibration parameter
α_{st}	Initial static stress ratio
α_z	Impedance ratio
$\alpha_{\sigma,max}$	Maximum inclination of major principal stress to the vertical axis
$\alpha_{\sigma,min}$	Minimum inclination of major principal stress to the vertical axis
$\alpha_{\sigma,range}$	Range of rotation
α_{σ}	Inclination of major principal stress to the vertical axis
$\alpha_{\sigma c}$	Inclination of major principal stress to the vertical axis at the end of consolidation
α_{ε}	Inclination of major principal strain to the vertical axis
β_3	Non-uniformity parameter
β_R	Non-uniformity coefficient
ν	Poisson's ratio
ν_{vh}	Poisson's ratio for the effect of vertical strain on horizontal strain
ν_{hh}	Poisson's ratio for the effect of horizontal on complementary

	horizontal strain
δ	Phase angle between the compression and shear wave
δ_{NS}	Phase angle between $\Delta\tau_{z\theta}$ and S/N
ϕ_{PT}	Friction angle mobilized at phase transformation
ϕ_{PeakPP}	Friction angle mobilized at the state of peak pore pressure
ϕ_{SS}	Friction angle mobilized at steady state
ϕ_{QSS}	Friction angle mobilized at quasi steady state
ϕ_{CSR}	Friction angle mobilized at peak shear strength state
σ_d	$\sigma_1 - \sigma_3$, Deviatoric stress
$\sigma_{d,cyc}$	Cyclic deviatoric stress
σ_h	Normal stress in horizontal direction
σ_v	Normal stress in vertical direction
σ_r	Radial stress
σ_θ	Circumferential stress
σ_z	Axial stress
σ_{zc}	Total vertical stress at the end of consolidation
σ'_r	Effective radial stress
σ'_z	Effective vertical stress
σ'_θ	Effective circumferential stress
σ'_{zc}	Effective vertical stress corrected for the membrane forces
σ'_{rc}	Effective radial stress corrected for the membrane forces
$\sigma'_{\theta c}$	Effective circumferential stress corrected for the membrane forces
σ_1	Major principal stress
σ_2	Intermediate principal stress
σ_3	Minor principal stress
σ_m	$(\sigma_1 + \sigma_2 + \sigma_3)/3$, Total mean normal stress
σ_{wi}	Stress amplitude of incident wave
σ_{wr}	Stress amplitude of reflected wave
σ_{wt}	Stress amplitude of transmitted wave

σ'_1	Effective major principal stress
σ'_{1c}	Effective major principal stress at the end of consolidation
σ'_2	Effective intermediate principal stress
σ'_3	Effective minor principal stress
σ'_{3c}	Effective minor principal stress at the end of consolidation
σ'_m	$(\sigma'_1 + \sigma'_2 + \sigma'_3)/3$, Effective mean normal stress
σ'_{mc}	Effective mean normal stress at the end of consolidation
ρ	Density of the material
τ_{max}	Maximum cyclic shear stress
$\tau_{max,ini}$	Initial maximum cyclic shear stress
τ_{min}	Minimum cyclic shear stress
τ_{static}, τ_{st}	Static shear stress
τ_{cyclic}	Cyclic shear stress
$\tau_{z\theta}$	Torsional shear stress
$\tau_{z\theta c}$	Torsional shear stress at the end of consolidation
τ_h	Shear stress on horizontal plane
ΔH	Change in height
Δl	Element size
ΔR_e	Change in external radius
ΔR_i	Change in internal radius
ΔV_m	Volume change induced by membrane penetration
Δu	Excess pore water pressure
Δu_{normal}	Excess pore water pressure due to normal stress increment
Δu_{shear}	Excess pore water pressure due to shear stress increment
Δu_{peak}	Peak excess pore water pressure
ΔW	Incremental energy dissipated per unit volume
$\Delta \alpha_\sigma$	Incremental principal stress rotation
$\Delta \theta$	Angular displacement
$\Delta \sigma_{zm}, \Delta \sigma_{rm}, \Delta \sigma_{\theta m}$	Axial, radial, and circumferential stresses acting on the membrane

$\Delta\sigma_z, \Delta\sigma_v$	Vertical stress increment
$\Delta\sigma_d$	Deviatoric stress increment
$\Delta\sigma_h$	Horizontal stress increment
$\Delta\sigma_\theta$	Circumferential stress increment
$\Delta\sigma_m$	Incremental mean normal stress
$\Delta\tau_{z\theta}$	Shear stress increment
ε_z	Axial strain
ε_r	Radial strain
ε_θ	Circumferential strain
ε_m	Unit membrane penetration
ε_1	Major principal strain
ε_2	Intermediate principal strain
ε_3	Minor principal strain
$\Delta\varepsilon_v$	Volumetric strain increment
ε_v	Volumetric strain
ε_{vL}	Limiting volumetric strain
$\varepsilon_{zmo}, \varepsilon_{\theta mo}$	Axial and circumferential strain in outer membrane
$\varepsilon_{zmi}, \varepsilon_{\theta mi}$	Axial and circumferential strain in inner membrane
$\gamma_{z\theta}$	Torsional shear strain
γ	Unit weight of soil
$\Delta\gamma_{max}$	Maximum shear strain increment
γ_{max}	Maximum shear strain
$\gamma_{max,ini}$	Initial maximum shear strain
θ_0	Angle of incidence
ξ	Damping ratio
ξ_r	Strain increment ratio

1. INTRODUCTION

1.1 Background

Understanding the cyclic response of saturated granular soil and evaluating its liquefaction potential due to seismic shaking has been a topic of research in geotechnical earthquake engineering since the devastating earthquakes of Alaska and Niigata in 1964. Liquefaction susceptibility of saturated sand is influenced by numerous factors such as void ratio, effective confining stress, sand fabric, pre-strain history and stress paths followed during cyclic loading (Castro and Poulos 1977; Vaid and Sivathayalan 2000). Since natural soil deposits are inherently anisotropic, the stress-strain response of soil depends not only on the magnitude of principal stresses but also on the direction of principal stresses with respect to the deposition direction (Vaid et al. 1990). Stress paths associated with routine geotechnical engineering problems such as excavation, construction of an embankment, tunnels and loading of foundations etc. involves the rotation of principal stress directions (Lade and Kirkgard 2000). Under dynamic loading conditions such as earthquake, wave and traffic loading, this rotation of principal stress direction is cyclic and continuous in nature (Ishihara and Towhata 1983; Jefferies et al. 2015). Several laboratory investigations have been carried out using the hollow cylinder torsional shear (HCT) apparatus to investigate the effects of offshore wave and traffic loading stress paths and the resulting rotation of principal stress axis on the cyclic deformation characteristics of soil. In wave loading stress path, the axial and horizontal normal stress difference and torsional shear stress were cyclically varied to maintain a continuous rotation of principal stress axis while maintaining a constant deviatoric stress throughout the cyclic loading. Laboratory tests

revealed that even cyclic tests with constant magnitude of deviatoric stress result in excess pore water pressure generation and plastic strain accumulation (Ishihara and Towhata 1983; Tong et al. 2010; Huang et al. 2015). In traffic loading stress path, the axial and torsional shear stress increments were varied simultaneously with time, to impose cyclic loading with simultaneous changes in the magnitude of the deviatoric stress and the direction of principal stresses. Cyclic tests with these stress path demonstrated that principal stress rotation (PSR) accelerates the development of excess pore water pressure, accumulation of permanent plastic deformation and degradation of resilient modulus of the subgrade layers (Inam et al. 2012; Grabe and Clayton 2014; Cai et al. 2015; Wu et al. 2017; Guo et al. 2018).

Liquefaction evaluation of granular soils in the laboratory is usually investigated either by applying a horizontal cyclic shear stress as in simple shear or by applying a cyclic deviatoric stress as in a triaxial test. Invariably in all the previous studies, the major focus was to evaluate the effect of vertically propagating shear waves triggered during earthquakes on the liquefaction characteristics of soil. This propagation of pure shear waves is based on the assumption that the soil strata are perfectly horizontal and homogenous, and the dynamic loading is due to vertically propagating shear waves. However, in reality the soil media is highly heterogeneous, and the plane of stratification is not always horizontal. Depending upon the differences of the seismic impedance between soil layers/bedrock, and the incidence angle of seismic waves, the seismic waves are reflected and refracted into waves of different nature and characteristics. These reflected and refracted waves may consist of both compression wave (P-wave) and shear wave (S-wave) components. Therefore, it is evident that during an earthquake the soil

element will be inevitably subjected to complex loading paths involving the simultaneous action of both normal and shear stresses.

The recent 2010-2011 Christchurch, New Zealand earthquake records and also past earthquake events such as Northridge, California 1994 and Kobe, Japan 1995 revealed that the soil also liquefied in places where the high peak vertical ground acceleration exceeded the horizontal acceleration (Tsaparli et al. 2017, 2018). Some case studies also reported that severe earthquake damages occurred in places where strong compression waves and shear waves propagated simultaneously (Bernardie et al. 2006, Lin et al. 2009). Hence, ignoring this combined action of P-waves and S-waves in a soil element could possibly be a factor contributing to the discrepancies in evaluating the liquefaction potential of the soil.

Though the normal and shear stresses were varied simultaneously in cyclic tests with wave and traffic loading stress paths, most of these studies were carried out on clay samples and subjected the soil to 1000s of stress cycles of relatively lower intensity. Hence, these may not be suitable to characterize the liquefaction potential of granular soil under short term seismic events. Only a few attempts were made to study the liquefaction potential of granular soil under the combined action of cyclic normal and shear stresses. Huang et al. (2015) and Xu et al. (2017) evaluated the cyclic strength of saturated sand under bi-directional loading and showed that this combined loading significantly influences the pore pressure generation when compared to the unidirectional loading. So far, to the best of our knowledge no comprehensive attempts were made to evaluate the nature and degree of stress rotation due to this combined action of compression and shear waves and its implications on the liquefaction resistance of saturated cohesionless soil.

The stress path dependent behaviour of natural soil deposit due to its cross-anisotropic fabric has been relatively well established. Several systematic studies conducted using a hollow cylinder torsional shear (HCT) device (Symes et al. 1984; Miura et al. 1986; Uthayakumar and Vaid 1998; Sivathayalan and Vaid 2002; Nishimura et al. 2007; Lade et al. 2013; Brosse et al. 2017; Georgiannou et al. 2018) revealed that orientation of major principal stress during shear has a considerable influence on the anisotropic strength and stiffness characteristics of soil. It has been observed that during monotonic shearing with a fixed principal stress direction, soil showed a weak softening response when the direction of major principal stress aligns along the weak bedding plane. Majority of these studies focused on the anisotropic characterization of reconstituted sands and clay specimens were carried out either under undrained or drained conditions. The assumption of completely undrained or drained condition is only valid if the soil is homogenous and no pore pressure gradient exists within the soil deposit. But this condition is highly idealized and not always realistic because of the heterogenous nature of the soil deposit. Hence, the actual drainage condition in-situ will be partially drained with the simultaneous change in pore pressure and volume. This might result in a more damaging condition than the undrained condition which is commonly adopted in the current geotechnical design practice. Hence it is crucial to understand the behavior of sand under strain paths with simultaneous change in pore pressure and pore volume for safer design practice.

So far, only very few laboratory studies attempted to assess the partially drained behavior of sands under various volumetric strain paths (Chu et al. 1992, 2015; Vaid and Eliadorani 1998, 2000; Lancelot et al. 2004; Sivathayalan and Logeswaran 2007, Lade and

Liggio Jr. 2014). These investigations were limited only to linear proportional strain paths in which the rate of volumetric inflow/outflow remained constant throughout shearing. However, the actual strain path encountered in-situ will be non-linear with steadily decreasing rate of volumetric inflow/outflow due to equalization of pore pressure gradients as a result of pore water migration (Sivathayalan and Logeswaran 2008). Invariably all these laboratory studies on partially drained behavior of sand were carried out under axisymmetric triaxial loading condition. Due to the stress path dependent behavior of soil, Logeswaran (2010) examined the anisotropic characteristics of Fraser River sand by monotonically shearing it along different orientation of principal stress axes under various linear volumetric strain path. No laboratory investigations pertaining to the response of Fraser River sand under generalized loading conditions along with non-linear volumetric strain paths have been found in the literature.

1.2 Objective of the thesis

In view of the lack of experimental database on the cyclic response of granular soil under the simultaneous action of compression and shear waves, and partially drained behavior of granular soils under generalized loading conditions, the major objectives of this research program are identified as follows:

- A simple numerical simulation to demonstrate simultaneous propagation of compression and shear waves in a soil element during an earthquake event, and to establish relative magnitudes of the S- and P- waves that could be typical during seismic shaking.

- Investigating the cyclic response of Fraser River sand under the simultaneous action of compression and shear waves. Examining the nature and magnitude of variation of principal stress direction under this loading scenario.
- Evaluating the effect of various initial stress state parameters such as initial effective confining stress (σ'_{mc}), consolidation stress ratio (K_c) and shearing parameters such as cyclic stress ratio (CSR), the ratio between shear stress and normal stress increments (S/N), phase shift (δ) between the waves and also exploring the effect of simultaneous action of shear wave and one-way compression wave on the cyclic response of sand.
- Characterizing the response of Fraser River sand under generalized loading conditions along with various non-linear volumetric strain paths.

1.3 Layout of thesis

Chapter 2 provides a brief discussion about the components of soil anisotropy, its origin and factors influencing it. It also describes the characteristics of the undrained response of soil under monotonic and cyclic loads. This chapter critically reviews the previous HCT investigations on the drained and undrained response of soil subjected to various monotonic and cyclic stress loading paths. The current state of understanding on the partially drained response of soil under various loading and drainage conditions is also discussed.

Chapter 3 describes the various features of the CU-HCT apparatus used in this research program. Chapter 4 documents the details of test materials, specimen preparation techniques and specimen assembly. This chapter also presents the results of preliminary

tests carried out to demonstrate the performance and control of CU-HCT apparatus, and to establish confidence in the measurements.

The effect of coupled action of compression and shear waves on the cyclic response of reconstituted sand specimens is demonstrated in chapter 5. The results of the finite difference simulation carried out to demonstrate the simultaneous propagation of compression and shear waves in a soil deposit during seismic shaking is discussed. The influence of initial effective confining stress (σ'_{mc}), cyclic stress ratio (*CSR*), the ratio between shear stress and normal stress increments (S/N) on the liquefaction characteristics of sand is examined.

The influence of consolidation stress ratio (K_c), phase shift (δ) between the waves and simultaneous action of shear wave and one-way compression wave on the cyclic response of sand is presented in chapter 6.

Chapter 7 discusses the stress path dependent behavior of Fraser River sand under partially drained condition and finally, chapter 8 presents the summary and conclusions derived from the experimental investigations carried out in this thesis.

2. LITERATURE REVIEW

2.1 *Introduction*

The first section of this chapter discusses the components of soil anisotropy, its origin and factors affecting it. Section 2.3 describes the different types of undrained response of soil under monotonic and cyclic loads with emphasis on the static and cyclic liquefaction. Section 2.4 reviews previous investigations to study the effect of principal stress direction and intermediate principal stress on the static shear strength characteristics of granular and cohesive soils. Section 2.5 describes the different types of seismic waves and their complex interaction with the soil layers beneath the earth's surface. The basics of seismic wave propagation, and wave refraction at geological interfaces are presented to demonstrate the need for better understanding the response of soils under multiple waves. The influence of stress paths resulting from the common dynamic loading conditions such as wave, earthquake, and traffic loading on the cyclic behaviour of soil is reviewed in section 2.6. Section 2.7 presents the current state of understanding of the partially drained behaviour of soil resulting from the simultaneous change in the pore water pressure and pore volume. Finally, section 2.8 summarizes the key points of interest and presents the research gap identified from this review.

2.2 *Anisotropy of soils*

Natural soil deposits are generally recognized to be anisotropic because of the directional dependence of their mechanical properties such as permeability, shear strength and stiffness. Casagrande and Carillo (1944) originally recognized that anisotropy arises on account of two mechanisms and termed them inherent anisotropy and induced anisotropy.

Inherent anisotropy is a physical characteristic of the soil which is a reflection of the material and the deposition process, but independent of the applied stresses and strains, whereas induced anisotropy entirely depends upon the strains associated with the applied stresses (Arthur and Menzies 1972; Arthur et al. 1977) and evolves during the loading process.

2.2.1 Inherent Anisotropy

Inherent anisotropy of granular materials results from the natural sedimentation process and particle-shape characteristics of the soil. During gravitational deposition, the particle's long axis aligns with the bedding plane, which is normal to the direction of deposition, creating an anisotropic soil structure. The existence of inherent anisotropy in soil has been identified by several researchers (Phillips and May 1967; Arthur and Menzies 1972; Arthur et al. 1977; Oda 1972; Wong and Arthur 1985; Mahmood and Mitchell 1974; Lade and Kirkgard 2000).

Arthur and Menzies (1972) developed a cubical triaxial cell which allowed the deposition of sand at any axis relative to the direction of principal stresses. They demonstrated that inherent anisotropy of granular soils depends mainly on the mode of deposition and deposition history. This was further proven and extended by a series of drained triaxial compression tests conducted by Oda (1972, 1978). It was shown that the degree of anisotropy depends on the shape characteristics of the soil grains and on the method of deposition. Different deposition modes yield different soil fabric, and the differences in initial soil fabric greatly influences the shear strength characteristics of the soil. Vaid et al. (1999) performed a series of undrained tests to show the effect of different deposition methods on the resulting soil fabric. It has been shown that under similar initial

stress states and density, water pluviated specimens exhibited strong dilative response (Figure 2.1) whereas moist tamped specimens were contractive.

Soils deposited under natural sedimentation process possess a vertical axis of symmetry, and thus the properties are identical in the horizontal plane and different in the direction of deposition. This is referred to as transverse-isotropy or cross-anisotropy. Previously, several studies on cross-anisotropy were carried out under triaxial condition, in which samples were deposited with bedding planes inclined at different angles to the vertical axis of the specimen (Oda 1972; Tatsuoka et al. 1986; Lade and Wasif 1988). However, it is reported that specimens with inclined bedding planes may not produce trustworthy results because the stress-strain behavior needs complex interpretations which are highly unreliable (Saada 1970; Lade and Kirkgard 2000). With the advent of advanced laboratory testing devices such as true triaxial, directional shear cell and hollow cylinder torsional shear apparatus the effects of cross-anisotropy were investigated by rotating the direction of principal stresses with respect to the deposition axis (Yamada and Ishihara 1979; Ochiai and Lade 1983; Symes et al. 1984; Uthayakumar and Vaid 1998).

With true triaxial Yamada and Ishihara (1979) and Ochiai and Lade (1983) observed that effects of cross-anisotropy is more prominent under pre-failure strain range and it vanishes completely when the strains are sufficiently large. Symes et al. (1984) and Uthayakumar and Vaid (1998) confirmed the existence of cross anisotropy in pluviated sand specimens using a hollow cylinder torsional shear device and showed that the undrained shear response is greatly influenced by the inclination of principal stress to the deposition axis.

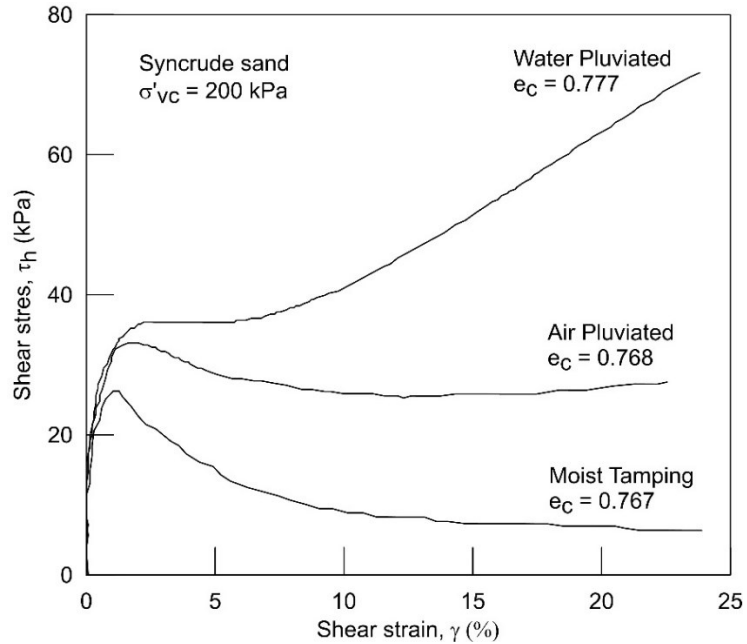


Figure 2.1: Effect of reconstitution methods on the undrained simple shear response of Syncrude sand (after Vaid et al. 1999)

2.2.2 Induced Anisotropy

Casagrande and Carillo (1944) defined induced anisotropy as the spatial re-orientation of solid particles and voids due to the strains associated with the applied stresses. When a granular soil assembly is subjected to shear deformation, it undergoes a continuous change in the interparticle contact forces and internal geometry. As the shear deformation progresses, the contact normals tends to align with the direction of the major principal stress (σ_1). New contact normals creating a load carrying structure, will be generated along the σ_1 -direction, leading to the formation of anisotropic soil fabric (Oda et al. 1985; Rothenburg and Bathurst 1989; Oda and Iwashita 1999). Arthur et al. (1977) recognized that any rotation of principal stress axes necessitates the re-alignment of the load carrying contacts and it is also shown that the soil exhibits weaker response when the principal stress direction changes from the deposition plane to bedding plane.

Most of the natural soil deposits possess a combination of both inherent and induced anisotropy. This combined anisotropy gives rise to the stress path dependent behaviour of the soil. This implies that the soil response depends not only on the magnitude of principal stresses but also on the initial direction of principal stresses with respect to the deposition direction, and any subsequent rotation of principal stresses. Almost all geotechnical problems such as excavations, embankment construction and loading of footings involve rotation of principal stresses (Lade and Kirkgard 2000). In a dynamic loading environment such as earthquake, wave or traffic loading, these rotations are continuous and cyclic in nature. Several studies have shown that the shear strength characteristics of soils are heavily influenced by the mode of load application (Uthayakumar and Vaid 1998; Foundoukos 2006; Minh 2006; Brosse 2012; Lade et al. 2013). The effect of loading mode on the drained and undrained shear behaviour of soil will be discussed in detail in the forthcoming sections.

2.3 *Undrained behaviour of soil*

The deformation characteristics of soil under undrained condition forms the basis for understanding the liquefaction of soil during earthquakes. Liquefaction is a phenomenon in which the saturated soil loses its strength and stiffness due to seismic or other rapid loading under undrained condition. During seismic shaking, excess porewater pressure develops in the soil, leading to loss of contact between the soil particles. As a result, soil softens and may behaves like a liquid at the extreme instance.

Over the last five decades, soil liquefaction was defined in many ways by several researchers. Some defined liquefaction as the condition of zero effective stress due to the accumulation of pore water pressure during cyclic loading (Seed and Lee 1966; Lee and

Seed 1967; Ishihara 1982). This zero-effective stress state may be temporary during each loading cycle, but the strains associated with it is large enough to cause the shear failure of the soil. On the other hand, the strain softening response of loose saturated sand under undrained loading is also termed as liquefaction (Casagrande 1975; Castro 1969).

Most of our understanding on the soil liquefaction is derived from the laboratory element tests. A knowledge on the undrained response of granular soils is very essential in evaluating the liquefaction and post liquefaction characteristics of soil. The following section discusses the current state of understanding of static and cyclic liquefaction.

2.3.1 Static undrained response of granular soils

Static undrained response of saturated sands has been extensively investigated under triaxial compression loading mode (Lee and Seed 1967; Castro 1969; Chern 1985; Ishihara 1993; Vaid and Thomas 1995). Figure 2.2 illustrates the three distinct types of stress-strain response obtained from the triaxial tests on saturated sand specimens. The type of response depends on the initial stress state variables such as relative density, confining pressure, initial static shear stress, soil fabric and loading mode. At a given initial stress state, as the relative density of the specimen increases, the type of response changes from strain softening (Type 1) to strain hardening response (Type 3).

Loose sand at high initial confining stress exhibits Type 1 response. At smaller shear strain (less than 1%) shear strength of the soil increases with the increase in shear strain, until reaching a peak value. After that, the shear strength drops and reaches a constant value accompanied by an unlimited deformation. This type of response is called as strain softening or contractive or flow type response. Castro (1969), Casagrande (1975) and Seed (1979) termed this response as flow liquefaction and Chern (1985) termed it as

true liquefaction. This state of sand with unlimited deformation at a constant shear stress and constant void ratio is termed as the steady state (Castro 1975; Castro and Poulos 1977). The shear strength of the sand at this steady state is known as the undrained steady state strength or residual strength.

Medium dense sand exhibits type 2 response, in which sand strain softens over a moderate shear strain range, and after that it strain hardens with the increase in shear strain. This behavior of sand is called flow type with limited deformation or limited liquefaction (Castro 1969; Vaid and Chern 1985) or partial liquefaction (Lee and Seed 1967). The state where a temporary drop in shear stress takes place over a limited strain is termed as Quasi steady state (Ishihara et al. 1975; Alarcon-Guzman et al. 1988; Been et al. 1991; Vaid et al. 1990). The transient state in which the response of the sand changes from contractive to dilative deformation is termed as the state of phase transformation. Dense sand or loose sand at low confining stress shows type 3 strain hardening response, where the shear strength increases with the shear strain. At larger strains, similar to type 1 response, both type 2 and type 3 response will ultimately reach a steady state once all the dilation got over.

2.3.2 Cyclic response of granular soil

Undrained cyclic loading causes a progressive accumulation of excess pore water pressure and an increase in cyclic shear strain with the increasing number of loading cycles. Like monotonic response, the following factors influence the cyclic response of saturated sand: (i) initial stress state variables such as void ratio, effective stress, sand fabric and pre-strain history prior to cyclic loading and (ii) prescribed stress paths. Apart from this, the ability of the testing devices, loading method and data acquisition system to track the true element behavior also affects the cyclic test results (Vaid and Sivathayalan 2000).

Most of the earlier investigations on cyclic behavior of soil were derived mostly from cyclic triaxial tests. From cyclic triaxial tests on saturated sand specimens, Vaid and Chern (1985) identified different strain development mechanisms depending upon the initial stress state of the sand specimens. These deformation mechanisms are true liquefaction, limited liquefaction, and cyclic mobility.

Figure 2.3 illustrates a typical true liquefaction response of sand under cyclic loading. It has the same characteristics as the Type 1 strain softening response under monotonic loading. Strain softening with unlimited flow deformation is triggered at a critical value of effective stress ratio called critical stress ratio (*CSR*). Very large deformation is initiated when the effective stress state reaches the steady state. The state of zero effective stress is not realized in this response. The soil is deemed to have not liquefied, if the liquefaction criteria is based on the 100% excess pore pressure criteria.

A typical limited liquefaction response which has similar characteristics of the type 2 monotonic response is shown in Figure 2.4. Strain softening with limited liquefaction is triggered when the effective stress state crosses the *CSR* line. The softening response is arrested when the stress state touches the phase transformation (*PT*) line. Following the liquefaction, the subsequent application of cyclic loading causes progressive accumulation of shear strain with the number of cycles. True liquefaction and limited liquefaction can occur when the cyclic stress amplitude is larger than the minimum undrained shear strength of sand.

Cyclic mobility is characterized by the progressive increase in pore pressure and cyclic shear strain without any strain softening. Shear strain development is small, when the effective stress state is below the stress ratio corresponds to the *PT* line. Large

deformation occurs when the effective stress state crosses the PT line. In some cases, when the cyclic loading is continued beyond phase transformation, the increase in excess pore pressure, bring the sand specimen to a state of zero effective stress (Figure 2.5). Further cyclic loading results in a transient state of zero effective stress. This state is responsible for the development of large deformation. For this transient state to occur, the net shear stress during cyclic loading should be zero. If the initial static shear stress is greater than the cyclic shear stress, cyclic mobility occurs without realizing the state of zero effective stress. Gradual accumulation of shear strain is witnessed in this case of cyclic mobility (Figure 2.6).

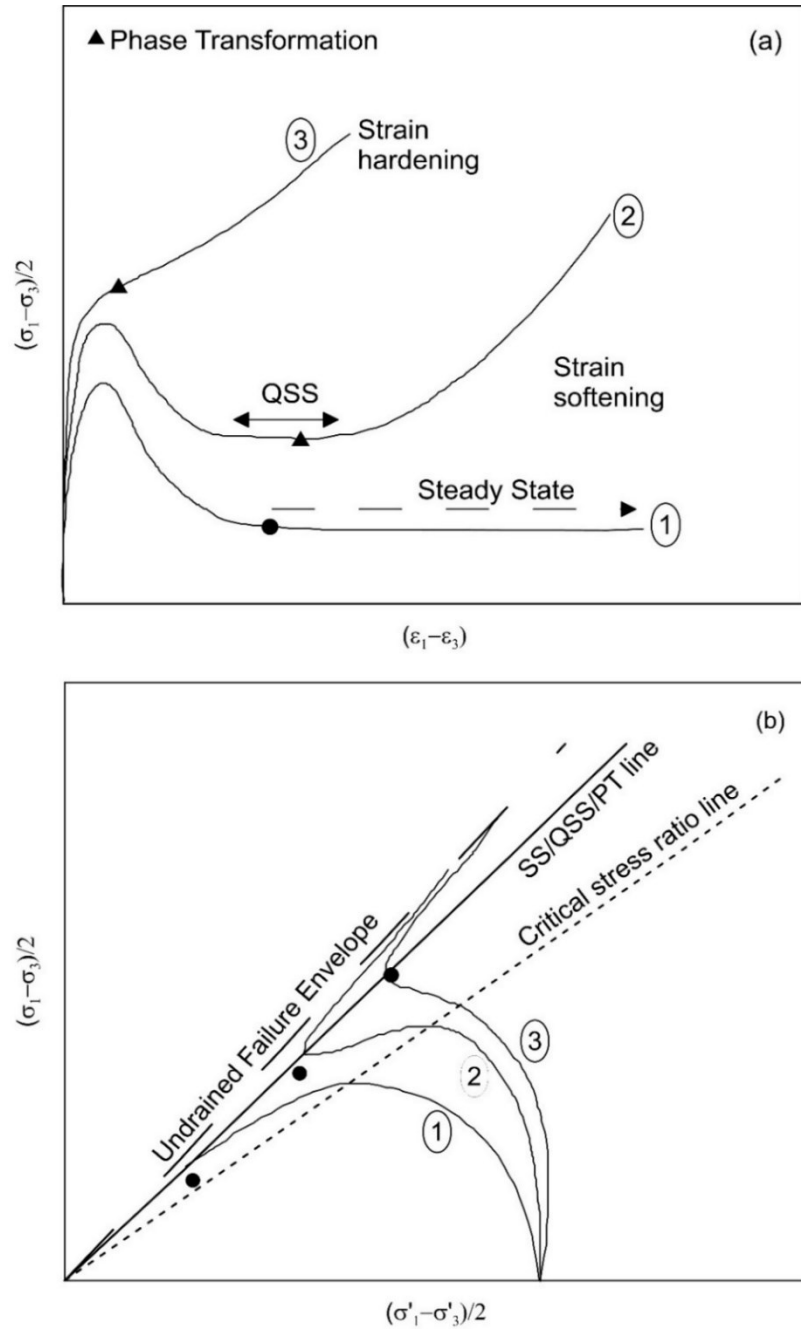


Figure 2.2: Typical undrained monotonic response of saturated sand (a) stress-strain responses (b) stress paths

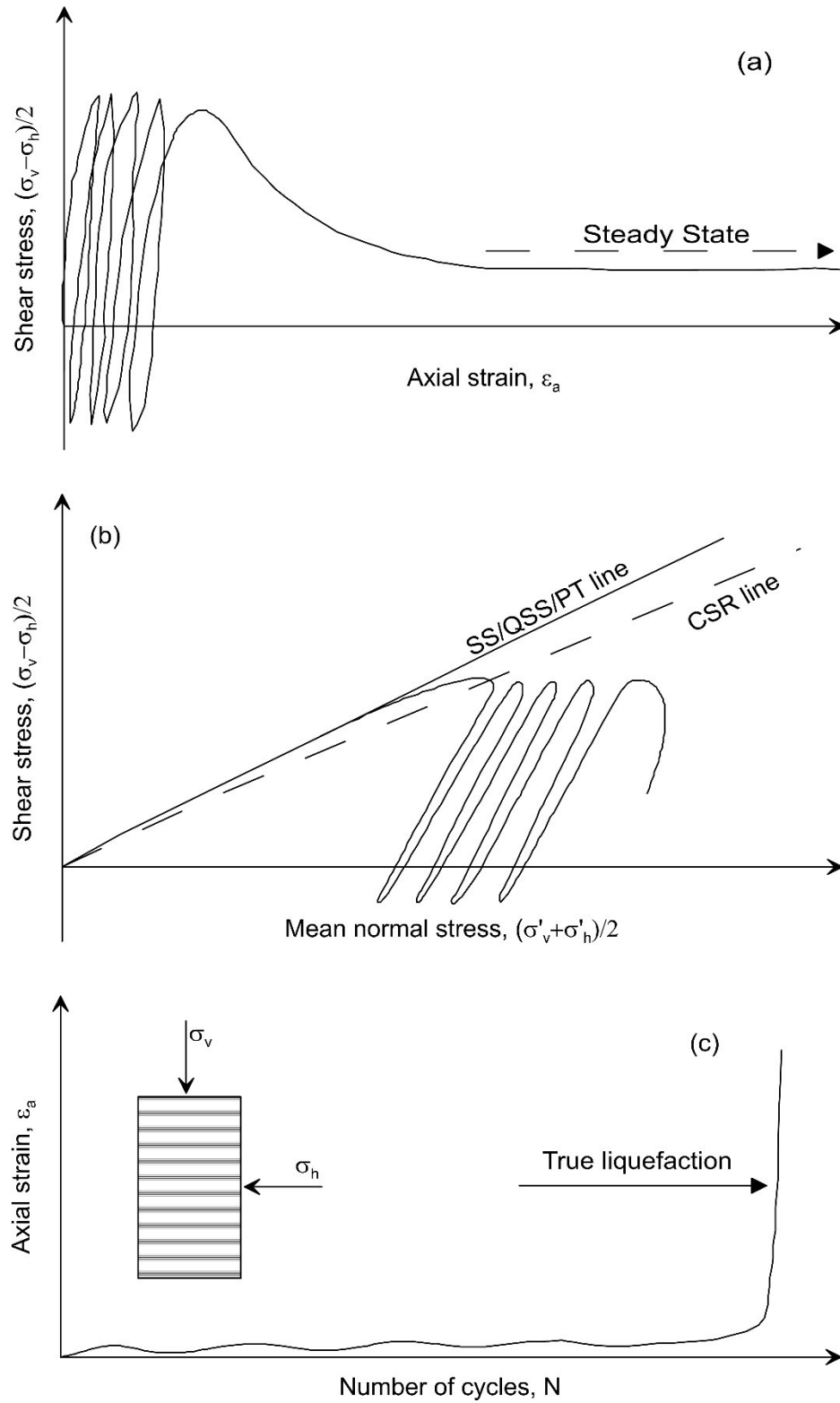


Figure 2.3: True liquefaction response of sand under cyclic loading (after Vaid and Chern 1985)

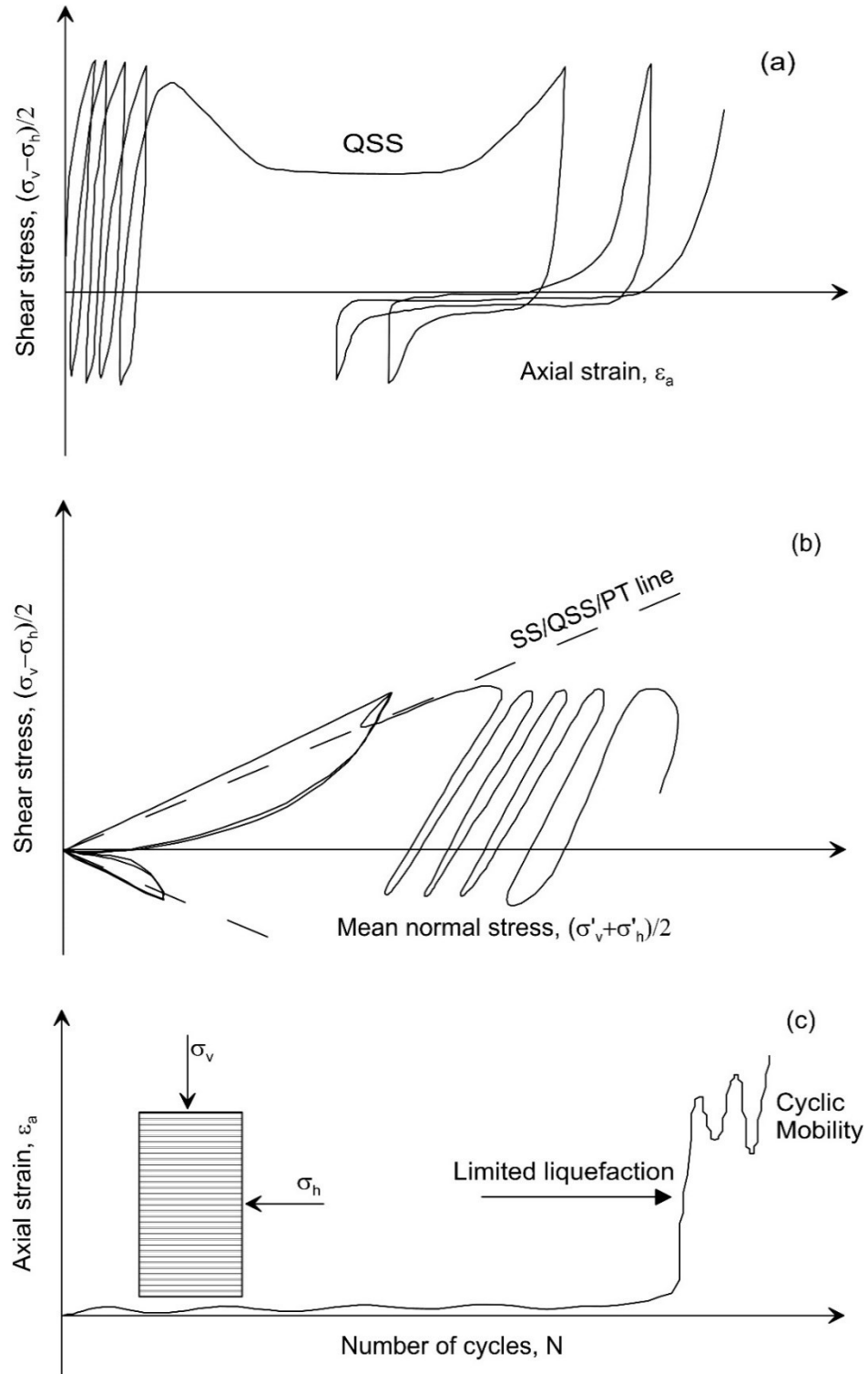


Figure 2.4: Limited liquefaction of sand under cyclic loading (after Vaid and Chern 1985)

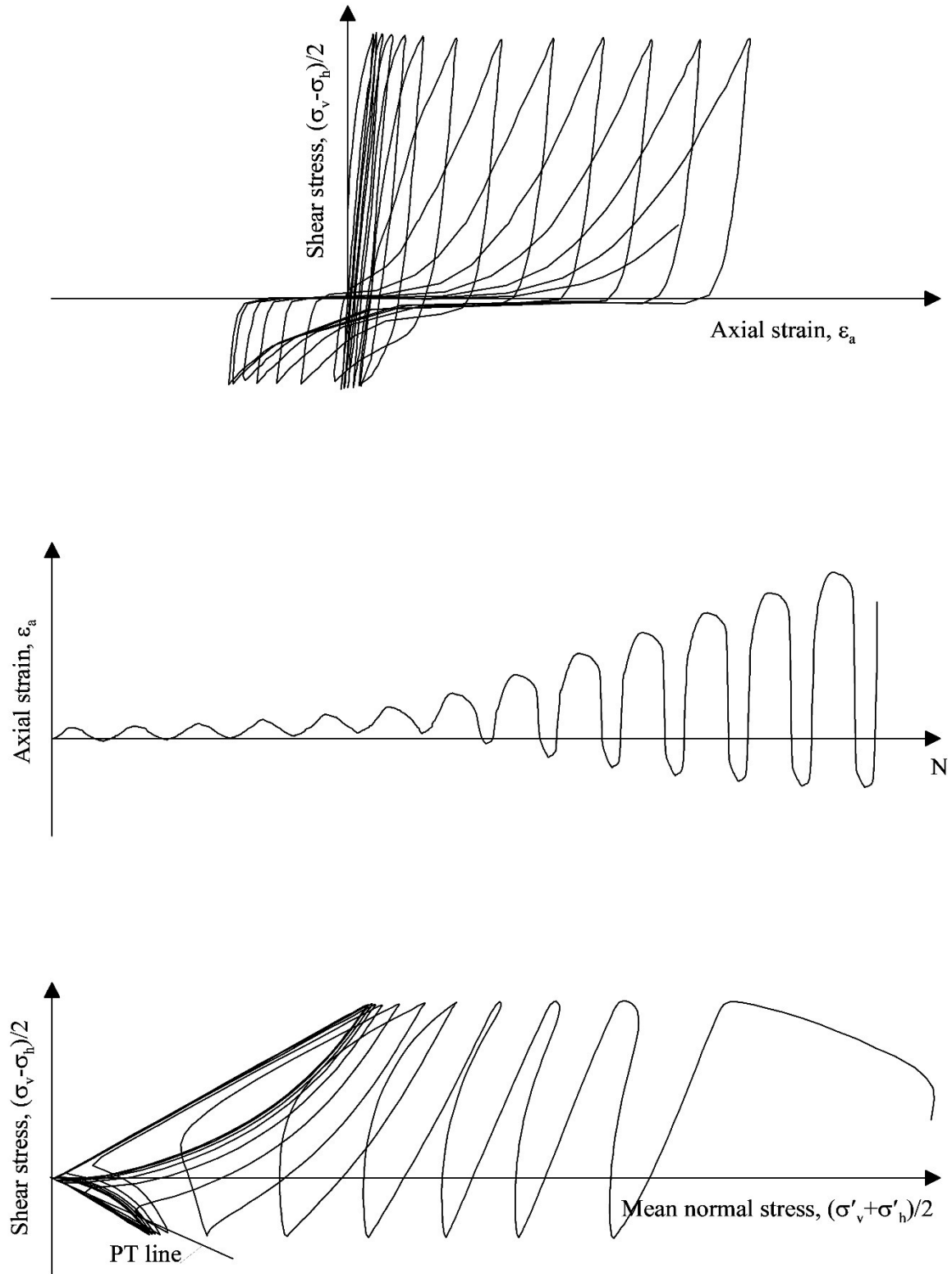


Figure 2.5: Cyclic mobility with transient zero effective stress state (after Vaid and Chern 1985)

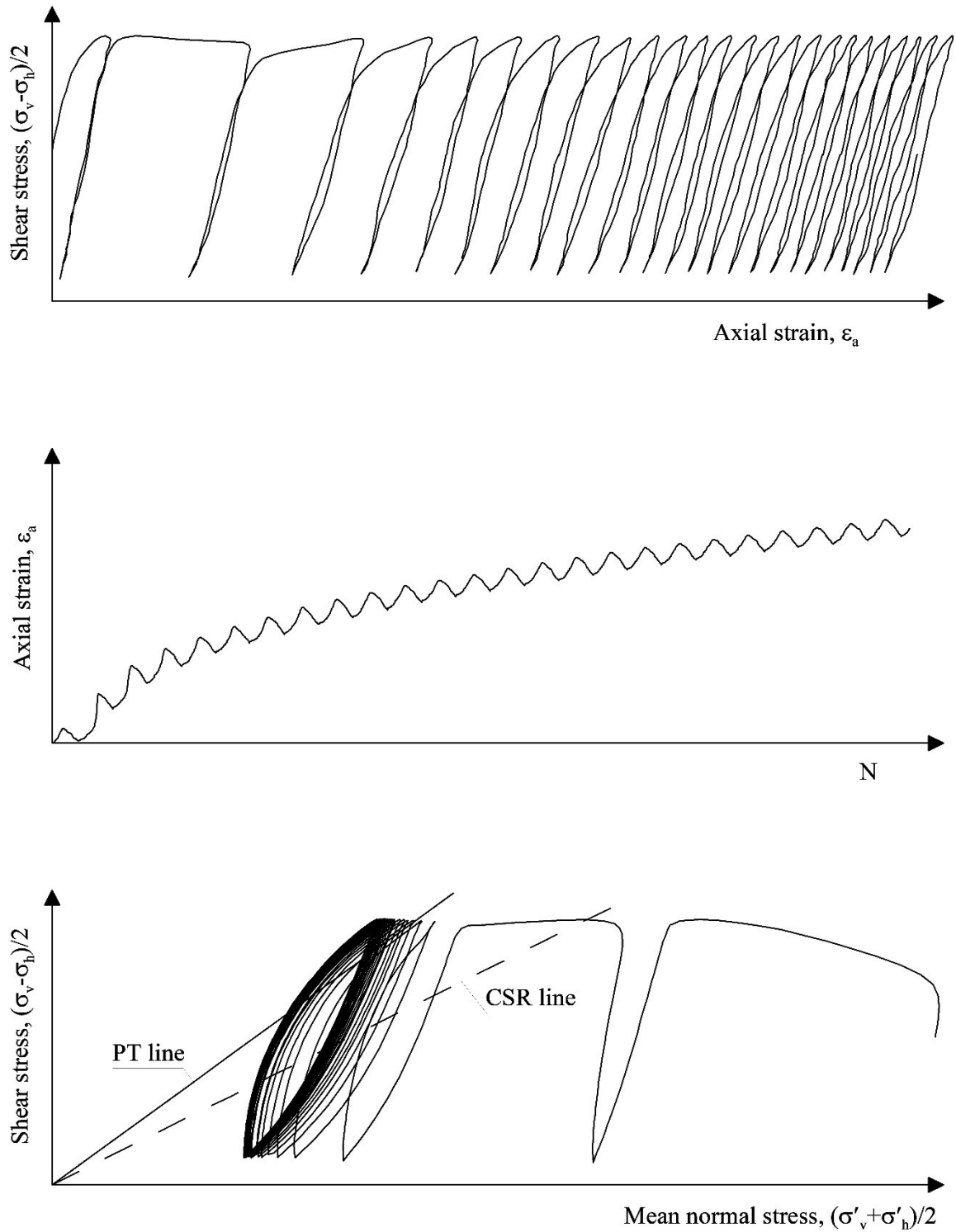


Figure 2.6: Cyclic mobility without transient zero effective stress state (after Vaid and Chern 1985)

2.4 *Stress path dependent behaviour of soil*

As mentioned earlier, the cross-anisotropic nature of soil gives rise to the stress path dependent behavior. This combined with the dependence of dilation on confining stress level implies that soil response depends on both the magnitude of effective principal stresses ($\sigma'_1, \sigma'_2, \sigma'_3$) and the orientation of major principal stress with respect to the axis of deposition (α_σ). Several researchers highlighted the necessity of laboratory devices which allow direct and independent control over the rotation of principal stresses and intermediate principal stress parameter, (b_σ) (Finn et al. 1978; Arthur et al. 1980; Hight et al. 1983; Zdravkovic et al. 2002; Leroueil and Hight 2003).

In a conventional triaxial cell, the values of α_σ and b_σ are null during compression tests and $\alpha_\sigma = 90^\circ$ and $b_\sigma = 1$ during extension tests; whereas in simple shear tests, there is an uncontrolled rotation of the principal stress direction between $\pm 45^\circ$. In a true triaxial apparatus, which tests cubical and prismatic soil samples, b_σ can be varied continuously but α_σ can only change abruptly from 0° to 90° . The directional shear cell (DSC) developed by Arthur (1988) can be employed to study the stress path dependent behavior by controlling the direction of principal stresses. However, this is a plane strain device and it is inefficient in controlling the effective mean normal stress (σ'_m) and b_σ independently. DSC also has limitations in strain measurement, pore pressure measurements and drainage control (Menkiti 1995).

Therefore, to understand the effects of stress paths on soil behaviour, it is necessary to isolate the effects of α_σ or b_σ while keeping other stress parameters constant. In this regard, a hollow cylinder torsional (HCT) shear device is versatile device, which can control the parameters such as $\alpha_\sigma, b_\sigma, \sigma'_m$ and deviatoric stress (σ_d) independently, with

full control on drainage. The following section reviews the research outcomes of the tests carried out using HCT under different monotonic stress paths.

2.4.1 Behaviour of granular soil under monotonic shearing

It is observed from a series of undrained triaxial tests that many soils exhibit more contractive or softer response in triaxial extension than in triaxial compression (Tatsuoka and Ishihara 1974; Miura and Toki 1982; Vaid and Thomas 1995; Vaid et al. 1990). This demonstrated the effect of principal stress direction and intermediate principal stress on the undrained shear response of cross-anisotropic granular deposits since $\alpha_\sigma = 0$ & $b_\sigma = 0$ in triaxial compression and $\alpha_\sigma = 90$ & $b_\sigma = 1$ in triaxial extension. Therefore, to characterize the effect of loading mode on sand behavior, several researchers conducted drained and undrained monotonic tests using a hollow cylinder torsional shear apparatus by independently varying α_σ and b_σ .

Undrained shearing of pluviated sand specimens with different inclination of major principal stress axis (α_σ) reveals that the response of the sand systematically changes from strain hardening to strain softening as the σ_1 direction changes from axis of deposition towards the direction of bedding plane (Symes et al. 1984; Uthayakumar and Vaid 1998; Yoshimine et. al. 1998; Logeswaran 2010). It is also noted that the above conclusion holds true even for different relative densities and b_σ values (Uthayakumar and Vaid 1998; Yoshimine et. al. 1998). Yoshimine et al. (1998) demonstrated that for any density, larger maximum excess pore pressure is generated under the conditions of larger b_σ and α_σ values.

Symes et al. (1984) explained the influence of α_σ on soil response through a state boundary surface (SBS) concept modified after Roscoe et al. (1958). This modified state

boundary surface helps to predict the response of granular materials subjected to different stress paths involving principal stress rotation. The SBS proposed was based on the tests on sub-angular Ham River sand with limited α_σ values of 0° , 24.5° and 45° . Shibuya and Hight (1987) extended this SBS model for the full range of α_σ values between 0° and 90° and also for spherical particles. It was also observed that the anisotropy is more pronounced for natural sand with angular to sub angular grains when compared with the spherical glass particles.

Uthayakumar and Vaid (1998) from a series of undrained tests on Fraser River sand subjected to various stress paths, observed that the friction angle mobilized at phase transformation (ϕ_{PT}) is unique for a given material and it is independent of the applied stress paths and initial conditions. The brittleness index (I_B), proposed by Bishop (1971) to characterize the flow potential of a contractive sand, was found to increase with an increase in α_σ . Sivathayalan and Vaid (2002) extended the above study for Fraser River sand consolidated to different initial stress states. It is observed that irrespective of the different effective consolidation stress ratios ($K_c = \sigma'_{1c}/\sigma'_{3c}$), the undrained response of sand remains unaltered; i.e. the sand strain softens more when σ_1 aligns towards the bedding plane. Figure 2.7 demonstrates the effect of α_σ on the undrained shear behavior of Fraser River sand consolidated with $K_c = 1.5$ and tested under plane strain condition. This study proposed a modified brittleness index ($I_{\bar{B}}$) to characterize the flow potential of anisotropically consolidated specimens. For higher α_σ values, increasing K_c increases $I_{\bar{B}}$ which implies that the potential for flow failure is more in these cases. It is also established that the minimum undrained shear strength of the sand depends not only the initial void

ratio but also the initial confining pressure, initial static shear stress and the orientation of major principal stress with respect to the deposition axis.

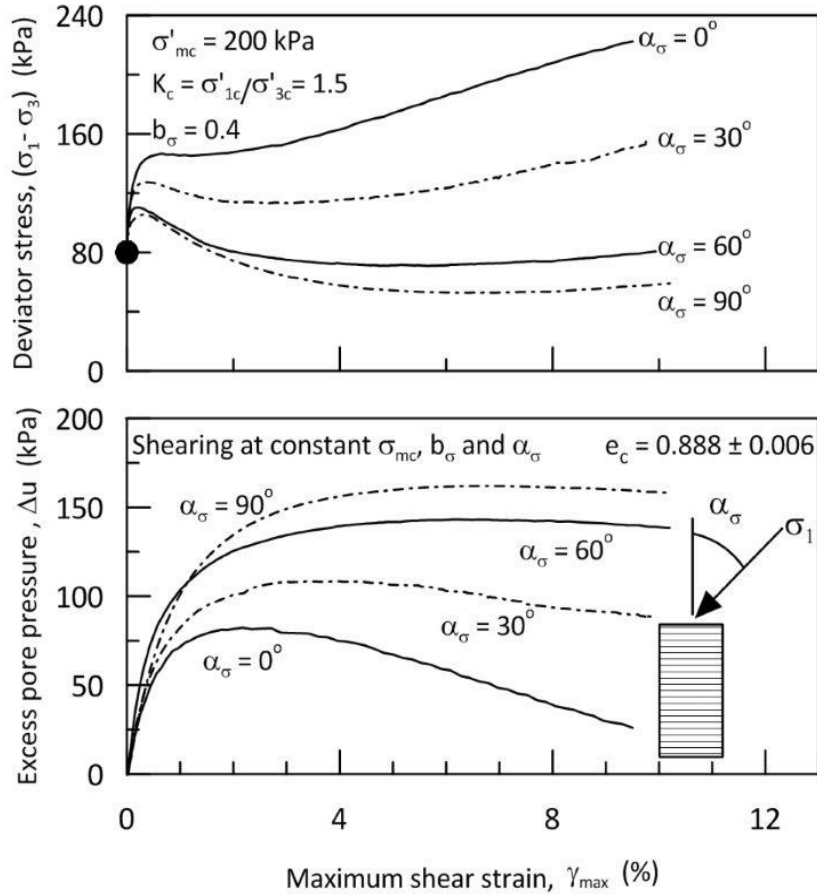


Figure 2.7: Direction-dependent monotonic behavior of water-deposited Fraser River sands (after Sivathayalan and Vaid 2002)

Logeswaran (2010) observed that the undrained shear strength of the loose Fraser River sand significantly reduces when α_σ varied from 0° to 45° , beyond which the strength reduction was insignificant. It has also been shown that the undrained effective stress path is independent of applied total stress paths involving the changes in both α_σ and b_σ .

Drained tests on cross-anisotropic sand deposits with different α_σ values also confirmed the existence of weak shear resistance along the bedding plane (Miura et al.

1986; Lade et al. 2008; Wijewickreme and Vaid 2008; Lade et al. 2013; Yang 2013). This weak resistance is attributed due to the poor interlocking of elongated sand particles along the bedding plane. Miura et. al. (1986) demonstrated that a mere rotation of principal stress axis without any alteration in the magnitudes of the principal stresses, triggers contractive response even in dense sand specimens.

The effects of α_σ and b_σ on the drained strength of Santa Monica beach sand was investigated by Lade et al. (2008). Here the α_σ and b_σ are linked to each other by maintaining same inner and outer pressure in the hollow cylinder apparatus ($b_\sigma = \sin^2 \alpha_\sigma$). Experimental result shows that with this superimposed effect, the drained friction angle increases with an increase in b_σ value until plane strain condition ($b_\sigma = 0.4$) and after that it reduces until the b_σ value reaches the triaxial extension condition ($b_\sigma = 1$). Lade et al. (2013) studied the independent influence of α_σ and b_σ on the drained shear response of dense Nevada sand. Test results shows that for all b_σ values, lowest friction angle was observed when the direction of major principal stress coincides with the direction of the bedding plane.

The drained response of loose Ottawa sand under simultaneous increase in principal stress ratio ($R = \sigma'_1/\sigma'_3$) and α_σ was examined by Wijewickreme and Vaid (2008). A unique relationship was observed between the horizontal shear stress ($\tau_{z\theta}$) vs horizontal shear strain ($\gamma_{z\theta}$) response and it is independent of the applied linear stress paths in R- α_σ space. Linear strain paths were observed in all the tests which suggests that inherent anisotropy is preserved even for loading involving the simultaneous increase in R and α_σ . It is also demonstrated that along linear R- α_σ path, the direction of principal strain

increment coincides with the direction of principal stress increment when the direction of stress increment remains close to the deposition direction.

The shear band formations are significant in medium dense to dense sand subjected to drained shearing involving various stress paths. These shear bands predominantly develop along the weak bedding plane (Lade et al. 2008). Lade et al. (2014) examined shear banding formation in dense Nevada sand for different combinations of α_σ and b_σ . Experimental observation shows that irrespective of all the α_σ , a canyon type of shear bands was formed for higher b_σ values. This shear band formation significantly influences the friction angle of the sand.

Another important aspect in the shear response of cross-anisotropic materials is non-coaxiality between the direction of principal strain increment and the direction of principal stress. Non-coaxiality is pronounced more for the cases where the direction of major principal stress is not aligned with the direction of deposition during shearing (Gutierrez and Ishihara 2000; Tsutsumi and Hashiguchi 2005; Lade et al. 2009; Blanc et al. 2011; Yang 2013; Rodriguez and Lade 2014). Under drained shearing, the degree of non-coaxiality reduces when the sand specimens reach failure (Lade et al. 2009; Yang 2013). Yang (2013) noted that the particle shape and relative density has less significant influence on the non-coaxial behaviour of granular materials when compared to its pre-shear history. Jiang et al. (2016) investigated the elemental and non-coaxial behavior of granular soil subjected to a highly complex stress path due to vertical excavation. In this study, discrete element modelling (DEM) is used to simulate the excavation process supported by the retaining wall, and the stress path obtained from DEM is used as an input

data for the HCT test. It is observed from the drained tests on HCT that the non-coaxiality is significantly influenced by the deviator stress than the mean normal stress.

2.4.2 Behaviour of cohesive soil under monotonic shearing

Most of the available investigations on the stress path dependent behaviour of soil using HCT focused mainly on the reconstituted granular materials. Only very few HCT studies are available on the reconstituted or natural clay samples. This is because of the complexities associated with the preparation of the tall and thin wall specimens from natural and reconstituted clays, and the laboriousness in conducting long duration hollow cylinder tests (Minh 2006).

Hong and Lade (1989a) conducted a series of undrained torsional shear tests to study the effect of stress rotation on the shear strength characteristics of K_0 -consolidated reconstituted clay samples. Test results revealed that the reconstituted specimen behaved isotropically, which suggest that cross anisotropy is more pronounced in natural clay than in the remolded clays. The stress conditions of the remolded clays at failure are unaffected by the stress paths and principal stress rotation. Due to this isotropic behaviour, the direction of major principal strain increment coincides with the direction of major principal stress increment at small shear strain and the specimen progress towards the failure with this co-axiality (Hong and Lade 1989b).

Frydman et al. (1995) presented the results of HCT tests on normally consolidated marine clay to evaluate the validity of the assumption of co-linearity between plastic strain increment and principal stress throughout the shearing range. It is shown that for natural clays, when the rotation of principal stress occurs, the direction of principal plastic strain

increment does not coincide with the direction principal stresses. Coaxiality was observed after the onset of yielding.

The effects of coupled α_σ and b_σ on the undrained strength characteristics of K₀-consolidated natural soft clay was investigated by Lade and Kirkgard (2000). It was observed that for the tested natural clay, the undrained shear strength decreases systematically as the coupled α_σ and b_σ changes from triaxial compression to triaxial extension condition. Test results also indicated the existence of non-coaxiality between principal stress direction and principal strain increment direction at failure.

Nishimura et al. (2007) investigated the influence of α_σ on the peak shear strength anisotropy of natural, highly over-consolidated stiff London clay. At $b_\sigma = 0.5$, minimum shear strength was observed at $\alpha_\sigma = 45\sim 67^\circ$ and maximum strength was observed at $\alpha_\sigma = 0^\circ$. There is almost 40% reduction in the peak shear strength as the α_σ increases from 0° to 45° . HCT tests on samples at different depths revealed that the degree of anisotropy increases with the increase in depth.

The elastic stress-strain response of cross-anisotropic materials are characterized by five elastic constants. These elastic constants are young's modulus in the vertical and horizontal direction (E_v, E_h), shear modulus in vertical plane ($G_{vh} = G_{hv}$), Poisson's ratio for the effect of vertical strain on horizontal strain (ν_{vh}) and for the effect of horizontal on complementary horizontal strain (ν_{hh}). Characterizing the stiffness response of cross anisotropic materials is important in developing efficient constitutive models. Only a few attempts were made to study the stiffness anisotropy of natural clays. Brosse et al. (2017, 2018) evaluated the directional dependency of undrained stiffness characteristics of four medium plastic, heavily over-consolidated stiff marine clays. Experimental results showed

that the horizontal and vertical stiffness degradation curves vary with α_σ . E_h degradation curves showed wider variation than the E_v curves. The torsional shear stiffness is unaffected by the loading direction. It is also shown that the stiffness degradation curves from the triaxial compression may overestimate the E_v response and underestimate the E_h response over the operational strain range in the practical geotechnical problems involving stress rotations.

2.5 Seismic wave propagation

Earthquakes are manifested as ground shaking triggered by the sudden release of energy in the earth's lithosphere. This energy release is caused by various sources such as fault rupture, volcanic eruption, manmade explosions, collapse of underground cavities and reservoir induced. Almost 10% of the total plate tectonic energy is dissipated in the form of seismic waves due to fault ruptures (Elnashai and Sarno 2008). The seismic waves are elastic waves and they can propagate within the interior of the Earth ("body waves") or along Earth's surface ("surface waves").

2.5.1 Body waves

Body waves propagate through the interior of the earth and depending upon the particle motion associated with it, body waves are classified into primary waves (P- waves) and secondary waves (S-waves). In case of primary wave (or longitudinal wave) the particle motion is along the direction of wave propagation (Figure 2.8). Since P-wave exerts successive compression and rarefaction on particles, it only causes change in particle dimension or volume. P-waves are the fastest waves and it travel through both solids and fluids.

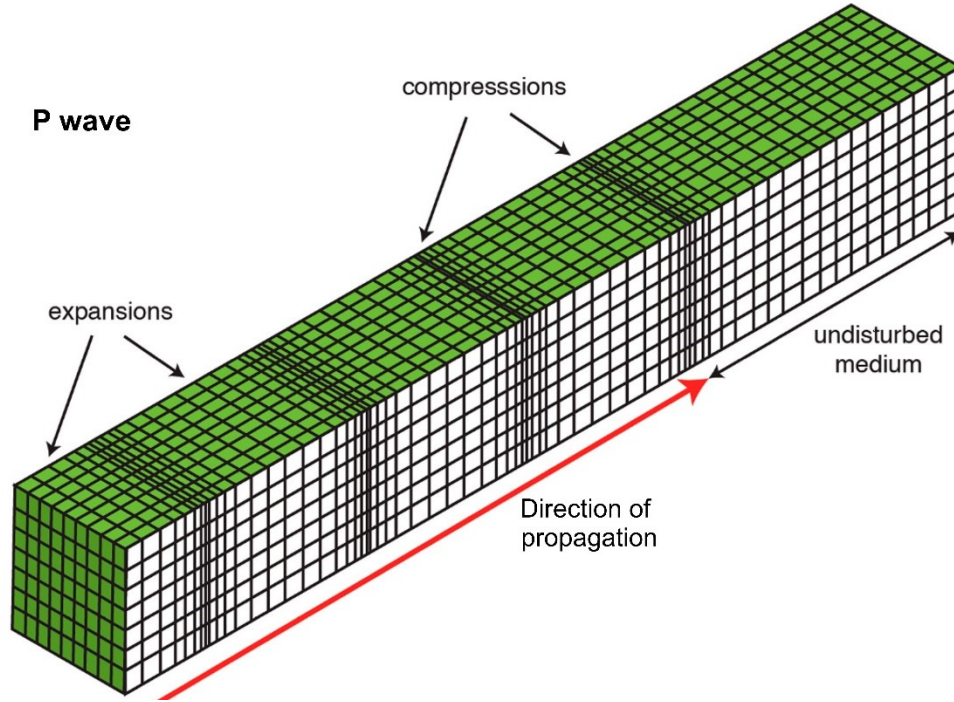


Figure 2.8: Particle motion induced by P-wave (adopted from Shaw et al. 2018)

In secondary or shear waves, the particle motion caused by the shear stress is in the direction normal to the direction of wave propagation (Figure 2.9). Depending upon the direction of particle movement, the S-waves are divided into two components, SH (horizontally transverse motion) and SV (vertically transverse motion). Shear waves does not change the particle dimension, it only changes the particle shape. Since fluids have no shearing stiffness, they cannot sustain the shear waves. In a homogeneous, isotropic, and infinite elastic medium, the propagation velocities of the body waves v_P and v_S are given by:

$$v_P = \sqrt{\frac{E(1-\nu)}{\rho(1+\nu)(1-2\nu)}} \quad (2.1)$$

$$v_S = \sqrt{\frac{E}{2\rho(1+\nu)}} = \sqrt{\frac{G}{\rho}} \quad (2.2)$$

where ρ , E , G and ν are the density, Young's modulus, shear modulus and Poisson's ratio of the elastic medium, respectively.

The ratio between v_P and v_S is given by:

$$\frac{v_S}{v_P} = \sqrt{\frac{(1-2\nu)}{2(1-\nu)}} \quad (2.3)$$

For geological material, ν ranges between 0.3 to 0.5, and thus $0 \leq v_S \leq 0.53 v_P$.

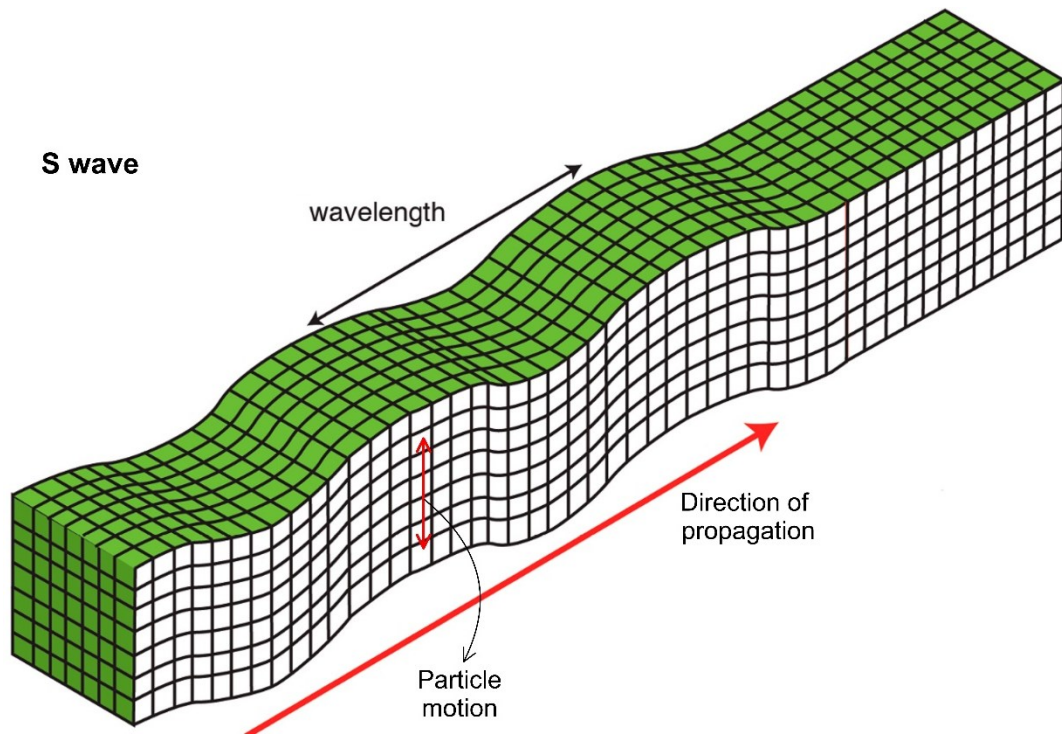


Figure 2.9: Particle motion induced by S-wave (adopted from Shaw et al. 2018)

2.5.2 Surface waves

Surface waves are generated by the interaction of body waves with the surficial layers of the earth. Surface waves travel along the earth's surface with exponentially decreasing amplitude with depth. Generally, these waves are dispersive in nature i.e., waves with different frequency components travel with different velocities. Based on the type of interaction with the earth's surface, there are two important surface waves: Rayleigh wave and

Love wave. In a homogeneous elastic half space, Rayleigh waves are generated by the interaction of P and SV-waves with the earth surface. Rayleigh waves cause an elliptical motion of particles with no transverse or perpendicular motion (Figure 2.10).

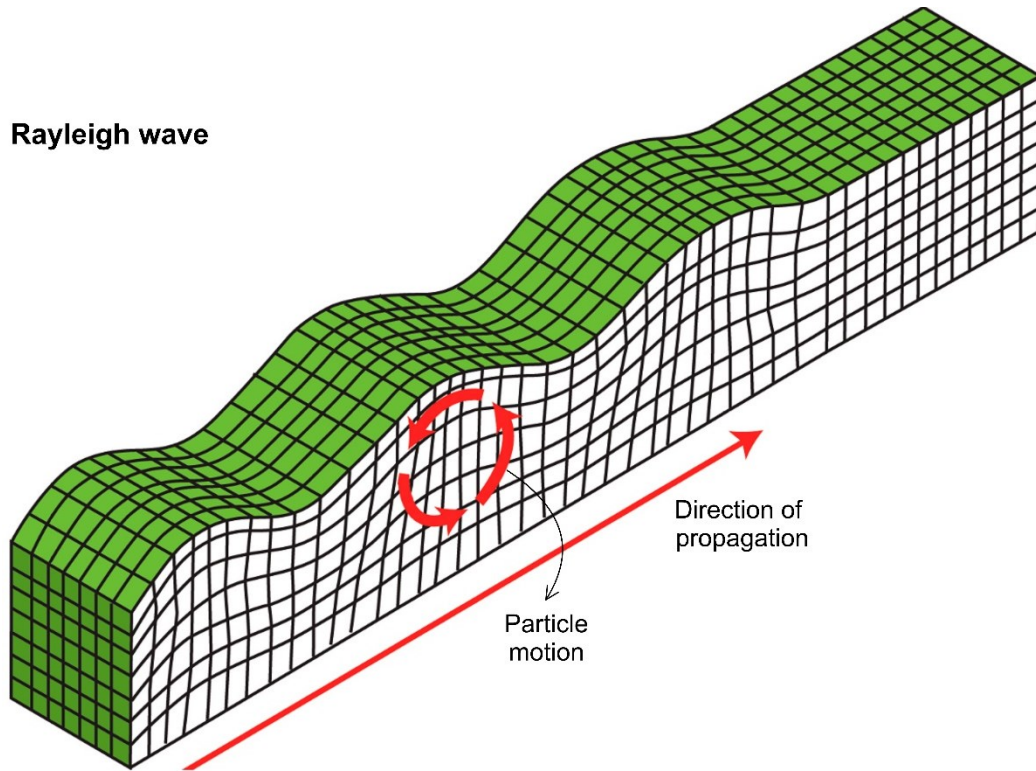


Figure 2.10: Particle motion induced by Rayleigh wave (adopted from Shaw et al. 2018)

Love waves are generated by the interaction of SH waves with the soft surficial layers. It results in a horizontal particle motion which is perpendicular to the direction of wave propagation (Figure 2.11). For love waves generation, the shear wave velocity of the surface layers should be less than the underlying elastic half space (Aki and Richards 1980). The surface wave velocities are generally less than the body wave velocities. The order of the wave velocities of seismic waves are: $v_p > v_s > v_R > v_L$ (Bolt 1999). It should also be noted that body waves damp more rapidly than the surface waves.

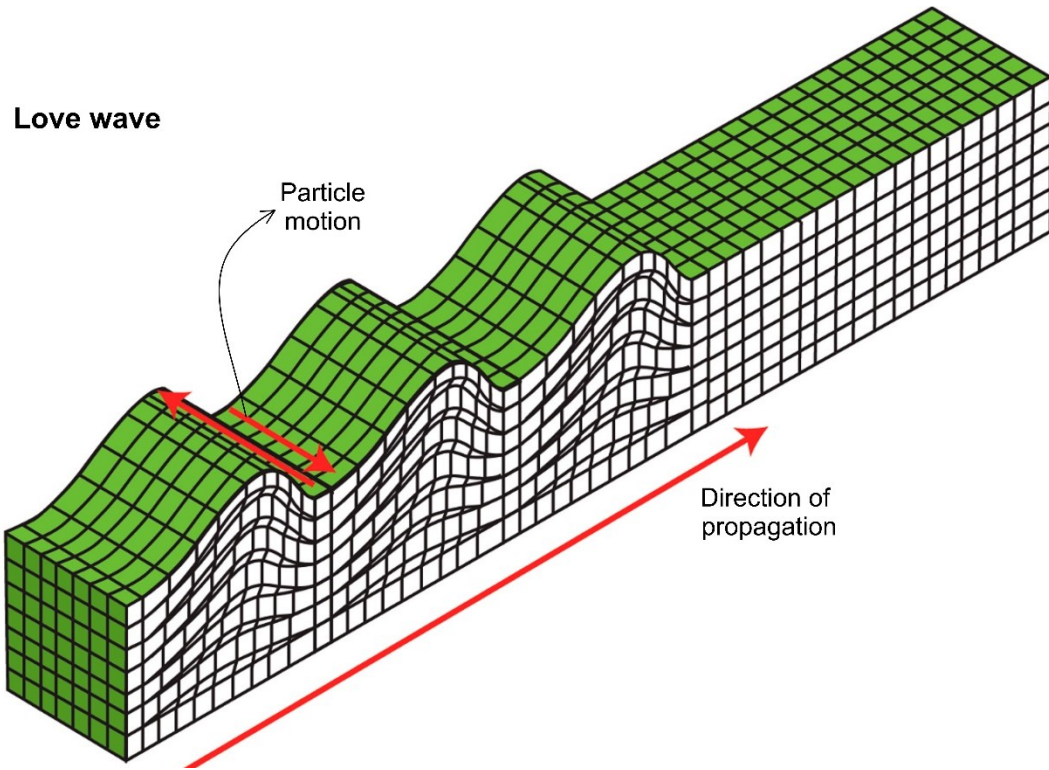


Figure 2.11: Particle motion induced by Love wave (adopted from Shaw et al. 2018)

2.5.3 Reflection and refraction of seismic waves at interface

2.5.3.1 Normal incidence of seismic waves

The earth's subsurface is quite complicated with materials of different properties and stratification. Interaction of seismic waves with these layers results in a generation of reflected and refracted waves with more complex waveforms. Therefore, to understand the wave propagation through the interfaces some simple idealizations were made. Firstly, a simple case of normally incident seismic wave in a horizontally stratified soil deposit is considered. A harmonic stress wave normally incidenting an interface between two materials is shown in Figure 2.12; where ρ_1, v_1 is the density and wave velocity in layer 1 and ρ_2, v_2 is density and wave velocity in layer 2. At interface, a part of the incidenting harmonic wave will be transmitted to material 2 and the remaining part will be reflected back into material 1. Since the incident wave is normal to the interface, the generated

reflected and refracted waves also propagate normal to the interface. The displacement amplitude of the transmitted, reflected and incident waves are related as follows:

$$A_r = \frac{\rho_1 v_1 - \rho_2 v_2}{\rho_1 v_1 + \rho_2 v_2} A_i \quad (2.4)$$

$$A_t = \frac{2\rho_1 v_1}{\rho_1 v_1 + \rho_2 v_2} A_i \quad (2.5)$$

Impedance ratio (α_z) is defined as: $\alpha_z = \frac{\rho_2 v_2}{\rho_1 v_1}$ (2.6)

So, $A_r = \frac{1 - \alpha_z}{1 + \alpha_z} A_i$ (2.7)

$$A_t = \frac{2}{1 + \alpha_z} A_i \quad (2.8)$$

The stress amplitudes are related as follows:

$$\sigma_{wr} = \frac{\alpha_z - 1}{1 + \alpha_z} \sigma_{wi} \quad (2.9)$$

$$\sigma_{wt} = \frac{2\alpha_z}{1 + \alpha_z} \sigma_{wi} \quad (2.10)$$

The nature and characteristics of refracted and reflected wave depends significantly on the seismic impedances between two layers. For $\alpha_z < 1$, the incident wave is approaching a softer material in which the reflected wave will have smaller stress amplitude than the incident wave with its sign reversed. For $\alpha_z > 1$, the incident wave is approaching a stiffer material, in which transmitted wave will have larger stress amplitude than the incident wave and reflected wave will have smaller stress amplitude with same sign as the incident wave. $\alpha_z = 0$, implies that the wave is approaching a free end, where $\sigma_{wt} = 0$, $A_t = 2A_i$, and $\sigma_{wr} = -\sigma_{wi}$. $\alpha_z = \infty$, implies that the wave is approaching a fixed end, where the displacement $A_t = 0$, $A_r = -A_i$, and $\sigma_{wt} = 2\sigma_{wi}$. In case of $\alpha_z = 1$, no reflected waves will be generated.

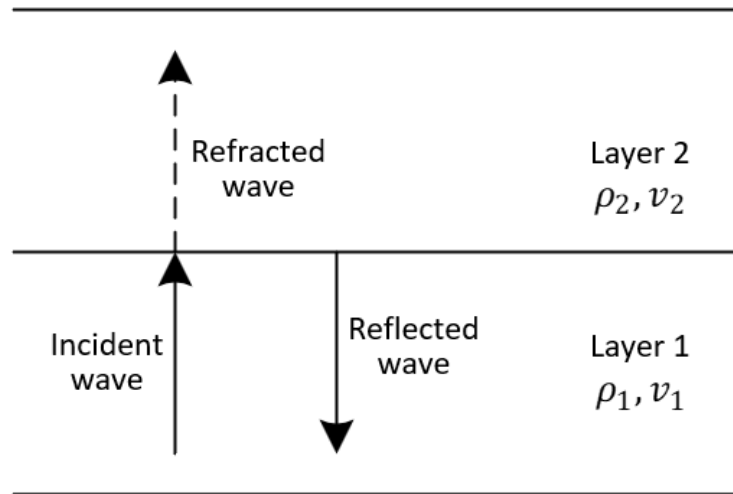


Figure 2.12: Reflected and refracted waves from normally incident harmonic wave

2.5.3.2 *Non-normal incidence of seismic waves*

In the general case, body waves will not make normal incidence with the interface between two materials. The angle of incidence of an incident body wave plays a significant role in affecting the refracted and reflected wave characteristics. If a P-wave or S-wave impinges the layer boundary at an angle of incidence θ_0 , it will result in a generation of reflected and refracted waves of both compressional and shear characteristics (Figure 2.13). For non-normal incidence of SH wave, no mode conversion occurs at the interface.

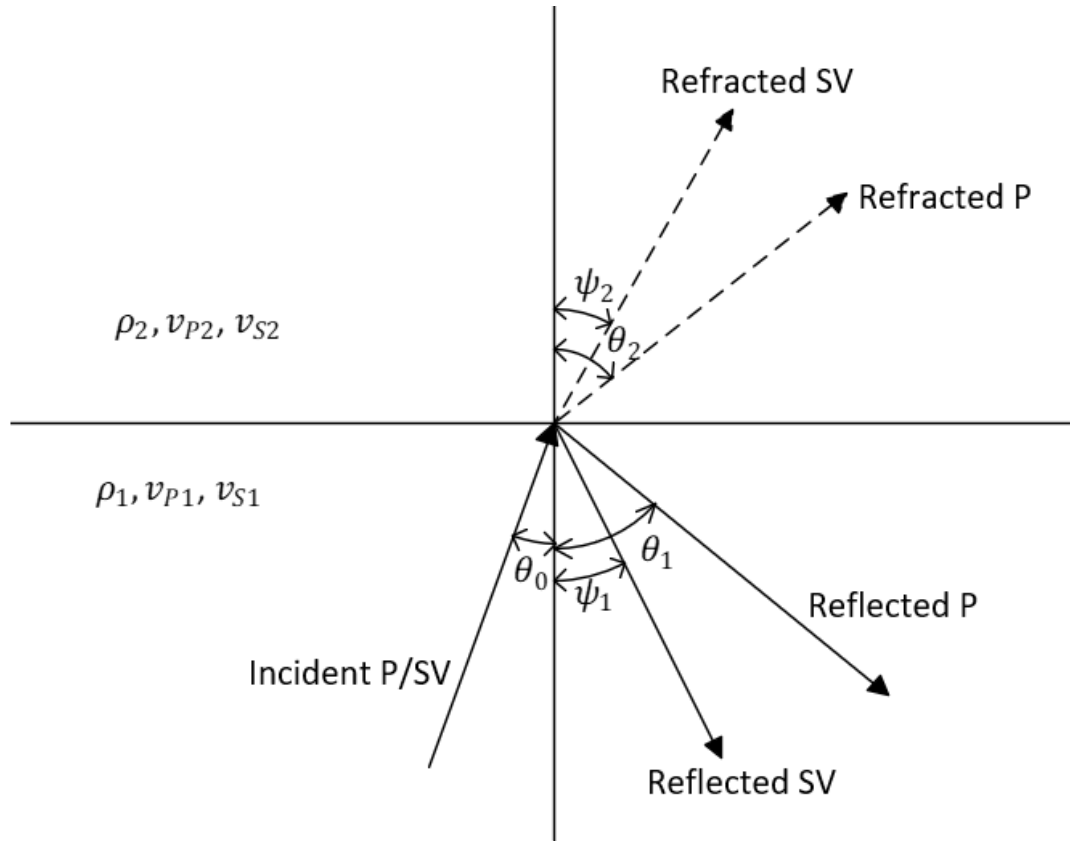


Figure 2.13: Reflected and refracted waves from non-normal incident body waves

The amplitude and direction of the reflected and refracted wave can be determined using the Snell's law. The angles of refraction and reflection are uniquely related to the angle of incidence by the ratio of wave velocities of the soil media on the either side of the interface:

$$\frac{\sin \theta_0}{v_{P1}} = \frac{\sin \theta_1}{v_{P1}} = \frac{\sin \psi_1}{v_{S1}} = \frac{\sin \theta_2}{v_{P2}} = \frac{\sin \psi_2}{v_{S2}} \quad (2.11)$$

Snell's law also implies that when an incident wave propagates upwards through the successive horizontal layers of lower velocity, the refracted wave tends to get closer to the normal of the interface, and eventually will propagate vertically upwards. This forms the basis of several methods of site response analysis, and the reliance of cyclic simple shear as the preferred means of assessing liquefaction susceptibility.

It is evident from the above discussion that due to the difference of the seismic impedances between two soil layers and angle of incidence of the incident wave, seismic waves are reflected and refracted into various complicated paths with different amplitudes. Moreover, these reflected and refracted waves are multiple phase waves, and consists of both P-wave and S-wave components. Another important aspect is that the earth's crust is characterized by heterogeneities and discontinuities which will give rise to a phenomenon known as Moho bounce (Elnashai and Sarno 2008). Moho bounce is due to the simultaneous arrival of both direct wave and reflected waves at the earth surface from the discontinuities on account of path effects. Hence as a result of complicated interaction of seismic waves with the earth's crust and also due to the local amplification factors, the soil element will be subjected to a complex loading paths involving various combinations of simultaneous action of compressional and shear stresses.

2.6 Cyclic behaviour of soil under different stress paths

The most common dynamic loading environment encountered in geotechnical earthquake engineering are earthquake, wave, and traffic loading. These loading environments are associated with continuous and cyclic rotation of principal stress directions. Figure 2.14 illustrates the typical stress paths encountered in these dynamic loading conditions. The stress path induced in offshore soil deposits due to wave action is characterized by the continuous rotation of principal stress direction without any change in the magnitude of deviatoric stress. Traffic loading is characterized by a heart shaped stress path with α_σ rotates between $-\pi/2$ to $+\pi/2$ in a loading cycle (Cai et al. 2015). Ishihara (1996) suggested a linear stress path for seismic shaking in which the shear stress in the horizontal plane (τ_h) tends to increase or decrease in proportion to the increase or decrease in stress

difference in the vertical and horizontal directions ($\sigma_v - \sigma_h$). As a result, the direction of principal stress axes remains almost unchanged during the entire duration of the shaking. But this suggestion put forwarded by Ishihara (1996) is not applicable in all cases. Even with the linear stress paths, the direction of principal stresses will get reversed when the stress difference ($\sigma_v - \sigma_h$) changes its sign. Jefferies et al. (2015) also suggested that in an idealized earthquake loading the direction of principal stress axes rotates cyclically. But this effect of cyclic variation of α_σ on the liquefaction resistance of soil has long been neglected.

Ishihara and Towhata (1983) were the first to demonstrate that the continuous and cyclic rotation of principal stress axes alone can generate excess pore water pressure and plastic strain accumulation. It is recommended that the yield function in defining the failure of soil should not only be a function of principal stresses but also a function of principal stress direction during cyclic loading. Tong et al. (2010) also noticed from a series of drained torsional shear test on Toyoura standard sand, that plastic strain accumulation is induced due to the cyclic rotation of principal stress axes without any variation in the magnitude of effective principal stresses. The volumetric strain induced due to principal stress rotation (PSR) is generally contractive, irrespective of the b_σ values.

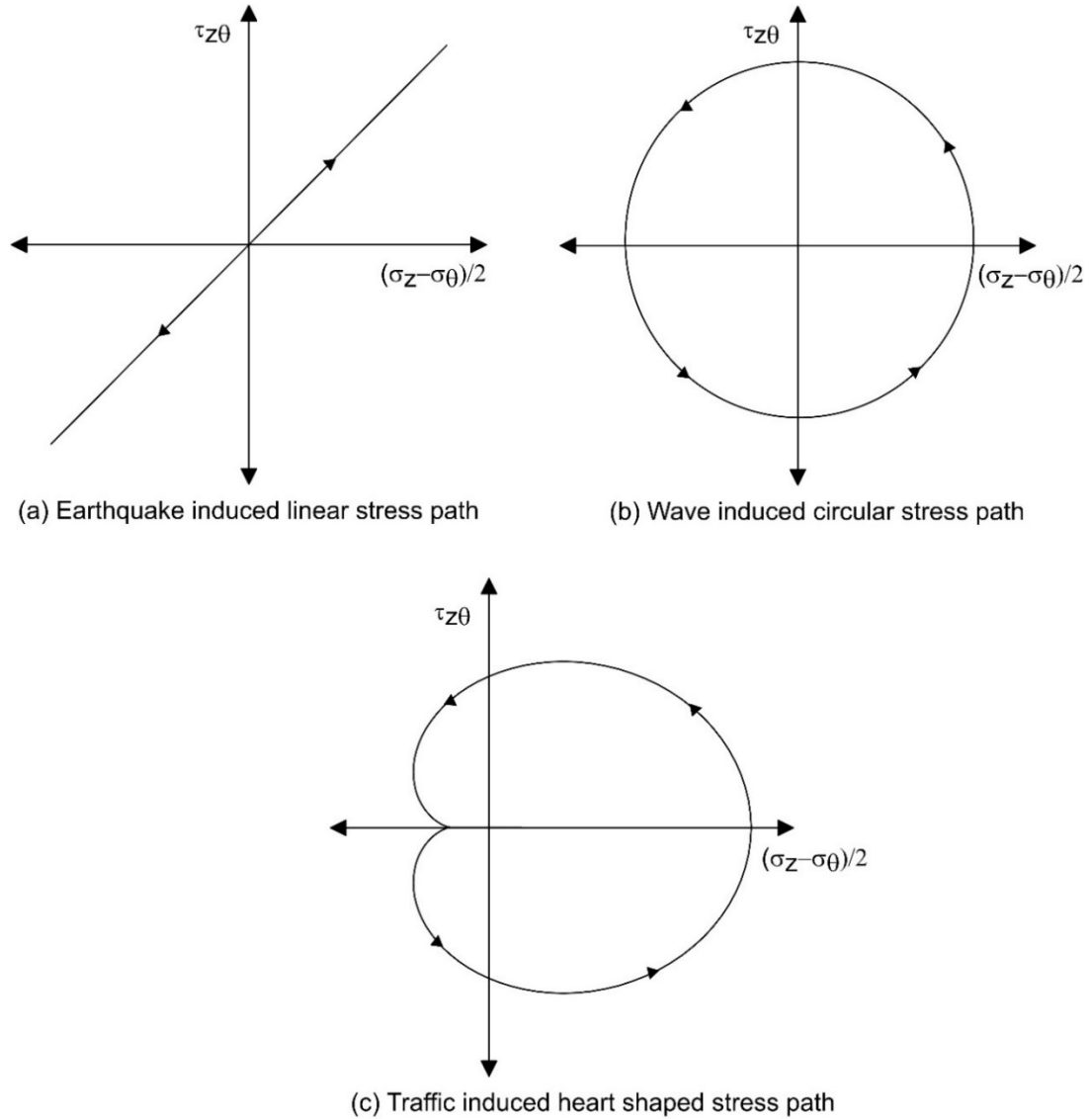


Figure 2.14: Stress paths due to three typical dynamic loading conditions

Followed this, several studies were carried out to study the influence of various stress paths with principal stress rotation (PSR) on the cyclic behaviour of soil. Invariably much of these studies were conducted using an automated hollow cylinder torsional shear apparatus. Chiaro et al. (2012) conducted a series of undrained cyclic torsional shear tests to study the influence of initial static shear stress on the large deformation behavior of loose

sand due to liquefaction. In a cyclic torsional shear test in HCT, α_σ rotates cyclically according to the applied torsion as per Eq. 2.1.

$$\alpha_\sigma = \tan^{-1} \left(\frac{\tau_{z\theta}}{\sigma_1 - \sigma_\theta} \right) \quad (2.1)$$

In this study, it is observed that the presence of initial static shear may either increase or decrease the liquefaction resistance depending upon the combined shear stress and type of loading. In reversal ($\tau_{max} = \tau_{static} + \tau_{cyclic} > 0$; $\tau_{min} = \tau_{static} - \tau_{cyclic} < 0$) and intermediate loading condition ($\tau_{max} > 0$; $\tau_{min} = 0$), the soil liquefied and exhibits extremely large post liquefaction deformation. In non-reversal loading ($\tau_{max} > 0$; $\tau_{min} > 0$), no liquefaction was observed but residual deformation brought the sample to failure. Similar observations using cyclic triaxial tests have been reported by Vaid et al. (2001).

The effect of consolidation stress ratio and relative density on the cyclic behaviour of anisotropically consolidated Ottawa sand under cyclic torsional loading was investigated by Konstadinou and Georgiannou (2013) and Georgiannou and Konstadinou (2014). During cyclic loading, the principal stress was rotated continuously as per Eq. 2.1 but with the constant magnitude of principal stresses. Test results revealed that cyclic resistance of sand decreases with the decrease in the consolidation stress ratio. Lower stiffness and high damping ratio were observed for anisotropically consolidated (AC) specimens when compared to isotropically consolidated (IC) specimens. For AC specimens, the failure is governed by the axial strain criteria rather than the excess pore water pressure criteria. It is also observed that cyclic resistance increases with density for both IC and AC specimens. The cyclic resistance of loose AC specimens is only about half of the resistance of loose

IC specimens whereas in dense state AC specimens are strong when compared to the IC specimens.

The significance of pre-shear history on the cyclic torsional response of dense Fujian sand was investigated by Ye et al. (2015). After isotropic consolidation, the samples are subjected to a drained torsional shear to a desired pre-shear strain value, followed by a cyclic torsional loading till liquefaction. Experimental results showed that the effective mean normal stress of samples with pre-shear history decreased in a faster rate than that of samples with no pre-shear history. For dense sand specimens, the liquefaction resistance of sand decreases with the increase in the pre-shear strain. Huang et al. (2015) compared the effect of different stress paths (linear, circular, and ellipsoidal stress paths) on the liquefaction resistance of Fujian standard sand and Qiantang silt. It is shown that the specimen subjected to circular stress path showed lowest liquefaction resistance. This study also highlighted that the traditional *CSR* used for evaluating the liquefaction potential of soils considers only the amplitude of the maximum shear stress and did not take the different types of stress paths into account. Therefore, a new equivalent stress ratio as a function of the average absolute value of shear stress in a cycle is proposed, which normalizes different stress paths and makes the liquefaction index independent of stress paths.

Soralump and Prasomsri (2016) performed cyclic torsional shear tests to analyze the stiffness degradation and pore pressure generation characteristics of saturated compacted clays collected from two earth dams. From the multistage strain controlled cyclic shear tests, it is noticed that the cyclic volumetric threshold shear strain of the compacted clays decreases with decrease in *PI*. The cyclic stiffness degradation and cyclic

pore water pressure generation in compacted clays is greatly influenced by the over consolidation ratio (OCR) and effective consolidation pressure (σ'_c). Higher the OCR, lesser the stiffness degradation and cyclic pore pressure accumulation.

The stress path resulting from traffic loading imposes significant rotation of principal stress axis. This repeated loading with PSR due to vehicular motions induces irrecoverable plastic strain accumulation to the pavement layers. In recent times, several investigations were carried out to examine the effect of traffic loading stress path on the deformation characteristics of pavement layers. The effect of principal stress rotation and sample moisture content on plastic strain accumulation of an unsaturated base course material is investigated by Inam et. al. (2012). From a series of undrained cyclic tests using a ring shear apparatus, it is noticed that the degree of permanent plastic strain development is more for cyclic loading with PSR when compared to the tests with no PSR. Test results also revealed that oven dried samples developed less permanent axial strain than the samples with moisture content under traffic loading condition.

Gräbe and Clayton (2014) and Cai et al. (2015) also confirmed through a series of cyclic tests using HCT, that PSR due to traffic stress path induces permanent deformation to the pavement layers. Gräbe and Clayton (2014) highlighted the importance PSR in determining the resilient modulus for the long-term design of rail track foundation. It is noticed that the samples tested with PSR exhibited low resilient modulus than the samples tested without PSR. Test results also revealed that the effect of PSR is less pronounced for anisotropically consolidated specimens. Cai et al. (2015) examined the response of soft clay deposits subjected to traffic loading over 10000 cycles under undrained conditions. Test results showed that the resilient and permanent strain developed in cyclic torsional

test is larger than the cyclic triaxial test due to the rotation of principal stresses. Frequency of wheel loading also significantly influences the settlement behaviour of soft clay deposits. For a constant stress ratio, pore pressure and vertical strain development is inversely proportional to the loading frequency (Guo et al. 2016).

Apart from the above-mentioned studies, there were only few studies which specifically focuses the effect of the magnitude of α_σ on the cyclic behaviour and dynamic properties of the soil. Logeswaran (2010) and Sivathayalan et al. (2015) investigated the effects of the nature and magnitude of PSR on the cyclic resistance of soil. The lowest cyclic resistance was observed in tests with PSR of $\pm 45^\circ$ to $\pm 60^\circ$ with respect to deposition direction. The weakest resistance is attributed to the combination of high shear stress on the horizontal plane and the alignment of the plane of maximum shear stress with the bedding plane. It is also demonstrated that cyclic resistance ratio (CRR) used in practice can be highly affected by the degree of principal stress rotation (Figure 2.15). Sinthujan (2013) extended the above study and examined the effect of initial principal stress orientation and subsequent cyclic rotation of principal stress direction on the liquefaction resistance of loosely deposited Fraser River sand. Experimental results showed that regardless of the initial principal stress direction, the lowest cyclic resistance always corresponds to the PSR of $\pm 45^\circ$ from its initial position. It is also shown that the degree of stress rotation influences CRR more significantly than the initial principal stress orientation.

Guoxing et al. (2015) studied the influence of different consolidation state parameters such as various effective mean consolidation stresses (σ'_{mc}), principal stress direction at the end of consolidation ($\alpha_{\sigma c}$), stress ratio ($K_c = \sigma'_{1c}/\sigma'_{3c}$), and $b_{\sigma c}$ on

dynamic properties of saturated micaceous fine sand specimens over a wide strain range in the order of 10^{-5} to 10^{-2} . Shearing was carried out by cyclically varying both axial load and torsion. It is observed that the maximum shear modulus G_{max} increases with the increase in σ'_{mc} and K_c and with the decrease in $\alpha_{\sigma c}$ and $b_{\sigma c}$. Dynamic damping ratio is influenced strongly by σ'_{mc} and $\alpha_{\sigma c}$, and less influenced by K_c , and $b_{\sigma c}$. The dynamic Poisson's ratio ν increases with increasing $\alpha_{\sigma c}$ and $b_{\sigma c}$ and with decreasing σ'_{mc} and K_c .

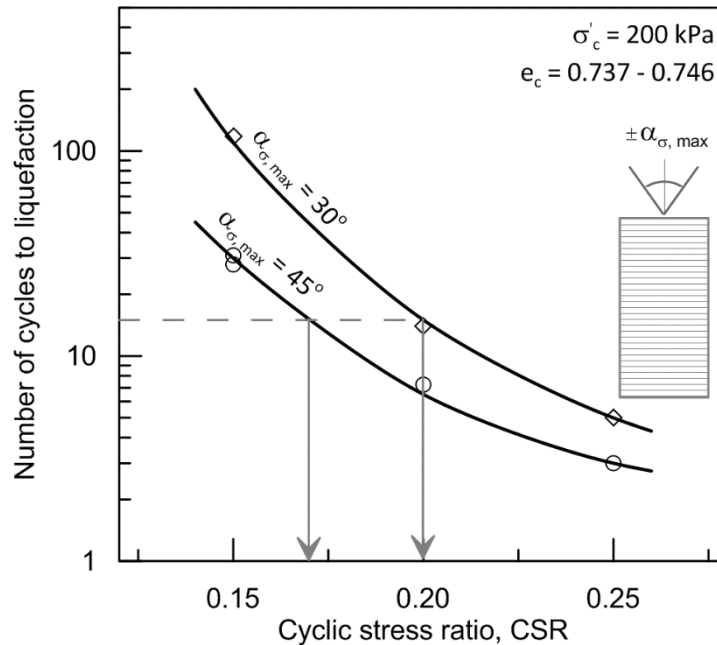


Figure. 2.15: Influence of the degree of principal stress rotation on the measured CRR_{15} on otherwise identical specimens (modified after Sivathayalan et al. 2015)

The seismic waves generated due to earthquakes are multidirectional in nature and involves a complex combinations of compression waves and shear waves (Aggour and Zhang 2006; Gu et al. 2012; Gu et al. 2016). The case studies on the 1999 Chi-Chi earthquake reported by Bernardie et al. (2006) and Lin et al. (2009) showed that the catastrophic earthquake damages happened in areas where S-waves and strong P-waves propagate simultaneously. This simultaneous action of P-wave and S-wave leads to the cyclic variation of both normal and shear stress components. Though the previously

mentioned studies on HCT investigated the combined effect of normal and shear stress components by adopting paths such as circular, elliptical and heart shaped stress paths, much of these investigations focused on clay samples and also these cyclic tests were carried out for 1000s of cycles and hence it may not be suitable to characterize the liquefaction potential of granular soil under short term seismic events. Only very limited studies focused on this simultaneous effect of seismic waves on the dynamic characteristics and cyclic behaviour of soil. Gu et al. (2012) and Gu et al. (2016) simulated this combined action by cyclically varying the deviatoric stress and confining pressure using a cyclic triaxial apparatus. From their tests on saturated clay samples, it is noticed that the conventional cyclic triaxial tests may overestimate the cyclic strength of clays. This combined loading results in a faster accumulation of excess pore water pressure and cyclic shear strain. The phase difference between this coupled cyclic deviatoric stress and cyclic confining pressure significantly affects the G/G_{max} characteristics of the saturated clays.

Tsaparli et al. (2016) numerically evaluated the effect of bidirectional seismic shaking on the liquefaction resistance of saturated sand deposits. Simulations revealed that liquefaction occurs when the frequency of the vertical ground motion matches with the frequency of the soil deposit. It is also noted that the common assumption of the linear elastic behaviour of saturated sand during the propagation of compression waves is not valid during this resonance condition. Xu et al. (2017) examined the cyclic strength of saturated sand under the combined action of cyclic shear stress and axial stress using a hollow cylinder torsional shear apparatus. This study mainly focused on the elliptical stress path due to the combined effect of wave and earthquake loading. Experimental results

showed that the ratio and phase between the cyclic horizontal stress and cyclic axial stress greatly affects the number of cycles to liquefaction.

2.7 Partially drained or strain path dependent behaviour of soil

Traditionally, the monotonic and cyclic behaviour of soil has been studied either under fully drained or fully undrained conditions. A purely drained condition represents the state of deformation under constant pore water pressure. Drained condition is generally assumed if the rate of loading is slow and the material has relatively high permeability. On the other hand, a fully undrained condition represents the deformation under constant volume state. This is the case for faster loading rate in a material with low permeability. However, the actual drainage conditions in the field are neither fully drained nor undrained, it will be partially drained. Therefore, the response of soil is presumed to be bounded between the drained and undrained responses.

The response of sand subjected to seismic shaking is generally treated as undrained because of the faster loading rate in a short interval of time, and the extensive spatial area that is loaded. Therefore, the liquefaction characteristics of the soil are evaluated based on its undrained shear strength. The experimental and field observations demonstrated that due to the high permeability of granular soil, a small drainage of pore water does occur during seismic shaking (Seed 1987; Liu and Qiao 1984; Whitman 1985). Moreover, the assumption of completely undrained condition is valid only if the initial piezometric gradient is uniform within the soil deposit. But the actual soil deposit is highly heterogenous, so a significant pore pressure gradient would develop during an earthquake loading. As a result, the pore water migrates from the regions of high pore pressure leading to a localized deformation due to void redistribution. Hence, it is evident that the

deformation of granular deposits during and following a seismic event occurs with the simultaneous change in effective stress and pore volume.

Apart from this, the condition of partial drainage is quite common in offshore shallow foundations. Due to wave loading, the shallow foundation resting on an offshore sand deposit, must resist the simultaneous action of cyclic vertical, horizontal and moment loads. In some cases, it needs to endure tensile loads too. To resist tensile forces, these foundations are designed to induce negative pore pressure in its bases, resulting in a partially drained response of the foundation soil (Mangal 1999).

Only a limited number of laboratory investigations are available to understand the elemental response of sand under partially drained condition (Chu et al. 1992, 2015; Vaid and Eliadorani 1998, 2000; Lancelot et al. 2004; Sivathayalan and Logeswaran 2007; Lade and Liggio Jr. 2014). Vaid and Eliadorani (1998, 2000) and Sivathayalan and Logeswaran (2007) examined the partially drained monotonic response of Fraser River sand along various linear proportional volumetric strain paths under triaxial loading condition. It is demonstrated that partially drained condition resulting due to the imposition of slight expansive volumetric strain can transform a stable undrained behaviour into an unstable one. This implies that the fully undrained condition cannot always be treated as a critical condition in assessing the liquefaction characteristics of soil. The effect of post liquefaction seepage under an initial static shear stress was examined by Sento et al. (2004) through a series of hollow cylinder tests along linear volumetric strain paths. This study also confirmed that the pore water injection has detrimental effect on the soil response by promoting its strain softening tendency.

However, the actual strain path encountered in-situ will be highly non-linear with steadily decreasing rate of volumetric inflow due to the equalization of pore pressure caused by the migration of pore water. Sivathayalan and Logeswaran (2008) evaluated the behavior of loose Fraser river sand subjected to linear strain paths with limiting volumetric strain and non-linear strain paths. It is shown that the rate of volume inflow plays a significant role in affecting the shear strength response of sand. Invariably in all these investigations, the behavior of sand is evaluated under triaxial axisymmetric loading condition which may not represent the actual stress path encountered in-situ. Therefore, it is very important to assess the loading mode dependent behavior of sand under various volumetric strain paths. Logeswaran (2010) examined the anisotropic characteristics of Fraser River sand under various linear volumetric strain path using CU-HCT. Though these linear strain paths are theoretical, this study is a first step to quantify the effect of expansive volumetric strain under different loading modes.

2.8 *Summary*

It is evident from the review of previous investigations that the natural deposition process under the action of gravity results in a cross-anisotropic soil fabric. Due to this anisotropic fabric, the soil response depends not only on the magnitude of principal stresses but also on the direction of principal stresses with respect to the deposition direction. Several laboratory studies under both drained and undrained monotonic conditions revealed that the strength and deformation characteristics of granular soil depends significantly on the applied loading paths. However, only very limited studies explored the influence of cyclic rotation of principal stress axes on the cyclic response of granular soil and most of these

investigations are confined to specific loading paths such as traffic loading and offshore wave loading paths.

Moreover, majority of laboratory studies on the cyclic behavior of saturated cohesionless soil under seismic loading are derived either by using a cyclic triaxial or cyclic simple shear apparatus, which subject the soil to relatively simpler loading paths. The major objective in these studies is to characterize the dynamic behavior of soil due to the action of vertically propagating shear waves generated during an earthquake. This propagation of pure shear waves is based on the assumption that the soil strata is subjected to purely shear waves that are vertically propagating. But, in reality the soil media is highly heterogeneous, and the plane of stratification is not always horizontal. Depending upon the differences of seismic impedance between soil layers/bedrock, and the incidence angle of seismic waves, the seismic waves are reflected and refracted into waves of different nature and characteristics. These reflected and refracted waves are multiple phase waves and may consist of both compression wave (P-wave) and shear wave (S-wave) components. Therefore, it is evident that during an earthquake the soil element will be inevitably subjected to complex loading paths involving the simultaneous action of both normal and shear stresses. So far, no studies relate the nature and degree of principal stress rotation that will be encountered in an actual seismic loading scenario, involving the coupled action of both normal and shear stresses, to the liquefaction potential of the soils.

Secondly, in conventional geotechnical design, the undrained condition is generally assumed to represent the worst-case scenario while evaluating the response of soils under earthquake loading. This assumption may not be accurate if the pore water pressure gradients exist in-situ during or after the seismic event. During short duration

dynamic events, volume changes might occur in granular deposits due to the pore water migration ensued from uneven pore pressure distribution. Therefore, the partial drained condition prevails in the field during or following earthquake shaking. Most of the previous studies focused mainly on the influence of linear volumetric strain paths on the monotonic response of granular soil under triaxial axisymmetric condition. Such loading paths provide an insight into soil behaviour but are not realistic representation of the actual behaviour expected in-situ. The literature is clearly lacking on the response of soils subjected to representative loading paths with simultaneous volumetric and pore pressure changes under generalized loading conditions. As mentioned earlier, the shear strength characteristics of natural soil depends significantly on the inclination of major principal stress axis with respect to the deposition axis during the shearing process. In laboratory soil testing, in order to evaluate the stress-strain behavior of granular soils precisely, it is crucial to replicate the in-situ deposition process, drainage condition and loading paths as accurately as possible. So far, to the best of our knowledge, no laboratory studies focused on the stress path dependent behavior of gravity deposited sand specimens along different non-linear volumetric paths which closely imitate the actual loading and drainage condition in the field.

Therefore, the major objective of this research program is to address the above-mentioned research gaps through an extensive hollow cylinder torsional shear testing program. The intention is to develop high quality data that sheds light into the effects of the variables discussed. Cyclic tests were carried out on water pluviated Fraser River sand specimens under different relative magnitudes and combinations of normal and shear stresses to understand the liquefaction potential of saturated sands under the simultaneous

action of P-waves and S-waves. Monotonic tests along different stress paths and non-linear strain paths were carried out to have a better clarity on the anisotropic behavior of sands under various loading and drainage conditions. In order to obtain high quality and reliable test data, extreme care was taken in laboratory testing to reduce the undesirable effects from any specimen apparatus interactions. The effects of membrane compliance and membrane strength were properly accounted and removed if necessary. Moreover, the highly repeatable soil samples and test results adds confidence and reliability to the sample preparation technique and testing procedures adopted in this thesis.

Hence it is believed that the outcome of this thesis will throw light on the unnoticed grey area in the evaluation of liquefaction potential and anisotropic characteristics of natural soil deposits under different drainage conditions for safe and reliable geotechnical design practice.

3. DESCRIPTION OF THE CU-HCT APPARATUS AND ITS WORKING PRINCIPLES

3.1 Introduction

The Carleton University hollow cylinder torsional shear (CU-HCT) apparatus (Logeswaran and Sivathayalan 2014) was employed to assess the liquefaction susceptibility and anisotropic characteristics of Fraser River sand under various stress paths and strain paths. The HCT apparatus have been used by several researchers to investigate the influence of principal stress rotation on the anisotropic and liquefaction characteristics of soil (Hight et al. 1983; Vaid et al. 1990; Nishimura et al. 2007; Chiaro et al. 2012; Lade et al. 2013; Sivathayalan et al. 2015; Brosse et al. 2016). In HCT, a relatively thin walled hollow cylindrical soil sample is subjected to vertical stress, torsional shear stress on the horizontal plane, and internal and external confining pressures on the either side of the cylindrical boundaries. These four surface tractions enable HCT to independently control the magnitude of three principal stresses and the direction of major principal stress with respect to the axis of deposition. Therefore, with HCT it is possible to simulate stress paths that may be encountered in-situ under various loading conditions. However, HCT devices have been seldom used because of the apparatus intricacies and difficulty in testing procedures. It also has some shortcomings due to non-uniform stress distribution across the wall of the specimen (Sayao 1989). This non-uniformity can be reduced to an acceptable level with the careful selection of specimen dimensions.

This chapter provides a detailed description of the various features of CU-HCT apparatus and its data acquisition system. This chapter also reviews the general theories in HCT testing and stress non-uniformities on HCT specimen.

3.2 *CU Hollow cylinder torsional shear apparatus*

CU-HCT apparatus is a custom-built apparatus capable of performing both controlled stress path and strain path testing on reconstituted/undisturbed soil specimens. It is one of the first devices designed specifically to analyze the partially drained response of soils under three-dimensional loading conditions (Logeswaran and Sivathayalan 2014). The schematic outline of CU-HCT apparatus is shown in Figure 3.1.

Thin walled, large diameter specimen with a height to outer diameter ratio of two was adopted to minimize the influence of stress non-uniformities on test results (Sayao 1989). The test specimen which is confined between two flexible rubber membranes of about 0.3 mm thick, has an outer diameter of 150 mm, wall thickness of 25 mm and an approximate height of 300 mm. These large dimensions of the test specimen facilitate a better resolution on strain measurements. The test specimen is fixed at the top and subjected to normal and shear loads at the bottom. The application of axial load at the bottom of the specimen eliminates the vertical stress correction due to weight of the loading ram and load cell. Annular ribbed aluminum platens located at the top and bottom boundaries of the soil sample ensures the transfer of applied loads without introducing any relative displacements. Each platen has six equally spaced interconnected porous stones, which covers only about 8% of the sample area, facilitates the free drainage of pore water from the test specimen. This minimal porous stone surface area also helps to reduce the end

restraint effects. Figure 3.2 shows the location of porous stones and radial ribs at the end platen.

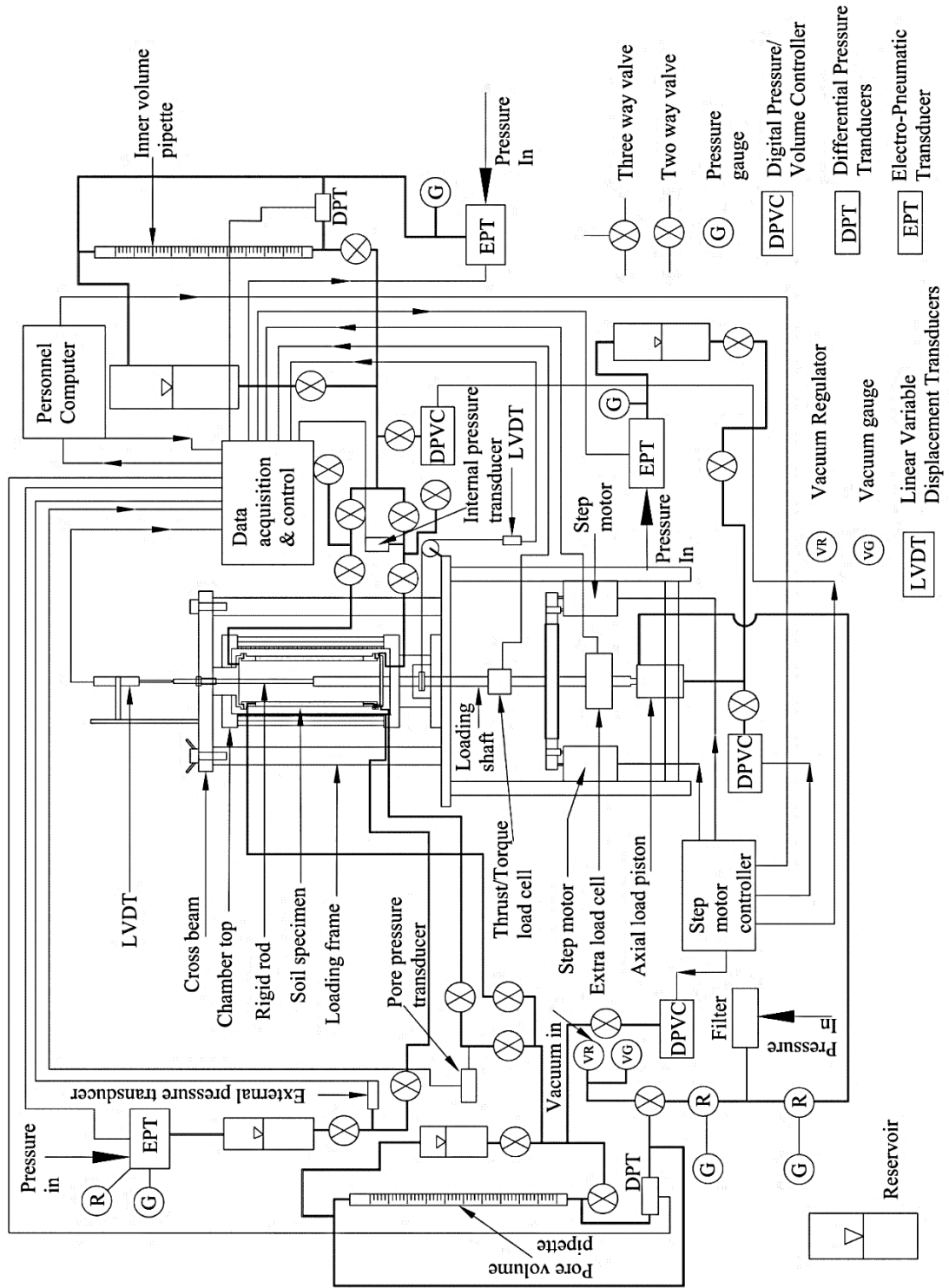


Figure 3.1: Schematic diagram of CU-HCT apparatus (Logeswaran 2010).

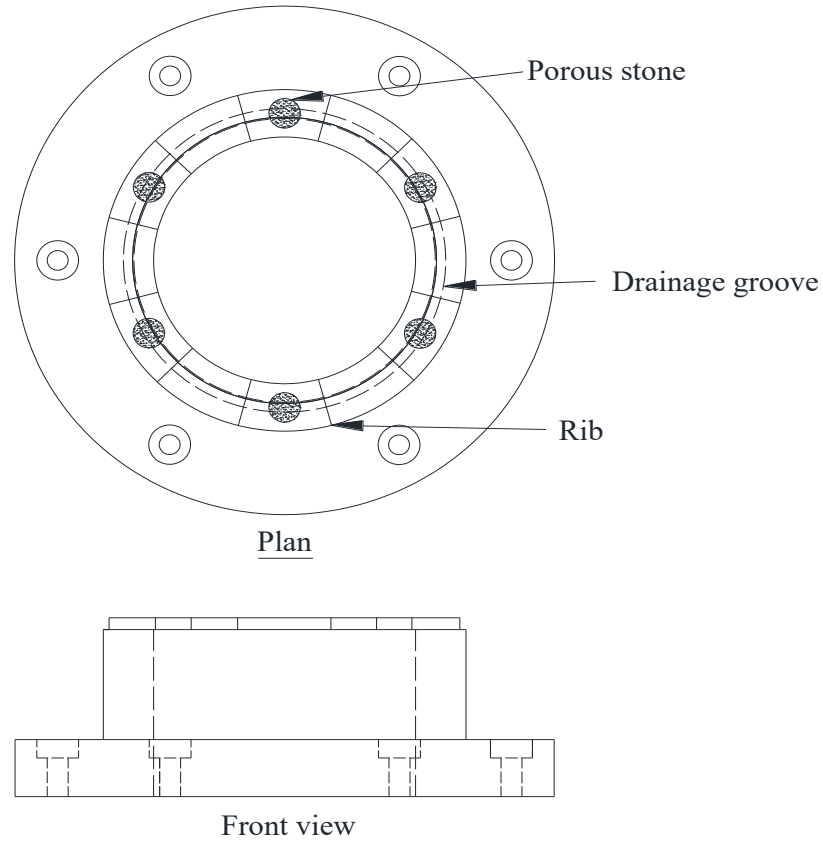


Figure 3.2: End platen with porous stones and radial ribs (Logeswaran 2010)

In order to follow the prescribed loading paths precisely, it is vital to keep track of and control the four surface tractions, four strain components and pore water pressure. Manual control of all these parameters is extremely cumbersome, and impossible while dealing with complex cyclic loading paths. Therefore, an automated computer feedback control system is used for improved stress path (or strain path) control.

3.2.1 HCT loading and measurement system

The stress-controlled loading in CU-HCT is carried out using three Electro-Pneumatic transducers (EPT). Figures 3.3 to 3.6 show the various stress-controlled loading components of CU-HCT. The electro-pneumatic pressure transducers have an output pressure range of about 0-700 kPa and enable independent control of the pressures in the

inner cell, outer cell, and the bottom chamber of the double acting piston. Before applying the stresses to the soil sample, the air pressure from EPTs are converted into water pressure through the air water interfaces.

The double acting piston at the bottom of the supporting table applies the axial load to the soil specimen. The bottom chamber of the piston is connected to an EPT whereas the top chamber is connected to a manual pressure regulator. The top chamber pressure along with the weight of the loading ram counteracts the bottom chamber pressure. During loading, the pressure at the top is held constant and the pressure at the bottom is varied according to the imposed loading scheme. CU-HCT does not have a stress controlled torsional shear loading system, and instead uses two precision stepper motor drives (SMD) connected by a belt and gear arrangement to apply torsional loads to soil specimens. These SMDs apply pulses to reach the targeted torque. A feedback control loop of the data acquisition program is used to achieve the targeted torque value. As mentioned earlier, this torque is transmitted to the soil specimen through the annular ribbed end platens to avoid any slip at the interfaces.

The major drawback in a stress-controlled loading system is that it cannot accurately capture the post peak strain softening response of soil, and this shortcoming can be eliminated with the help of strain-controlled loading system. In CU-HCT, three Digital Pressure/Volume controllers (DPVCs) connected to inner chamber (Fig 3.4), axial piston (Fig 3.5), and sample's pore space (Fig 3.7) along with two torque SMDs forms the strain-controlled loading system.

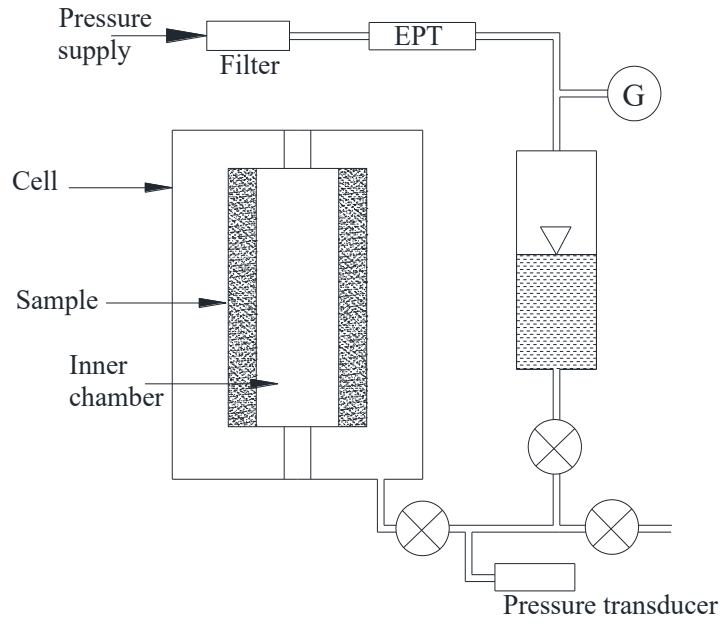


Figure 3.3: Cell pressure control of CU-HCT (Logeswaran 2010)

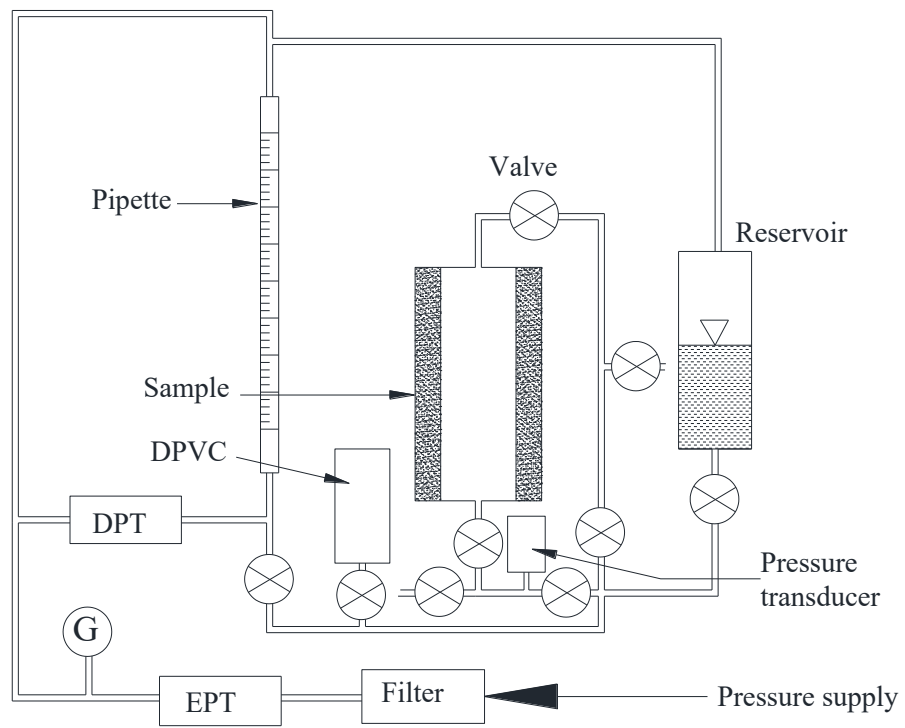


Figure 3.4: Inner chamber volume and pressure control (Logeswaran 2010)

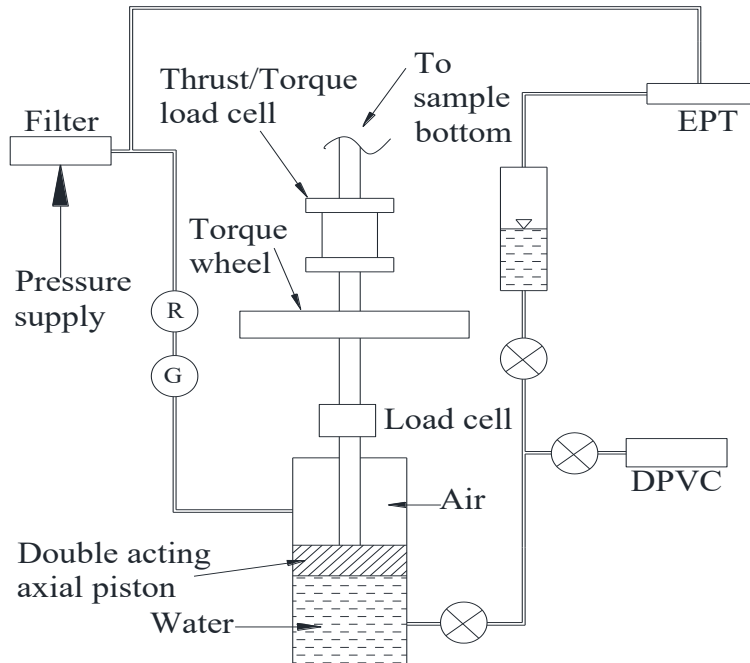


Figure 3.5: Schematic arrangement of vertical load control (Logeswaran 2010)

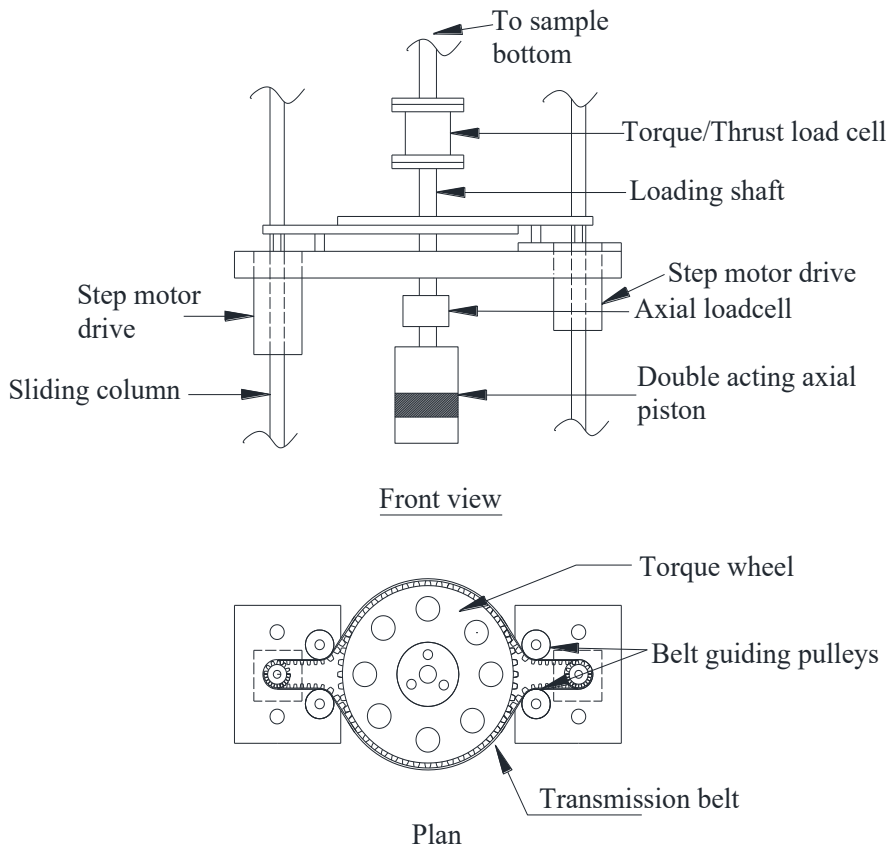


Figure 3.6: Schematic arrangement of torsional load control (Logeswaran 2010)

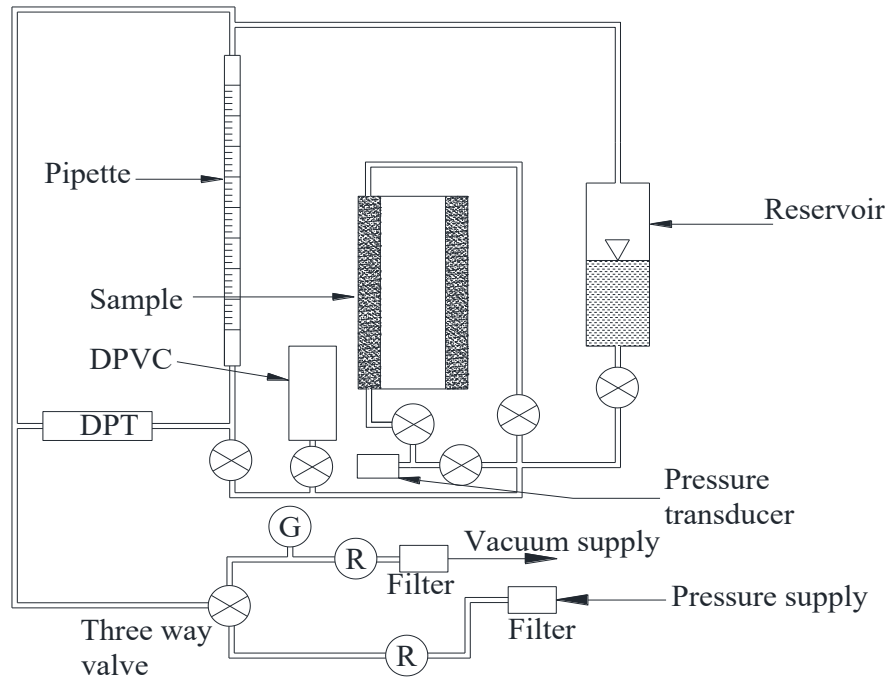


Figure 3.7: Back pressure and sample volume control of CU-HCT (Logeswaran 2010)

A single pulse of the torsional SMD yields a rotation of about 6.5×10^{-4} degrees, which translates to about 2.4×10^{-6} torsional shear strain. The DPVCs which has an independent control over the axial displacement, inner volume, and sample volume achieves the target strain state either by injecting or extracting a specific volume of water from the loading system. Each pulse of the DPVC connected to the axial piston causes an axial strain of 2.5×10^{-8} . A single pulse of the DPVCs connected to inner and sample volume causes a volumetric strain of 2.5×10^{-8} and 2×10^{-8} respectively. In order to achieve a precise control over the strain state, it is very important to keep these systems fully saturated without entrapping any air bubbles. However, the accuracy of the DPVC system also depends upon the timer which is used to control the hardware, and the overall system compliance.

In CU-HCT, the stress-strain components are determined using ten externally mounted transducers. Three precision transducers with accuracy of about ± 0.1 kPa measures the inner cell pressure, external cell pressure and pore water pressure. A combined torque-thrust biaxial load cell is used to measure both torque and axial load. This load cell has a resolution of ± 0.05 Nm for torque and ± 4 N for axial load. This translates to a resolution of about ± 0.01 kPa for shear stress and ± 0.5 kPa for vertical stress. An additional load cell mounted below the torque loading system was also used to measure the axial load. The resolution of this load cell is ± 1 N, translating to about 0.1 kPa.

The axial and torsional displacements are measured using two linear variable differential transducers (LVDT). Torsional LVDT measures the angular displacement of the soil specimen by converting the rotation into an equivalent linear tangential displacement. Figure 3.8 shows the schematic representation of torsional displacement measuring system. The vertical LVDT which is mounted on the top of the crossbeam of the loading frame as shown in Figure 3.1 measures the movement of a thin vertical rod connected to the center of the specimen's pedestal. The resolution of these two LVDTs are in the order of 10^{-3} mm, which results in an accuracy of about 5×10^{-4} for axial and shear strains. The volume changes in the inner cell and sample are measured using two differential pressure transducers (DPT). These volume changes are required for the calculation of radial and tangential strains. A resolution in the order of about 10^{-4} on both radial and tangential strains were achieved from these DPTs.

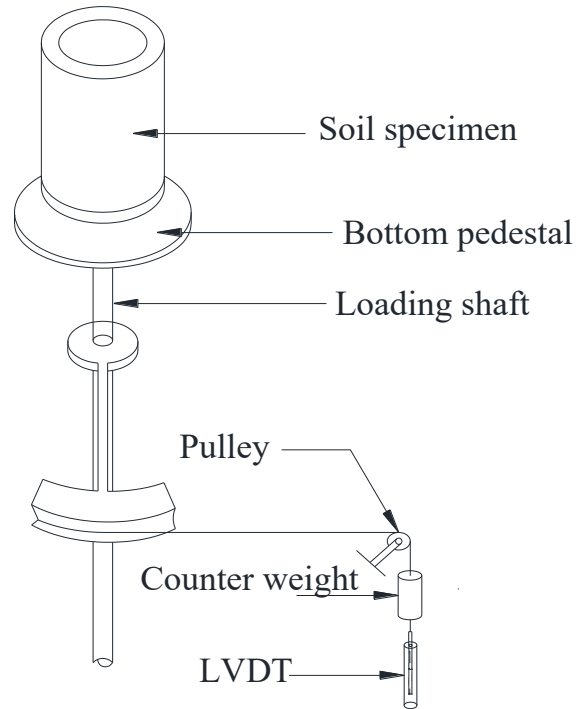


Figure 3.8: Schematic arrangement of torsional displacement measuring system (Logeswaran 2010)

3.2.2 Data acquisition of CU-HCT

A multichannel signal conditioner (MSC-10), an Analog to Digital converter (ADC), and a Digital to Analog converter (DAC) together with three National Instruments PCI bus driven interface cards (PCI-6052E, PCI-6601 and PCI-6703) form the major components of CU-HCT data acquisition hardware. The schematic representation of CU-HCT data acquisition procedure is shown in Figure 3.9. MSC-10 conditioner amplifies and filters the analog voltages from all the ten measurement transducers. ADC converts these analog voltages to digital signal and communicates it to the PC. The NI PCI cards serves as an interface between the DAQ hardware and computer. PCI-6052E is a 16-bit multifunctional ADC card with 16 analog inputs and 2 analog output. This card processes the inputs from the measurement transducers. PCI-6703 is a 16-bit analog output device with 16 channels

and this card communicates the analog signal to the 3 EPTs which regulates the pressure to the HCT loading system.

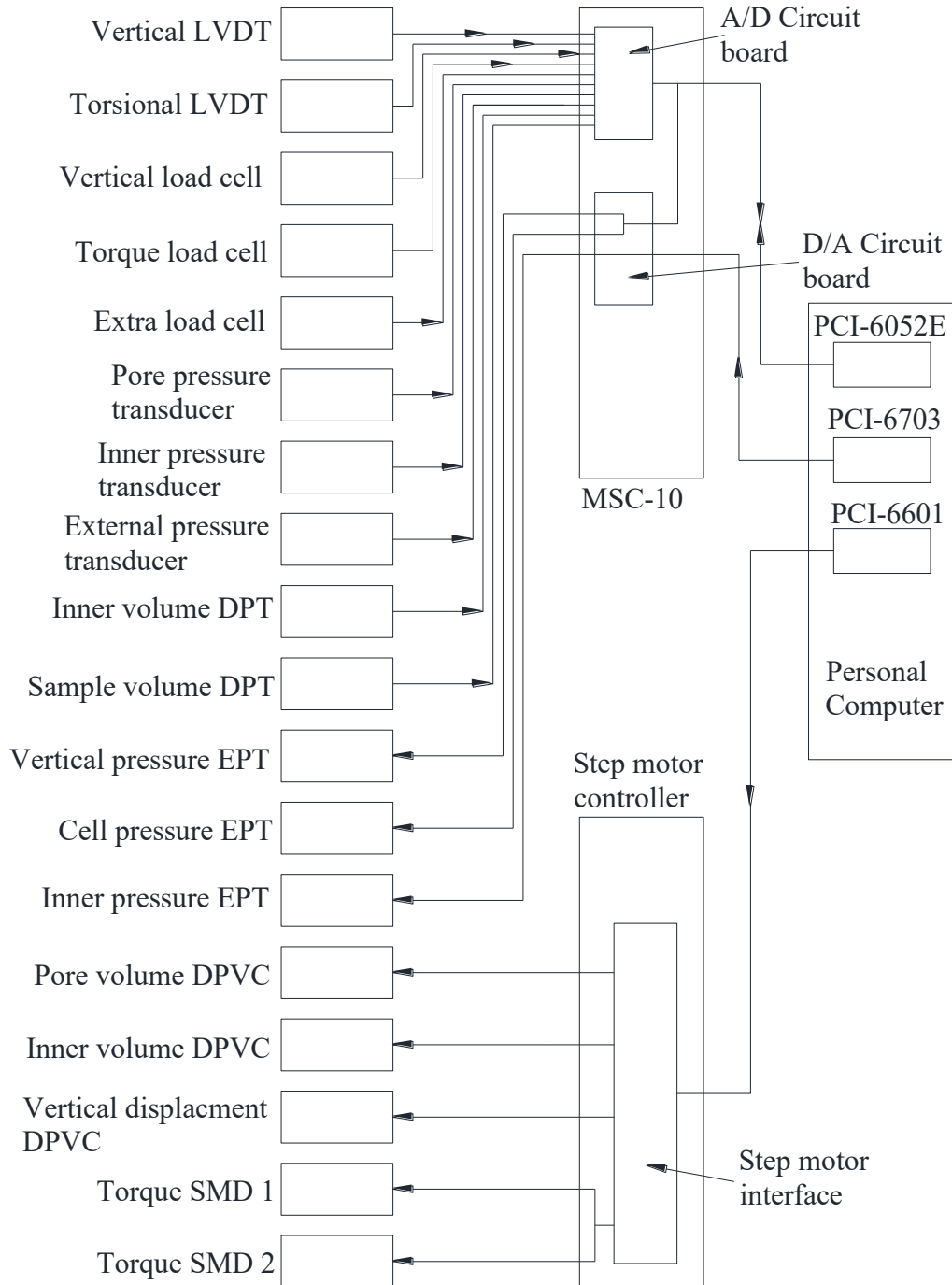


Figure 3.9: Schematic representation of data acquisition procedure in CU-HCT (Logeswaran 2010)

The five stepper motor drives of the HCT are connected to the stepper motor controller which is interfaced to the computer using a NI PCI-6601 card. PCI 6601 is a 32-bit, four channel counter/timer device which controls the pulse generation in SMDs.

An in-house developed, multi-threaded data acquisition program is used to control the loading systems of HCT and also records data from the measurement transducers. With multi-threading, each thread handles a specific function, such as scanning the transducers, controlling an SMD, or EPTs, file system access and responding to user interface events. This enabling a precise feedback-controlled loading system (Logeswaran and Sivathayalan 2014). The data acquisition software uses seven parallel threads during execution, and hence a computer with an eight-core CPU is used for this DAQ system.

3.3 Formulation of stresses and strains

3.3.1 Stress analysis

The four stress components acting on a HCT specimen are radial stress (σ_r), circumferential stress (σ_θ), axial stress (σ_z) and shear stress on the horizontal plane ($\tau_{z\theta}$). These stresses are determined from the four imposed surface tractions such as vertical load (F_z), Torque (T_h), inner cell pressure (P_i) and outer cell pressure (P_e). Figure 3.10 shows the stress state and loading conditions on an HCT specimen.

Since the stress-strain distribution in a hollow cylinder specimen is not uniform, the conventional equations of equilibrium and compatibility conditions alone is not enough for the determination of stresses and strains. Also, the presence of varied boundary conditions such as flexible boundary in the horizontal direction and rigid boundaries in the vertical direction further complicates this calculation. Therefore, in addition to equilibrium

and compatibility conditions, a constitutive relation is required for the determination of stresses. The major assumptions involved in this derivation are as follows:

- Material is isotropic and linear elastic
- The effects of end restraint on sample deformation is negligible
- Stress distribution is symmetrical about the Z axis. Therefore, the stress functions depend only on r and not on θ
- The pressure distribution on the inner and outer surface of the hollow cylindrical specimen is uniform
- Shear stress is generated only in the direction of applied torque and it is independent of Z and θ .

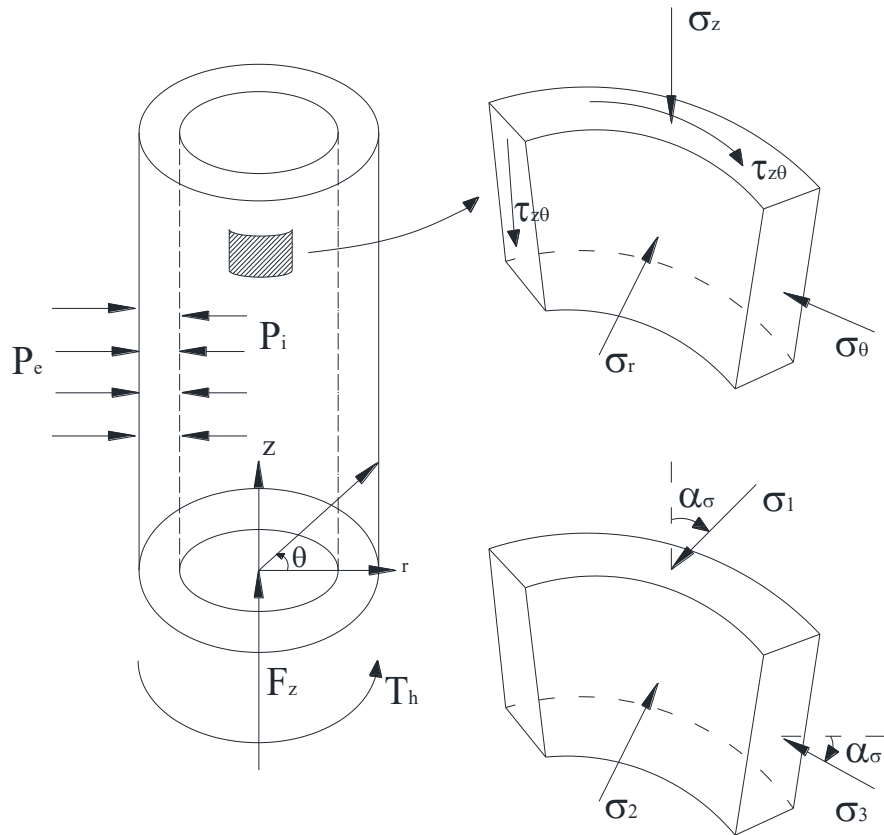


Figure 3.10: Stress state in a hollow cylindrical specimen

Since the stress-strain components vary spatially in an HCT specimen, the averaged values are used to determine the soil response. The average vertical stress (σ_z), which is independent of the material constitutive behavior is given by:

$$\sigma_z = \frac{F_z + \pi(P_e R_e^2 - P_i R_i^2)}{\pi(R_e^2 - R_i^2)} \quad (3.1)$$

where R_e and R_i are external and internal radii of the specimen. This averaged vertical stress is appropriately corrected for the membrane forces, shaft friction and soil weight.

The stresses σ_r , σ_θ , and $\tau_{z\theta}$ at a given radius R is obtained by considering the deformation of an isotropic linearly elastic hollow cylinder under plane strain condition (Timoshenko and Goodier 1951).

$$\sigma_r(R) = \frac{P_e R_e^2 - P_i R_i^2}{R_e^2 - R_i^2} - \frac{(P_e - P_i) R_e^2 R_i^2}{R_e^2 - R_i^2} \frac{1}{R^2} \quad (3.2)$$

$$\sigma_\theta(R) = \frac{P_e R_e^2 - P_i R_i^2}{R_e^2 - R_i^2} + \frac{(P_e - P_i) R_e^2 R_i^2}{R_e^2 - R_i^2} \frac{1}{R^2} \quad (3.3)$$

$$\tau_{z\theta}(R) = \frac{T_h}{\pi(R_e^2 + R_i^2)(R_e - R_i)} \quad (3.4)$$

The average stresses are obtained by integrating Eq. 3.3 to 3.5 over the cross-sectional area of the specimen. The following expressions are used for the determination of average stresses:

$$\sigma_r = \frac{P_e R_e^2 - P_i R_i^2}{R_e^2 - R_i^2} - \frac{2(P_e - P_i) R_e^2 R_i^2 \ln(R_e/R_i)}{(R_e^2 - R_i^2)^2} \quad (3.5)$$

$$\sigma_\theta = \frac{P_e R_e^2 - P_i R_i^2}{R_e^2 - R_i^2} + \frac{2(P_e - P_i) R_e^2 R_i^2 \ln(R_e/R_i)}{(R_e^2 - R_i^2)^2} \quad (3.6)$$

$$\tau_{z\theta} = \frac{4T_h(R_e^3 - R_i^3)}{3\pi(R_e^4 - R_i^4)(R_e^2 - R_i^2)} \quad (3.7)$$

However, different expressions were used by different researchers for the determination of average σ_r and σ_θ (Symes et al. 1984, Hight et al. 1983 and Nishimura 2005). These differences arise because of the various methods adopted for averaging the stresses. Averaging stresses over the entire area of the sample is advantageous because it accounts for the curvature of the sample (Vaid et al. 1990). For obtaining $\tau_{z\theta}$, some researchers considered the hybrid combination of elastic and plastic constitutive behavior (Hight et al. 1983, Chiaro 2010) but to avoid inconsistency, a single constitutive behavior is assumed to derive the stress components for CU-HCT.

3.3.2 Strain analysis

The axial strain (ε_z) is readily determined based on sample height measurements, and is given by:

$$\varepsilon_z = -\frac{\Delta H}{H} \quad (3.8)$$

where ΔH and H are the change in height, and the height of the specimen respectively.

The definitions of the radial (ε_r) and circumferential strain (ε_θ) on a soil element are shown in Figure 3.11 and it is given by Timoshenko and Goodier (1951):

$$\varepsilon_r(R) = \frac{R_e R_i (R_e \Delta R_i - R_i \Delta R_e)}{R_e^2 - R_i^2} \frac{1}{R^2} - \frac{R_e \Delta R_e - R_i \Delta R_i}{R_e^2 - R_i^2} \quad (3.9)$$

$$\varepsilon_\theta(R) = -\frac{R_e R_i (R_e \Delta R_i - R_i \Delta R_e)}{R_e^2 - R_i^2} \frac{1}{R^2} - \frac{R_e \Delta R_e - R_i \Delta R_i}{R_e^2 - R_i^2} \quad (3.10)$$

The average strain values are expressed as follows:

$$\varepsilon_r = \frac{\int_{R_i}^{R_e} \varepsilon_r dr}{\int_{R_i}^{R_e} dr} = - \left(\frac{\Delta R_e - \Delta R_i}{R_e - R_i} \right) \quad (3.11)$$

$$\varepsilon_\theta = \frac{\int_{R_i}^{R_e} \varepsilon_\theta dr}{\int_{R_i}^{R_e} dr} = - \left(\frac{\Delta R_e + \Delta R_i}{R_e + R_i} \right) \quad (3.12)$$

ΔR_e and ΔR_i are the changes in external and internal radius respectively.

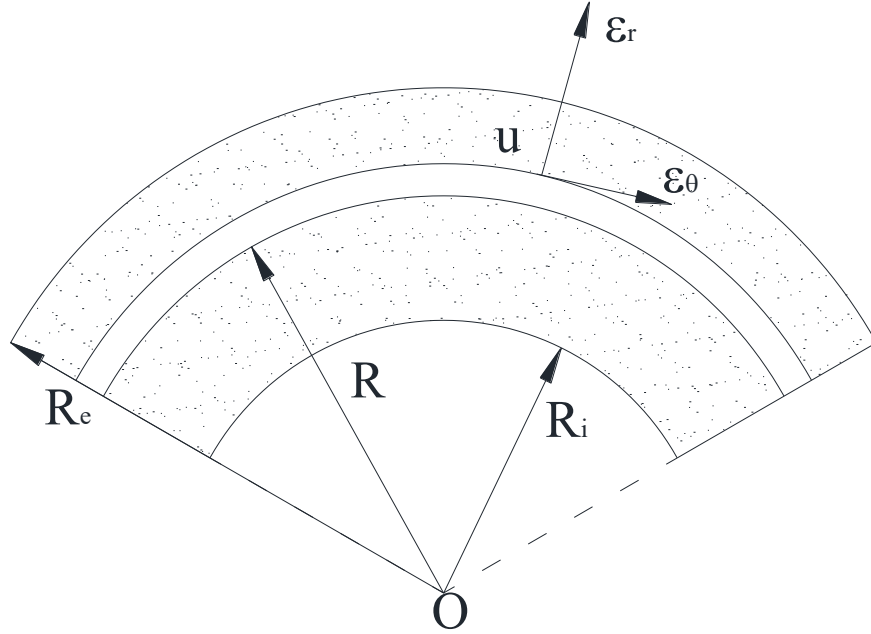


Figure 3.11: Strains in horizontal plane on a soil element

The torsional shear strain is expressed as:

$$\gamma_{z\theta}(R) = \left(\frac{R \cdot \Delta\theta}{H} \right) \quad (3.13)$$

where $\Delta\theta$ is the angular displacement.

The average torsional shear strain is obtained by integrating Eq. 3.13 over the cross section of the specimen and it is expressed as follows:

$$\gamma_{z\theta} = \frac{\int_0^{2\pi} \int_{R_i}^{R_e} \gamma_{z\theta} r dr d\theta}{\int_0^{2\pi} \int_{R_i}^{R_e} r dr d\theta} \quad (3.14)$$

$$\gamma_{z\theta} = \frac{2\Delta\theta(R_e^3 - R_i^3)}{3H(R_e^2 - R_i^2)}$$

3.3.3 Principal stresses and strains

The principal stresses and strains are obtained by using the principles of Mohr's circle.

Figure 3.12 shows the Mohr's circle for the stress components. The principal stresses and strains are expressed as follows:

$$\begin{aligned}\sigma_1 &= \frac{\sigma_z + \sigma_\theta}{2} + \sqrt{\left(\frac{\sigma_z - \sigma_\theta}{2}\right)^2 + \tau_{z\theta}^2} \\ \sigma_2 &= \sigma_r\end{aligned}\tag{3.15}$$

$$\begin{aligned}\sigma_3 &= \frac{\sigma_z + \sigma_\theta}{2} - \sqrt{\left(\frac{\sigma_z - \sigma_\theta}{2}\right)^2 + \tau_{z\theta}^2} \\ \varepsilon_1 &= \frac{\varepsilon_z + \varepsilon_\theta}{2} + \sqrt{\left(\frac{\varepsilon_z - \varepsilon_\theta}{2}\right)^2 + \left(\frac{\gamma_{z\theta}}{2}\right)^2} \\ \varepsilon_2 &= \varepsilon_r\end{aligned}\tag{3.16}$$

$$\varepsilon_3 = \frac{\varepsilon_z + \varepsilon_\theta}{2} - \sqrt{\left(\frac{\varepsilon_z - \varepsilon_\theta}{2}\right)^2 + \left(\frac{\gamma_{z\theta}}{2}\right)^2}$$

The inclination (α_σ) of major principal stress with respect to the axis of deposition and intermediate principal stress parameter (b_σ) is given by:

$$\alpha_\sigma = \tan^{-1}\left(\frac{\tau_{z\theta}}{\sigma_1 - \sigma_\theta}\right)\tag{3.17}$$

$$b_\sigma = \frac{\sigma_2 - \sigma_3}{\sigma_1 - \sigma_3}\tag{3.18}$$

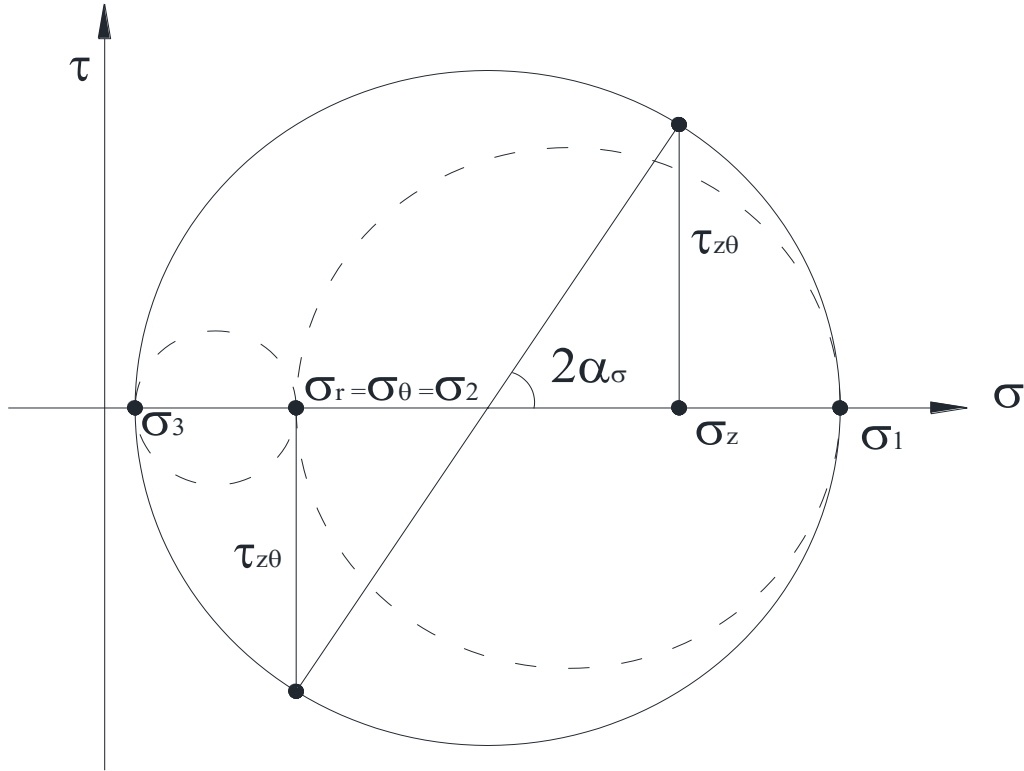


Figure 3.12: Mohr's circle of stresses in z - θ plane

3.3.4 Stress and strain non-uniformities in HCT specimen

Non-uniformity of stresses and strains across the specimen wall is an inherent problem in HCT testing. HCT test is interpreted as an element test, in which average stresses and strains are used to represent a stress state of the specimen. Therefore, these average stresses should not deviate much from the true stresses. Non-uniformity in an HCT specimen is caused by various factors such as rigid end restraints, curvature of the specimen, and differences between the inner and external pressures and the application of torque.

Numerical analyses have been carried out by several researchers to propose a suitable specimen dimensions that will reduce the level of non-uniformity (Hight et al. 1983; Sayao and Vaid 1991; Wijewickreme and Vaid 1991; Rolo 2003; Xu et al. 2013). Hight et al. (1983) proposed a parameter β_3 to quantify the level of non-uniformity of each

stress components due to wall curvature. From the results of finite element (FE) analysis with the assumption of linear elastic behaviour, an acceptable criterion of $\beta_3 < 0.11$ was suggested to have a tolerable level of non-uniformity for a particular specimen dimension.

Sayao and Vaid (1991) assessed the degree of non-uniformity in terms of stress ratio. It has been recommended that the influence of stress non-uniformity would be negligible if the non-uniformity coefficient (β_R) is less than 0.2. Wijewicreme and Vaid (1991) investigated the non-uniformity due to curvature using an incremental hyperbolic model to represent the non-linear behavior of soil. It is reported that the assumption of linear elastic behavior over-estimates the level of non-uniformity. Rolo (2003) numerically investigated the effect of specimen's height (H) to outer diameter (OD) ratio on the degree of non-uniformity using a modified cam clay model. It is concluded that larger the H/OD ratio lesser will be the degree of non-uniformity. Xu et al. (2013) also proposed similar conclusions from a 3D coupled FE analysis.

The sample dimensions adopted in CU-HCT apparatus is same as the dimensions adopted by Sayao and Vaid (1991) and it has larger H/OD ratio as suggested by Rolo (2003) and Xu et al. (2013). Therefore, the stress non-uniformity due to curvature and end restraint is well within the admissible limit for CU-HCT apparatus.

3.4 Membrane strength correction

In HCT, the soil specimen is confined between two flexible rubber membranes. When soil sample is subjected to surface tractions, a part of it is transferred to the membranes thereby affecting the magnitude of stress acting on the sample. Therefore, the stresses σ_z' , σ_r' , σ_θ' and τ_h should be corrected for the membrane forces. Membrane forces may be significant

for undrained tests on loose sands, tests on soft sediments and tests at low confining pressure (Kuerbis and Vaid 1990).

The membrane forces are determined based on the theory of elasticity. The assumptions involved in deriving the membrane forces are (Fauzi 2015):

- The membrane is perfectly elastic
- The thickness is same for both inner and outer membranes.
- The change in membrane thickness during straining is neglected
- Pressure in the inner and outer chamber are same ($P_e = P_i$). During undrained shearing of large specimens, the differences in these pressures are typically less than 5% (Ampandu 1991). Also, in this present study, during cyclic coupled loading and also during monotonic shearing under undrained and partially drained condition, the difference between inner and outer pressure is varying only between 5 to 7%. Hence the assumption of $P_e = P_i$ for deriving membrane forces is reasonable.

The equations used for membrane force correction are given as follows (Fauzi 2015):

$$\sigma_{zc}' = \sigma_z' - \Delta\sigma_{zm} \quad (3.19)$$

$$\Delta\sigma_{zm} = \frac{4t_mE_m}{3(R_e^2 - R_i^2)} [R_e(2\varepsilon_{zmo} + \varepsilon_{\theta mo}) + R_i(2\varepsilon_{zmi} + \varepsilon_{\theta mi})] \quad (3.20)$$

$$\sigma_{rc}' = \sigma_r' - \Delta\sigma_{rm} \quad (3.21)$$

$$\Delta\sigma_{rm} = \frac{2t_mE_m}{3(R_e + R_i)} [(\varepsilon_{zmo} + 2\varepsilon_{\theta mo}) - (\varepsilon_{zmi} + 2\varepsilon_{\theta mi})] \quad (3.22)$$

$$\sigma_{\theta c}' = \sigma_{\theta}' - \Delta\sigma_{\theta m} \quad (3.23)$$

$$\Delta\sigma_{\theta m} = \frac{2t_m E_m}{3(R_e - R_i)} [(\varepsilon_{zmo} + 2\varepsilon_{\theta mo}) + (\varepsilon_{zmi} + 2\varepsilon_{\theta mi})] \quad (3.24)$$

$$T_{hc} = T_h - T_m \quad (3.25)$$

$$T_m = \frac{2\pi t_m E_m \theta}{3H} (R_e^3 + R_i^3) \quad (3.26)$$

Where σ_{zc}' , σ_{rc}' and $\sigma_{\theta c}'$ are axial, radial, and circumferential effective stress corrected for membrane stresses;

T_{hc} – Torque corrected for the membrane forces;

T_m – Torque acting on the membrane

$\Delta\sigma_{zm}$, $\Delta\sigma_{rm}$, $\Delta\sigma_{\theta m}$ – axial, radial, and circumferential stresses acting on the membrane;

ε_{zmo} , $\varepsilon_{\theta mo}$ – Axial and circumferential strain in outer membrane;

ε_{zmi} , $\varepsilon_{\theta mi}$ – Axial and circumferential strain in inner membrane;

E_m and t_m – Young's Modulus and thickness of the membrane.

3.5 Membrane penetration correction

Membrane penetration effect or membrane compliance is an important phenomenon which affects the measured volume change (or excess pore water pressure) in laboratory test results on granular soils. Membrane penetration induces a partially drained state in a conventional undrained test (Sivathayalan and Vaid 1998). In an undrained test, when pore water pressure increases, the membrane moves outward from the interstices. As a result, the pore water migrates from the soil sample and hence the measured excess pore pressure will be less than that of the truly undrained test. This underestimation of excess pore water pressure results in the overestimation of liquefaction resistance of soil. Therefore, it may be necessary to correct the excess pore water pressure for the membrane penetration effects.

In a conventional drained test, the membrane penetration affects the measured volumetric strain, but unlike in undrained tests, it does not influence the effective stress state of the sand specimen. Whereas in a drained test involving the change in effective stress, the measured volumetric strain consists of both volumetric strain from soil skeleton and volumetric strain from membrane penetration. Hence, in order to obtain the actual volumetric strain, the measured volumetric change has to be corrected for the effects of membrane penetration.

The magnitude of membrane penetration is usually expressed in terms of unit membrane penetration (ε_m). Unit membrane penetration is defined as the change in volume per unit surface of the membrane in contact per 10-fold change in the effective stress. The change in volume induced by membrane penetration (ΔV_m) is given by:

$$\Delta V_m = \varepsilon_m A_m \log \left(\frac{\sigma'_{current}}{\sigma'_{initial}} \right) \quad (3.27)$$

Where A_m is the surface area of the membrane and σ' is the effective confining stress.

The magnitude of membrane penetration is influenced by various factors such as average grain size, gradation, relative density, and soil fabric. The effect of relative density and soil fabric is negligible when compared to the influence of mean particle size (D_{50}) (Ramana and Raju 1982; Seed et al. 1989 and Nicholson et al. 1993 a,b).

Several researchers proposed membrane penetration corrections for both drained and undrained tests (Vaid and Negussey 1984; Kramer and Sivaneswaran 1989; Tokimatsu and Nakamura 1987; Ansal and Erken 1996; Sivathayalan and Vaid 1998). Sivathayalan and Vaid (1998) performed a truly undrained test on Fraser River sand ($D_{50} = 0.27$ mm) by injecting the volume of water calculated from Eq. (3.28) into the specimen to compensate for volume changes induced by the membrane penetration. The result obtained

is compared with the conventional undrained test and it is observed that the difference in maximum excess pore water pressure between these two tests was only about 7%.

In this present study, Fraser River sand with a mean particle size of 0.27 mm is used to investigate the cyclic response of sand under the combined action of compression and shear waves and partially drained response of sand under non-linear volumetric strain paths. The Fraser River sand used in this research work and in the work of Sivathayalan and Vaid (1998) has similar D_{50} and gradation and hence, in this study the excess pore water pressure is not corrected for the effects of membrane penetration in undrained cyclic tests and partially drained tests. However, in partially drained test, the volumetric strain is corrected for the effects of membrane penetration based on the unit membrane penetration resistance ($\epsilon_m = 3 \times 10^{-3} \text{ cm}^3/\text{cm}^2$ per logarithmic change in effective confining stress) obtained from Sivathayalan and Vaid (1998) for D_{50} of 0.27.

4. TEST MATERIAL AND PROCEDURES

4.1 *Introduction*

This chapter describes the details of test materials, specimen preparation techniques and specimen assembly. It also presents the results of preliminary undrained monotonic and cyclic tests carried out to demonstrate the performance and control of CU-HCT apparatus and establish a baseline for comparison with the data reported in the literature.

4.2 *Test Materials*

4.2.1 *Fraser River sand*

The cyclic tests were performed on sand dredged from the Fraser River near Abbotsford, British Columbia, Canada. The original sand was dry-sieved through #20 sieve to remove coarse particles and wet-sieved through #200 sieve to remove fines. Figure. 4.1 shows the grain size distribution of Fraser River sand, as received, and as used in this research program. The removal of the coarse and fine materials yielded a uniform sand with a mean diameter (D_{50}) of 0.27 mm, uniformity coefficient C_u of 2.3, and coefficient of curvature C_c of 1.1. The specific gravity, maximum and minimum void ratios of this batch of Fraser River sand determined according to the ASTM test standards [ASTM D854, D4253, D4254 (ASTM 2014a, b, c)] are 2.71, 0.866 and 0.511, respectively.

4.3 *Reconstitution of sand specimens*

To understand the mechanical response of granular soils through laboratory element tests, it is necessary to have several homogenous and identical soil specimens, which replicate the in-situ soil fabric as closely as possible. Ideally, undisturbed sand specimens are preferred for laboratory soil testing but obtaining undisturbed sand specimens through in-

situ ground freezing techniques are very expensive. Moreover, it is nearly impossible to find in-situ soil specimens that are homogenous and identical. Therefore, numerous reconstitution methods have been developed in the past to simulate the in-situ fabric of granular materials deposited under different conditions. The most notable methods are Air pluviation (AP), Water pluviation (WP) and Moist tamping (MT). It has been shown that pluviation in water mimics the alluvial deposition process, and the soil fabric resulting from water pluviation has been found to be similar to that of undisturbed fluvial sands (Oda et al. 1978; Vaid et al. 1999). So, the sand specimens used in this research program was reconstituted by water pluviation method to simulate the in-situ deposition process in an alluvial environment.

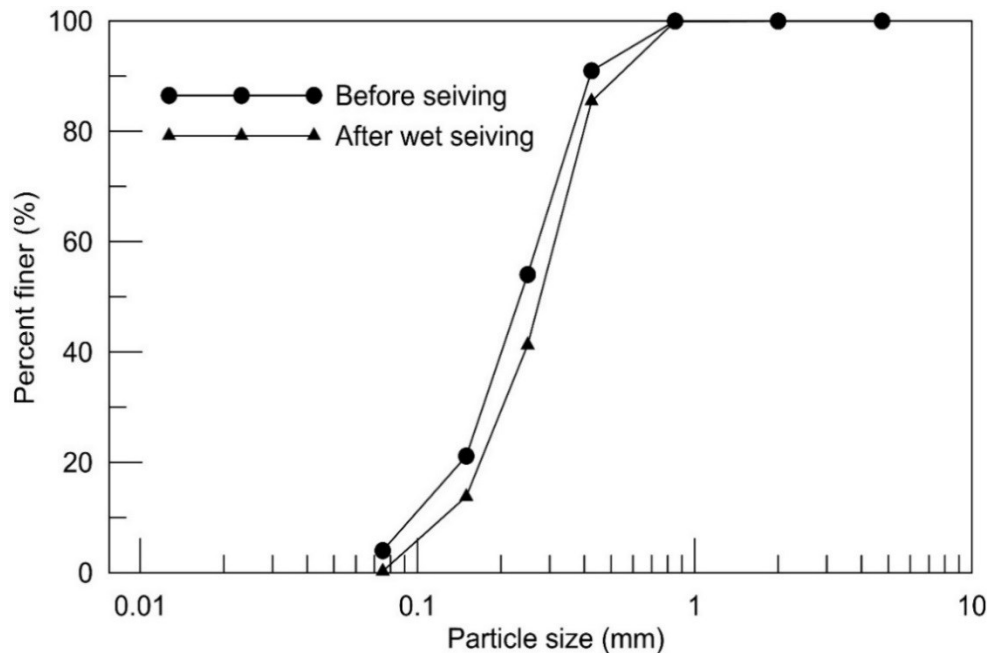


Figure 4.1: Particle size distribution of Fraser River sand

4.3.1 Preliminary preparation steps

A known amount of oven-dried sand (approximately 5 kg) is boiled in four flasks for about two hours to remove the entrapped air between the soil particles. After that, the flasks

containing boiled sand is filled with de-aired water, covered, and allowed to cool under room temperature without any contact with the surrounding air. The porous stones are also boiled to remove the entrapped air. The drainage lines in HCT are flushed with de-aired water and kept saturated. Before specimen preparation, both inner and outer membranes are checked for punctures. Adequate quantity of deaired water prepared by using Nold deaerator model 2100 (Geokon Inc. 2007) is used to fill the inner, cell and pore pressure containers and this deaired water is also used during specimen pluviation. A dial gauge is mounted on a movable stand and it is used to obtain the height of the sample during each stage of sample preparation. The transducers offset values are also reset in the data acquisition program before starting the sample preparation.

The base platen with inner membrane sealed in its position is placed on the base pedestal using two locating pins and it is locked in its position using six evenly spaced screws. The inner membrane is stretched around the four-piece inner split mold and it is held together by a thick metallic disc at the bottom and by an annular platen and O-ring at the top. De-aired water is flushed through the cavities in the base platen and saturated porous stones are placed in that saturated cavities. Outer membrane is placed around the base platen and it is sealed with an O-ring. Two-piece outer split mold is then assembled around the base platen. The outer mold has its inner surface lined with porous plastic, through which vacuum is applied for stretching the outer membrane.

4.3.2 Specimen preparation steps

The annular cavity formed by inner and outer mold is filled with de-aired water. The flasks with saturated sand are filled with de-aired water till its top and inverted into the annular cavity so that the deposition of sand proceeds under the action of gravity with mutual

displacement of water (Figure 4.2). During pluviation, the flasks are slowly traversed along the annular cavity to maintain the uniform level of deposition. Pluviation is continued till an excess of sand over the required height has been deposited. The top surface of the deposited sand is then levelled carefully by siphoning off the excess sand. This excess sand is oven dried and then weighed to determine the density and void ratio of the specimen.

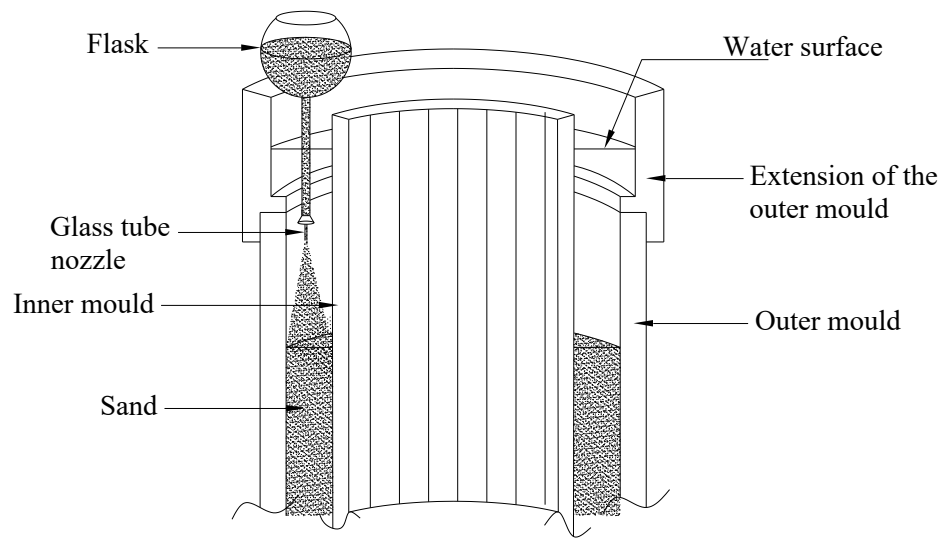


Figure 4.2: Specimen preparation by water pluviation method (after Logeswaran 2010)

The top platen with saturated porous stones is then seated on the levelled sand surface without disturbing the specimen. De-aired water is then allowed to percolate upwards through the specimen under a small pressure gradient to remove entrapped air between the membranes and the vertical wall of the top platen. The inner and outer membranes are then flipped carefully and sealed with O-rings. The top drainage line is closed and a vacuum of about 20 kPa is applied through the bottom drainage line. This suction provides confinement to the specimen and facilitates the removal of inner and outer split molds. From this stage till the end of specimen preparation, the change in specimen height and volume are recorded carefully using the dial gage and differential pressure

transducer, respectively. The top loading cap is now placed on the top platen, thus completing the specimen preparation.

4.3.3 Test preparation steps

The cell chamber is placed on the chamber base and de-aired water is allowed to fill the inner and outer chambers simultaneously. The cell top is now placed on the cell chamber and it seals the outer chamber. The top crossbeam is then swiveled in position and bolted to the reaction frame. The central rod which is used to monitor vertical displacement is then bolted to the loading shaft, thus sealing the inner chamber (Figure. 4.3). The specimen is then slowly moved upwards by pressurizing the double acting piston until the top-cap contacted the cross beam. The top loading cap is then bolted to the cross beam to ensure the perfect alignment of specimen's vertical axis and central axis of the frame. Two locating pins, protruding from the crossbar, is then inserted into the top loading cap to prevent the rotation of loading cap during torque application.

The specimen is made undrained and a hydrostatic confining pressure of 30 kPa is applied to increase the pore-water pressure to a small positive value before checking the specimen's saturation. Skempton's B value for checking specimen's saturation is measured by several increments of confining pressure under undrained conditions. The complete saturation of the test specimen is ensured by achieving a Skempton's B value greater than 0.99 and by applying a back pressure of at least 250 kPa. The specimens were subsequently consolidated to a targeted effective stress level in stages and sheared according to the desired stress paths or strain paths.

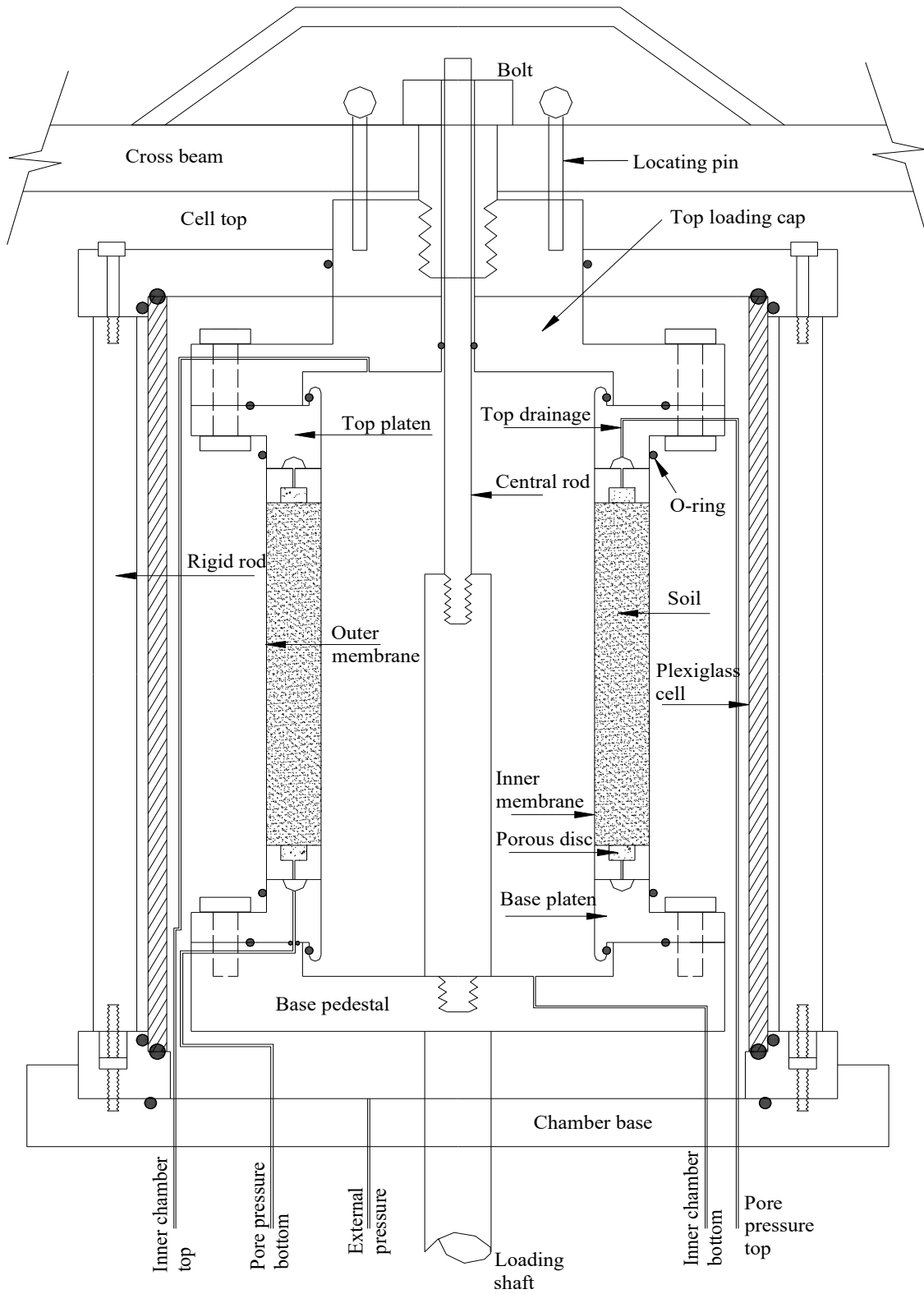


Figure 4.3: HCT specimen setup (after Logeswaran 2010)

4.4 Determination of void ratio

Reliable and consistent estimation of void ratio of the test specimen is very important for assessing the undrained response of granular soils and it also enables the valid comparison of test data. Void ratio of the soil is estimated from the known quantities such as mass of the dry soil (M_s), specific gravity of the solids (G_s) and volume of the specimen. Generally, volume is determined by measuring the height and circumference of the specimen. The conventional estimation of height using a dial gage yields a better resolution whereas the estimation of circumference using a tape or caliper imposes error in the measurement due to the effect of membrane covering the specimen's surface and the limited resolution of such measurements (Vaid and Sivathayalan 1996b). Therefore, in this study, the procedure outlined by Vaid and Sivathayalan (1996b) was used to estimate the specimen's circumference for the confident assessment of void ratio.

To determine the outer diameter, the membrane lined cavity formed by the outer mold is filled with water. The outer diameter is then deduced by measuring the mass of water required to fill the cavity, density of water at room temperature and height of the water column in the cavity. To determine the inner diameter, the cavity formed between the membrane lined outer and inner mold is filled with water. Then the inner diameter is calculated by using the same procedure adopted for finding the outer diameter.

The void ratio of the sample is then determined from these known values of initial inner and outer diameter and from the volume and height changes measured during each stage of sample preparation.

4.5 Preliminary tests

4.5.1 Undrained response of Fraser River sand under generalized stress states

Two monotonic undrained tests were carried out to characterize the basic undrained response of Fraser River sand and to demonstrate the influence of principal stress rotation on the shear strength characteristics. Figure 4.4 presents the stress strain and effective stress path response of Fraser River sand sheared at constant α_σ values of 0° and 45° . The specimens were hydrostatically consolidated to an effective mean normal stress of 100 kPa. Shearing was carried out at a constant total mean normal stress (σ_m) and a constant intermediate principal stress parameter (b_σ) of 0.4.

A profound undrained anisotropy is evident from the obtained test results. Sand strain hardens significantly when the major principal stress is aligned with the direction of deposition ($\alpha_\sigma = 0$) and the hardening tendency decreases when the major principal stress aligns towards the bedding plane. The maximum excess pore pressure was approximately 11 kPa for $\alpha_\sigma = 0^\circ$ test and it increases to 30 kPa for $\alpha_\sigma = 45^\circ$ test. There is almost a 15% reduction in the shear strength at phase transformation (S_{PT}) when the inclination of principal stress changes from 0° to 45° . Figure 4.5 presents the variation of strength ratio S_{PT}/σ'_{mc} with α_σ from this test series and also compares it with the result from Sivathayalan et al. (2015) for Fraser River sand. Though these test results cannot be compared directly due to the variation in specimen density and b_σ during shearing, the similar variation of S_{PT}/σ'_{mc} with α_σ from both the studies serves as a benchmark and adds confidence to the test data.

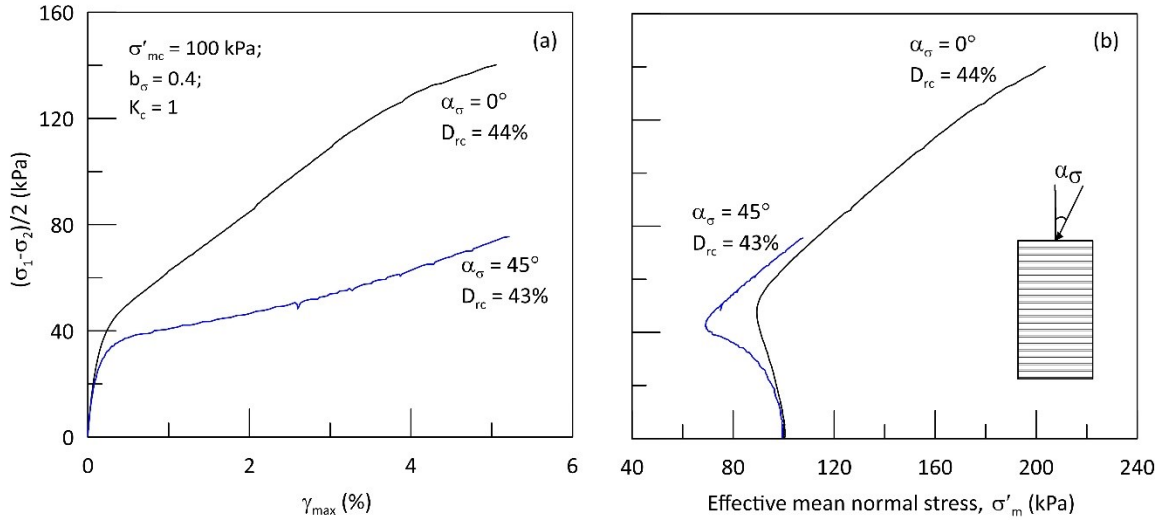


Figure 4.4: Monotonic response of the tested sand under different stress paths

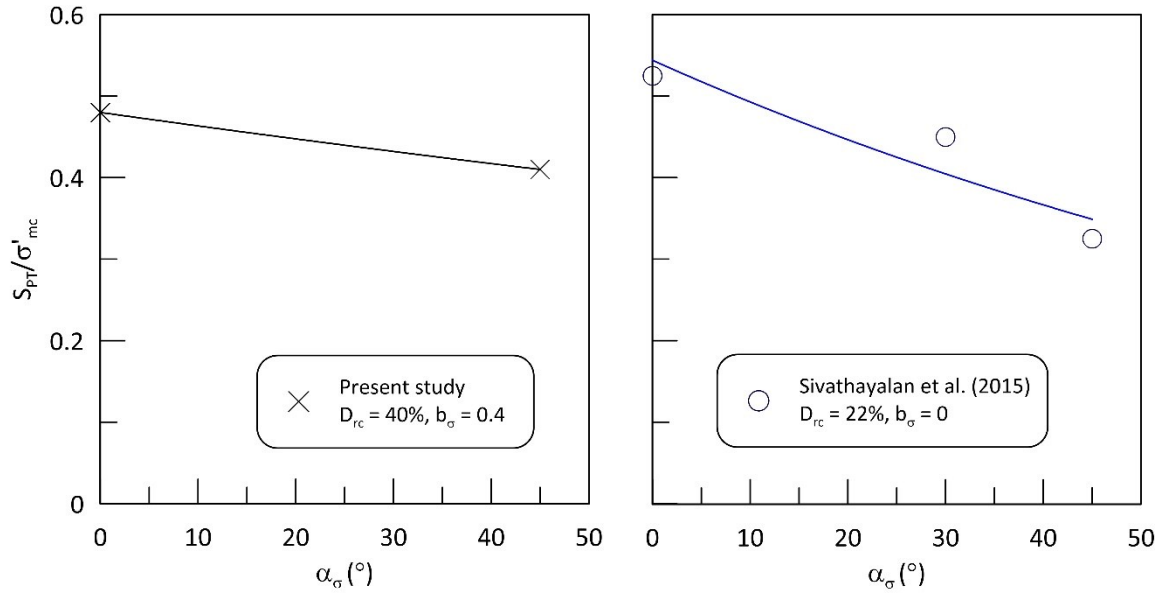


Figure 4.5: Variation of S_{PT} with α_{σ}

4.5.2 Undrained behavior of Fraser River sand under generalized strain paths

The one of the major objectives in this thesis is to examine the partially drained response of sand under non-linear volumetric strain paths. In CU-HCT, the strain paths are controlled with the help of Digital Pressure/Volume controllers (DPVCs). Hence, it is imperative to calibrate and assess the ability of DPVCs in performing such partially drained

tests. So, in this section, to assess the ability of DPVCs, undrained monotonic tests were carried out by controlling the direction of major principal strain axis (α_ε) with vertical and intermediate principal strain parameter (b_ε). So far, no studies have been carried out to assess the anisotropic characteristics of granular soil by controlling α_ε and b_ε . These tests were never attempted before using HCT because it required complex feedback control system to precisely control the all three normal strains ($\varepsilon_z, \varepsilon_r, \varepsilon_\theta$) and shear strain ($\gamma_{z\theta}$) independently.

Table 4.1 tabulates the details of HCT tests carried out for this test series. These tests were carried out on isotropically consolidated water pluviated Fraser River sand specimen. The specimens were isotropically consolidated in stages to an effective mean normal stress of 100 kPa and subsequently sheared along the specified loading path at a very slow maximum shear strain rate of 2%/hour. This slow rate of loading is adopted to ensure a proper feedback control response. During shearing the direction of major principal strain axis to vertical (α_ε), intermediate principal strain parameter (b_ε) and the volumetric strain (ε_v) was held constant.

Table 4.1: Initial and shearing parameters for generalized strain path tests

<i>Test No</i>	<i>Consolidation stage</i>			<i>Shearing stage</i>	
	<i>Stress state</i>	e_c	D_{rc} (%)	b_ε	α_ε (°)
SP01	$\sigma_1 = \sigma_2 = \sigma_3;$ $\sigma'_{mc} = 100$ kPa	0.732	37.7	0.4	0
SP02a		0.728	39.0		30
SP02b		0.717	41.8		30
SP03		0.725	39.8		45

SP04		0.723	40.2		60
SP05		0.713	43.1	1	90

A typical response of Fraser River sand subjected to undrained monotonic shearing ($\varepsilon_v = 0\%$) with α_ε of 30° and b_ε of 0.4 is plotted in Figure 4.6. At this loading condition the sand exhibits strain hardening response with the development of maximum excess pore pressure of about 30 kPa. An another important aspect to be noted in this test series is that, even though the volumetric strain remains unchanged, the shearing of sample involves simultaneous change in both total stress path and effective stress path. Figure 4.7 shows the variation of actual parameters with the targeted ε_v , α_ε and b_ε , and it can be observed that the differences are relatively insignificant. The variation of respective α_σ and b_σ is also plotted in the figure and it can be noticed α_ε and α_σ differs by about 3° and b_ε and b_σ differs by about 0.1 to 0.2. This non-coincidence of α_ε and α_σ is due to the non-coaxial behavior of sand during shearing. The non-coaxial behavior of granular soils has been recognized several researchers through HCT testing of sands under different α_σ (Gutierrez and Ishihara 2000; Tong et al. 2010; Cai et al. 2013; Rodriguez and Lade 2014).

In this test series, the samples are sheared at a globalized loading rate of $\gamma_{max} = 2\%/hr$. For every increment of γ_{max} , to maintain a fixed α_ε and b_ε , the DPVCs has to either inject or extract water to control axial strain, inner volume and pore volume. These DPVCs has a separate localized frequency apart from the globalized rate of γ_{max} and this frequency is expressed as hertz (*Hz*) or *pulses/second*. Each pulse of the DPVC connected to the axial piston causes an axial strain of 2.5×10^{-8} . Single pulse of the DPVCs connected to inner and sample volume causes a volumetric strain of 2.5×10^{-8} and

2×10^{-8} respectively. Therefore, this local frequency of DPVCs has to be selected in such a way that it should not affect the response of sand specimen. Since the shearing is carried out under undrained condition, the role of pore volume DPVC is irrelevant. Several trial analyses were carried out to determine the optimal frequency of axial and inner volume DPVCs. Figure 4.8 shows the variation of pore pressure and inner pressure at different frequencies of axial and inner volume DPVC. Pore pressure and inner pressure shows erratic variation at larger frequencies and it is reduced as the frequencies gets lowered. Based on this trial run, an optimum frequency of 1000 Hz for axial DPVC and 250 Hz for inner volume DPVC is selected and also these frequencies are sufficient enough to maintain a proper feedback control response. Figure 4.9 presents the responses of identical Fraser River sand specimen subjected to shearing along $\alpha_\varepsilon = 30^\circ$ and $b_\varepsilon = 0.4$. Though there is a 7% difference noticed in the pore pressure response, the identical stress-strain, effective and total stress path response confirms the good repeatability in specimen preparation and capability of DPVCs in following prescribed loading path.

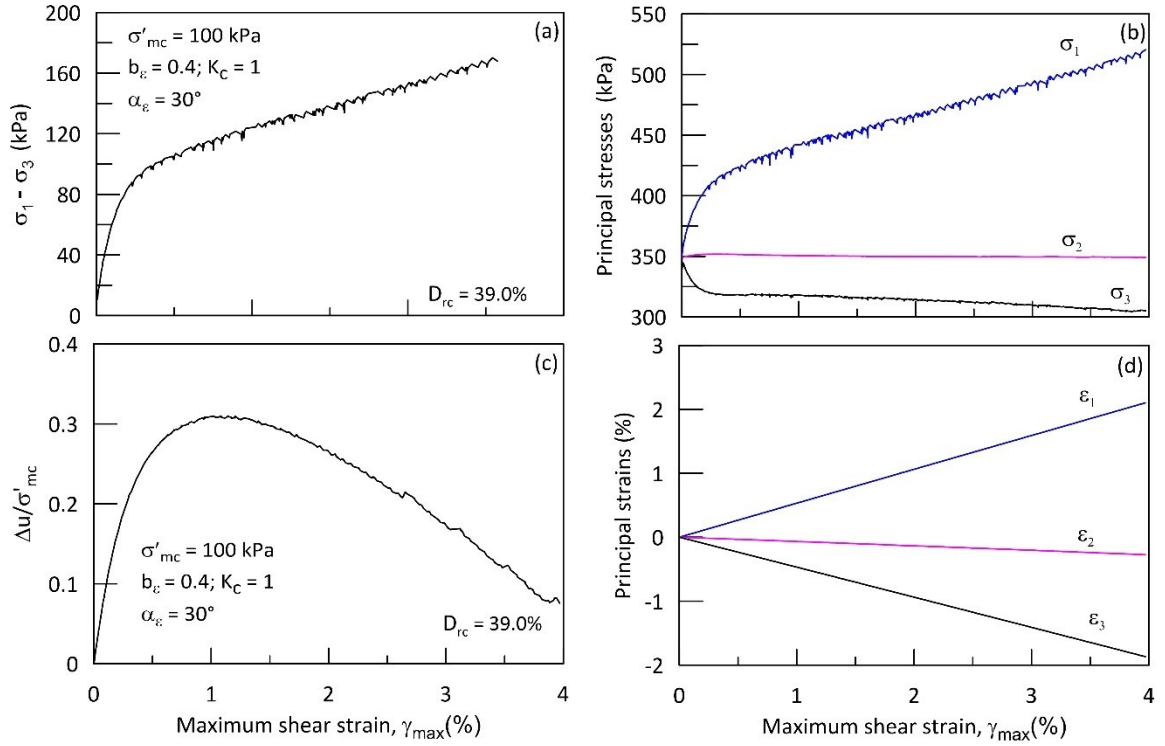


Figure 4.6: Typical response of Fraser River Sand under shearing with $\alpha_\varepsilon = 30^\circ$

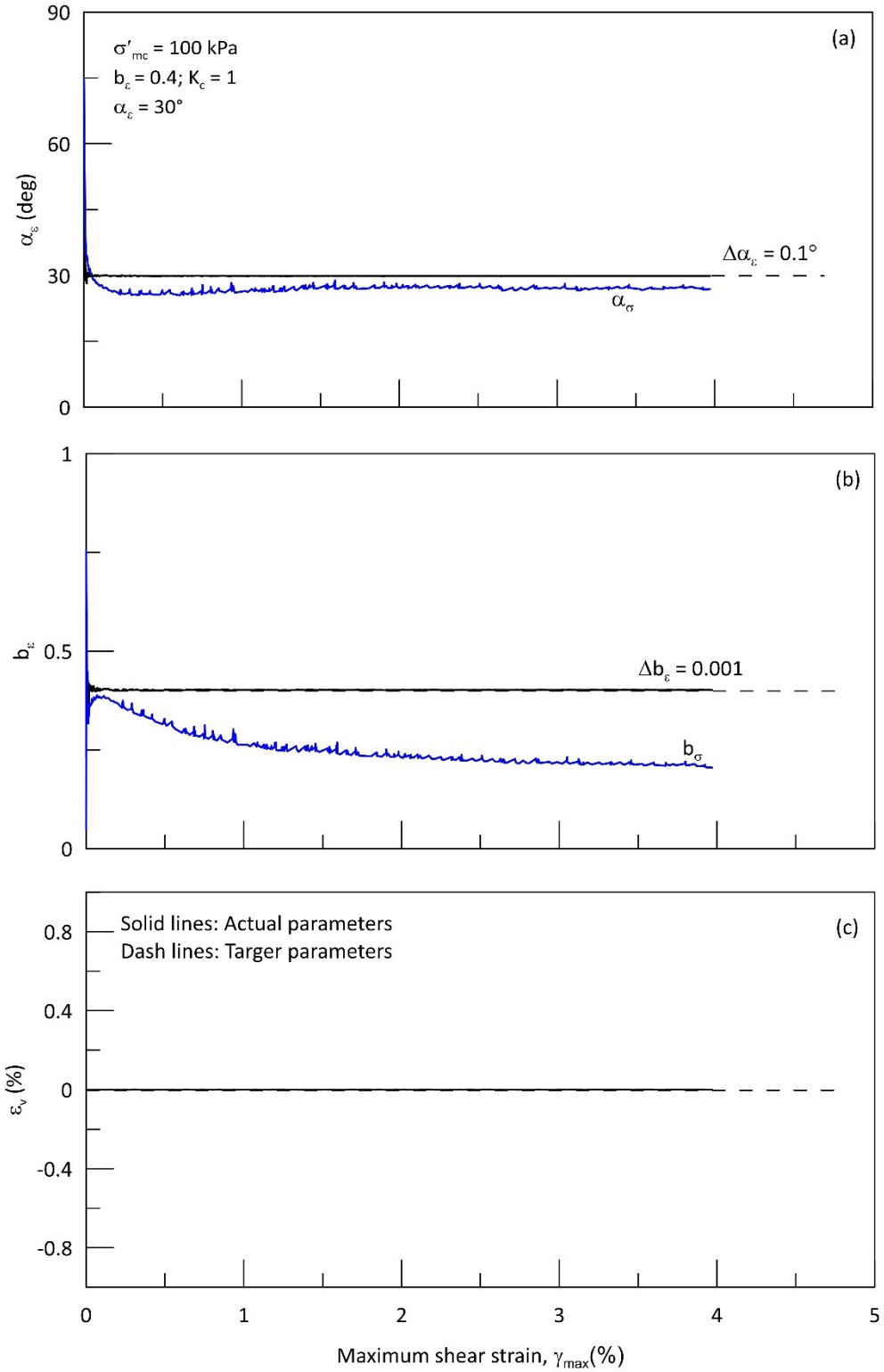


Figure 4.7: Comparison of actual and targeted parameters for shearing with $\alpha_e = 30^\circ$

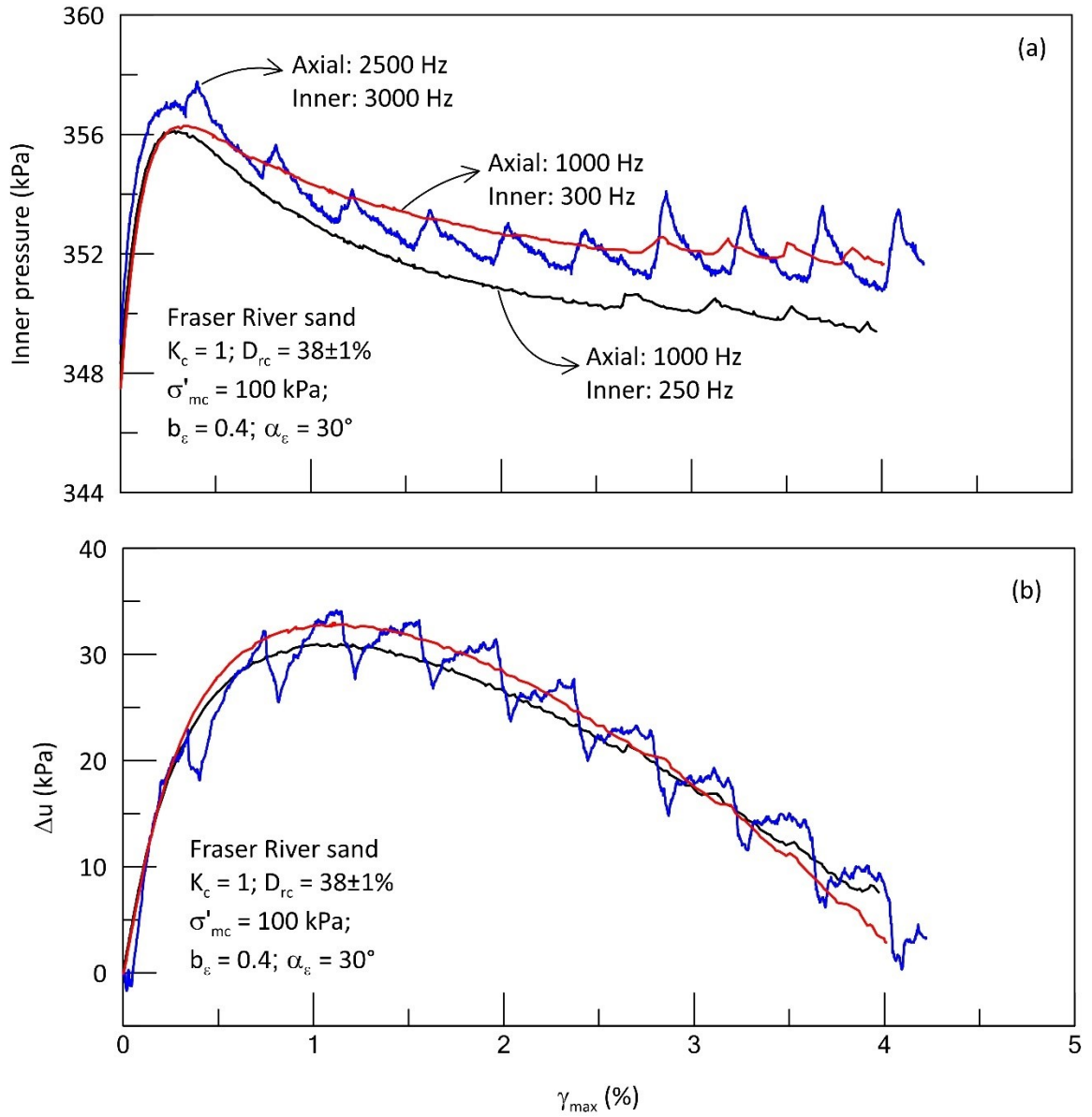


Figure 4.8: Variation of inner pressure and pore pressure at different DPVC frequencies

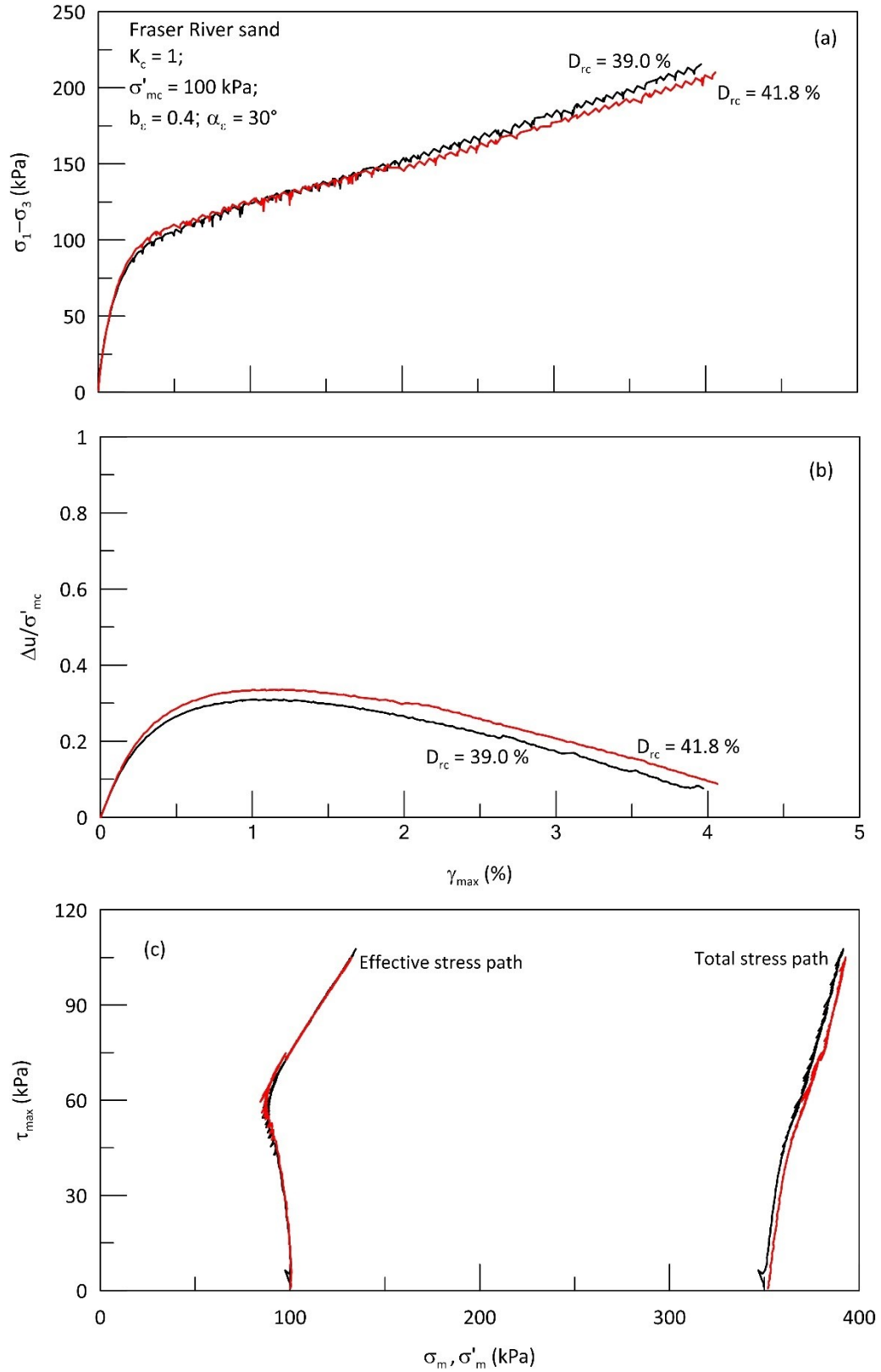


Figure 4.9: Repeatability of HCT undrained tests at $\alpha_\varepsilon = 30^\circ$ and $b_\varepsilon = 0.4$

4.5.2.1 Undrained behavior under shearing along different α_ε

The undrained monotonic response of isotropically consolidated sand specimens sheared at a constant α_ε varying from 0° to 90° is presented here. Except for $\alpha_\varepsilon = 90^\circ$, b_ε of 0.4 is maintained fixed throughout the shearing. For $\alpha_\varepsilon = 90^\circ$ test, b_ε of 1 is fixed inadvertently to verify the functioning of DPVC at this loading condition.

The variation of imposed normal strains ($\varepsilon_z, \varepsilon_r, \varepsilon_\theta$) and shear strain ($\gamma_{z\theta}$) and the variation of corresponding surface tractions ($\sigma'_z, \sigma'_r, \sigma'_\theta, \tau_{z\theta}$) induced in sand specimens sheared at different α_ε are illustrated in Figure 4.10 and 4.11. The computed principal strains, and the induced principal stresses and mobilized effective stress ratio for the same test series are plotted against axial strain ε_z in Figure 4.12 and 4.13. The imposed ε_z changes gradually from major principal strain to minor principal strain as α_ε changes from 0° to 90° . Since normal strains are the controlling variable in $\alpha_\varepsilon = 0^\circ$ & 90° tests, no torsional shear stress is induced in the test specimen in these tests. Figure 4.14 shows the variation of imposed α_ε and b_ε and Figure 4.15 shows the variation of α_σ and b_σ with maximum shear strain γ_{max} . The precision in which the α_ε and b_ε traced in this test series shows the capability of CU-HCT in controlling the direction of principal strains to evaluate the anisotropic characteristics of Fraser River sand. So far, no investigations have been attempted to study the anisotropic behaviour of granular soils by controlling the direction of major principal strain and intermediate principal strain parameter due to the complexity in testing apparatus and data acquisition and control systems.

It can be noticed from Figure 4.15 that at shearing with fixed b_ε and α_ε , the intermediate principal stress parameter b_σ shows a gradual decline with the increase in γ_{max} . Eventhough the induced b_σ is not close to the plane strain condition ($b_\sigma = 0.4 -$

0.45), the magnitude of ε_2 is much less than the absolute magnitude of ε_1 and ε_3 . It can also be noted that the non-coaxial behaviour is not observed in tests with $\alpha_\varepsilon = 0^\circ$ & 90° since the direction of major principal stress aligns with the direction of major principal strain. The non-coaxial behaviour is pronounced more in tests with $\alpha_\varepsilon = 30^\circ, 45^\circ$ & 60° and this existence of non-coaxiality when the major stress direction is not aligned along the direction of deposition during shearing is consistent with the observation noted in the literature (Lade et al. 2009; Blanc et al. 2011; Yang 2013; Rodriguez and Lade 2014).

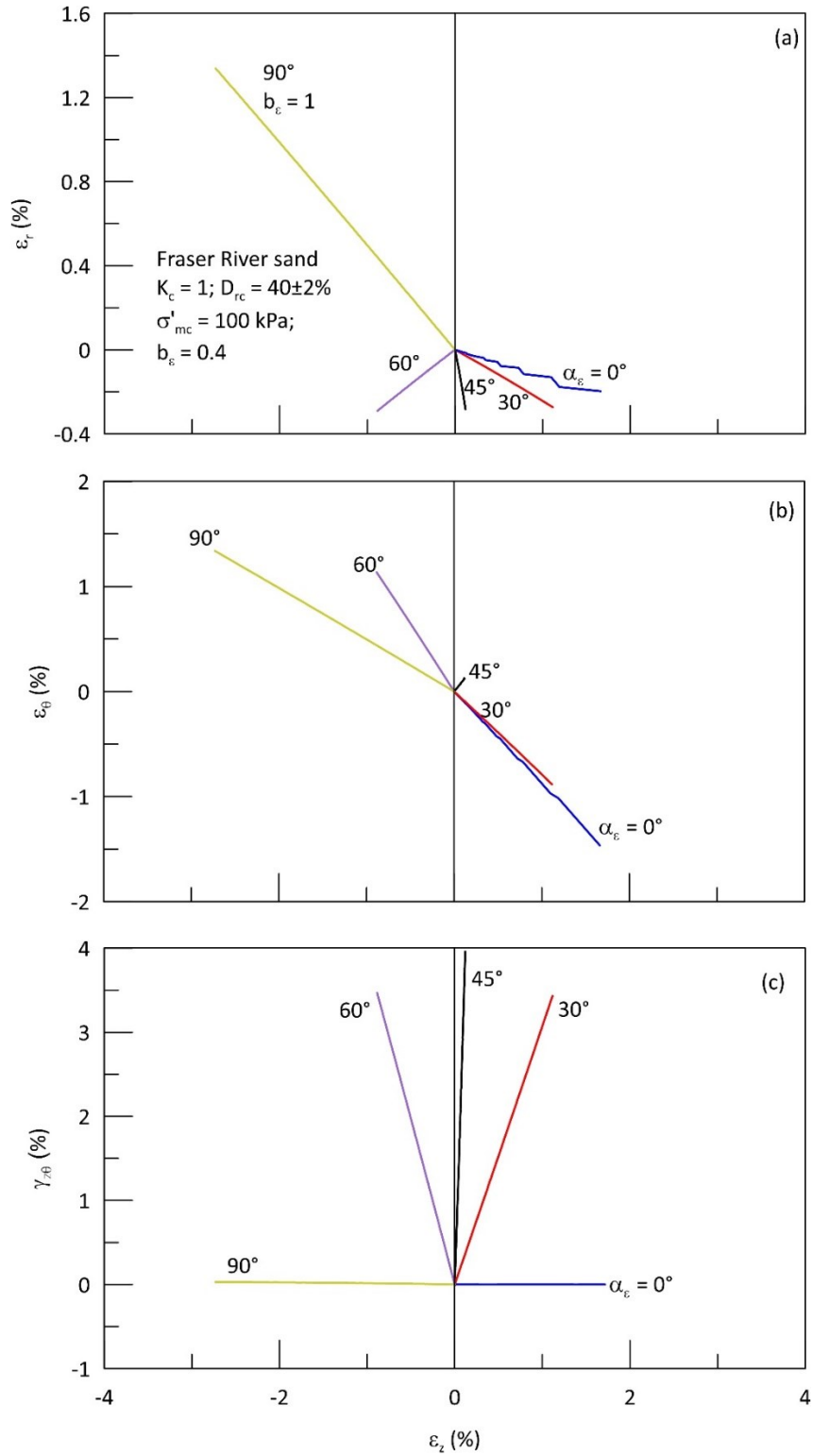


Figure 4.10: Variation of radial, tangential, and torsional shear strain with vertical strain during shearing with different fixed α_ϵ

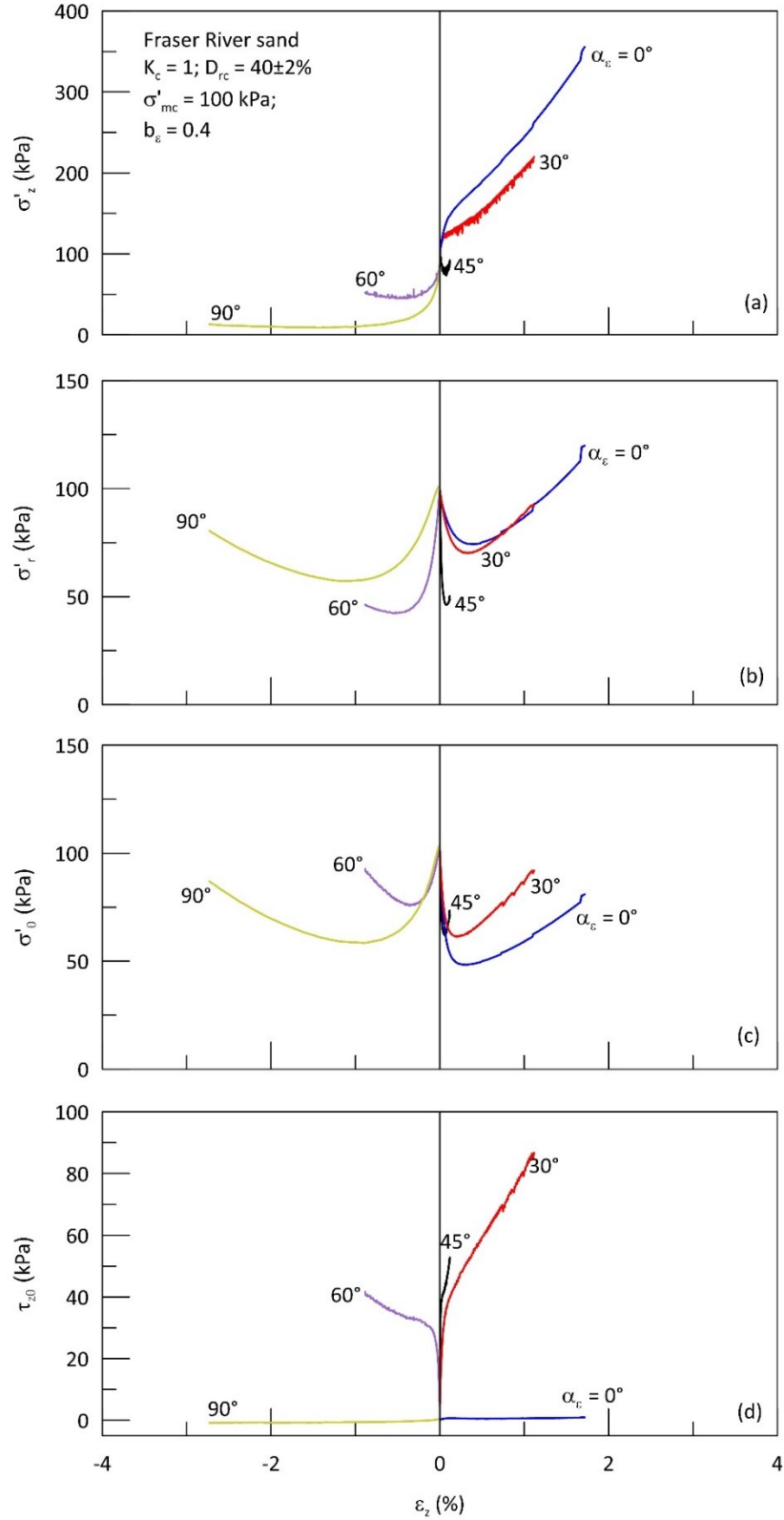


Figure 4.11: Variation of surface tractions during shearing with different fixed α_ε .

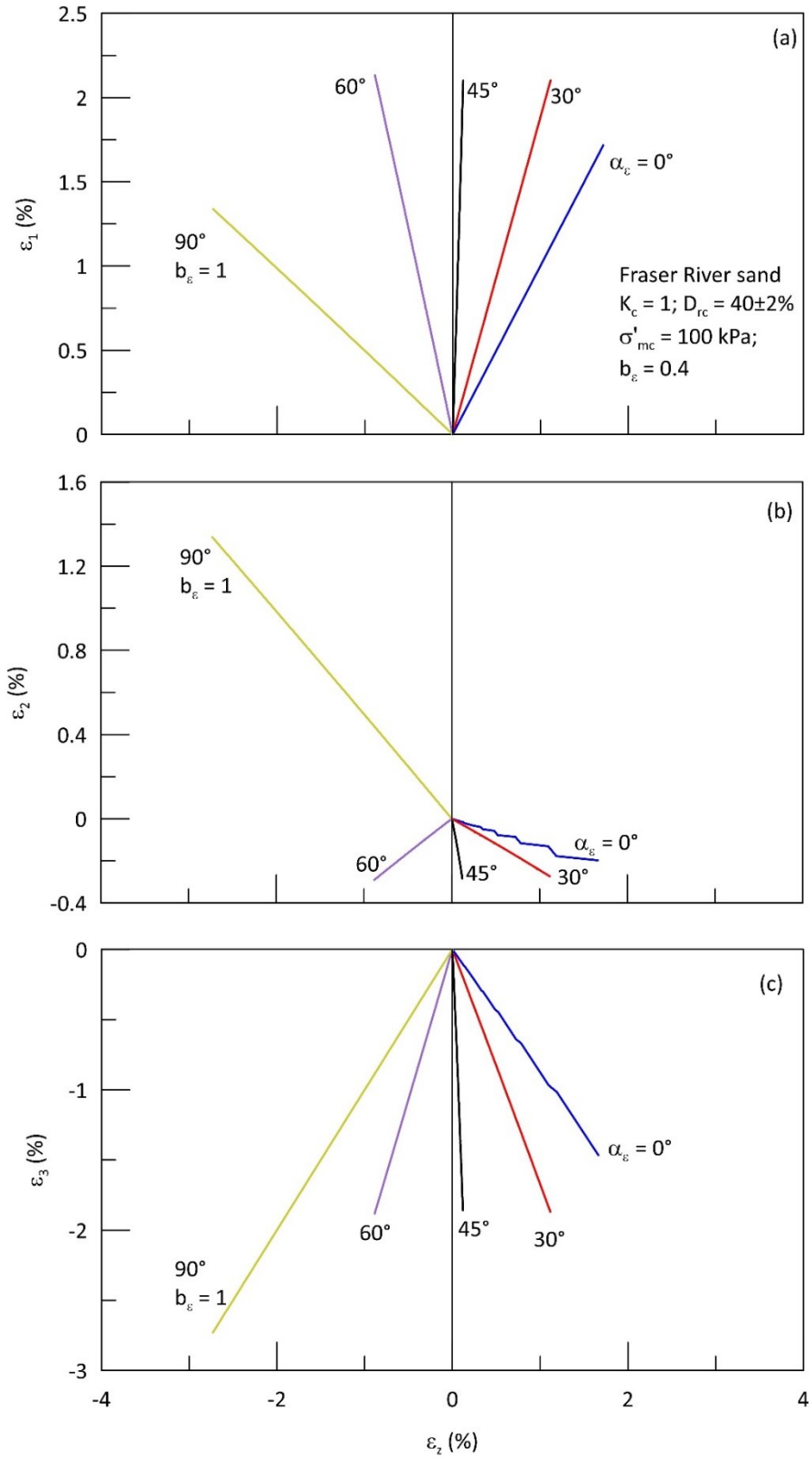


Figure 4.12: Variation of principal strains during shearing with different fixed α_ε

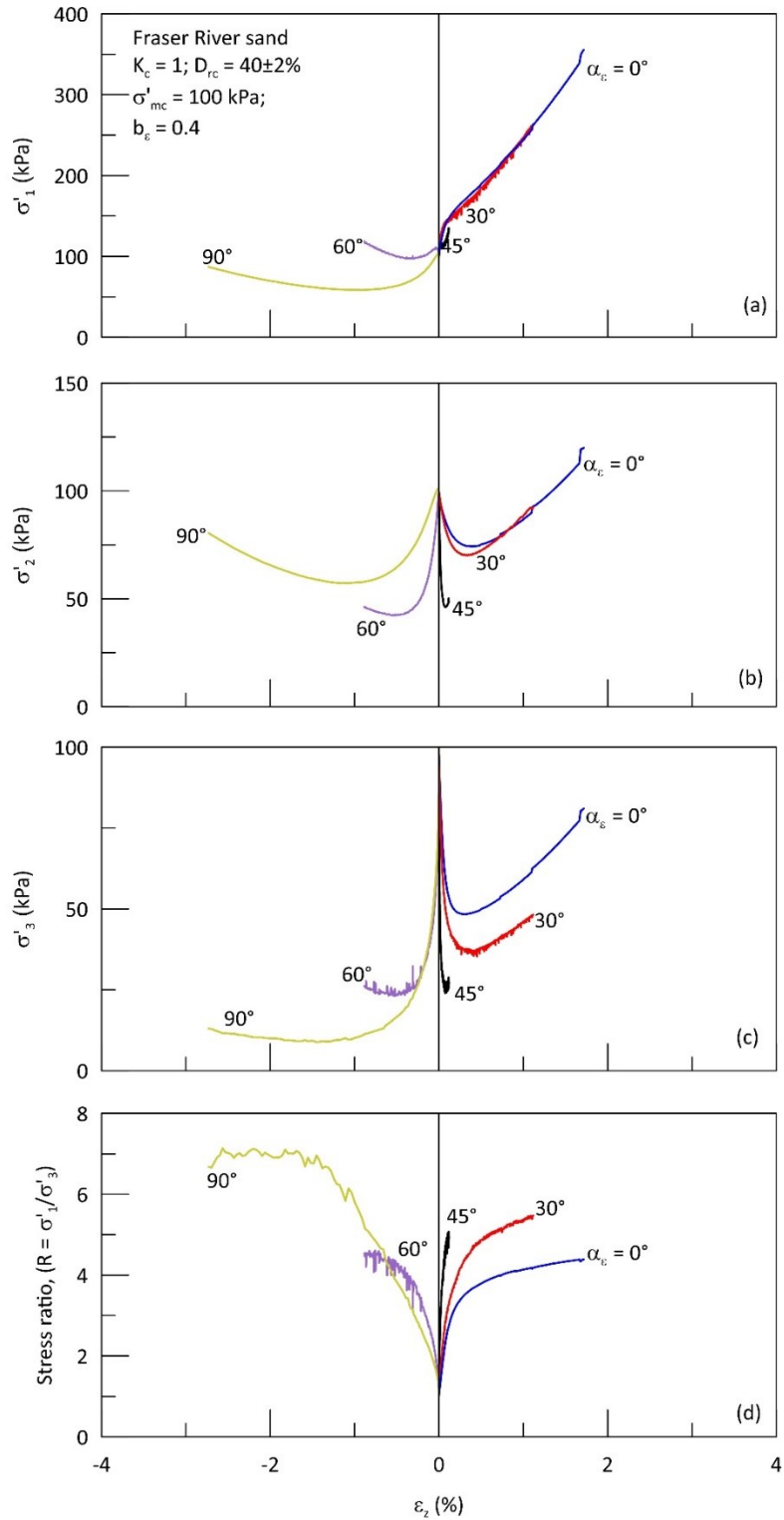


Figure 4.13: Variation of principal stresses and effective stress ratio during shearing with different fixed α_ϵ .

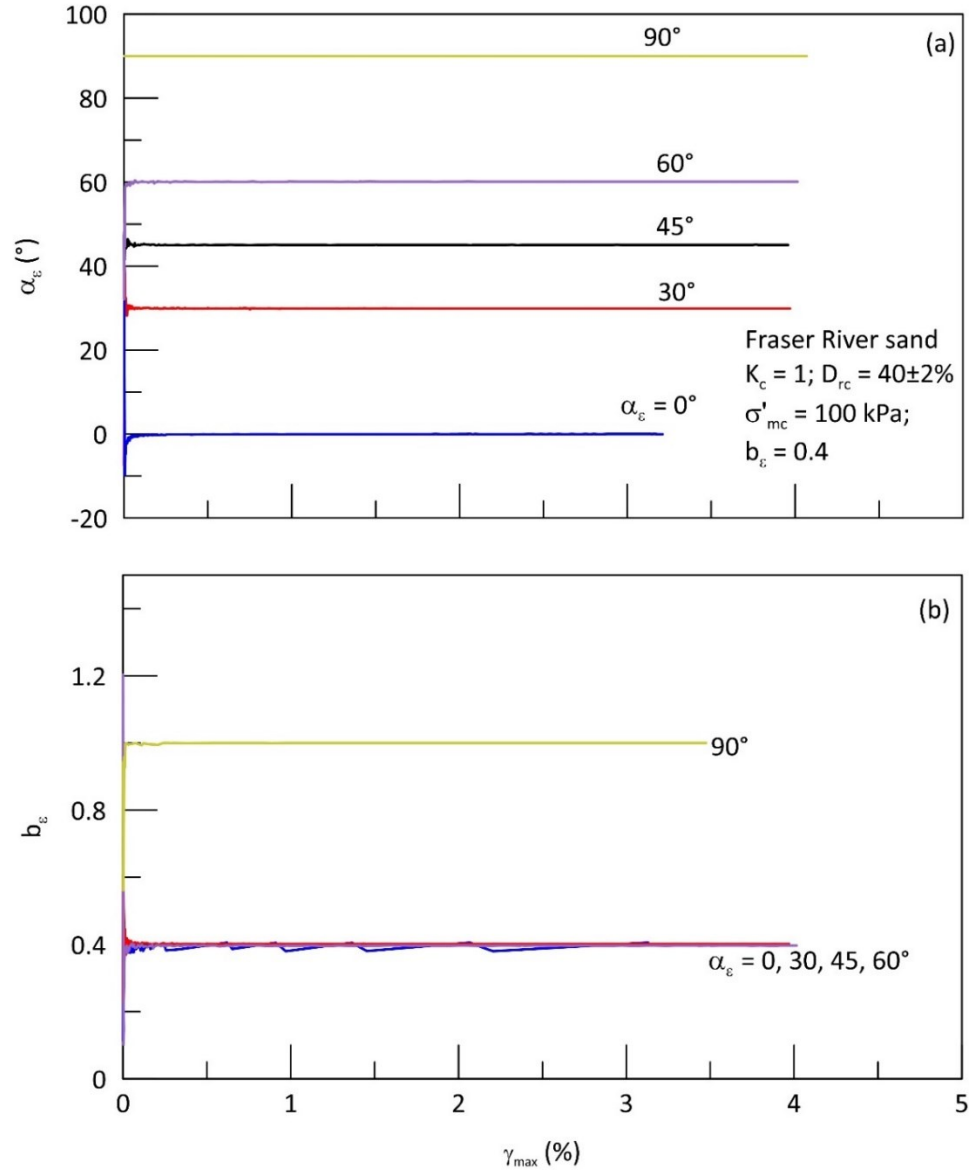


Figure 4.14: Variation of imposed α_ε and b_ε under shearing with different fixed α_ε .

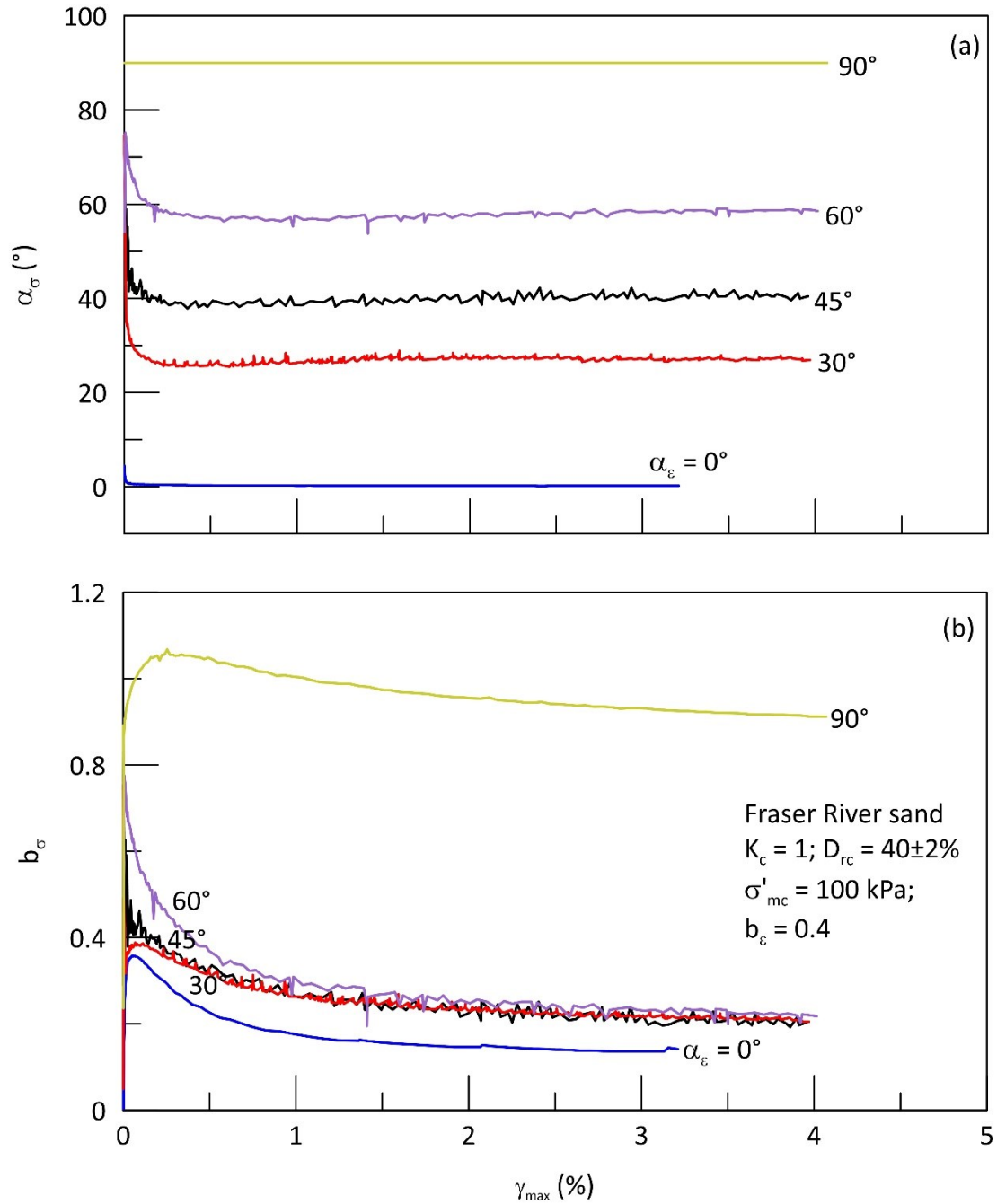


Figure 4.15: Variation of induced α_σ and b_σ under shearing with different fixed α_ϵ .

The undrained response Fraser River sand sheared along different α_ϵ is shown in Figure 4.16. The sand strain hardens significantly when the direction of major principal strain aligns with the direction of deposition and the hardening tendency decreases as the direction of major principal strain aligns with the weak horizontal bedding plane. The

maximum total excess pore pressure generated was about 27 kPa in the test with $\alpha_\varepsilon = 0^\circ$ and it increases systematically with increase in α_ε and reaches a maximum of about 51 kPa in the test with $\alpha_\varepsilon = 60^\circ$. At $\alpha_\varepsilon = 90^\circ$, the generated maximum excess pore water is about 42 kPa lower than the maximum Δu generated in $\alpha_\varepsilon = 45^\circ$ & 60° test. This reduction might be because the $\alpha_\varepsilon = 90^\circ$ test is conducted at a b_ε of 1. Figure 4.17 illustrates the total stress path response of sand sheared along different α_ε . Except for $\alpha_\varepsilon = 90^\circ$ test, an increase in the total normal stress from the initial consolidation stress state is noted in test specimens sheared along different α_ε . The absence of appreciable strain softening response at $\alpha_\varepsilon = 90^\circ$ for this batch of Fraser River sand is consistent with the observation reported in Sinthujan (2013) and Sivathayalan et al. (2015). Since total normal stress is not constant in these tests, both hydrostatic stress increment and shear stress increment contributes to the generation of excess pore water pressure. Figure 4.18 shows the variation of pore pressure generated by total normal stress increment (Δu_{normal}) and shear stress increment (Δu_{shear}) at different levels of α_ε . A systematic variation in both Δu_{normal} and Δu_{shear} is observed with the increase in α_ε . Δu_{normal} systematically decreases with the increasing α_ε whereas Δu_{shear} increases with the increasing α_ε .

The peak Δu_{shear} increased dramatically from 4 kPa to about 58 kPa with the increase in α_ε from 0° to 90° . Here the increase in α_ε is accompanied by the increase in α_σ as well and several investigations also reported a similar systematic increase in shear induced excess pore water pressure with the change direction of principal stress axis from direction of deposition to direction of bedding (Uthayakumar and Vaid 1998; Sivathayalan and Vaid 2002; Sivathayalan et al. 2015).

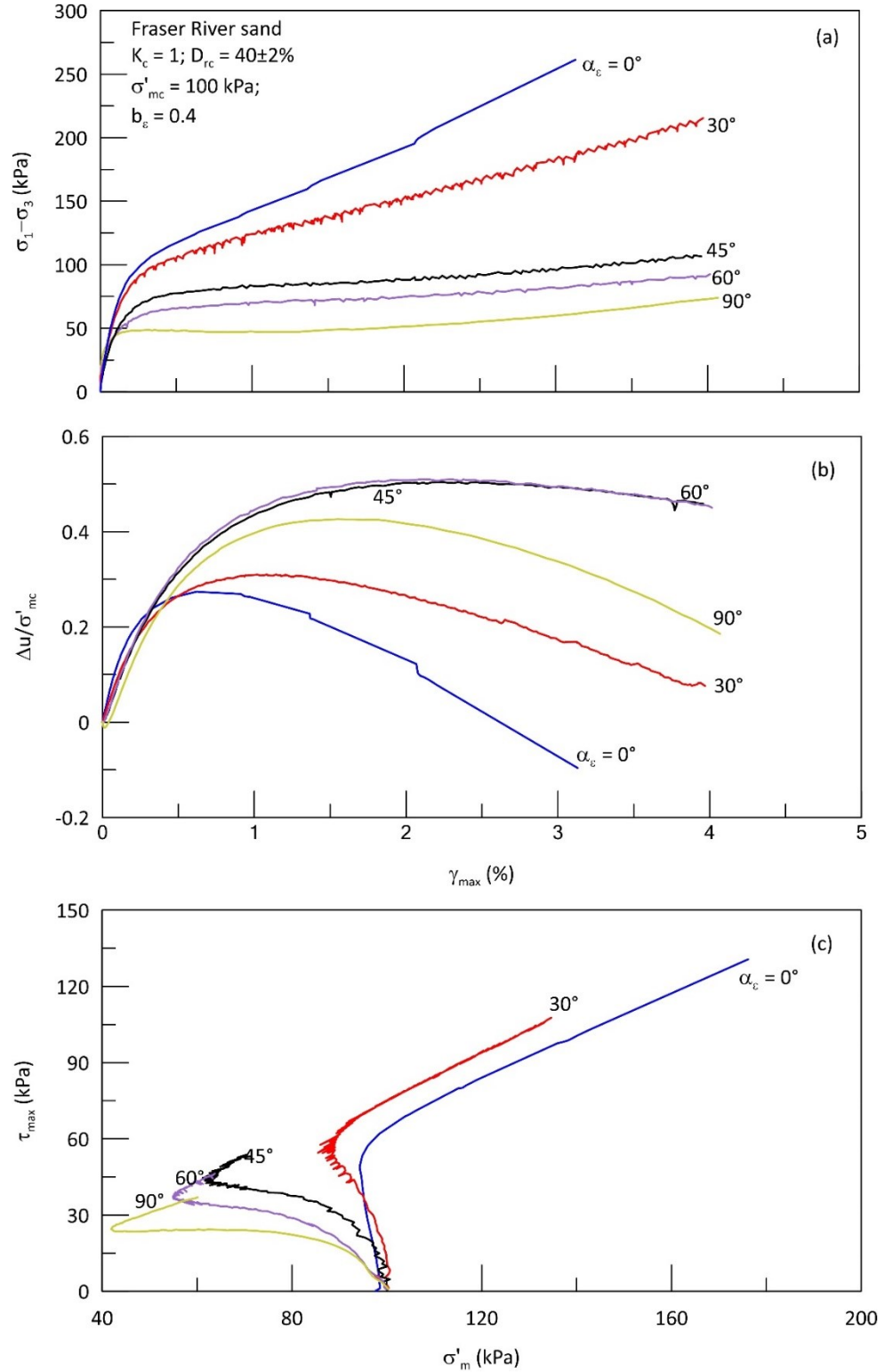


Figure 4.16: Undrained monotonic response of sand sheared along different α_ε .

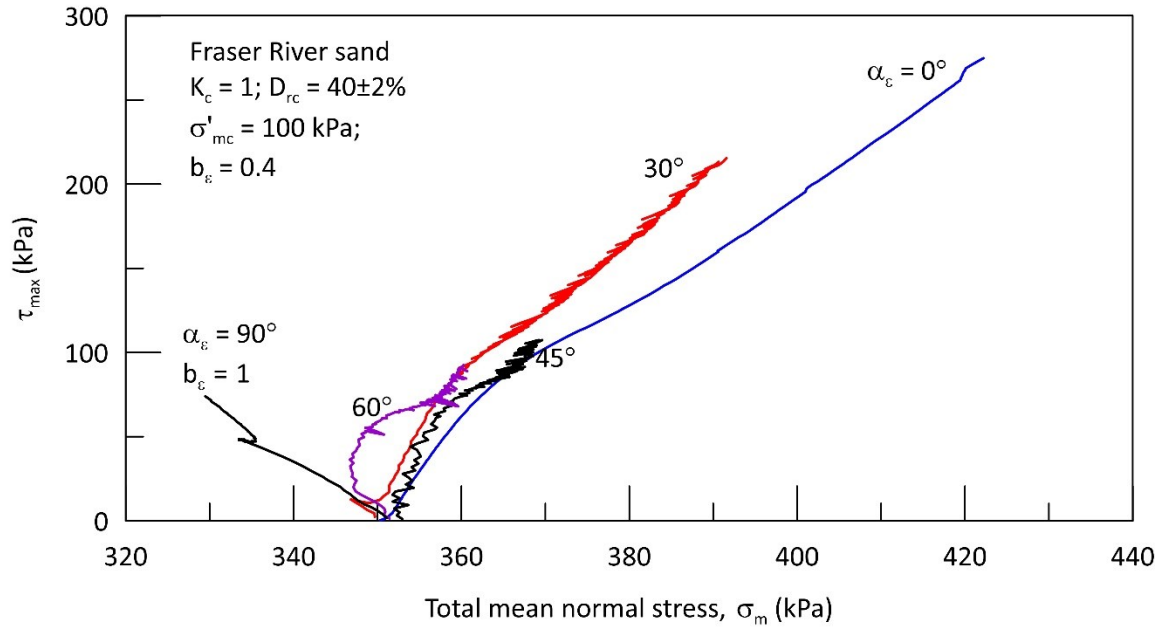


Figure 4.17: Total stress path response of sand sheared along different α_ϵ .

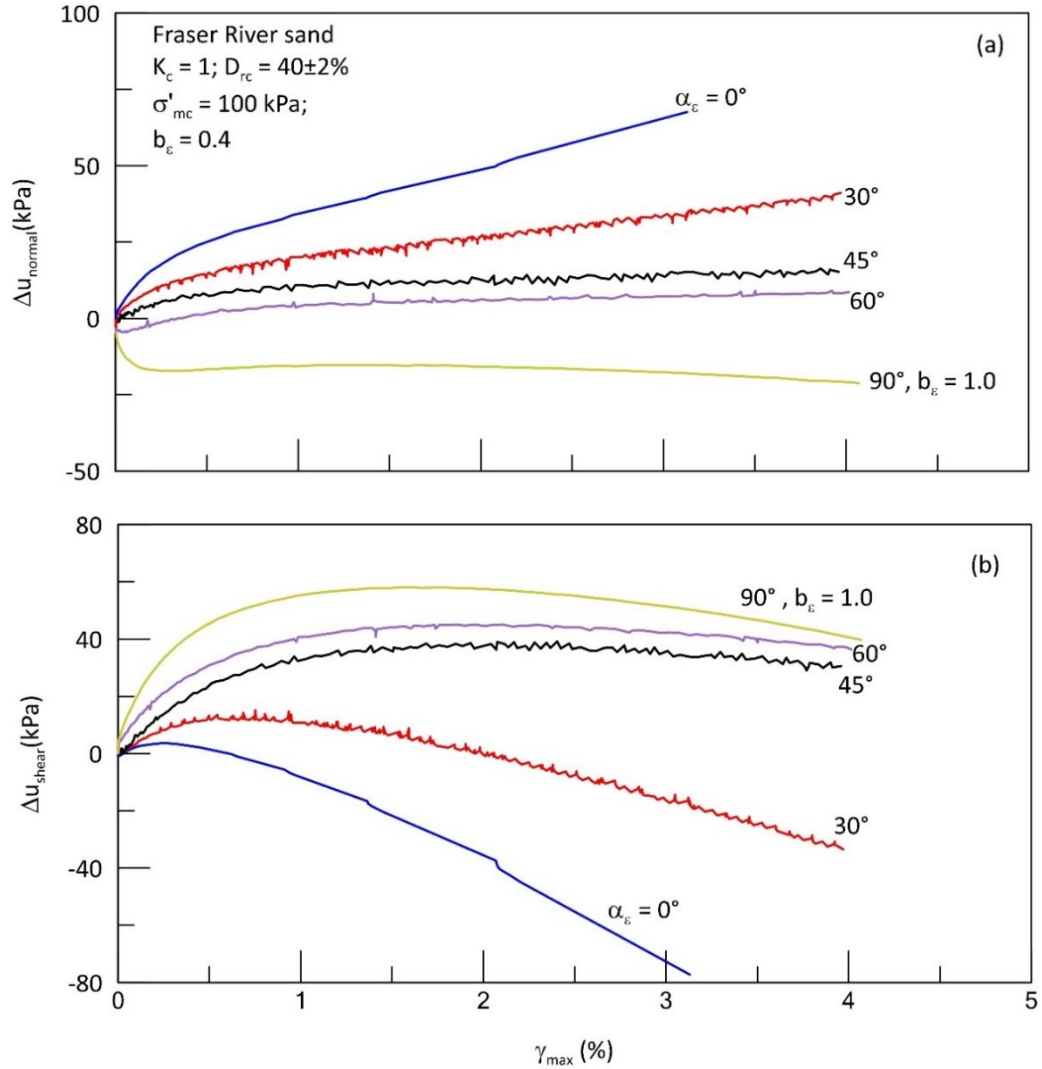


Figure 4.18: Pore pressure generated by mean normal stress increment and shear stress increment at different α_ε

Figure 4.19 shows that the shear strength of the sand at the phase transformation state (S_{PT}) decreases with the increase in the inclination of major principal strain axis. There is almost a 60% reduction in S_{PT} as the inclination of the major principal strain axis changes from the direction of deposition to the direction of bedding. The figure also compares the variation of (S_{PT}/σ'_{mc}) with α_σ from previous investigations on Fraser River sand. The trend of variation is almost identical in all these studies. The S_{PT} obtained from this present study is higher among other studies due to high relative density of the tested

specimen. S_{PT} from Sivathayalan et al. (2015) is higher when compared to Sivathayalan and Vaid (2002) and Uthayakumar and Vaid (1998) because of the low intermediate principal stress parameter b_σ . It is well established that shear strength decreases with the increase in b_σ . The effective stress conditions at phase transformation for all monotonic tests conducted in this study are shown in Figure 4.20. Irrespective of the change in both effective stress path and total stress path, the effective stress state at phase transformation lie on a unique straight line which passes through the origin. The friction angle mobilized at phase transformation (ϕ_{PT}) is about 36.9° and this independence of ϕ_{PT} with respect to the stress path is consistent with the data reported in several studies (Ishihara et al. 1975; Vaid and Chern 1985; Vaid and Thomas 1995; Vaid and Sivathayalan 1996a; Uthayakumar and Vaid 1998; Sivathayalan and Vaid 2002; Logeswaran 2010; Sinthujan 2013; Sivathayalan et al. 2015). This ϕ_{PT} reported herein is somewhat larger when compared to the other batches of Fraser River sand. It is not clear whether it is due to the material differences or minor errors in the measurement.

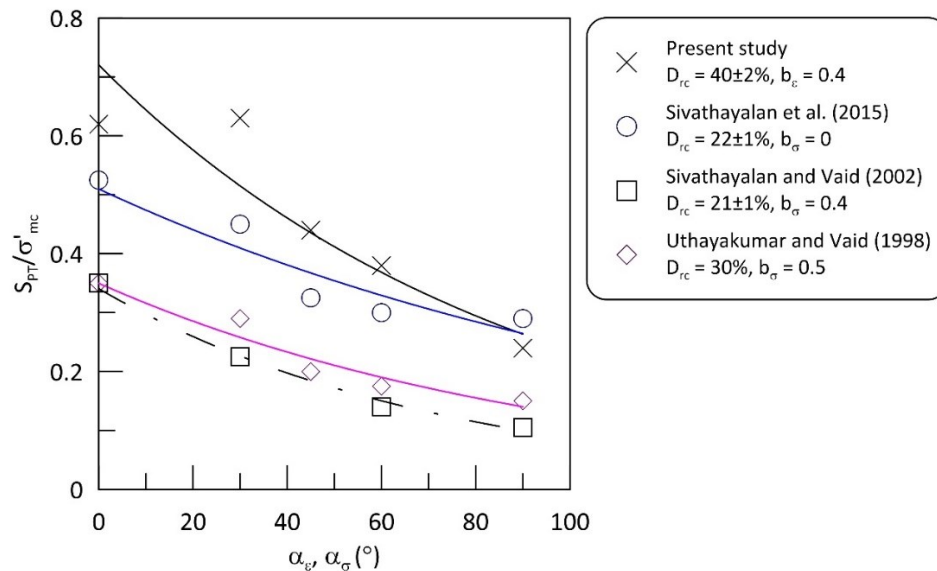


Figure 4.19: Variation of shear strength at phase transformation with $\alpha_\epsilon, \alpha_\sigma$.

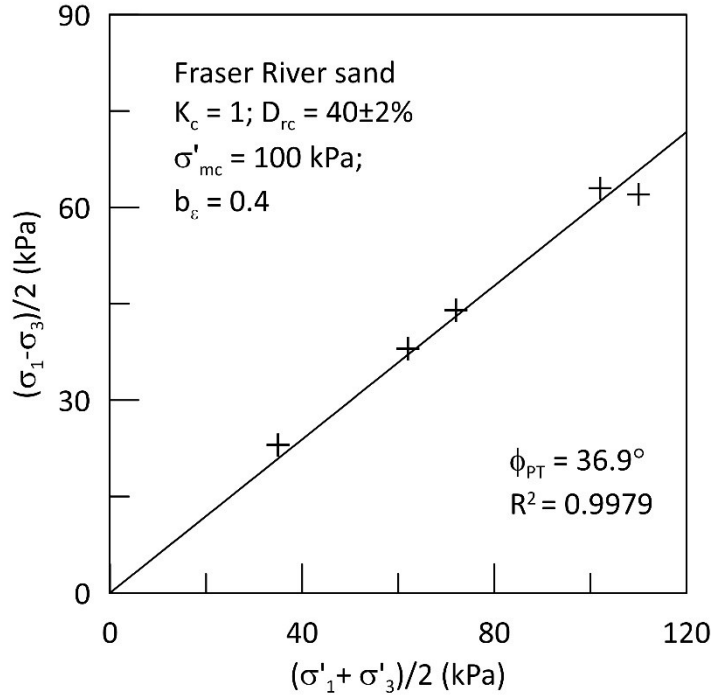


Figure 4.20: Effective stress state at the instant of peak pore pressure at different α_ε .

4.5.3 Cyclic response of Fraser River sand under smooth principal stress rotation

Three cyclic tests were carried out to characterize the effect of cyclic rotation of principal stress axis on the liquefaction behaviour of Fraser River sand. Table 4.2 shows the test parameters considered for these preliminary cyclic tests. A sinusoidal, constant stress amplitude cyclic deviatoric stress ($\sigma_{d,cyc}$) was applied at slow loading rate of 4 minutes per cycle. This slow loading rate facilitates the feedback control loop to closely follow the prescribed loading paths. The imposed loading paths in the cyclic tests corresponds to the systematic rotation of the principal stress about the vertical axis of the HCT specimen between $\pm\alpha_{\sigma,max}$. During cyclic tests, the prescribed stress paths may not be followed if the material softens and cannot sustain loading along the specified path. Such loss of control occurred during the final stages of the last loading cycle in some tests as the soil liquefied. In these hollow cylinder tests, the cyclic stress ratio (CSR) is defined by

normalizing the peak cyclic shear stress $\tau_{max}(= \sigma_{d,cyc}/2)$ by the effective mean normal stress at the end of consolidation, σ'_{mc} . The specimens were deemed to have liquefied when the single amplitude maximum shear strain exceeded 3.75% as per the recommendations of the National Research Council, (NRC 1985).

Table 4.2: Details of preliminary cyclic tests

<i>Test ID</i>	<i>End of Consolidation</i>		<i>Stress parameters during cyclic loading</i>				
	<i>Stress state</i>	<i>D_{rc} (%)</i>	<i>σ_m (kPa)</i>	<i>b_σ</i>	<i>α_{σ,max}</i>	<i>CSR</i>	<i>N</i>
CYT 01	$\sigma_{mc} = 200 \text{ kPa}; \sigma'_{mc} = 100 \text{ kPa}; \alpha_{\sigma c} = 0; b_{\sigma c} = 0$	30.82	200	0	-30↔30	0.25	27
CYT 02		27.57			-45↔45	0.25	12
CYT 03		29.2			-60↔60	0.25	16

Figure 4.21 presents the cyclic response of Fraser River sand subjected to a smooth rotation of principal stress axis between +45° to -45° at a cyclic stress ratio (CSR) of 0.25. The sand specimen is consolidated to an effective mean normal stress of 100 kPa and cyclic loading was carried out with constant σ_m of 200 kPa. It can be noticed that the effective stress path is symmetrical about the shear stress axis which indicates the existence of a transversely isotropic fabric because of water pluviation. This symmetry vanishes when the sand specimen reaches the large strain values, and the material undergoes significant changes in its stress state within each cycle. At this range of stress rotation, the sand liquefied in 12 cycles. The excess pore water pressure builds up gradually and reaches a maximum value of approximately 80 kPa which is almost equivalent to 80% of the initial effective confining stress. The sand developed a maximum shear strain of 0.15% during the first 9 stress cycles, but subsequently the shear strain increased rapidly resulting in the liquefaction of sand specimen.

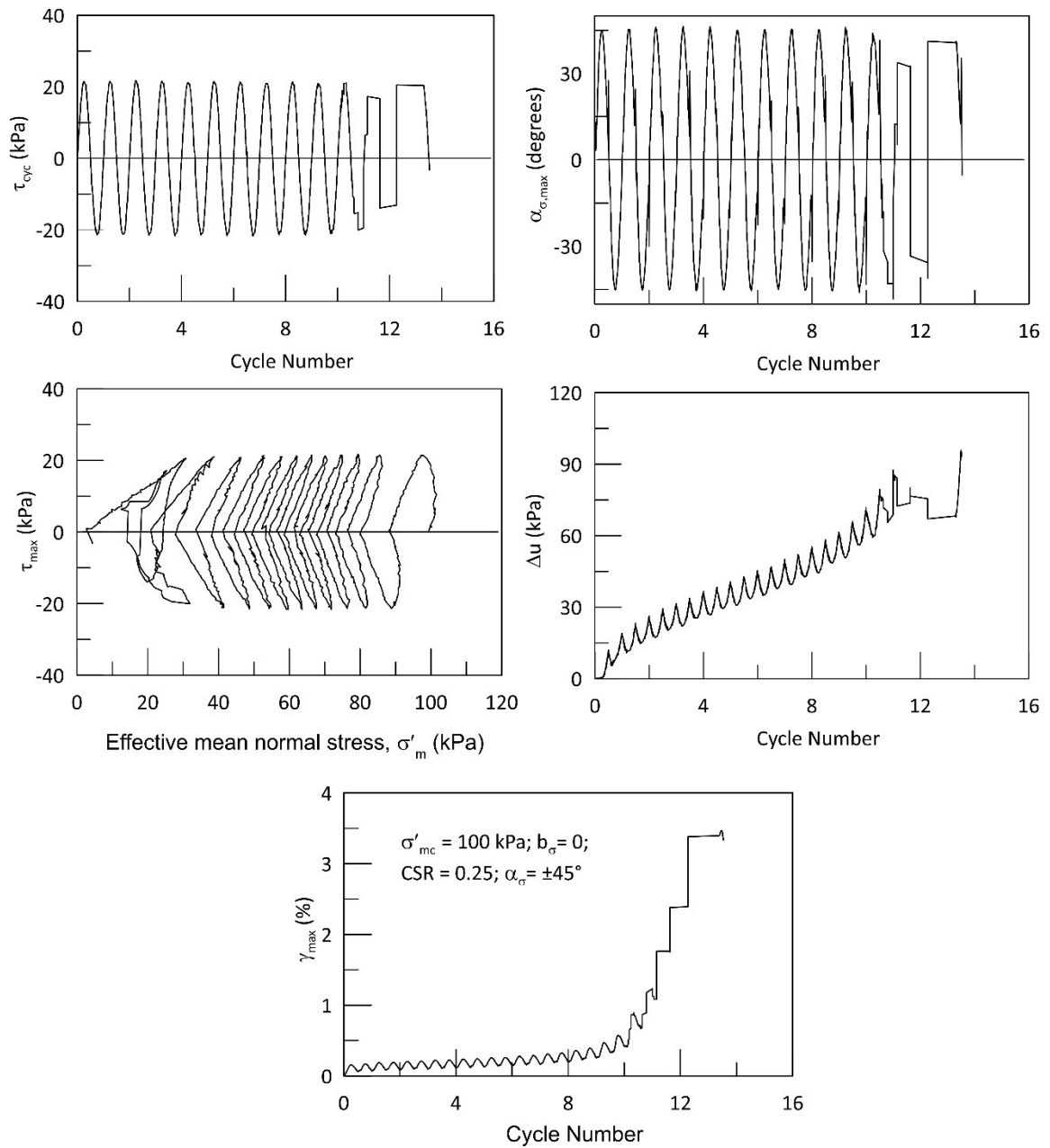


Figure 4.21: Cyclic response of sand subjected to a principal stress rotation of $\pm 45^\circ$

Figure 4.22 compares the excess pore pressure and maximum shear strain induced during the cyclic loading with different degree of principal stress rotation. It can be observed that the sand showed weakest response when the principal stress is rotated between $+45^\circ$ to -45° . It can also be noted that the excess pore water pressure accumulated

steadily and reaches a maximum value which approximately equals to 80% of the initial effective confining stress. 100% excess pore water pressure was not realized in these tests since the loading was stopped based on a strain criterion of $\gamma = 3.75\%$. 100% excess pore water pressure would have been realized had the loading been continued for another few cycles.

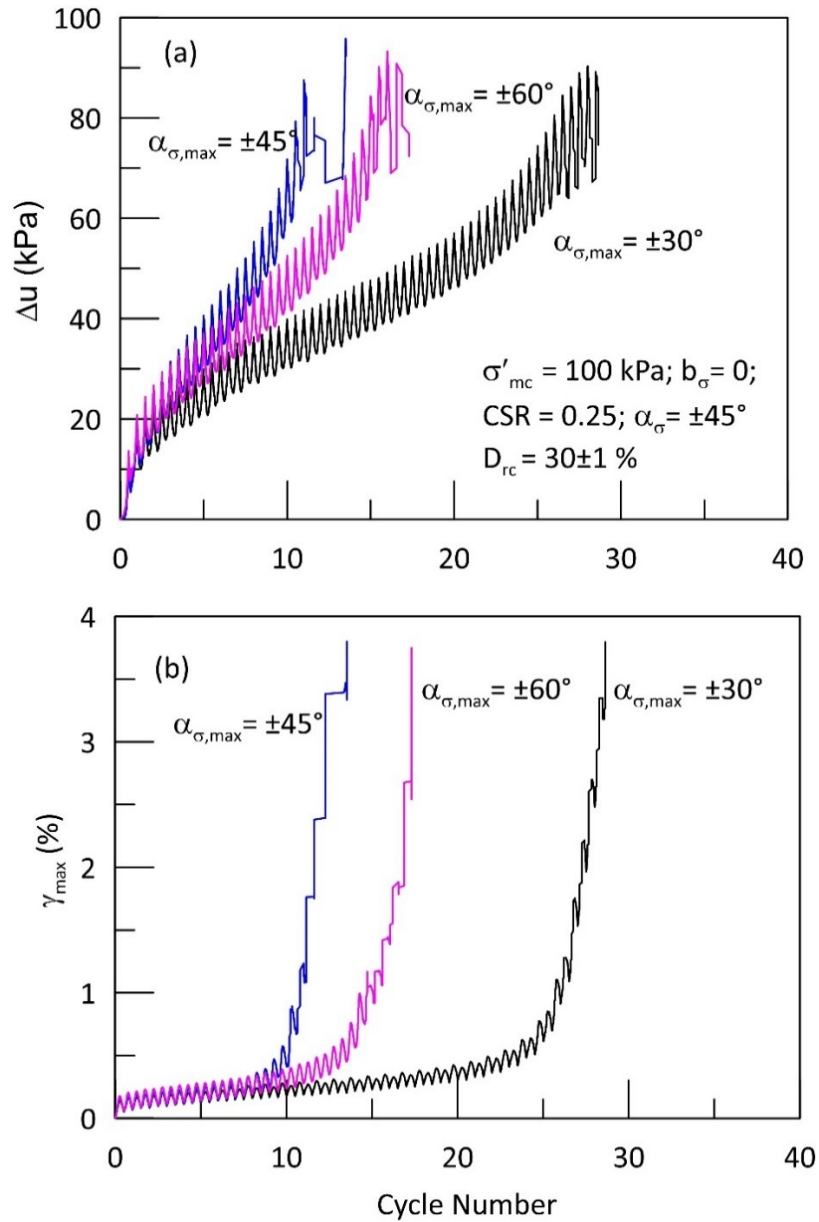


Figure 4.22: (a) Excess pore pressure and (b) shear stress development during different loading paths

Figure 4.23 shows the variation of number of cycles to liquefaction with the magnitude of stress rotation. It is evident that the degree of stress rotation significantly affects the number of cycles to liquefaction. Increasing the degree of stress rotation decreases the liquefaction resistance only up to a certain value ($\alpha_{\sigma,max} = 45^\circ$), and beyond that, the liquefaction resistance increases. This observation is consistent with the cyclic test results reported in Sinthujan (2013) and Sivathayalan et al. (2015) at different initial confining stress levels and b_σ . Tests conducted with $\alpha_{\sigma,max} = 45^\circ$ yielded the lowest number of cycles to liquefaction irrespective of the initial effective confining stress and intermediate principal stress parameter. For tests carried out with $\alpha_{\sigma,max} = 45^\circ$, the plane of maximum shear stress coincides with the horizontal bedding plane. For test with $\alpha_{\sigma,max}$ of 30° and 60° , this τ_{max} plane is inclined at an angle of 15° with the bedding plane. Furthermore, for a particular CSR, the value of τ_h is highest in the $\alpha_{\sigma,max} = 45^\circ$ test. The weakest resistance measured in the $\alpha_{\sigma,max} = 45^\circ$ tests can thus be attributed to the combination of high shear stress on the horizontal plane and the alignment of the plane of maximum shear stress with the bedding. Hence the test results from this section demonstrates that the conclusion drawn by Sinthujan (2013) and Sivathayalan et al. (2015) holds true even for the different initial stress state variables such as initial confining stress and intermediate principal stress parameter (Prasanna et al. 2018).

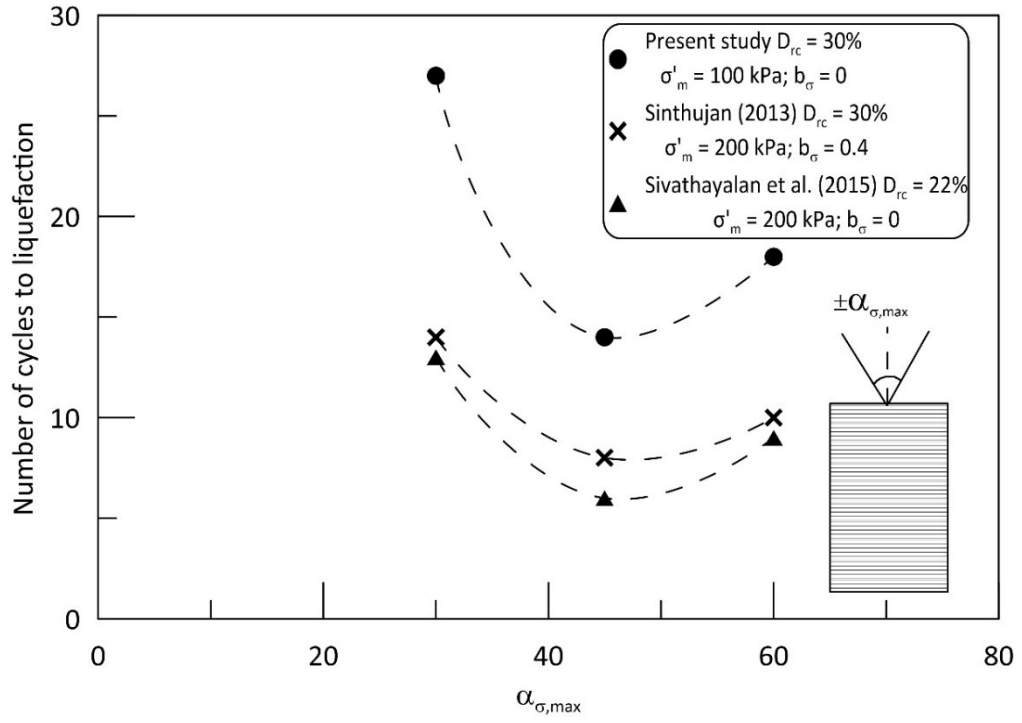


Figure 4.23: Variation of number of cycles to liquefaction with $\alpha_{\sigma,max}$

5. CYCLIC BEHAVIOUR OF SAND UNDER SIMULTANEOUS ACTION OF P-WAVE AND S-WAVE

5.1 Introduction

In laboratory, the undrained dynamic response of granular soils has been usually investigated either by applying a horizontal cyclic shear stress (simple shear) or by applying a vertical cyclic deviatoric stress (triaxial). Invariably in all the previous studies, the major focus was to evaluate the effect of vertically propagating shear waves triggered during earthquakes on the liquefaction characteristics of soil, and thus simple shear is often regarded as the preferred mode of loading. As pointed out earlier in Chapter 2, the major reason behind limiting the evaluation of cyclic behavior of soil only to the action of vertically propagating shear waves is the assumption of perfectly horizontal soil strata and the shear wave velocity of shallower layers are lower than deeper layers. With this assumption, when an inclined S-wave is striking the horizontal soil layers, it tends to refract nearly to a vertical direction while reaching the shallow surficial layers. Another aspect is that when a vertically propagating incident wave strikes the horizontal soil layer it will be refracted and reflected with the same characteristics as the incident wave. Hence, when a vertically propagating S-wave strikes a horizontal soil layer it will be refracted and reflected as S-waves with no phase transformation. However, in reality the soil stratification is not horizontal always and it is highly heterogenous. Therefore, the incident seismic wave always has an angle of incidence other than 90° , which reflects and refracts into different wave types with different amplitudes. The reflected and refracted seismic waves from the heterogenous, inclined soil strata are multiple phase waves consists of both

P-wave and S-wave components. Hence as a result of this complex interaction of seismic waves with earth's crust and also due to the local amplification factors, the soil element will be subjected to a complex loading paths involving various combinations of compressional and shear stresses simultaneously. Severe earthquake damages have also been reported in places where strong P-waves and S-waves propagated simultaneously (Bernardie et al. 2006, Lin et al. 2009). Thus, ignoring this combined action of P-waves and S-waves in a soil element, or the stress states/particle motion in a Rayleigh wave could possibly be a factor contributing to the discrepancies in evaluating the liquefaction potential of the soil. Therefore, this chapter aims to address this issue through a detailed experimental investigation using hollow cylinder torsional shear apparatus.

This chapter, firstly discusses the numerical simulation carried out to demonstrate the effects of simultaneous propagation of compression and shear waves in a soil element during an earthquake event, and the possible relative magnitudes of P- and S-waves that could be expected during seismic shaking. Secondly, this chapter provides a detailed description of the possible nature and degree of principal stress rotation that will be encountered in-situ during earthquake shaking. Lastly, a detailed analysis and discussion of the experimental studies carried out to study the various factors influencing the cyclic response of Fraser River sand, subjected to the coupled action of compression and shear waves, is presented.

5.2 Numerical simulation of the simultaneous propagation of compression and shear waves using FLAC 2D

The purpose of this numerical simulation is to demonstrate the simultaneous propagation of compression and shear waves in a soil media due to a seismic event, and to establish

appropriate loading parameters for the experimental research. A two-dimensional finite difference (FD) analysis was carried out using FLAC 2D v.8.0 (Itasca 2016) to assess the conditions that may lead to combined P- and S- wave loading, and to establish the relative magnitudes under simpler cases. Two numerical models one with horizontal soil strata and other with an inclined bedrock having a gentle dip angle of 2.5° is created for this purpose (Figure 5.1). The numerical model has a height and width of 100 m and 1000 m respectively (aspect ratio of 1:10) and it consists of three soil layers: top soft clay layer of 80 m thick followed by 10 m thick glacial till and bedrock. This reflects the soil profile found in some regions of the Ottawa valley.

It is a well-established fact that under cyclic loading, the soil exhibits non-linear behavior with progressive stiffness degradation and increase in damping with the increase in cyclic shear strain. In FLAC, this cyclic non-linear behavior is modelled using an elastic model with hysteretic damping. The material properties used in the analysis are representatives of the soils in the Ottawa region. The top soft clay layer has a unit weight of $\gamma = 17.2 \text{ kN/m}^3$ and the variation of shear wave velocity (V_s) with depth adopted from Kasgin (2010) is assigned to this layer and it is plotted in Figure 1c. V_s of 580 m/s & $\gamma = 18.1 \text{ kN/m}^3$ and V_s of 2700 m/s & $\gamma = 24.5 \text{ kN/m}^3$ is assigned for glacial till and bedrock respectively. The modulus reduction (G/G_{max}) and damping (ξ) curves are implemented as a continuous function in FLAC hysteresis model. The G/G_{max} and ξ curves from Seed and Sun (1989) for clay is used for the analysis. Fits for G/G_{max} and ξ curves for clay upper range were obtained using the FLAC default analytical function with parameters $L_1 = -3.156$; $L_2 = 1.904$ and it is assigned to the top soft clay and glacial till layers. In this default hysteresis model, the S- shaped curve of shear modulus versus

logarithmic shear strain ($\log_{10} \gamma_s$) is represented as a cubic equation with zero slope at both low and high strain (Itasca 2016). In this, the secant shear modulus (G_{sec}) and tangent shear modulus (G_{tan}) is given by:

$$G_{sec} = s^2(3 - s) \quad (5.1)$$

$$s = (L_2 - \log_{10} \gamma_s)/(L_2 - L_1) \quad (5.2)$$

$$G_{tan} = G_{sec} + \gamma_s(dG_{sec}/d\gamma_s) \quad (5.3)$$

Figure 5.2 shows the variation of G/G_{max} and ξ with cyclic shear strain obtained using the FLAC default analytical function.

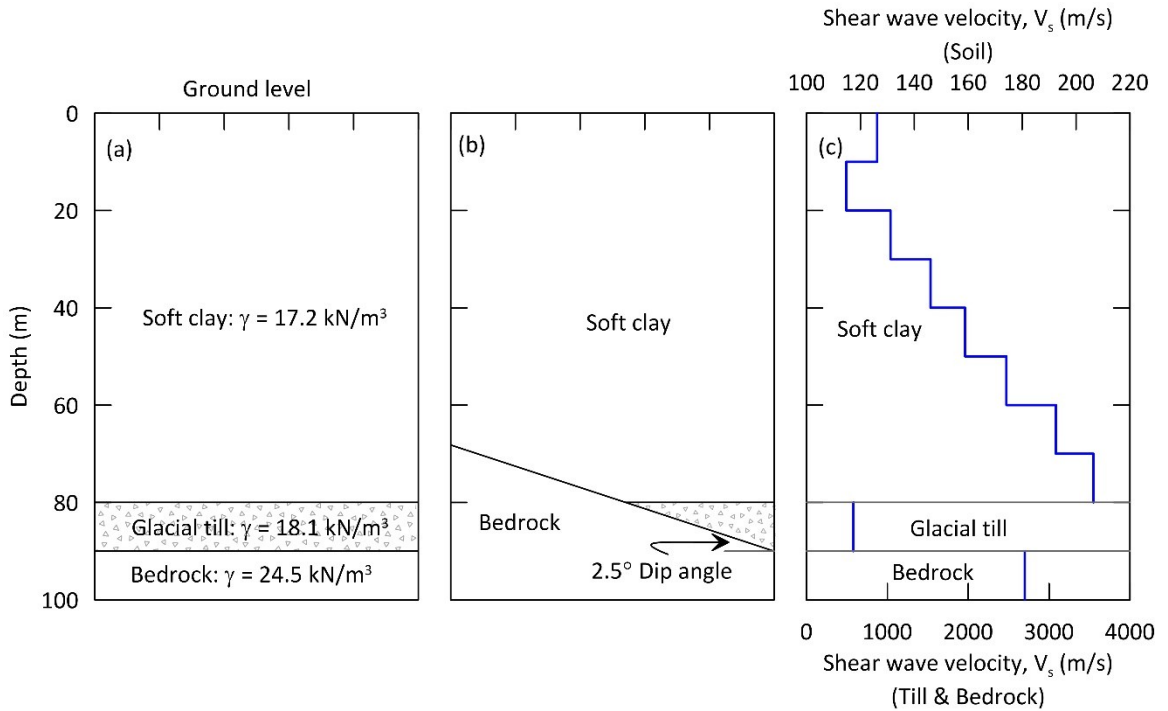


Figure 5.1: Schematic representation of the developed numerical model

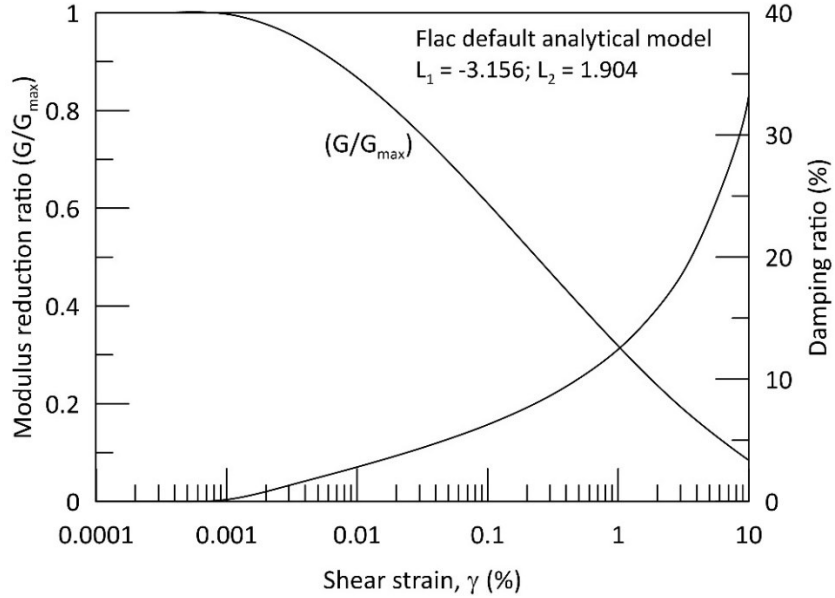


Figure 5.2: Modulus reduction and damping curves used in the numerical simulation

The grid size of the numerical model is fixed based upon the minimum shear wave velocity (V_s) and frequency content (f) of the input motion. For accurate wave propagation, the element size Δl should be smaller than one-tenth to one-eighth of the wavelength associated with the highest frequency component of the input wave ($\Delta l = 0.1(V_s/f)$ to $0.125(V_s/f)$). For minimum $V_s = 110 \text{ m/s}$ and cutoff frequency $f = 10 \text{ Hz}$, a minimum Δl of 1.1 m is required. Therefore, based on this criterion, a numerical grid of 1000×100 elements is used for the analysis (Figure 5.3). Quiet viscous boundary is applied at the bottom of the numerical model. This boundary consists of viscous dashpots attached independently to the boundary in both normal and shear directions which absorbs the reflected outward propagation waves from the model boundary. Free field boundary condition is applied at the lateral boundaries to simulate the free field condition. After solving the model for static equilibrium, ground motion analysis is carried out by applying a single frequency ($f = 1 \text{ Hz}$), amplitude modulated (AM) sine wave given by $a(t) = \sqrt{0.055 e^{-0.95t} t^{10}} \sin 2\pi f t \text{ gals}$ and 1989 Loma Prieta (California) earthquake (PEER

strong motion earthquake database, station: 090 CDMG STATION 47381) acceleration at the base of the numerical model. The peak ground acceleration (PGA) of the adopted AM wave and Loma Prieta EQ ground motion are 0.2 g and 0.367 g respectively. Figure 5.4 presents the acceleration time history adopted in this numerical analysis and these acceleration time histories were converted into shear stress history before applying at the base of the model.

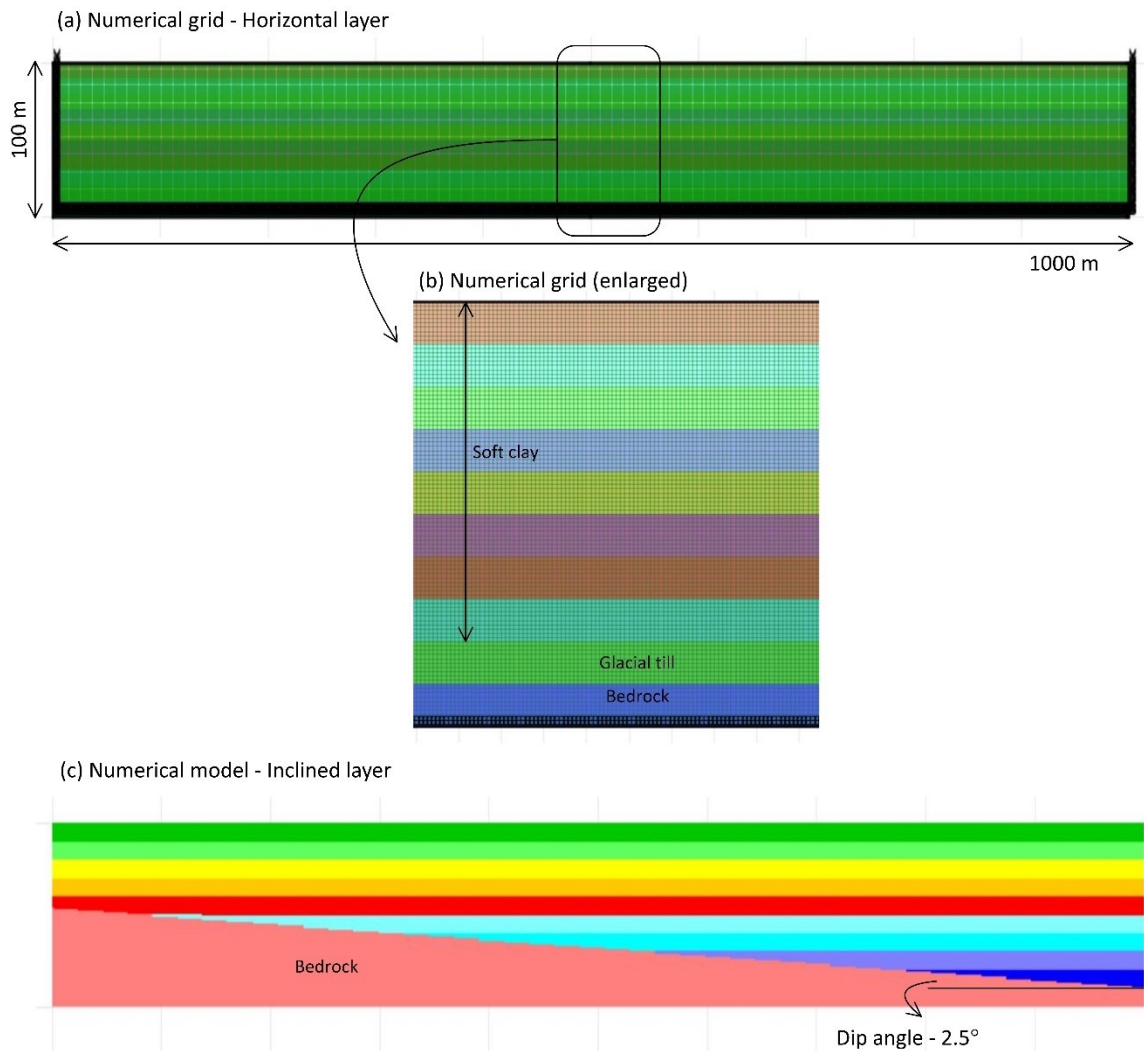


Figure 5.3: Finite difference model of horizontal and inclined bedrock soil strata with similar numerical grid

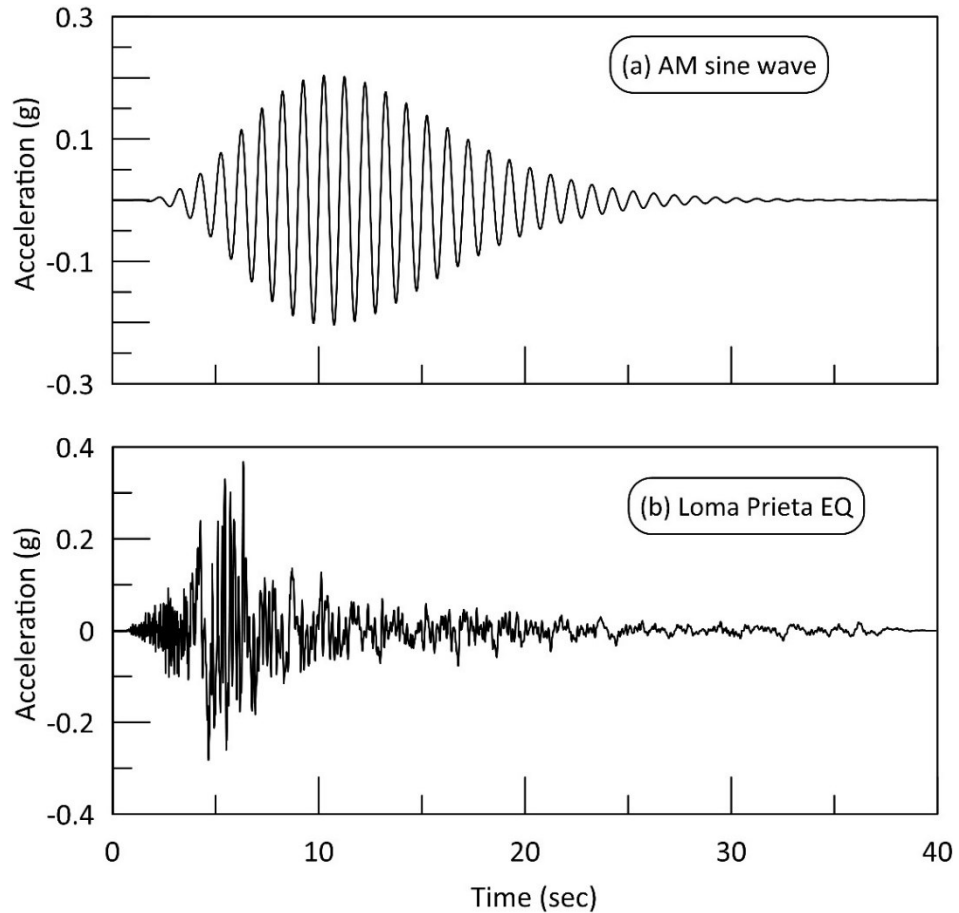


Figure 5.4: Acceleration time history (a) AM sine wave (b) Loma Prieta EQ (Seismosignal 2016)

To validate the developed numerical model, results from 2D horizontal layer model is compared with the results obtained from equivalent-linear SHAKE (Schnabel et al. 1972) analysis implemented in the GUI program ProShake. A one-dimensional equivalent linear model with similar properties as in the horizontal layer model is developed in ProShake and for making a reasonable comparison between FLAC and ProShake the modulus reduction and damping curves from FLAC default function is added to the SHAKE and it is used for the analysis. Figure 5.5 and 5.6 compares the variation of surface acceleration and its corresponding response spectra computed at the midpoint of FLAC model and

ProShake model for both AM sine wave and Loma Prieta input time histories. It can be observed that the trend of acceleration and response spectra variation is almost similar in both the programs. There is not much difference noted in the PGA and peak spectral acceleration (PSA) between FLAC 2D and Proshake for the input Loma Prieta ground motion whereas the PGA and PSA differs by about 30% between these two codes for the input AM sine wave. This deviation is primarily due to the fundamental difference between the implementation of cyclic nonlinear model (time-domain) in FLAC and the equivalent linear model (frequency domain) in ProShake. The deviation is pronounced more for uniform motion with constant frequency and less for random motion with varying frequency. To verify the deviation between FLAC and Proshake for uniform motion, ground motion analysis is carried out for AM sine wave (PGA of 0.2 g) with different frequencies ($f = 0.5, 1 \text{ and } 2.5 \text{ Hz}$). The response spectra of these input AM sine waves are shown in Figure 5.7a. Figure 5.7b compares the response spectra obtained from the ground motion computed at the ground surface from both FLAC and Proshake at different frequencies of input AM sine wave considered. It can be noticed that the at low frequency, almost identical spectral response is obtained from both FLAC and Proshake. The difference between the peak spectral acceleration (S_a) obtained from FLAC and Proshake increases with the increase in frequency of input AM sine wave.

A similar observation on the difference between cyclic nonlinear model and equivalent linear model is also reported by Strenk and Wartman (2011) and it is concluded that the time domain implementation in FLAC is more accurate for modelling random seismic wave propagation in soil media. Thus, the comparable response between FLAC & ProShake, and agreement with the previous finding gives confidence in our numerical

model for further analysis. Moreover, the major objective here is to demonstrate the simultaneous propagation of compression and shear waves in a soil media and to get a rough estimate of ratio between shear stress increment and normal stress increment induced during seismic shaking, to ensure that the laboratory simulations are relevant to the in-situ loading conditions. So, no further analysis on the cyclic nonlinear model and equivalent linear model is conducted since it was considered beyond the scope of this research program.

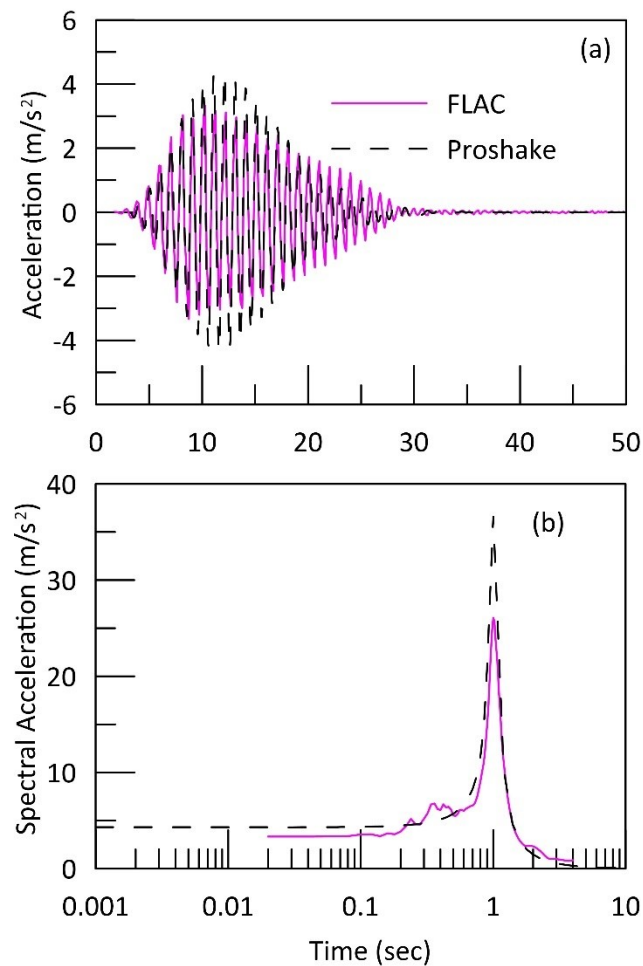


Figure 5.5: Comparison between FLAC and ProShake (a) Time history (b) Response spectra for AM sine wave

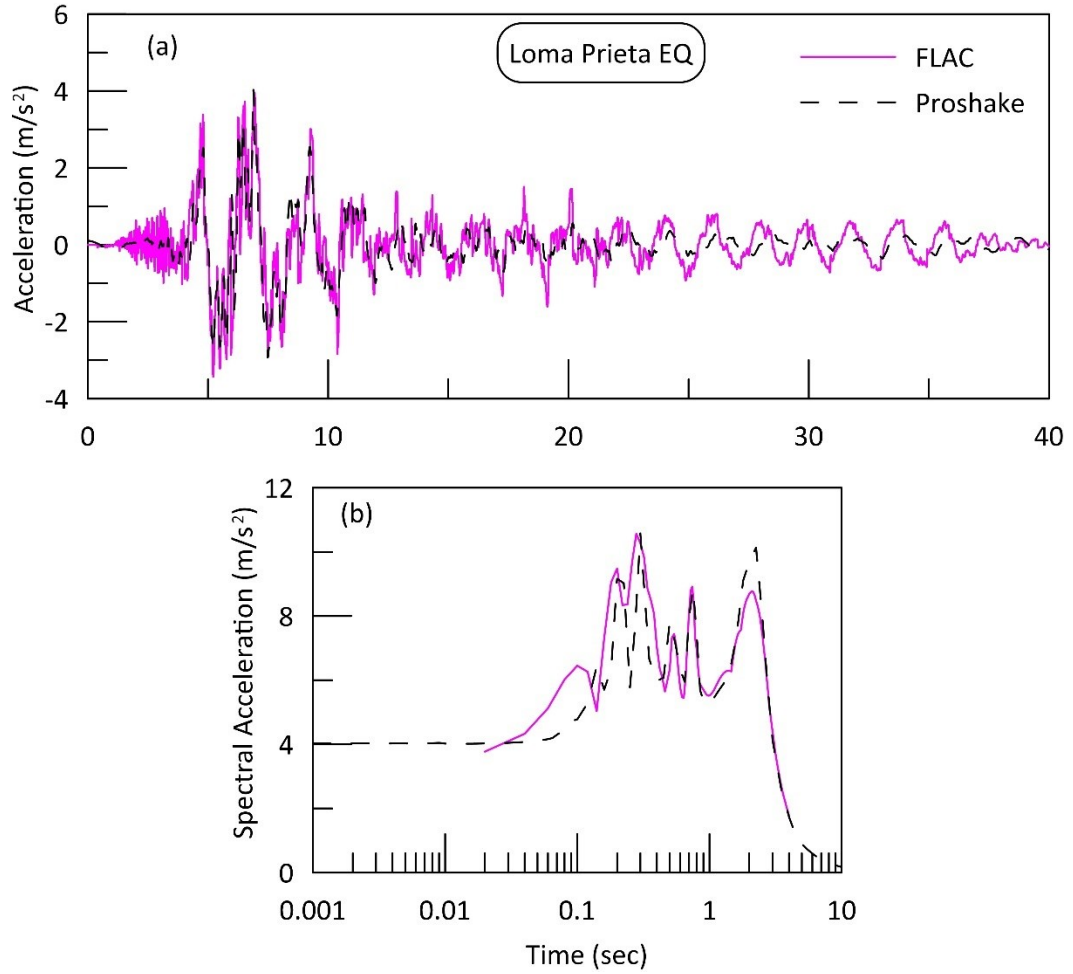


Figure 5.6: Comparison between FLAC and ProShake (a) Time history (b) Response spectra for 1989 Loma Prieta ground motion

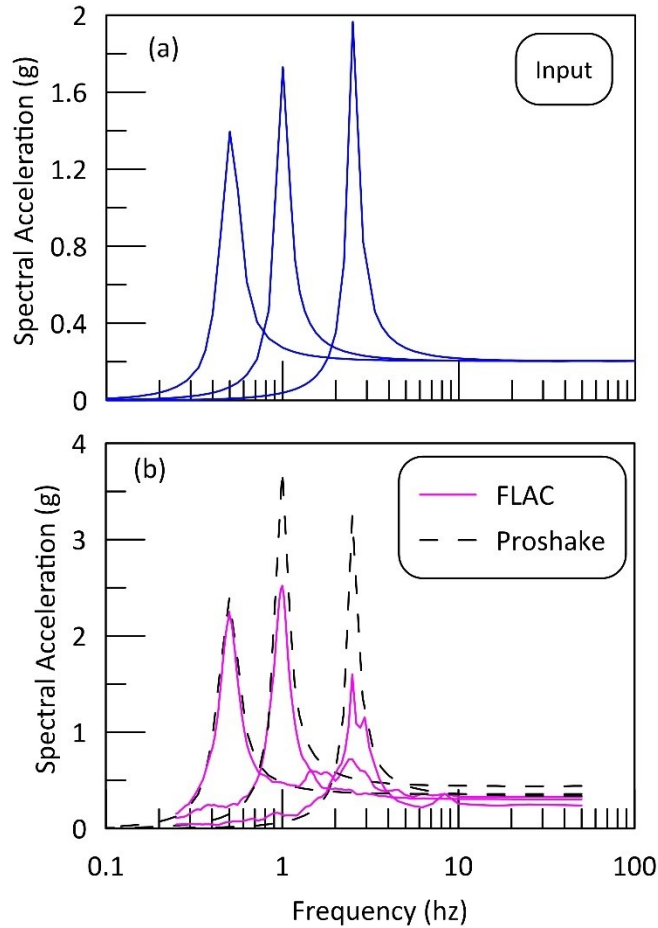


Figure 5.7: Comparison of response spectra between FLAC and ProShake for AM sine wave with different frequencies (a) Response spectra of input, (b) Response spectra of output

Figure 5.8 and 5.9 presents the variation of horizontal and vertical surface acceleration computed at the midpoint of horizontal and inclined bedrock models subjected to input ground motions shown in Figure 5.4. It can be observed that there is no notable vertical acceleration observed in the horizontal model whereas in the inclined bedrock model, a peak vertical acceleration of about 0.3 g and 0.17 g is observed for AM-sine wave and Loma Prieta ground motion respectively. This clearly demonstrates that even a slight deviation from the horizontal could result in a generation of both compression and shear waves in a soil media during an earthquake loading. The compression wave or P-wave give

rise to normal stresses whereas shear wave or S-wave give rise to shear stresses in the soil element.

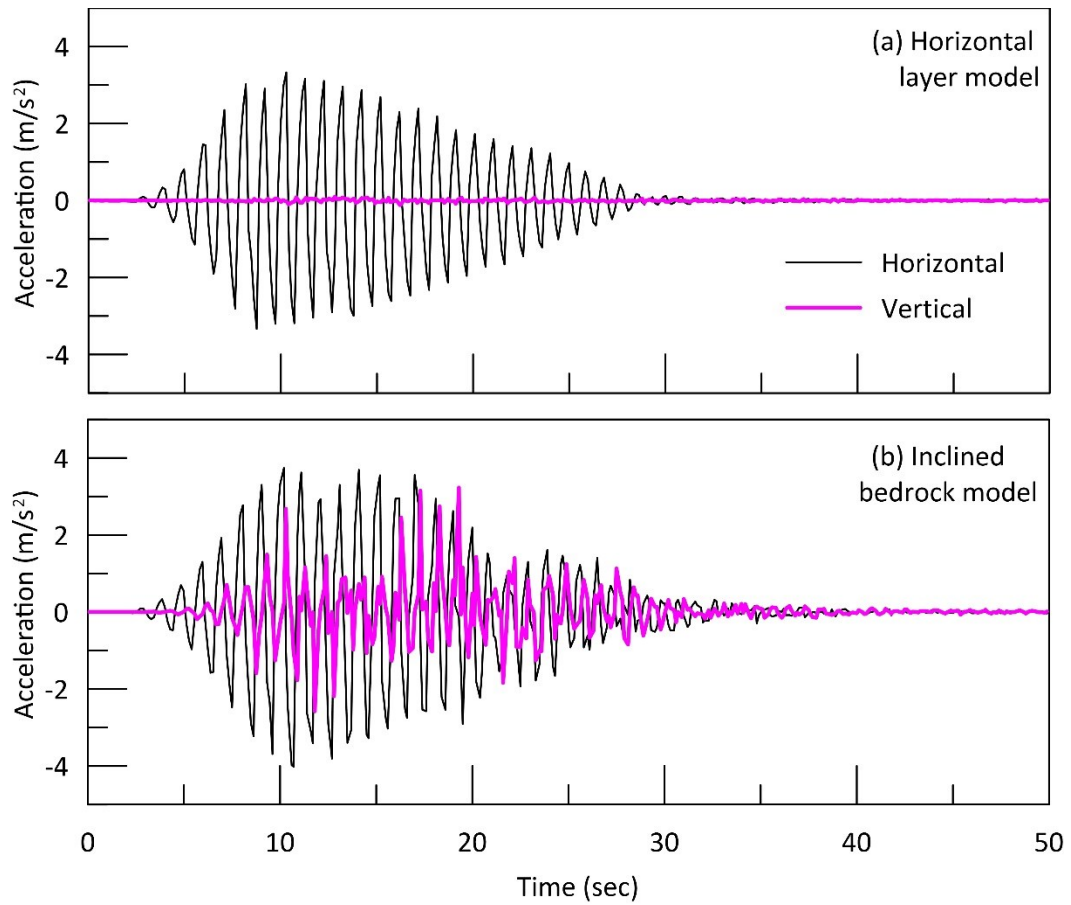


Figure 5.8: Horizontal and vertical surface acceleration at midpoint of (a) horizontal layer model (b) inclined bedrock model for AM sine wave

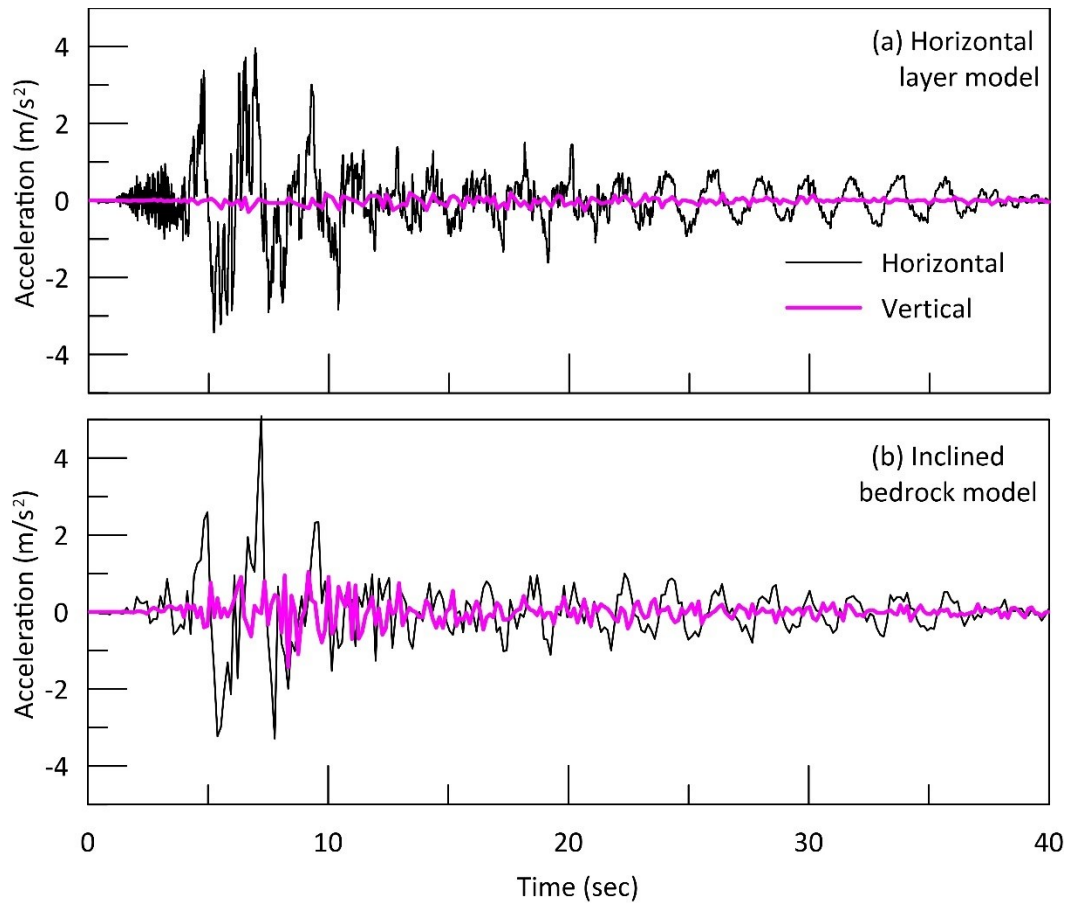


Figure 5.9: Horizontal and vertical surface acceleration at midpoint of (a) horizontal layer model (b) inclined bedrock model for 1989 Loma Prieta ground motion

Figure 5.10 and 5.11 presents the typical variation of normal and shear stresses determined at three different depths along the centerline of both horizontal and inclined bedrock models for the input ground motions considered in the analysis. It can be noticed that, no normal stresses were induced from the incident vertically propagating shear waves for perfectly horizontal soil strata but on the other hand a significant amount of normal stresses were induced in the inclined soil strata for the incoming shear waves. The normal and shear stress increments from the stress time histories are calculated and the ratio between peak shear stress and peak normal stress increments which is defined herein as $S/N = \Delta\tau_h / (\Delta\sigma_v - \Delta\sigma_h)$ is computed for different depths. The variation of S/N

determined at different depths along the midpoint of the model is plotted in Figure 5.12. Figure 5.13 and 5.14 presents the variation of S/N contours for a 100 m wide and 30 m depth grid. S/N is computed along 50 m on the either side of the centerline of the model for a depth of about 0 to 30 m from the ground surface. A maximum limit of 100 is set for S/N because the value tends to be large at very low normal stresses. The contour clearly shows that S/N is mostly 100 for horizontal soil strata which implies that no normal stresses were induced due to the vertically propagating S-wave. S/N varies as low as 0.05 to as high as 30 for the inclined bedrock strata with a gentle dip of 2.5° . Hence, from this numerical simulation it is clearly evident that even a slight dip of the soil strata could result in the simultaneous propagation of P-waves and S-waves from the incident seismic wave. The representative S/N ratios obtained from this finite difference simulations are later used in HCT apparatus to simulate the effect of simultaneous action of compression and shear waves on the liquefaction characteristics of Fraser River sand.

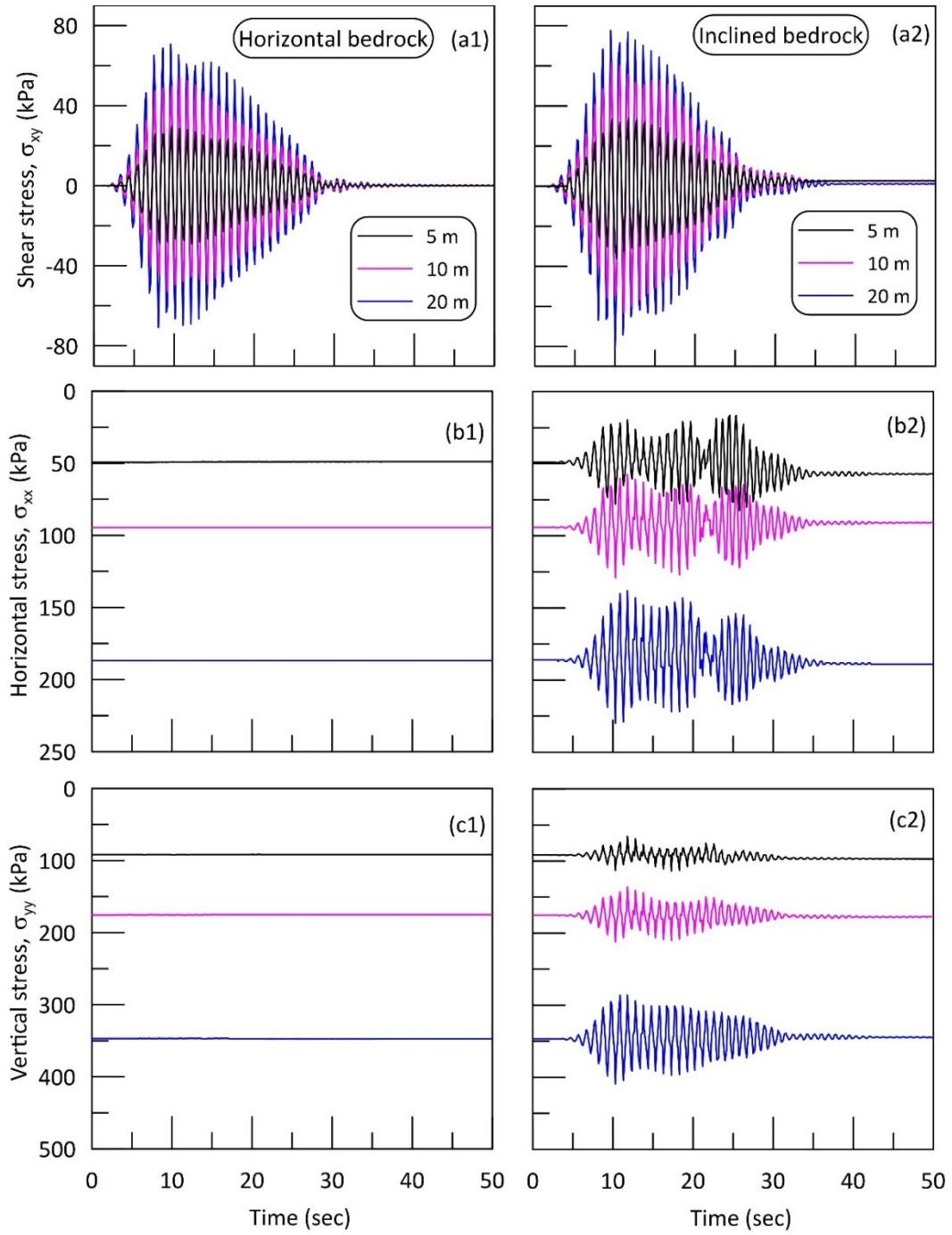


Figure 5.10: Variation of normal and shear stresses for AM sine wave

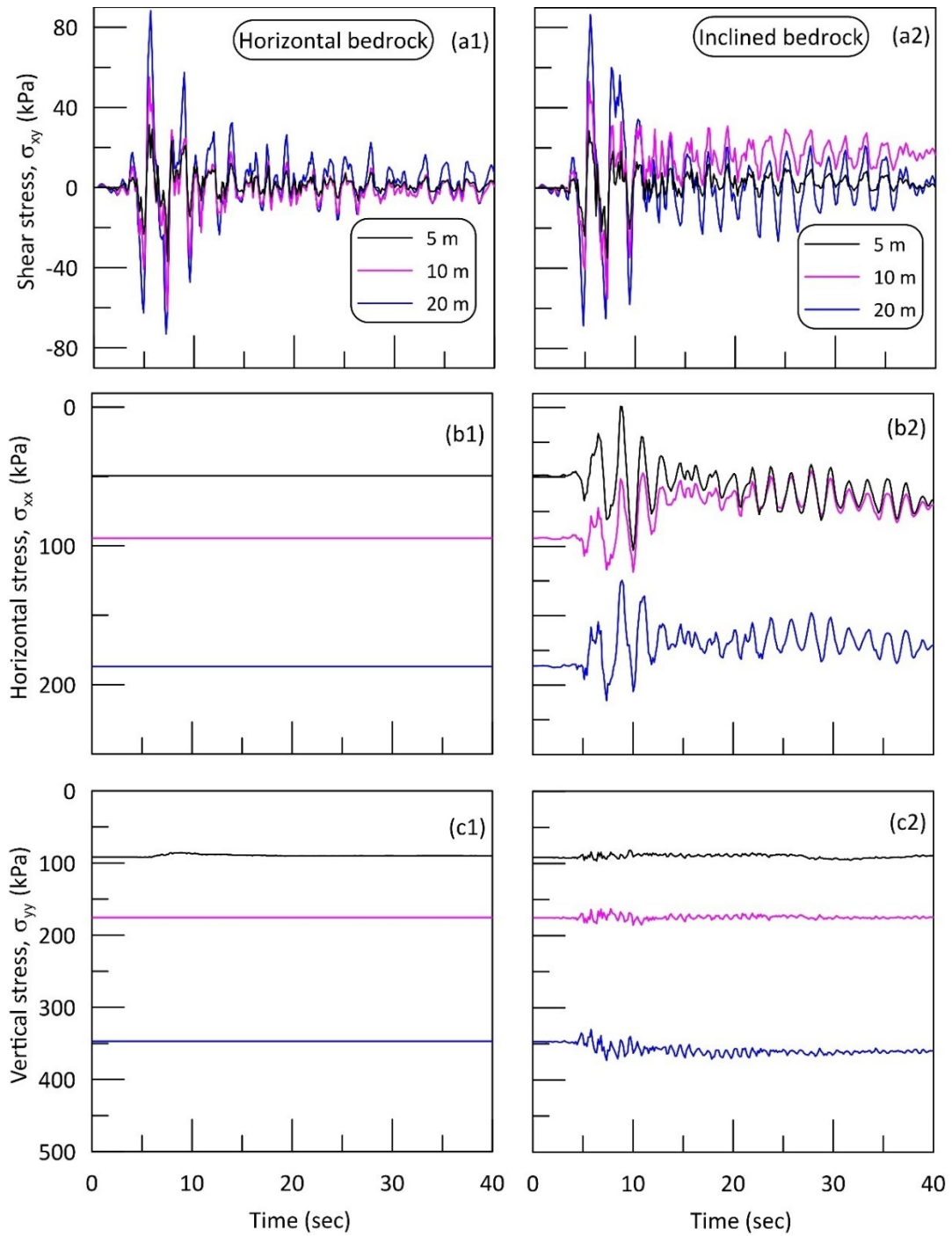


Figure 5.11: Variation of normal and shear stresses for Loma Prieta ground motion

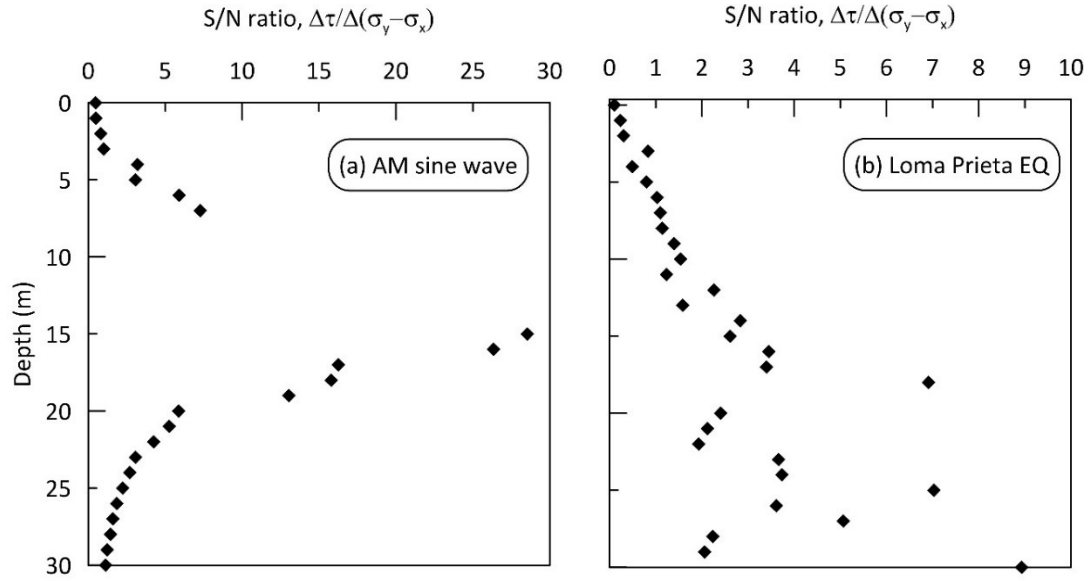


Figure 5.12: Variation of S/N at the centerline of inclined bedrock model

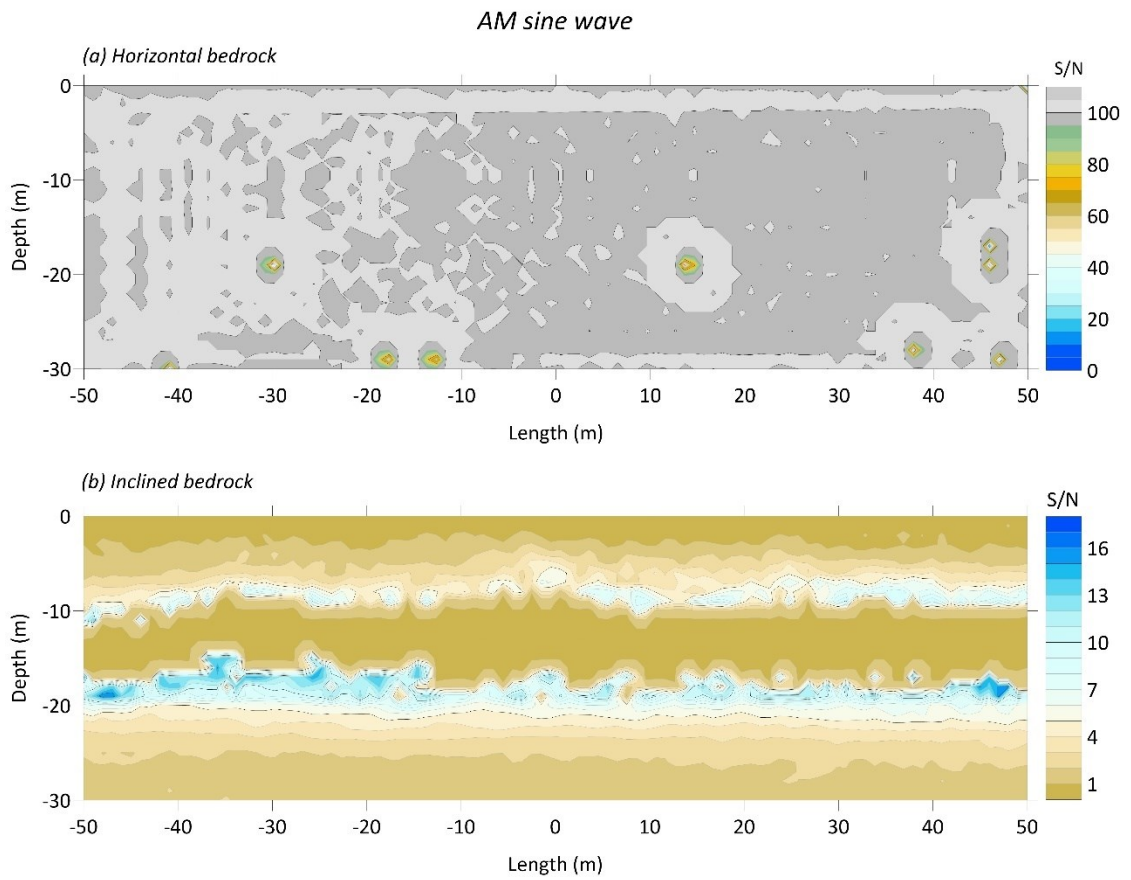


Figure 5.13: S/N contour for AM sine wave ground motion

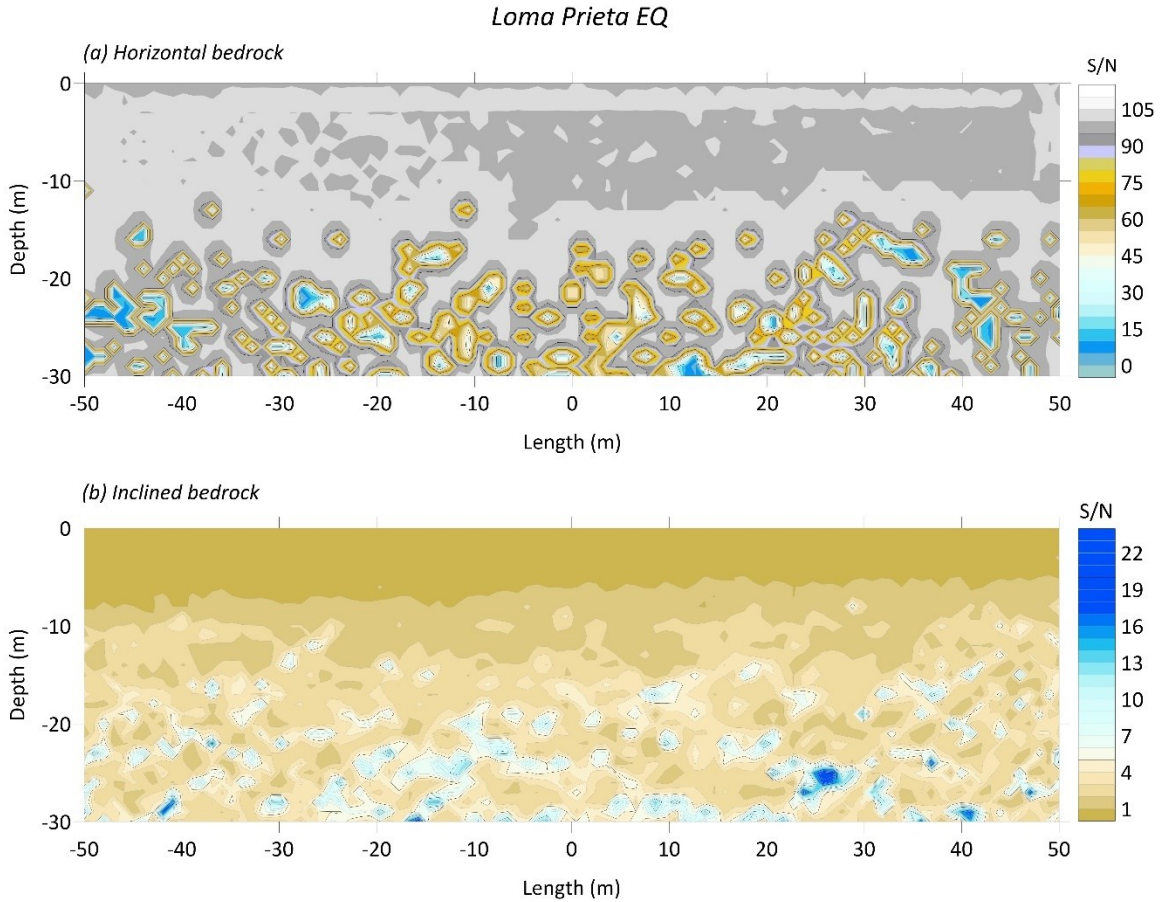


Figure 5.14: S/N contour for Loma Prieta EQ ground motion

5.3 *Simulation of coupled loading condition in a hollow cylinder torsional shear apparatus*

Naturally, a soil element could be subjected to both cyclic shear and cyclic normal stresses due to a Rayleigh wave, or due to simultaneous action of P- and S- waves. It is evident from the numerical investigation, presented in the previous section, that even a slight dip of bedrock could generate both compression and shear waves during a seismic event. Therefore, during earthquake shaking the soil element will be subjected to two components of shear stress i.e., the shear stress on the horizontal plane (τ_h or $\tau_{z\theta}$) due to S-wave and the shear stress due to the stress difference ($\sigma_v - \sigma_h$ or $\sigma_z - \sigma_\theta$) caused by the compression

wave. The nature and degree of stress rotation caused by this coupled loading scenario depends on the relative magnitude between $\tau_{z\theta}$ and $\sigma_z - \sigma_\theta$. So far, no studies have discussed the nature and degree of stress rotation which is possible in-situ during an earthquake loading and its implications on the liquefaction susceptibility of soils.

The cyclic behavior of soils, under such generalized loading conditions, is evaluated using the hollow cylinder torsional shear apparatus. The coupled loading condition is simulated by simultaneously varying the shear stress increment ($\Delta\tau_{z\theta}$) on the horizontal plane and the normal stress increment ($\Delta(\sigma_z - \sigma_\theta)$) in a sinusoidal manner as per Eq. 5.1 to Eq. 5.4.

$$\Delta\tau_{z\theta} = HSR * \sin(\omega t + \delta) * \sigma'_{mc} \quad (5.1)$$

$$S/N = \Delta\tau_{z\theta} / \Delta(\sigma_z - \sigma_\theta) \quad (5.2)$$

$$\Delta(\sigma_z - \sigma_\theta) = \left(\frac{1}{S/N}\right) * HSR * \sigma'_{mc} * \sin(\omega t) \quad (5.3)$$

$$\Delta\sigma_z = -\Delta\sigma_\theta = \Delta(\sigma_z - \sigma_\theta)/2 \quad (5.4)$$

where HSR , named herein the horizontal stress ratio, is defined as the shear stress ratio on the horizontal plane ($\Delta\tau_{z\theta}/\sigma'_{mc}$); S/N is the ratio of horizontal shear stress increment to the normal stress increment; δ is phase angle between the compression and shear wave and σ'_{mc} is the effective mean normal stress at the end of consolidation.

The direction of major principal stress (α_σ) with respect to vertical axis due to this simultaneous change in both normal and shear stresses can be determined from the known values of σ_z , σ_θ and $\tau_{z\theta}$. The maximum shear stress $\tau_{max} = (\sigma_1 - \sigma_3)/2$, assumes the sign of $\tau_{z\theta}$ and counterclockwise shear is taken as positive in this thesis. In hydrostatically consolidated specimens (i.e., initial isotropic stress state; $K_c = 1$) when the variation of

$\Delta\tau_{z\theta}$ and $\Delta(\sigma_z - \sigma_\theta)$ is in phase with each other ($\delta = 0$), τ_{max} varies sinusoidally with the initial value of zero. Figure 5.15 shows the typical variation of applied stress increments and τ_{max} for $K_c = 1$ and $S/N = 0.25$. The term cyclic stress ratio (CSR) typically defined $CSR = \tau_{max}/\sigma'_{mc}$ is commonly used to represent the intensity of cyclic loading in geotechnical engineering. In this type of loading condition, the definition of CSR is straightforward as the τ_{max} varies sinusoidally. CSR is defined as τ_{max}/σ'_{mc} as shown in Figure 5.15b. For either $K_c \neq 1$ or $\delta \neq 0$, the definition of CSR becomes problematic because τ_{max} variation is not simple harmonic anymore.

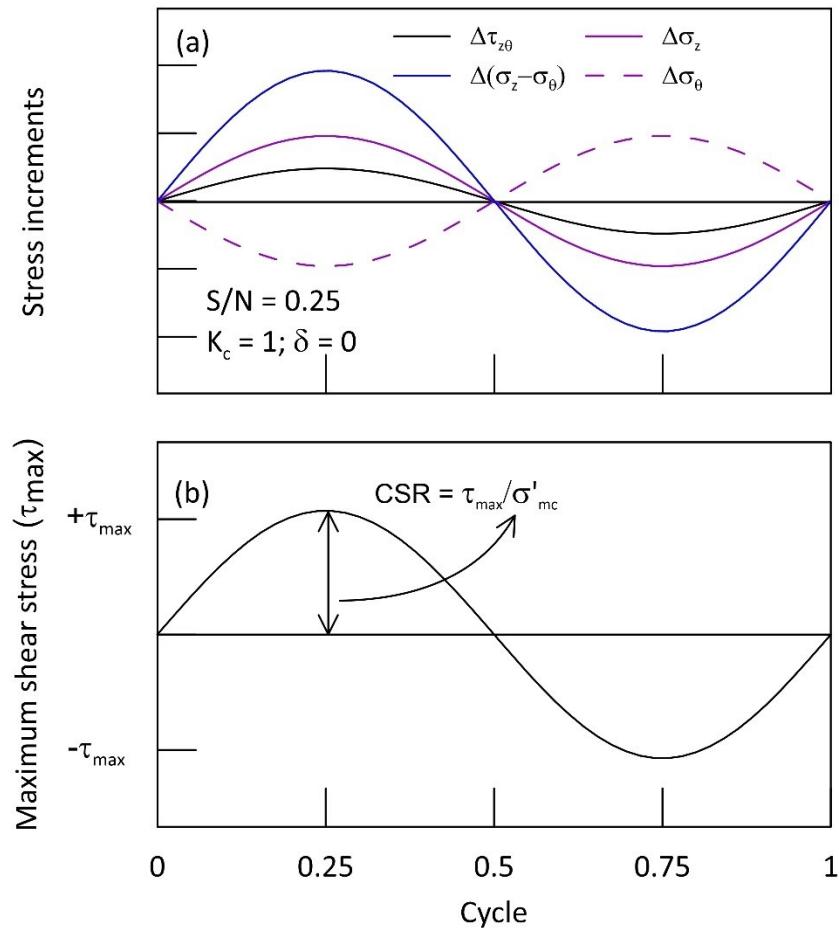


Figure 5.15: Variation of stress increments and maximum shear stress for $S/N = 0.25$

5.4 Nature and degree of stress rotation under coupled loading

The nature and degree of stress rotation due to simultaneous propagation of compression and shear waves in a soil element depends upon the initial stress state parameters such as K_c , $\alpha_{\sigma c}$ and shearing parameters such as S/N , and δ . For $K_c = 1$, the variation of α_σ , is independent of HSR but significantly depends on S/N and δ . Figure 5.16 shows the variation of α_σ for different S/N and $\delta = 0$ in an isotropically consolidated stress state. Under this condition, the applied stress path in $\tau_{z\theta} - (\sigma_z - \sigma_\theta)$ space varies linearly and the α_σ undergoes a jump rotation i.e., α_σ remains constant during the first half of the loading cycle and abruptly changes its direction when the shear stress ($\tau_{z\theta}$) reverses from positive to negative axis. The degree of rotation shifts upwards as the S/N increases from 0.25 to 4 (Figure 5.16d). At greater S/N , the shear stress increment is more predominant than the normal stress increment, therefore α_σ jump rotates between $\pm 45^\circ$ replicating a simple shear condition. At smaller S/N , the normal stress increment is more than the shear stress increment and hence the α_σ jump rotation approaches a range closer to 0° to 90° . When there are no shear stresses on the horizontal plane (i.e., $S/N = 0$), the loading is identical to triaxial conditions and the principal stress direction rotates between 0° and 90° .

When the stress waves are not in phase with each other ($\delta \neq 0$) which is a possible scenario in field due to the complex interaction of seismic waves with the soil layers, the applied stress path varies in an elliptical manner as shown in Figure 5.17a. This elliptical stress path expands with the increase in phase shift from 30° to 90° . Unlike linear stress path, the α_σ rotates continuously for $\delta \neq 0$ cases as shown in Figure 5.17 c. At $\delta = 90^\circ$, when the applied stress increments are equal ($|\Delta\tau_{z\theta}| = |\Delta\sigma_z| = |\Delta\sigma_\theta|$), the stress path

becomes circular i.e., the cyclic loading is carried out under constant deviatoric stress but with the continuous rotation of principal stress axes.

Figure 5.18a shows the influence of initial consolidation stress state on the degree and nature of principal stress rotation under coupled cyclic loading. It can be noticed that α_σ rotates in an asymmetric sinusoidal manner for $K_c \neq 1$ cases whereas it undergoes jump rotation for $K_c = 1$. The range of rotation ($\alpha_{\sigma,range} = \alpha_{\sigma,max} - \alpha_{\sigma,min}$) decreases with the increase in K_c . For $HSR = 0.2$ and $S/N = 0.5$, the range of rotation decreased from 90° to almost 29.4° for the increase in K_c from 1 to 2.5. Figure 5.18b shows the variation of α_σ for different S/N under $K_c = 1.5$ and $\delta = 0^\circ$. It can be observed that the rotation range decreases with the increase in S/N . For the case considered, the rotation range decreased from 76.1° to 45.8° for the increase in S/N from 0.25 to 2. Figure 5.18c shows the rotation of α_σ for different phase shifts between the waves under $K_c = 1.5$ and $S/N = 0.5$. For this case, α_σ undergoes a continuous rotation with $\alpha_{\sigma,range}$ increases with the increase in phase angle.

Figure 5.19 summarizes the variation of $\alpha_{\sigma,range}$ for various S/N and δ under different initial consolidation stress states. As mentioned before, the $\alpha_{\sigma,range}$ decreases with the increase in K_c . At a fixed HSR and δ , $\alpha_{\sigma,range}$ is independent of S/N for $K_c = 1$. For $K_c \neq 1$, $\alpha_{\sigma,range}$ decreases with the increase in S/N . The drop in the rotation range is more predominant for the increase in S/N from 0.25 to 1 and beyond that there is not much significant change in the $\alpha_{\sigma,range}$. For a fixed HSR and S/N , $\alpha_{\sigma,range}$ increases with increase in δ for $K_c = 1$ & 1.5 and it is almost independent of δ for $K_c \geq 2$.

Understanding the actual nature, degree and range of stress rotation in-situ due to seismic shaking is very crucial because these factors plays a significant role in affecting

the liquefaction resistance of soil (Sivathayalan et al. 2015; Sinthujan 2013) and so far these factors were not taken into account in the conventional design practice for evaluating the liquefaction potential of saturated cohesionless soil.

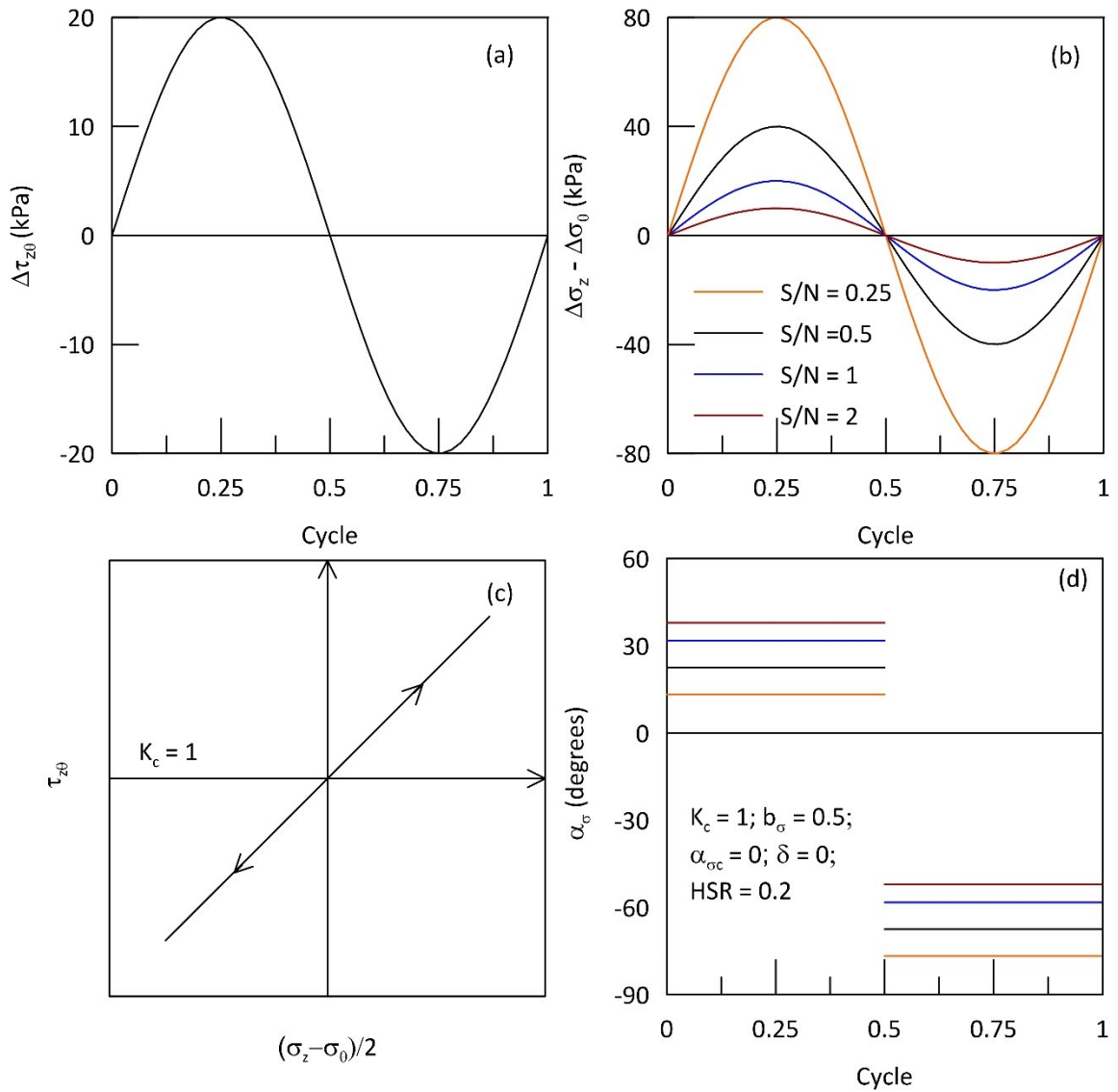


Figure 5.16: Variation of stress increments and α_σ for $K_c = 1$ under various S/N .

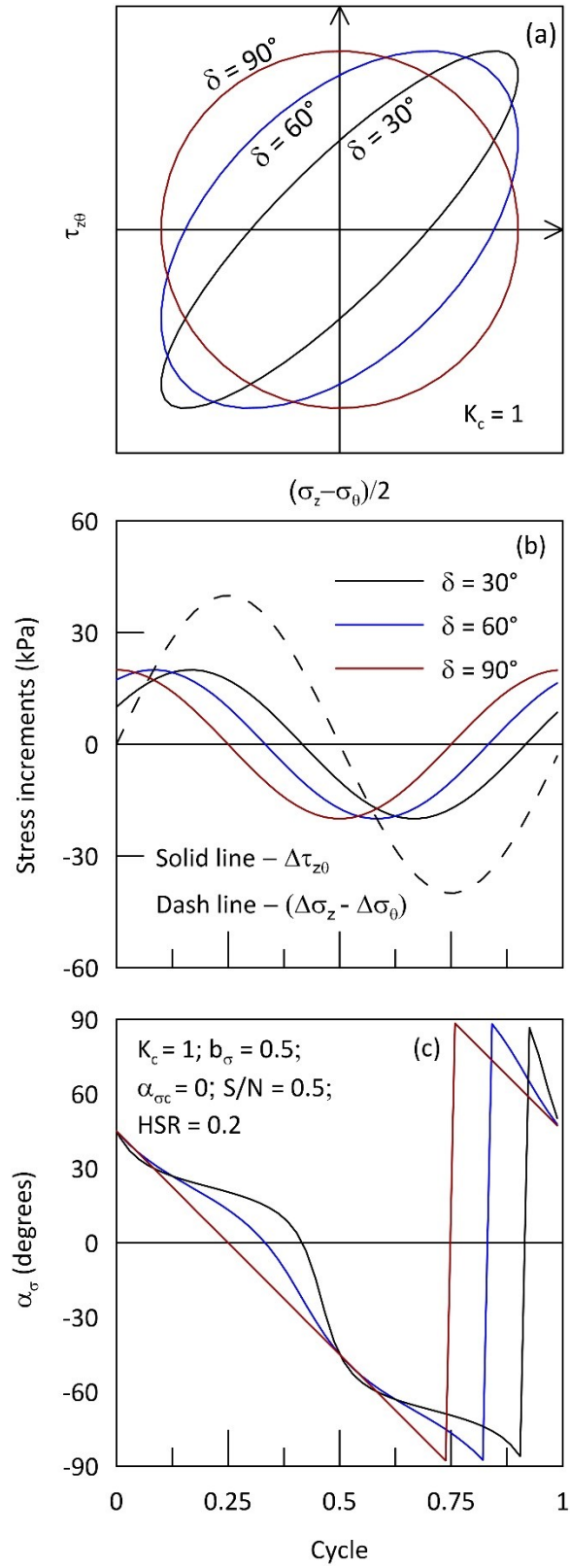


Figure 5.17: Variation of stress increments and α_{σ} for $K_c = 1$ under various phase shifts.

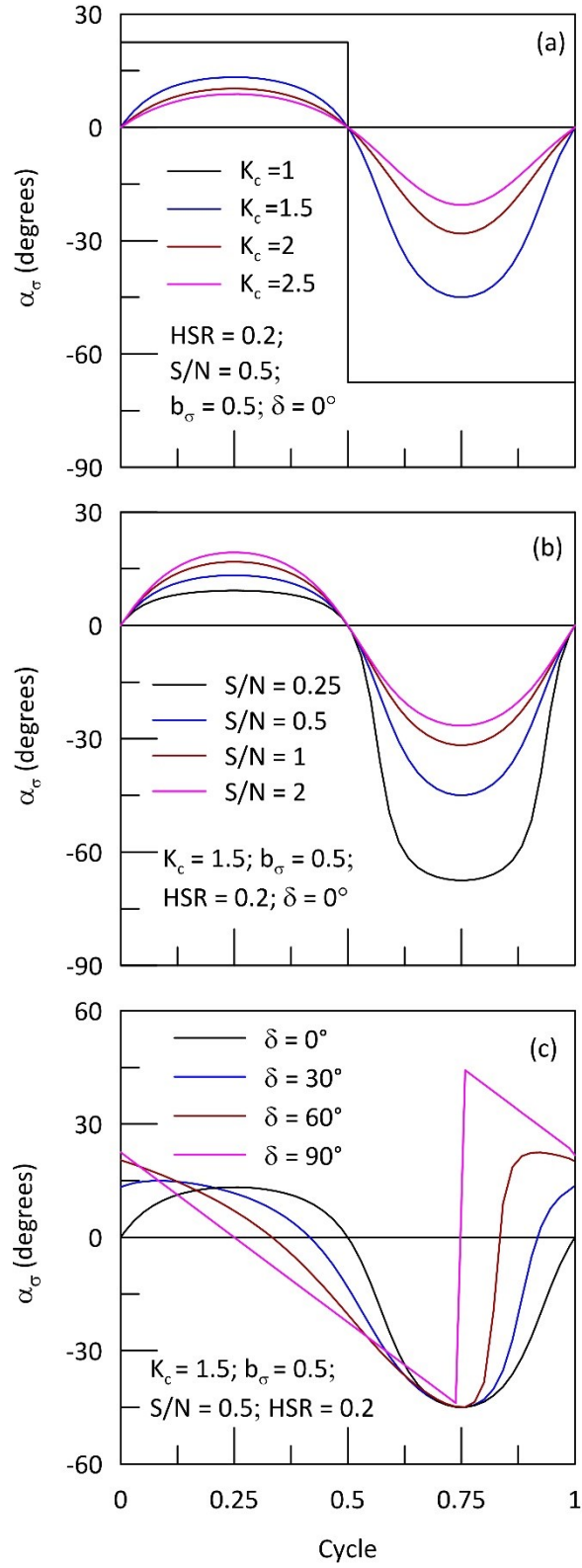


Figure 5.18: Variation of α_σ under different initial stress states and shearing conditions

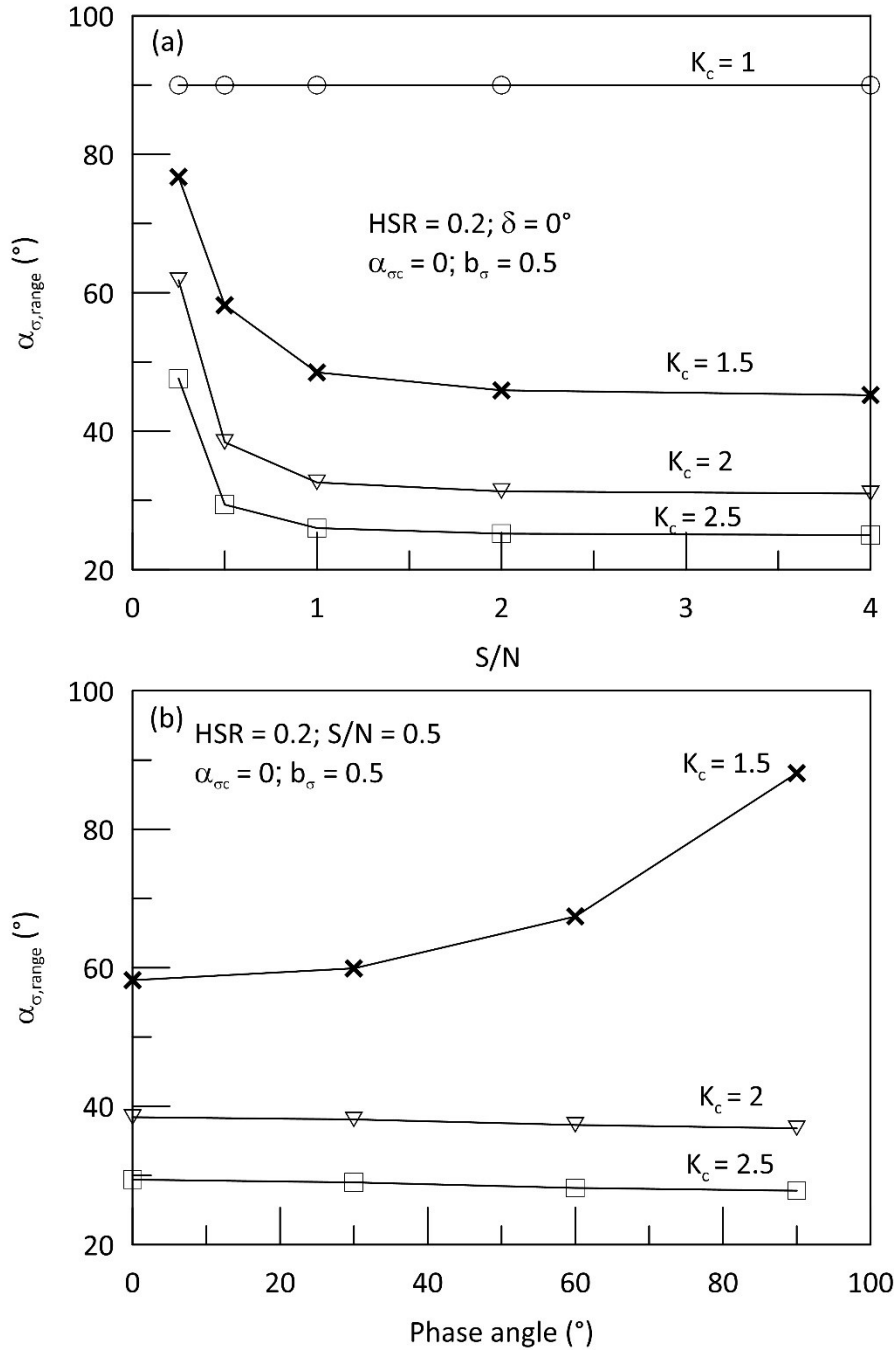


Figure 5.19: Variation of $\alpha_{\sigma,range}$ for different K_c under various S/N and phase shifts.

5.5 HCT studies on the liquefaction characteristics of sand under coupled loading

In this research program, a series of cyclic tests were performed on isotropically consolidated Fraser River sand specimens to investigate the effect of initial effective confining pressure (σ'_{mc}), cyclic stress ratio CSR (τ_{max}/σ'_{mc}) and S/N on the

liquefaction resistance of sand under the simultaneous action of compression and shear waves. Cyclic shearing was conducted on specimens consolidated to different effective mean normal stresses (50 kPa, 100 kPa and 200 kPa). Representative values of S/N obtained from the numerical analysis ranging from 0.25 to 2 and CSR ranging from 0.175 to 0.25 were considered for the analysis. In the tests with varying S/N , HSR is adjusted to reach a targeted CSR . Table 5.1 summarizes the details of cyclic tests carried out for this investigation. During cyclic loading, the total mean normal stress (σ_m) and intermediate principal stress parameter ($b_\sigma = 0.5$) were kept constant. The cyclic stress increments were applied at a loading rate of 4 minutes per cycle to maintain a proper feedback control response. The specimens were deemed to have liquefied when the single amplitude maximum shear strain exceeded 3.75% as per the recommendations of the National Research Council (NRC 1985).

Table 5.1: Details of initial and cyclic loading parameters

<i>Test No</i>	<i>Consolidation stage</i>			<i>Shearing stage</i>			
	<i>Stress state</i>	e_c	D_{rc} (%)	CSR	HSR	S/N	$\delta(^{\circ})$
CEQ01	$\sigma'_{mc} = 200 \text{ kPa};$ $k_c = 1;$ $b_\sigma = 0.5; \alpha_\sigma = 0^*$	0.706	45.1	0.2	0.09	0.25	0
CEQ02		0.717	42.0		0.144	0.5	
CEQ02-R		0.719	41.4		0.144	0.5	
CEQ03		0.712	43.4		0.183	1	
CEQ04		0.719	41.4	0.198	2		
CEQ05		0.725	39.7	0.25	0.115	0.5	
CEQ06		0.723	40.3	0.225	0.101	0.25	
CEQ07		0.723	40.3		0.160	0.5	
CEQ08	0.722	40.6	0.202		1		

CEQ08-R		0.719	41.4		0.202	1	
CEQ09		0.725	39.7		0.220	2	
CEQ10	$\sigma'_{mc} = 100 \text{ kPa};$ $k_c = 1;$ $b_\sigma = 0.5; \alpha_\sigma = 0^*$	0.727	39.2	0.175	0.079	0.25	0
CEQ11		0.737	36.3	0.2	0.09	0.25	
CEQ12		0.739	35.8		0.144	0.5	
CEQ13		0.727	39.2		0.183	1	
CEQ14		0.725	39.7		0.198	2	
CEQ15		0.724	40		0.225	0.101	
CEQ16		0.732	37.7	0.16		0.5	
CEQ17		0.722	40.6	0.202		1	
CEQ18		0.729	38.6	0.220		2	
CEQ19		0.723	40.3	0.25		0.115	
CEQ20		0.713	43.1		0.18	0.5	
CEQ21		0.724	40.0		0.23	1	
CEQ22		0.732	37.7		0.25	2	
CEQ23		0.725	39.7		0.3	0.142	
CEQ24		$\sigma'_{mc} = 50 \text{ kPa};$ $k_c = 1;$ $b_\sigma = 0.5; \alpha_\sigma = 0^*$	0.737	36.3	0.2	0.09	
CEQ25	0.724		40.0	0.225	0.101		
CEQ26	0.73		38.3	0.25	0.115		

*The values of α_σ and b_σ are technically undefined during isotropic consolidation. The values reported herein are the values maintained during shear loading

A typical response of Fraser River sand subjected to a simultaneous action of normal and shear stresses is discussed below. The specimen was isotropically consolidated to an effective mean normal stress of 200 kPa and sheared under a constant b_σ of 0.5. The soil specimen was subjected to an HSR of 0.144 and S/N of 0.5 which results in a CSR of 0.2. Figure 5.20 shows the variation of applied surface tractions and its corresponding

change in α_σ with respect to the number of cycles. Under these loading parameters, a maximum shear stress and normal stress increment of 28.8 kPa and 57.6 kPa was applied to the soil specimen and α_σ jump rotates between $+22.5^\circ$ and -67.5° . Since the cyclic shearing was performed under a b_σ of 0.5, the radial stress remained constant throughout the test. The total mean normal stress and radial stress essentially remain unchanged as seen in Figure 5.20b, and this demonstrates the excellent control of CU-HCT apparatus.

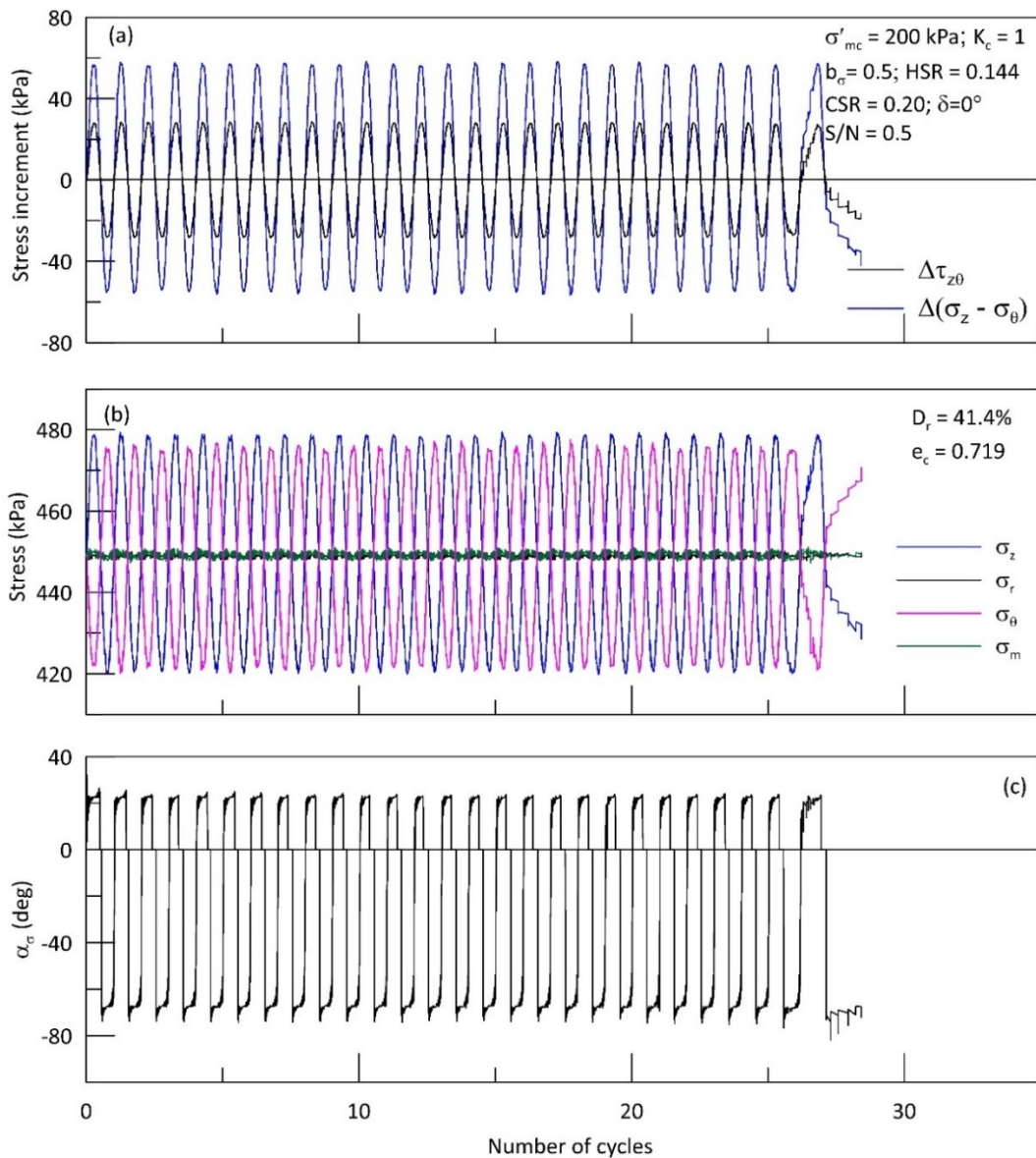


Figure 5.20: Variation of applied surface tractions and α_σ for $S/N = 0.5$

Figure 5.21 compares the targeted and achieved stress paths and the resulting α_σ variation in this test. It can be observed that the achieved loading path and the α_σ variation matches reasonably well with the targeted state. However, the prescribed stress paths may not be followed if the soil liquefies and cannot sustain the applied cyclic loads. Such a loss of control occurred during the final loading stage as the soil undergoes excessive deformation.

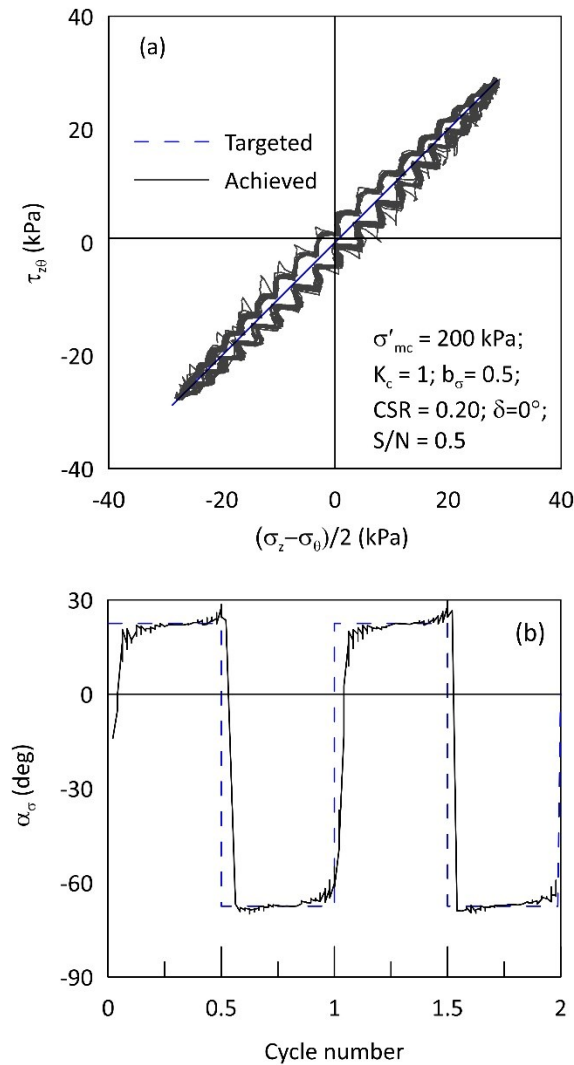


Figure 5.21: Targeted and achieved stress paths

The pore pressure, strain development and effective stress path response of Fraser River sand under this cyclic shearing condition is shown in Figure 5.22. It can be observed that the pore water pressure builds up steadily as the cyclic loading progresses and eventually reaches a maximum of 195 kPa which corresponds to almost 98% of the initial effective confining stress. The effective stress path crosses the phase transformation (PT) line when the excess pore water pressure reaches almost 70% of the initial effective confining stress. Larger strain begins to develop in the sand specimen following this stage. The specimen was deemed liquefied in 26 cycles due to the attainment of the prescribed maximum shear strain (γ_{max}) of 3.75%. The liquefaction can also be witnessed more clearly by observing the torsional stress-strain plot in Fig. 5.22e. At 25th cycle, the torsional shear strain increases suddenly indicating cyclic softening of the sand.

5.5.1 Repeatability of tests

It is always necessary to confirm the repeatability of test results in laboratory to assess the level of confidence in the testing apparatus and test procedures adopted. This repeatability check becomes more significant when the soil sample is subjected to complex shearing condition. The undrained response of two identical soil specimens subjected to coupled cyclic loading is shown in Figure 5.23 and 5.24, respectively. The specimens are consolidated to the same effective confining stress and almost same relative density prior to shearing. The essentially identical responses observed until the triggering of liquefaction indicates the good repeatability of specimen reconstitution and excellent control of the HCT feedback control system. Once liquefaction is triggered, the sample cannot sustain the applied cyclic loading path, and this might be the reason for the slight deviation noted in Figure 5.24.

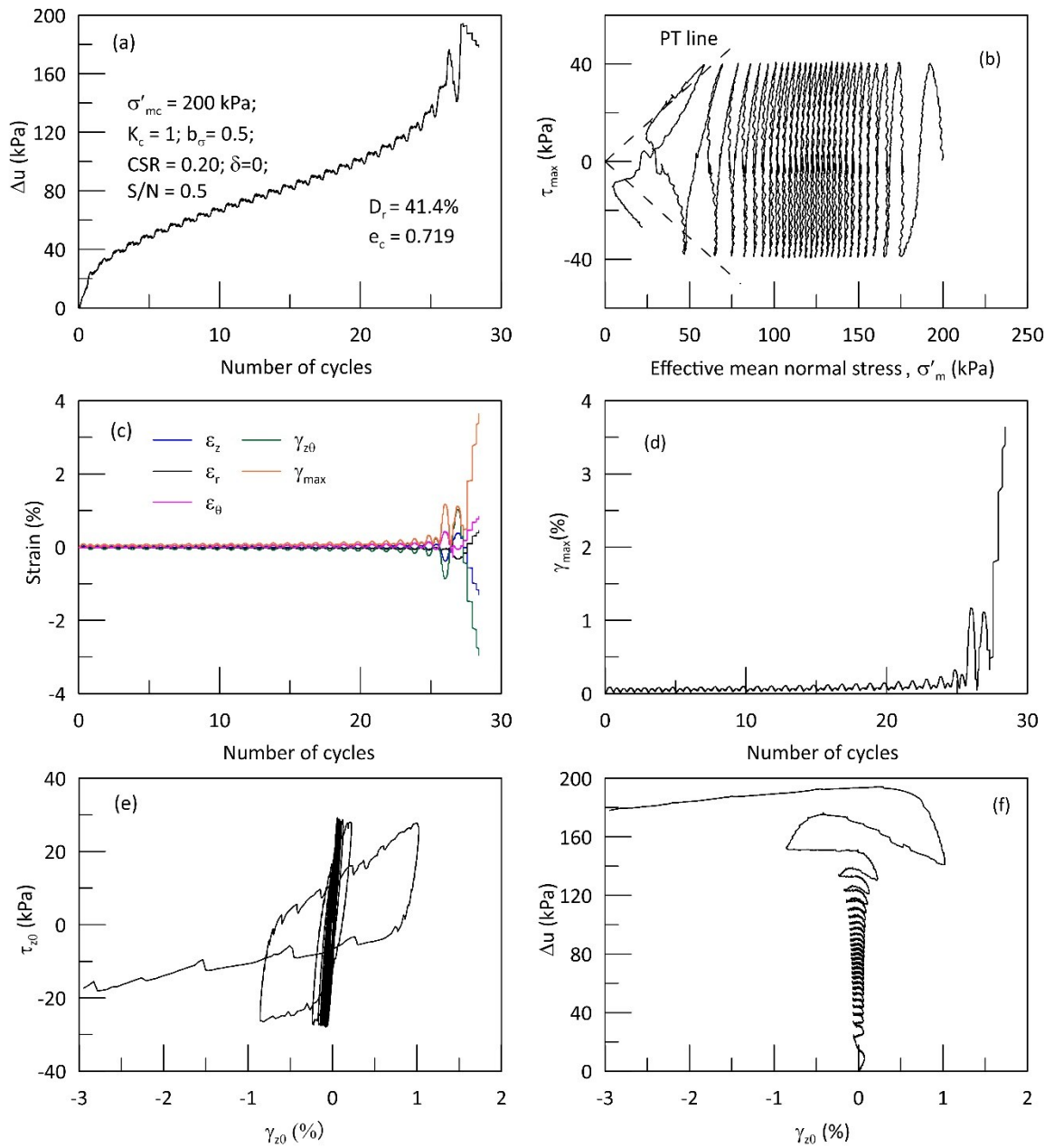


Figure 5.22: Typical response of sand subjected to coupled loading with $S/N = 0.5$

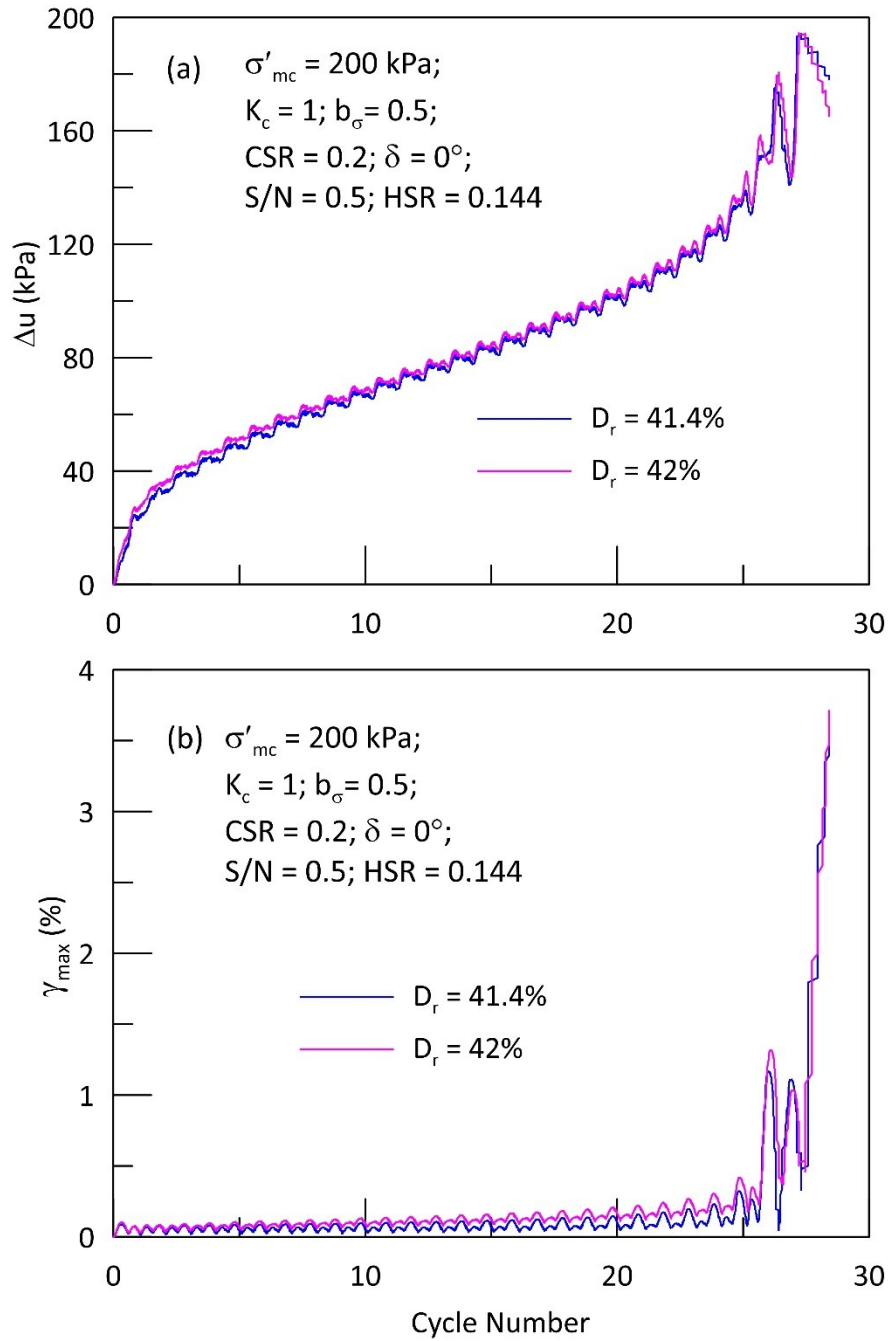


Figure 5.23: Repeatability test at $CSR = 0.2$ and $S/N = 0.5$

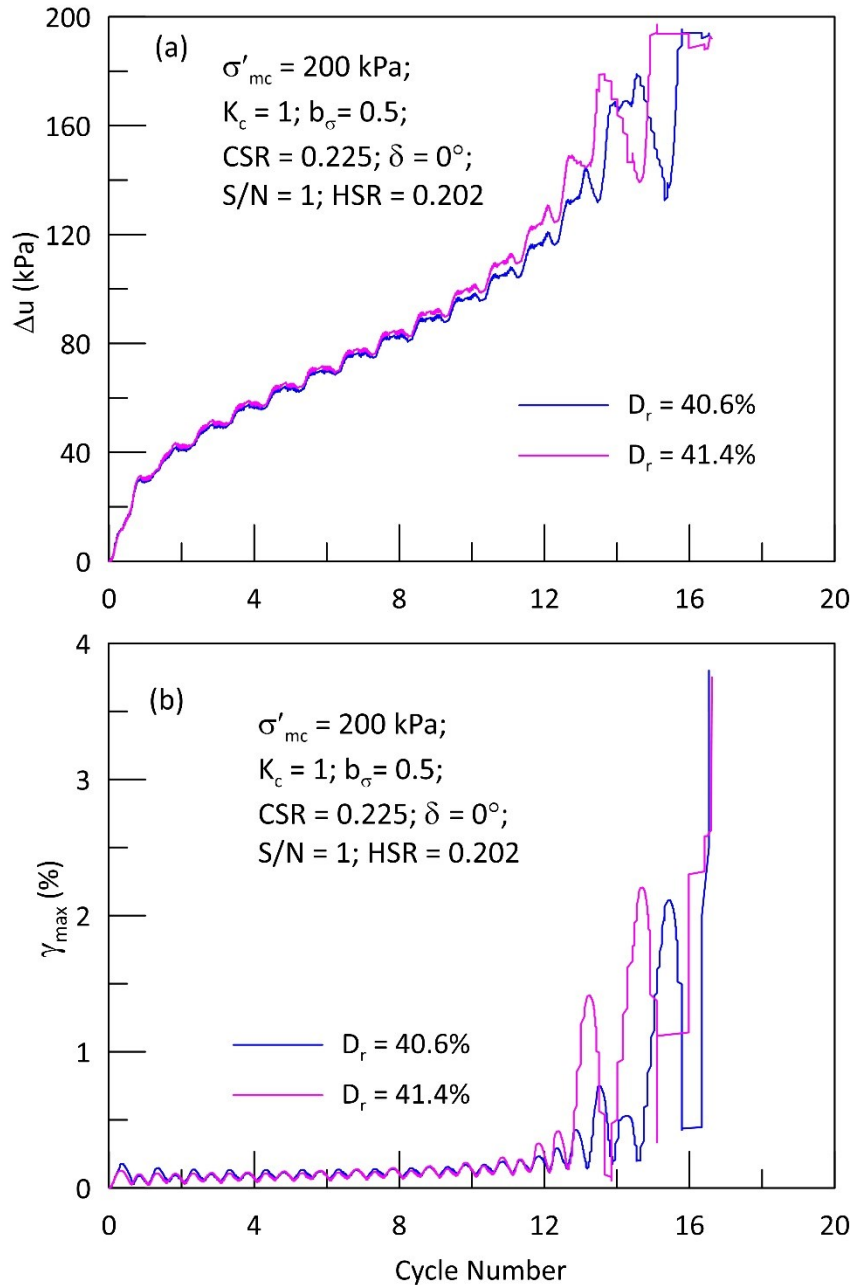


Figure 5.24: Repeatability test at $CSR = 0.225$ and $S/N = 1$

5.6 Coupled action of normal and shear stresses at different stress ratios and confining pressure

This section discusses the effect of cyclic stress ratio (CSR) and initial effective confining stress (σ'_{mc}) on the cyclic response of an isotropically consolidated Fraser River sand

subjected to a combined loading with the S/N of 0.25. CSR ranging from 0.175 to 0.3 and σ'_{mc} from 50 kPa to 200 kPa were considered for this analysis. For a fixed S/N ratio, HSR is adjusted to yield a targeted CSR . Figure 5.25 shows the variation of HSR with respect to CSR for the S/N of 0.25. HSR increases almost linearly from 0.079 for $CSR = 0.175$ to 0.142 for $CSR = 0.3$. In all these cases, α_σ jump rotates between $+13.3^\circ$ and -76.7° and it is noted that for a fixed S/N at $K_c = 1$, the stress rotation is independent of the initial σ'_{mc} , HSR and CSR .

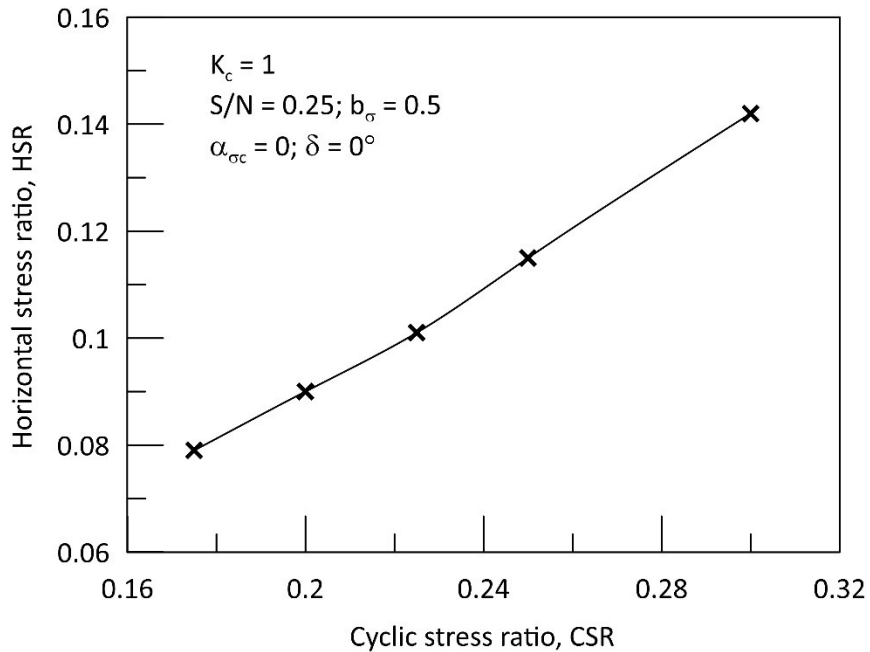


Figure 5.25: HSR variation with CSR for $S/N = 0.25$

Figure 5.26 to 5.28 shows the effective stress path responses of Fraser River sand consolidated to $\sigma'_{mc} = 200$ kPa and subjected to a CSR of 0.2, 0.225 and 0.25. It can be observed that as the CSR increases the mechanism of liquefaction changes from cyclic mobility to true liquefaction. At $CSR = 0.2$, sand liquefied in 42 cycles due to cyclic mobility i.e., the transient state of zero effective stress leads to the development of large shear deformations. At $CSR = 0.225$, the sand suffered limited liquefaction when the

stress path crosses the PT line and subsequently followed by cyclic mobility which leads to the development of maximum shear strain of 3.75%. At $CSR = 0.25$, sand suffered true liquefaction in 4 cycles. The state of zero effective stress is not realized and unlimited deformation occurs at a finite level of effective stress. The development of true liquefaction might be because the imposed cyclic shear stress (τ_{max}) could have exceeded the minimum undrained strength of sand at phase transformation state (S_{PT}). Sivathayalan et al. (2015) through undrained monotonic tests on isotropically consolidated Fraser River sand ($\sigma'_{mc} = 200 \text{ kPa}$) along different stress paths with a fixed $b_\sigma = 0$, reported that S_{PT} of sand reduces from 108 kPa when $\alpha_\sigma = 0^\circ$ to about 60 kPa when $\alpha_\sigma = 90^\circ$. Moreover, the S_{PT} of sand is also influenced by the intermediate principal stress parameter b_σ during shearing, it is reported that S_{PT} of sand decreases with the increase in b_σ (Uthayakumar and Vaid 1998; Logeswaran 2010). In this cyclic test with $CSR = 0.25$, maximum τ_{max} of 50 kPa is imposed to the sand specimen with $b_\sigma = 0.5$ and α_σ rotates between $+13.3^\circ$ and -76.7° . Hence, there is a high possibility that during cyclic loading the induced τ_{max} could have exceeded the S_{PT} of sand which triggered the flow failure of the sand specimen. Figure 5.29 to 5.31 shows the effective stress path responses of sand consolidated to $\sigma'_{mc} = 100 \text{ kPa}$. Soil liquefied in 63, 35 and 13 cycles for the CSR of 0.2, 0.225 and 0.25, respectively. Liquefaction is predominantly due to cyclic mobility though a slight tendency of limited liquefaction is noted at CSR of 0.2. Figure 5.32 to 5.34 presents the effective stress path response for $\sigma'_{mc} = 50 \text{ kPa}$. The sand specimen suffered liquefaction in 150, 42 and 20 cycles for the CSR of 0.2, 0.225 and 0.25, respectively. At this level of σ'_{mc} , cyclic mobility leads to the realization of γ_{max} of 3.75%. In all the cases of σ'_{mc} , large strains begin to develop when the effective stress path crosses the PT line. At larger shear

strains, the inability of the stress-controlled feedback control system to reach the targeted surface tractions is the major reason for the erratic fluctuations noted in the stress path towards the end of the tests. These fluctuations towards the end of tests can be safely ignored while estimating the liquefaction potential of the soil.

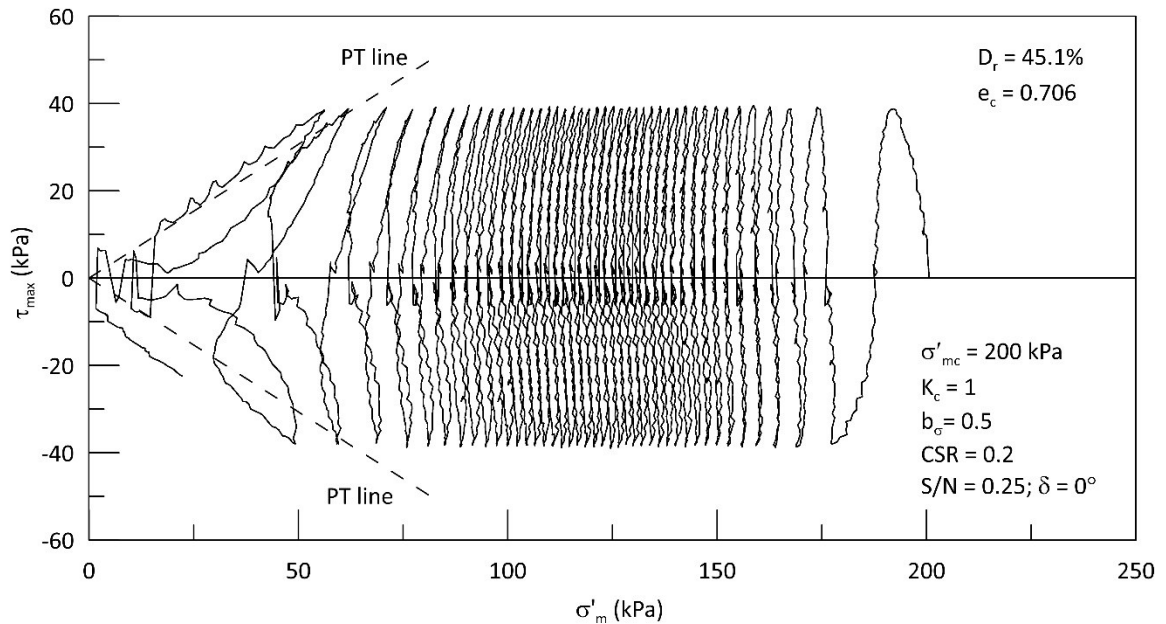


Figure 5.26: Effective stress path response at $\sigma'_{mc} = 200 \text{ kPa}$; $CSR = 0.2$ & $S/N = 0.25$

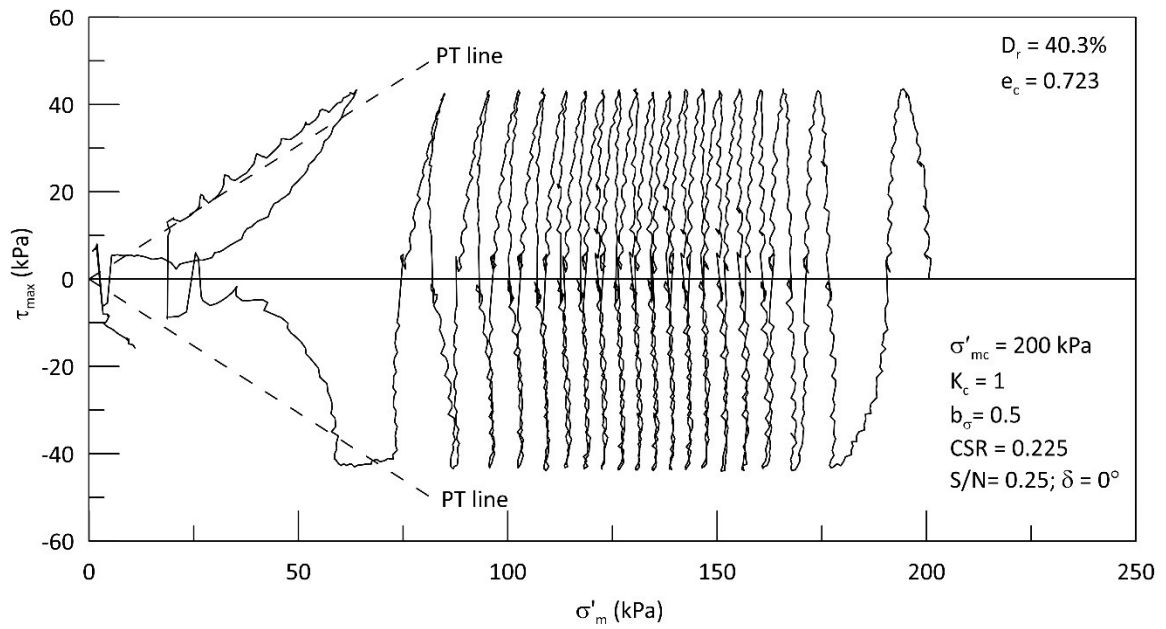


Figure 5.27: Effective stress path response at $\sigma'_{mc} = 200 \text{ kPa}$; $CSR = 0.225$ & $S/N = 0.25$

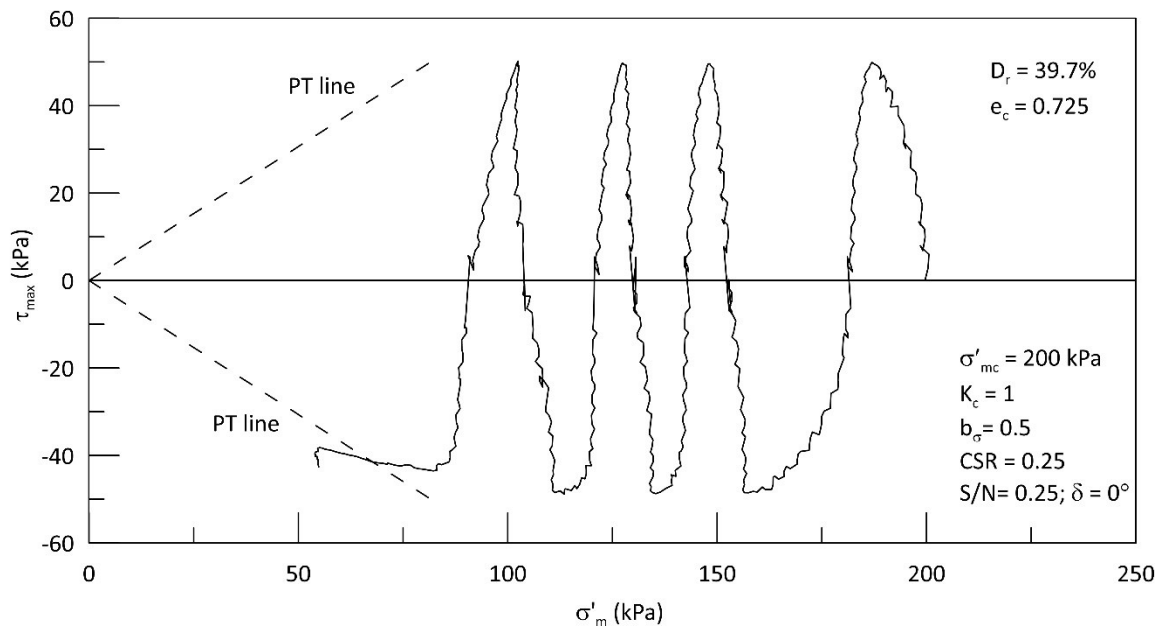


Figure 5.28: Effective stress path response at $\sigma'_{mc} = 200 \text{ kPa}$; $CSR = 0.25$ & $S/N = 0.25$

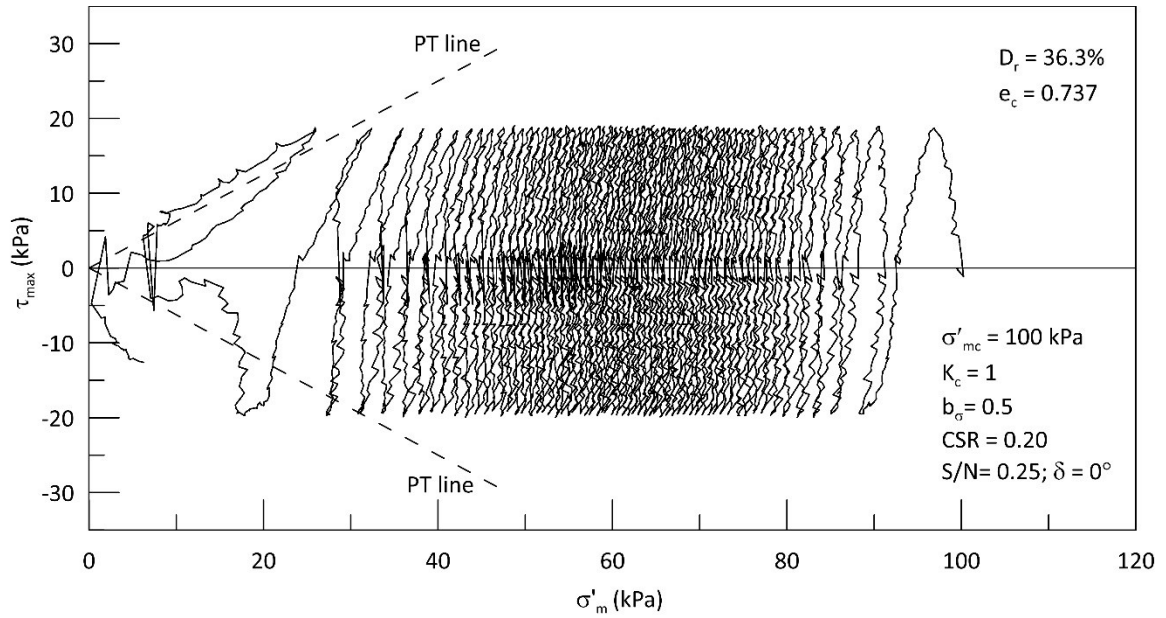


Figure 5.29: Effective stress path response at $\sigma'_{mc} = 100$ kPa; $CSR = 0.2$ & $S/N = 0.25$

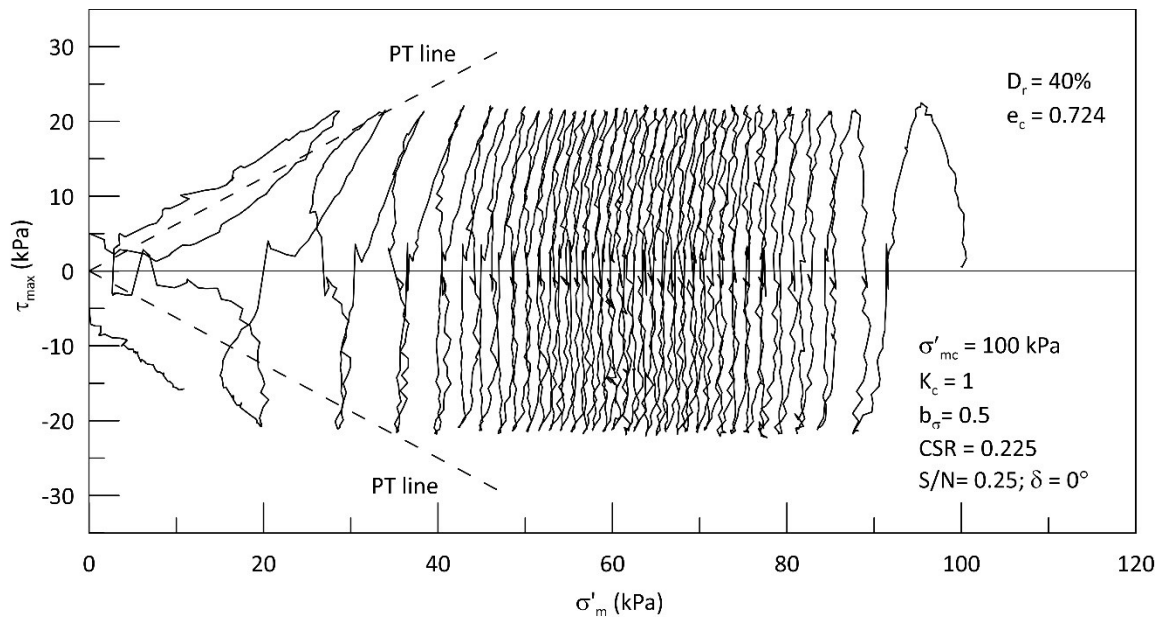


Figure 5.30: Effective stress path response at $\sigma'_{mc} = 100$ kPa; $CSR = 0.225$ & $S/N = 0.25$

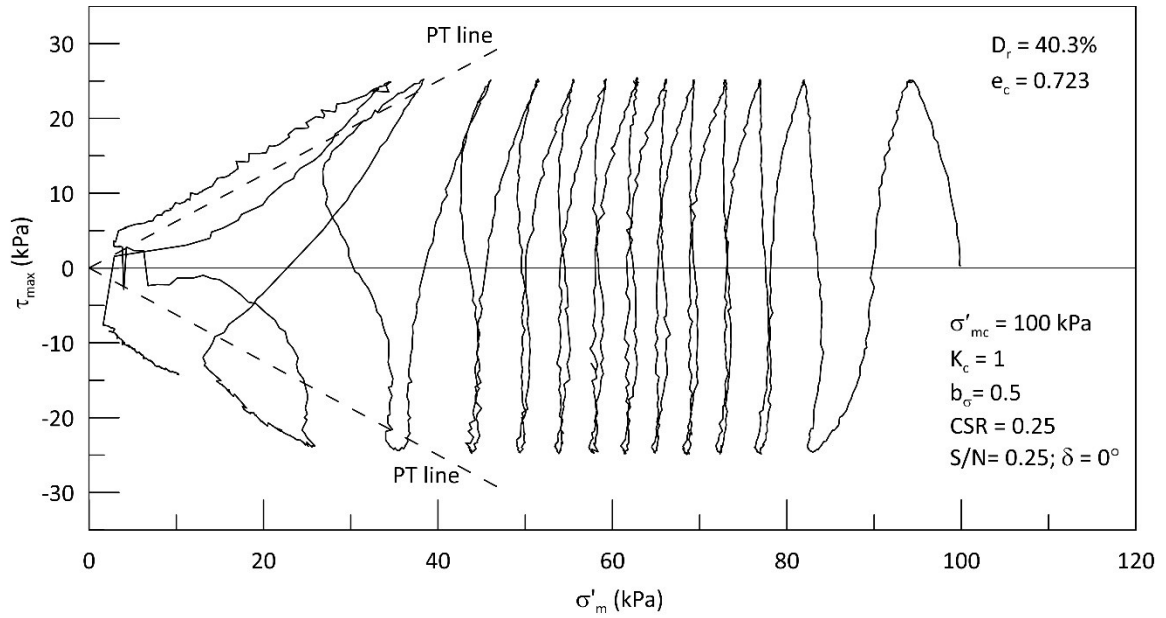


Figure 5.31: Effective stress path response at $\sigma'_{mc} = 100 \text{ kPa}$; $CSR = 0.25$ & $S/N = 0.25$

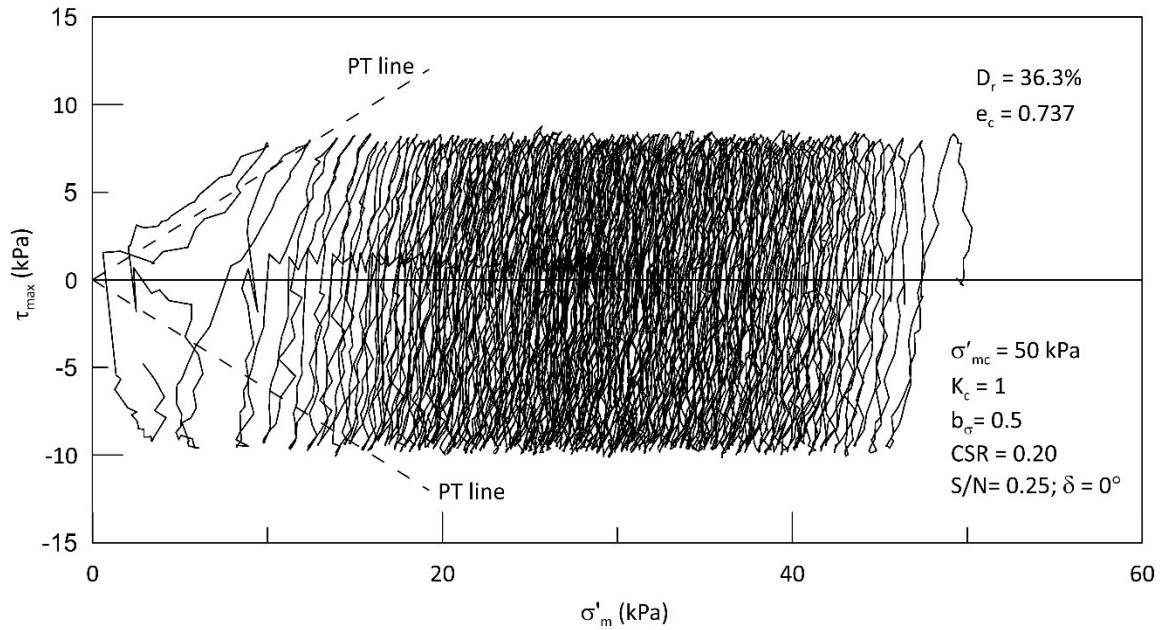


Figure 5.32: Effective stress path response at $\sigma'_{mc} = 50 \text{ kPa}$; $CSR = 0.2$ & $S/N = 0.25$

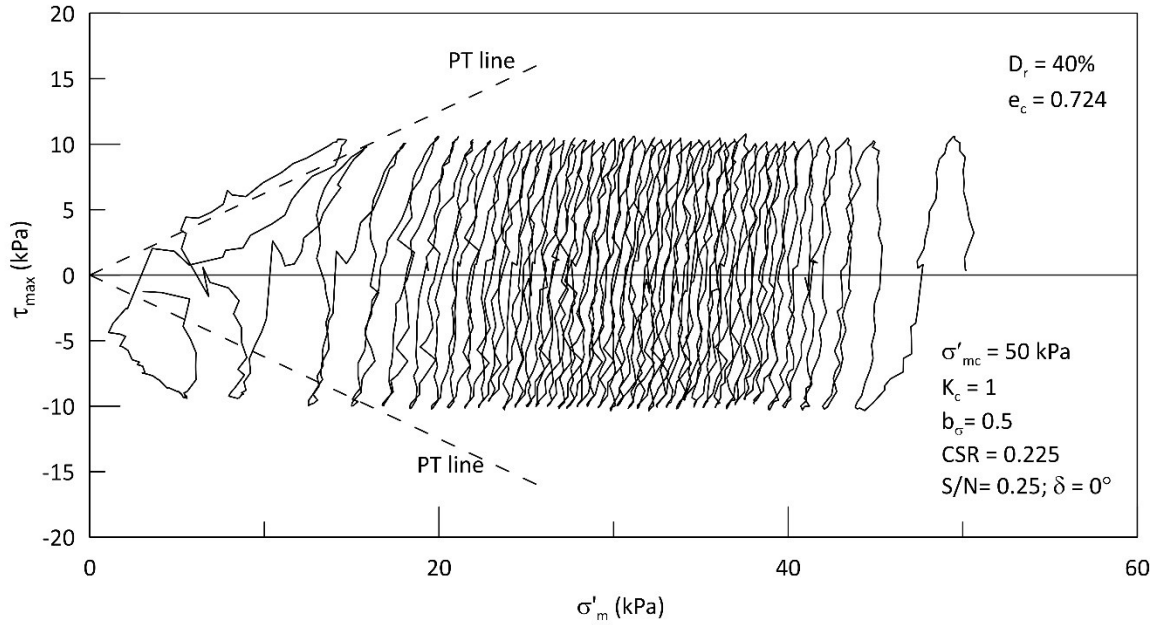


Figure 5.33: Effective stress path response at $\sigma'_{mc} = 50 \text{ kPa}$; $CSR = 0.225$ & $S/N = 0.25$

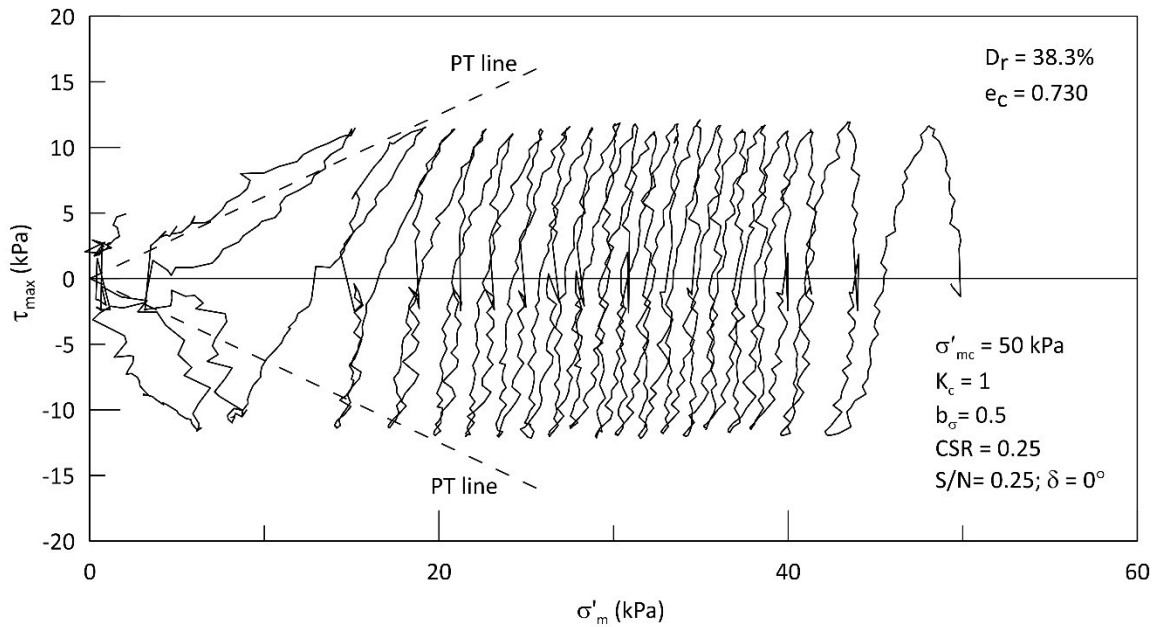


Figure 5.34: Effective stress path response at $\sigma'_{mc} = 50 \text{ kPa}$; $CSR = 0.25$ & $S/N = 0.25$

Figure 5.35 compares the pore pressure and shear strain development of sand consolidated to $\sigma'_{mc} = 100 \text{ kPa}$ and subjected to different levels of cyclic stress ratio.

The excess pore water pressure accumulated gradually as the loading cycle progresses and the rate of pore pressure generation systematically increases with the increase in *CSR*. At *CSR* = 0.175, the sand did not liquefy even after 100 loading cycles. A maximum pore water pressure of only about 35 kPa (35% of initial σ'_{mc}) was generated at the end of 100 cycles. The sand would have liquefied if the cyclic loading is continued for several hundreds of cycles. Such a condition is not realistic even during strong tremors, and therefore the cyclic test was stopped at 100th loading cycle. The sand liquefied within 4 cycles at a higher *CSR* of 0.3. Except for *CSR* = 0.175, a maximum pore pressure of almost equivalent to 100% of the initial effective confining stress was generated in the other tests (with higher *CSRs*). It can be noted in Figure 5.35b that the rate of shear strain development also increases with the increase in *CSR* analogous to the excess pore water pressure generation. The rate of shear strain development is very small (almost less than 0.5%) until the excess pore pressure generated reaches almost 65 to 75% of initial σ'_{mc} . After this stage, the rate of shear strain development increases rapidly and eventually the soil liquefied in another one or two additional loading cycles. This observation is consistent with the original findings of Seed (1979) that the strain development will be limited until the excess pore water pressure generated exceeds approximately 60% of the initial effective confining pressure.

Figure 5.36 shows the variation of number of cycles to liquefaction with *CSR* for the coupled loading test with $S/N = 0.25$ at two different stress levels. It also compares the cyclic test data reported in the literature for Fraser River sand from cyclic triaxial (Vaid and Thomas 1995), cyclic simple shear (Vaid and Sivathayalan 1996a) and cyclic hollow cylinder tests under different loading modes (Sivathayalan et al. 2015; Sinthujan 2013). As

expected, the number of cycles to liquefaction decreases with the increase in CSR and the rate of reduction is almost fairly consistent with the data in the literature. As expected the simple shear tests (Vaid and Sivathayalan 1996a) yielded low liquefaction resistance, but on the other hand, the triaxial test (Vaid and Thomas 1995) which should have yielded higher liquefaction resistance, showed cyclic resistance less than the test with $S/N = 0.25$. It should be noted that these data sets cannot be directly compared with each other as they are obtained from different batches of Fraser River sand tested under different loading modes with different b_σ and nature and degree of stress rotation. Hence, this differences in testing modes leads to the discrepancies noted between triaxial and $S/N = 0.25$ test in Figure 5.36a, but the general agreement with the trend of variation adds confidence to the data obtained from the coupled loading condition. On a similar note, the data sets reported in Figure 5.36b were also obtained from cyclic tests under different initial conditions and degrees of stress rotation, hence they cannot be compared directly with each other.

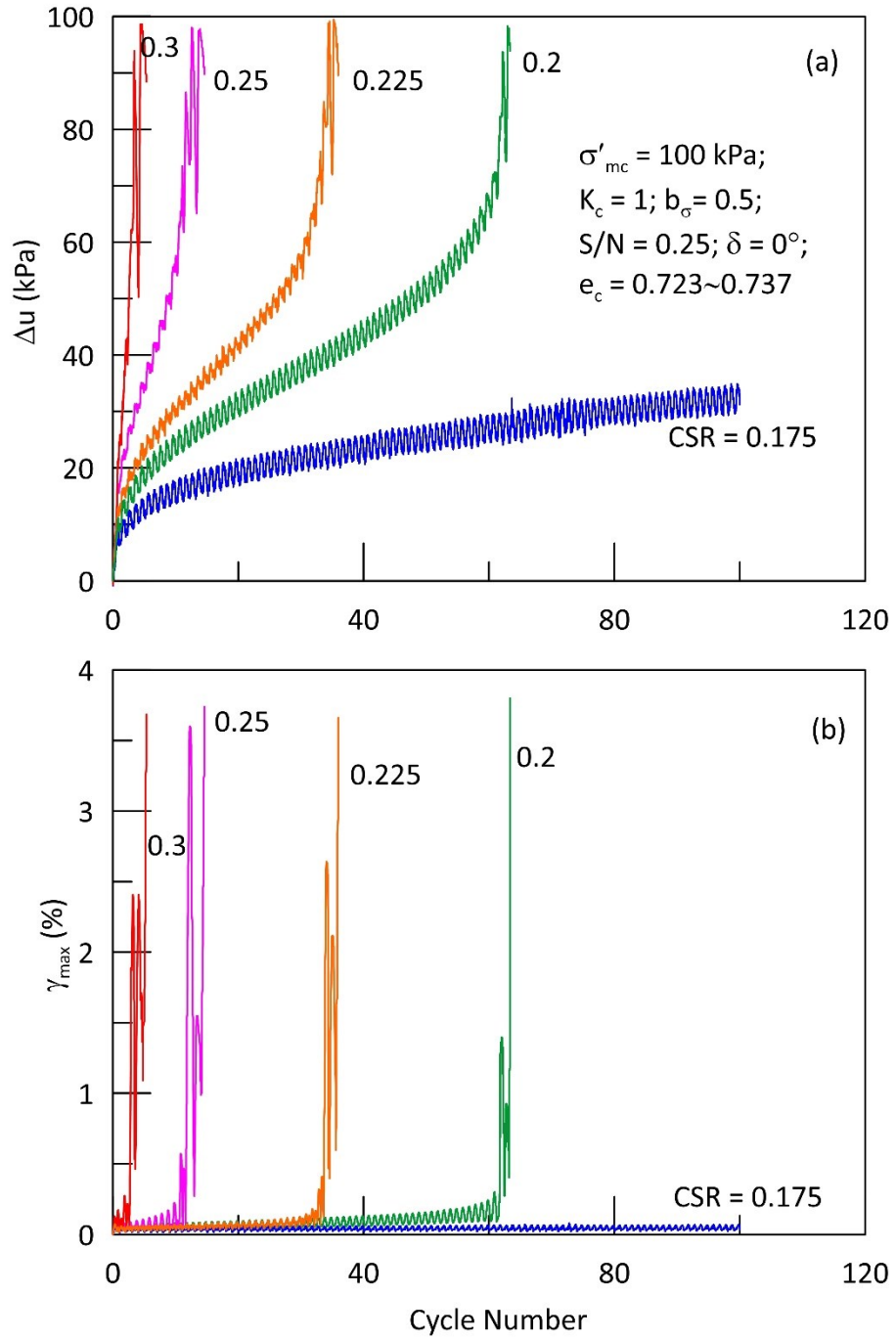


Figure 5.35: Excess pore pressure and shear strain development for different CSRs

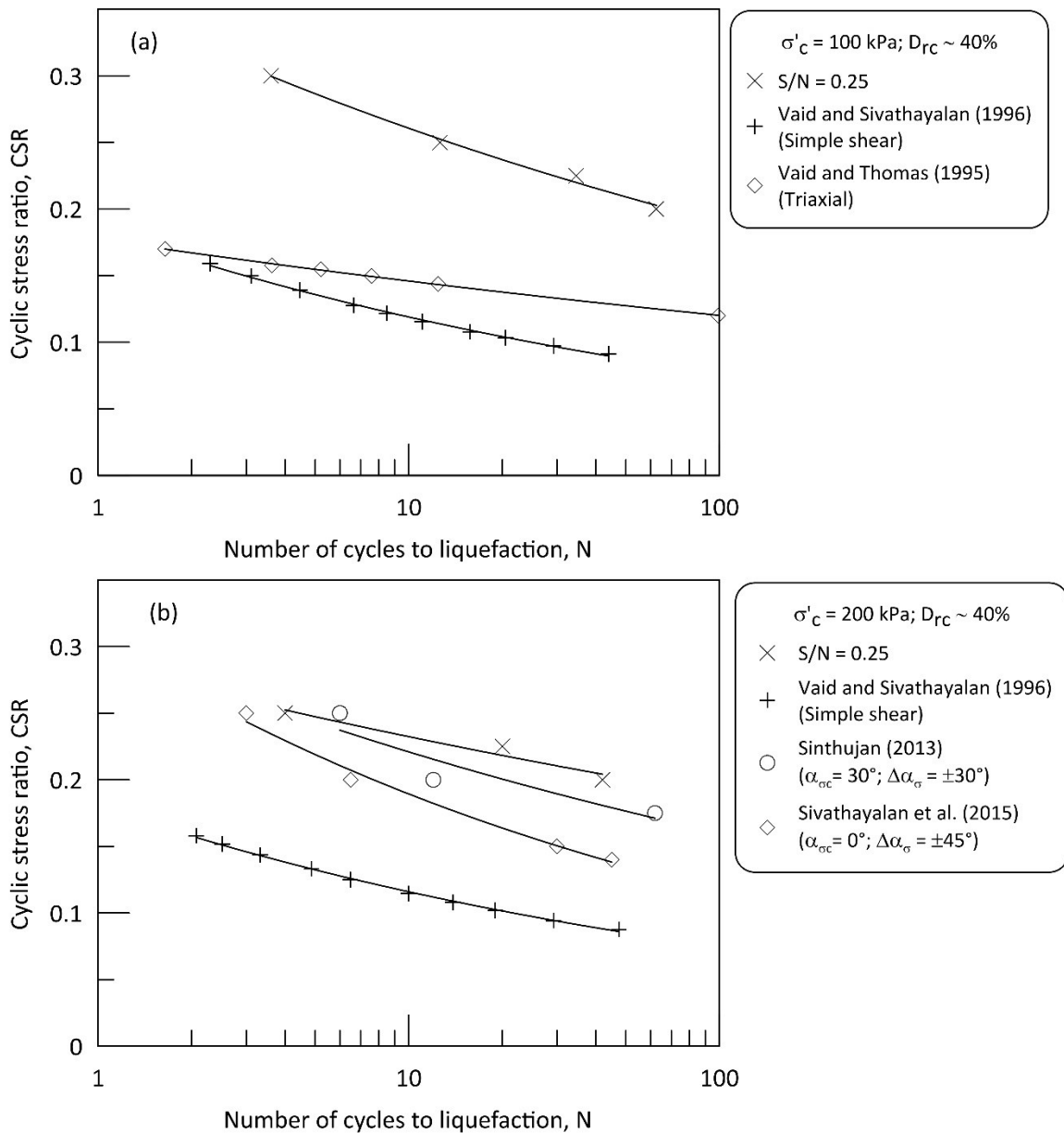


Figure 5.36: Cyclic resistance curves from different investigations on Fraser River sand

Figure 5.37 compares the pore pressure and shear strain development of sand consolidated to σ'_{mc} of 50, 100 and 200 kPa and subjected to a combined loading with $S/N = 0.25$ and $CSR = 0.225$. The void ratio at the end of consolidation is almost identical across the tested specimens. It can be observed that at the same level of relative density, the rate of pore pressure and shear strain accumulation increases with the increase

in initial σ'_{mc} . At this level of CSR, sand liquefied in 42, 35 and 20 cycles for σ'_{mc} of 50, 100 and 200 kPa respectively.

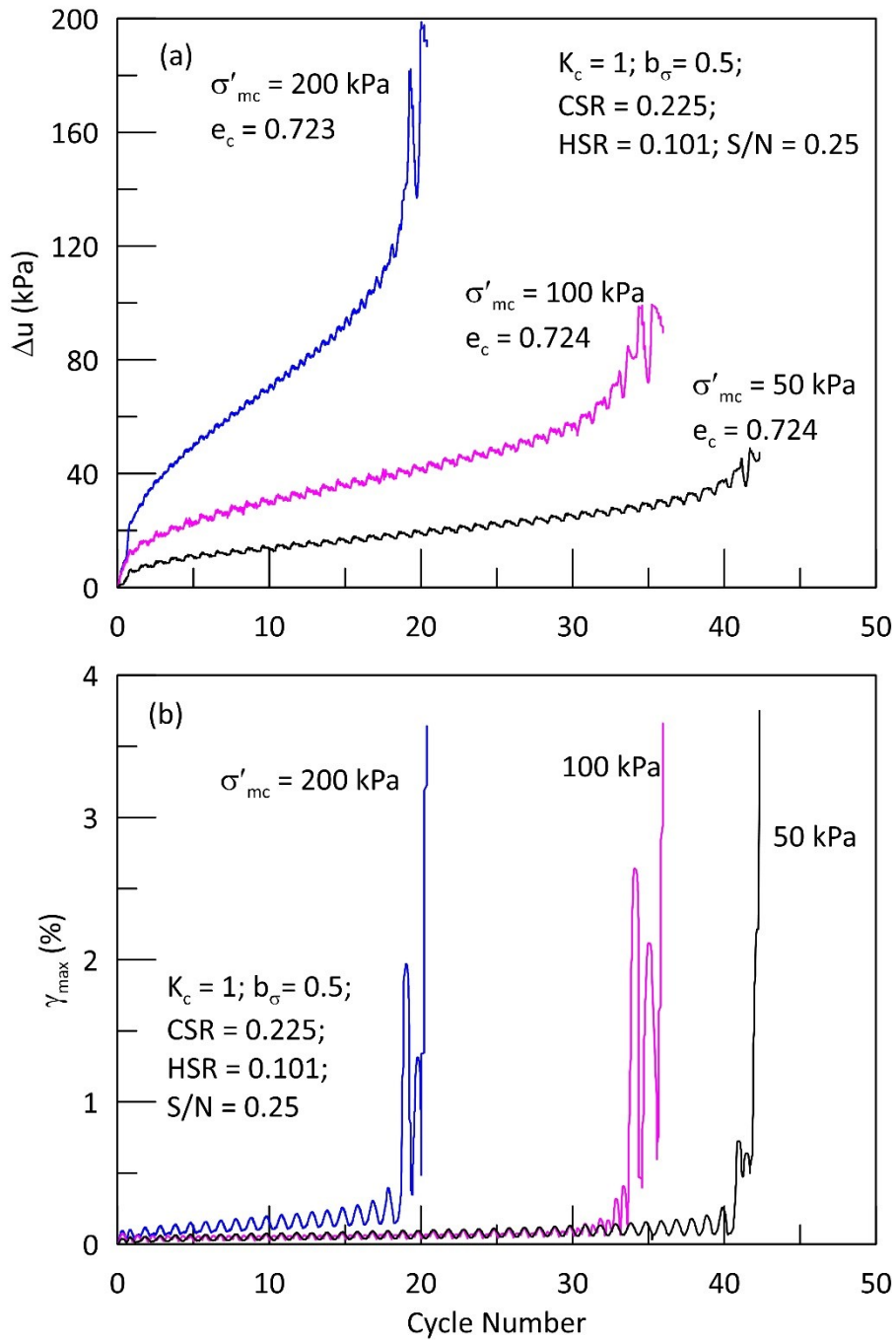


Figure 5.37: Excess pore pressure and shear strain development at different σ'_{mc}

Figure 5.38 shows the variation of the number of cycles to liquefaction with *CSR* at two different levels of initial effective confining pressure. It can be noted that for a given *CSR*, the number of cycles to liquefaction decreases with the increase in initial effective confining stress. This effect of confining pressure has a significant influence in analyzing the cyclic strength of foundation soils of embankment, dams and high-rise buildings (Ishihara 1996). In practice, the cyclic resistance of sand is usually represented by cyclic resistance ratio (*CRR*) which is defined as the cyclic stress ratio required to cause liquefaction in a specified number of loading cycles (typically $N_L = 10$ or 15). Figure 5.39 shows the variation of *CRR* required to reach 3.75% of maximum shear strain in 15 loading cycles with initial σ'_{mc} and it can be noted from the plot that *CRR* decreases from 0.256 to 0.225 with the increase in initial effective confining pressure from 50 kPa to 200 kPa.

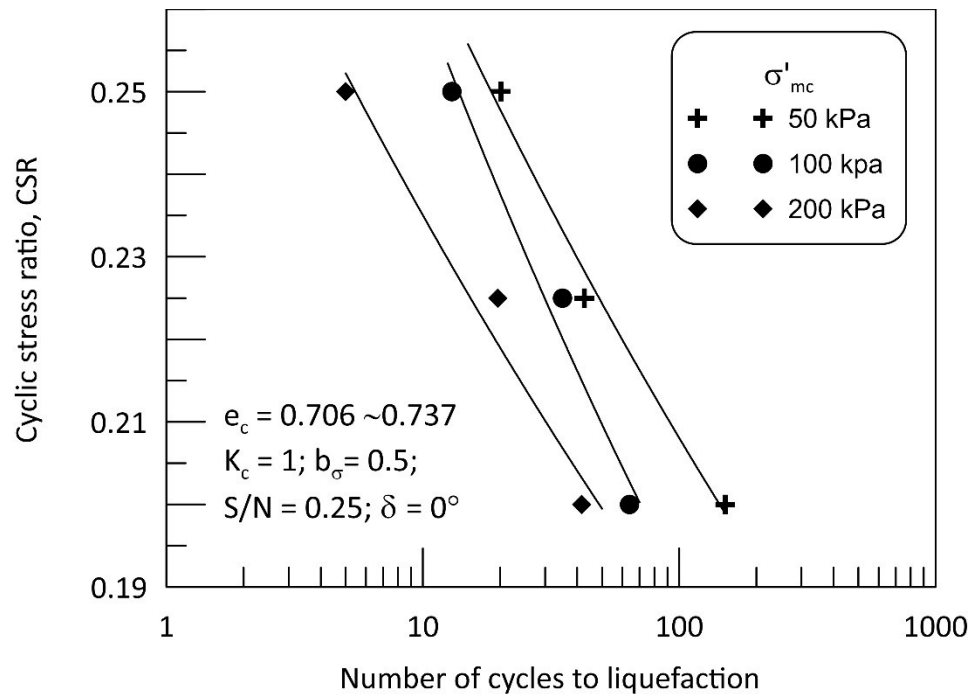


Figure 5.38: Cyclic resistance curve at different initial stress states

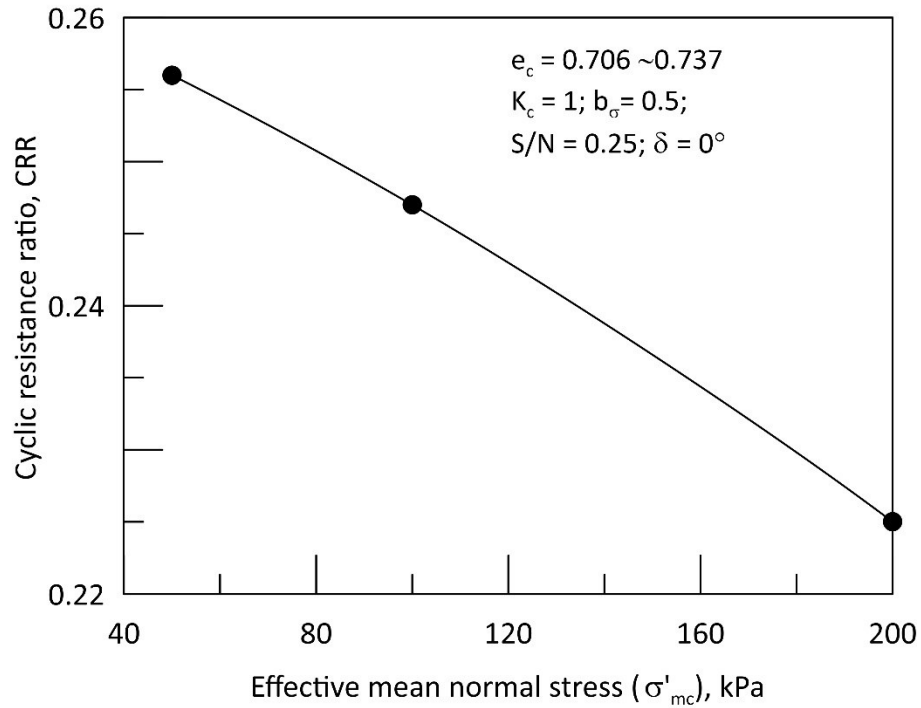


Figure 5.39: Variation of CRR with initial σ'_{mc}

In liquefaction analysis, the dependence of cyclic resistance of sand on the consolidation stress is accounted by introducing a correction factor K_σ , which is defined as the ratio of CRR of the soil at given σ'_{mc} to the CRR of the same soil at $\sigma'_{mc} = 100 \text{ kPa}$ ($\sim 1 \text{ atm}$) (Seed 1983; Seed and Harder 1990). Several studies have been carried out to examine the K_σ correction factor on the liquefaction resistance of sand (Seed and Harder 1990, Vaid and Thomas 1995; Vaid and Sivathayalan 1996a; Boulanger 2003; Koseki et al. 2005; Boulanger and Idriss 2007; Manmatharajan and Sivathayalan 2011; Sivathayalan and Ha 2011; Montgomery et al. 2014). However, most of the laboratory investigations on the K_σ correction factor is derived from the triaxial and simple shear testing on uniform sand specimens which ignores the effect of generalized three-dimensional loading conditions. Earlier in chapter 4 it is shown that the dependency of cyclic resistance on the initial confining pressure is pronounced for loose sand specimens even under 3D loading.

Though this comparison is based on two different shear stress levels ($\sigma'_{mc} = 100 \text{ kPa}$, $CSR = 0.25$; $\sigma'_{mc} = 200 \text{ kPa}$, $CSR = 0.2$) but it gives a clear picture of the K_σ effect under generalized stress state. Figure 5.40 shows the variation of K_σ with normalized effective consolidation stress for the coupled loading with $S/N = 0.25$. The K_σ value reduced from 1.04 for $\sigma'_{mc} = 50 \text{ kPa}$ to about 0.91 for $\sigma'_{mc} = 200 \text{ kPa}$. From this plot, it can also be noticed that the trend of variation of K_σ with effective overburden stress for the generalized coupled loading condition also follows the well-established trend reported in Vaid and Sivathayalan (1996a) for Fraser delta sand.

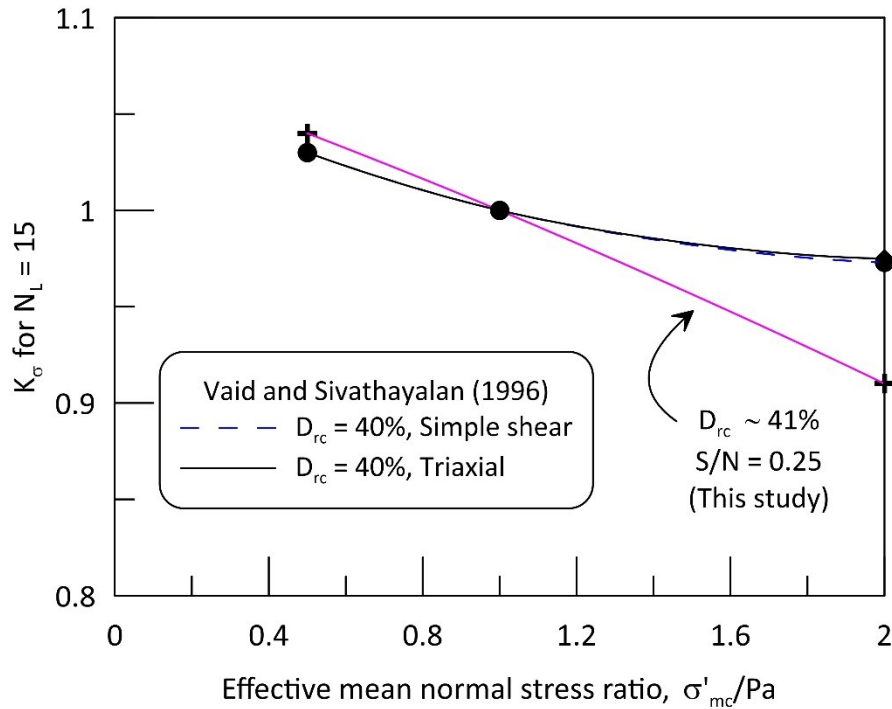


Figure 5.40: Variation of K_σ with effective overburden stress ratio

5.7 Influence of S/N ratios on the liquefaction characteristics of Fraser River sand

This section discusses the influence of ratio between shear stress increment ($\Delta\tau_{z\theta}$) and normal stress increment ($\Delta(\sigma_z - \sigma_\theta)$) on the cyclic behavior of sand. Cyclic tests were carried out on isotropically consolidated samples ($\sigma'_{mc} = 100 \text{ kPa}$ & 200 kPa) at CSR

of 0.2, 0.225 and 0.25 with S/N varying from 0.25 to 2. As mentioned earlier, for a particular S/N , HSR is adjusted to yield a targeted CSR . Figure 5.41 shows the variation of HSR with respect to S/N for all the $CSRs$ considered in this test series. For a given CSR , HSR increases non-linearly with S/N , but the rate of increase decreases as the S/N increases and HSR remains almost unchanged for S/N greater than 2. The cyclic tests were carried out at constant total mean normal stress, σ_m and intermediate principal stress parameter, b_σ of 0.5.

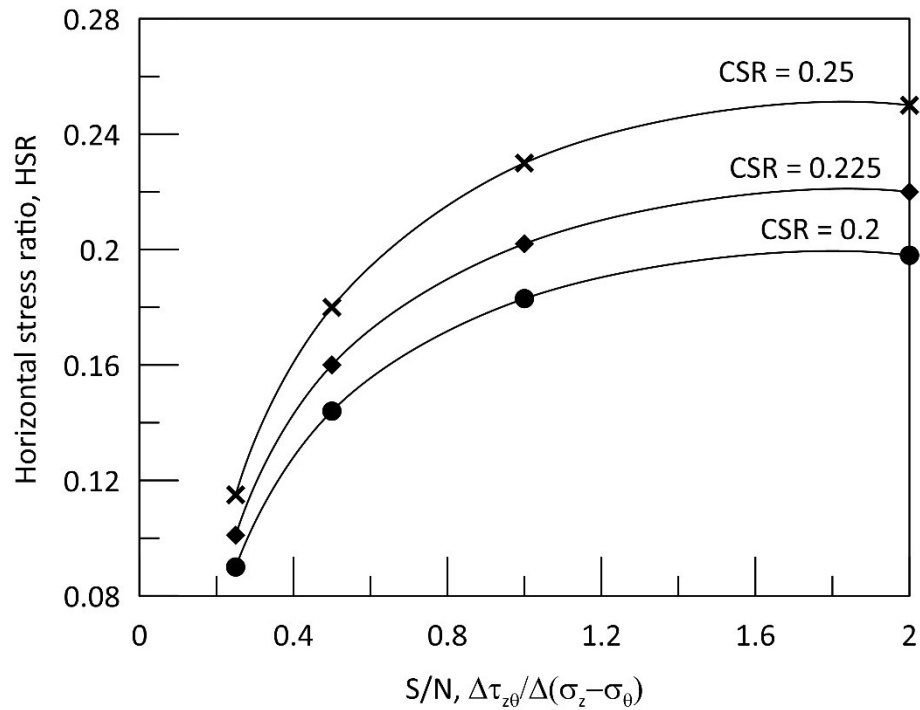


Figure 5.41: HSR variation with H/V for different $CSRs$

Figure 5.42 to 5.45 presents the set of data obtained from the cyclic tests on the Fraser River sand prepared at a relative density of $(D_{rc}) = 36\% \sim 39\%$ and subjected to following test conditions: $\sigma'_{mc} = 100 \text{ kPa}$, $CSR = 0.2$ and $S/N = 0.25, 0.5, 1 \text{ \& } 2$. At this loading condition, the sample is subjected to a maximum stress increments of $\Delta\tau_{z\theta} =$

9, 14.4, 18.3 & 19.8 *kPa* and $\Delta(\sigma_z - \sigma_\theta) = 36, 28.8, 18.3 \text{ \& } 9.9 \text{ kPa}$ for $S/N = 0.25, 0.5, 1 \text{ and } 2$ respectively. Correspondingly the α_σ jump rotates between $+13.3^\circ \text{ \& } -76.7^\circ, +22.5^\circ \text{ \& } -67.5^\circ, +31.7^\circ \text{ \& } -58.3^\circ$ and $+38^\circ \text{ \& } -52^\circ$ respectively. It can be observed that a significantly higher number of loading cycles are required to initiate liquefaction at lower S/N . The liquefaction resistance decreases as the S/N increases from 0.25 to 2. Within a given CSR of 0.2, the sand liquefied in 63 cycles for $S/N = 0.25$ and 20 cycles for $S/N = 2$. A maximum excess pore water pressure almost equaling the initial effective confining stress was generated in the all these tests. Liquefaction is predominantly manifested due to the development of cyclic mobility except at $S/N = 0.25$ where sand exhibits limited liquefaction prior to cyclic mobility.

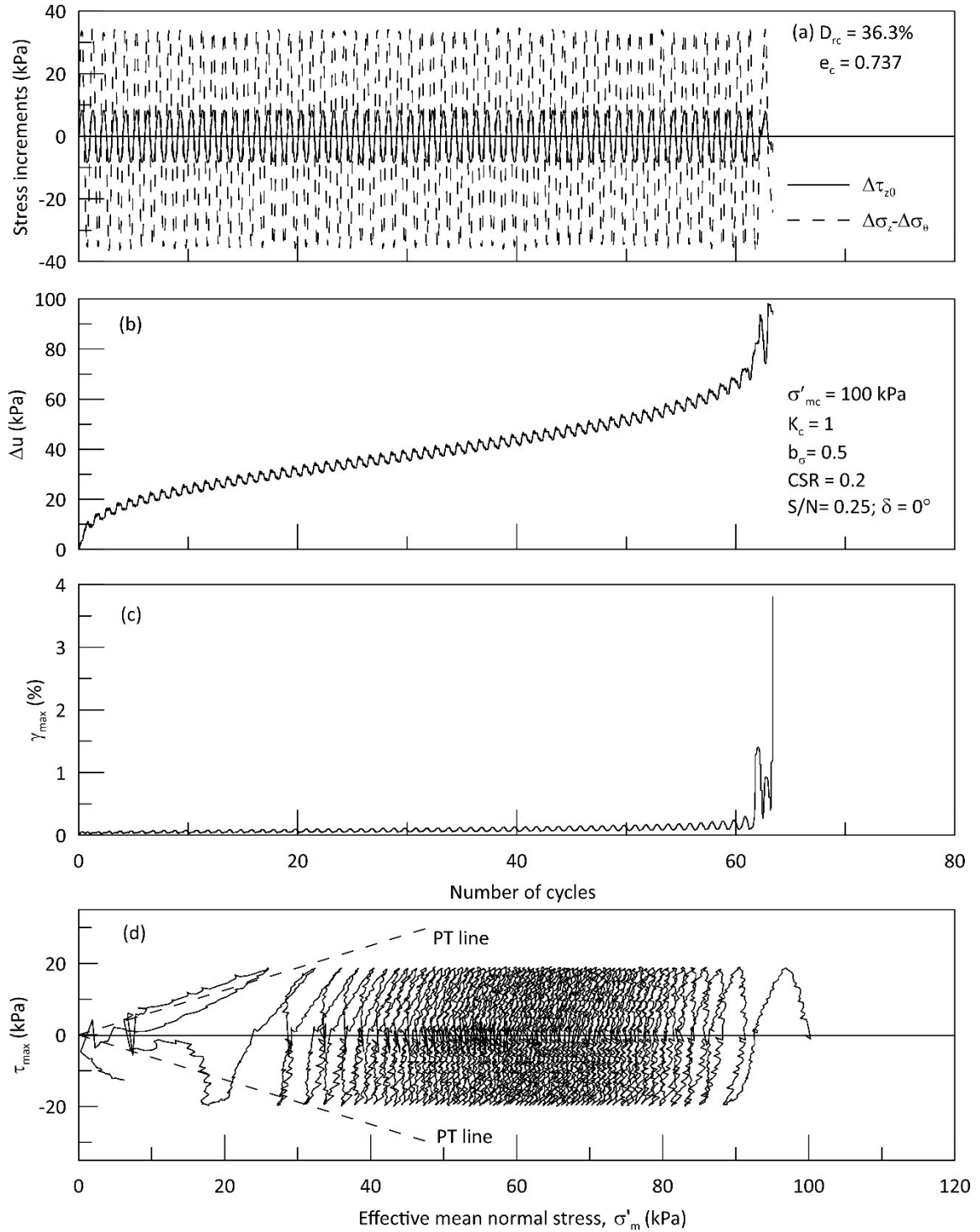


Figure 5.42: Cyclic response of loose Fraser River sand at $CSR = 0.2$ & $S/N = 0.25$

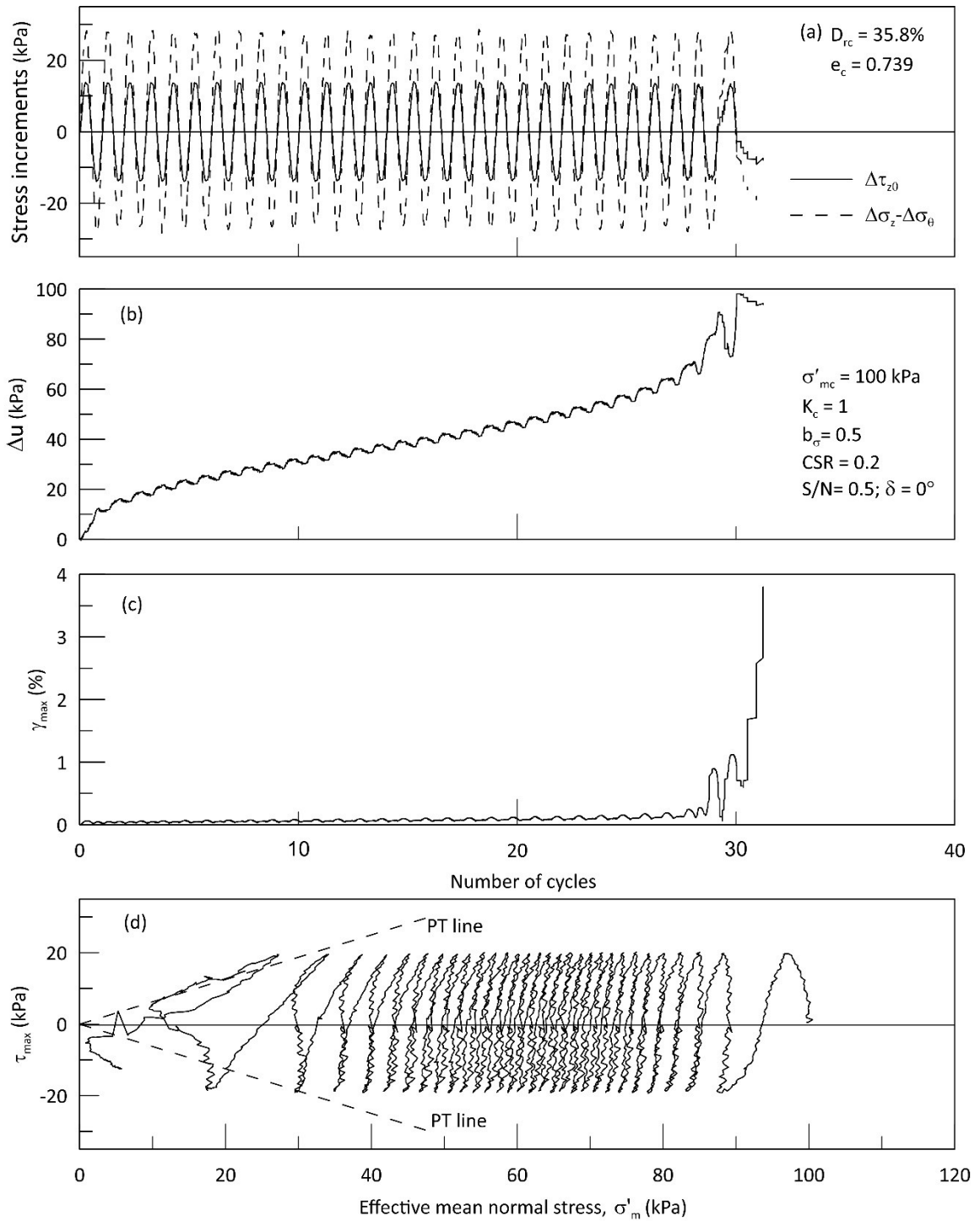


Figure 5.43: Cyclic response of loose Fraser River sand at $CSR = 0.2$ & $S/N = 0.5$

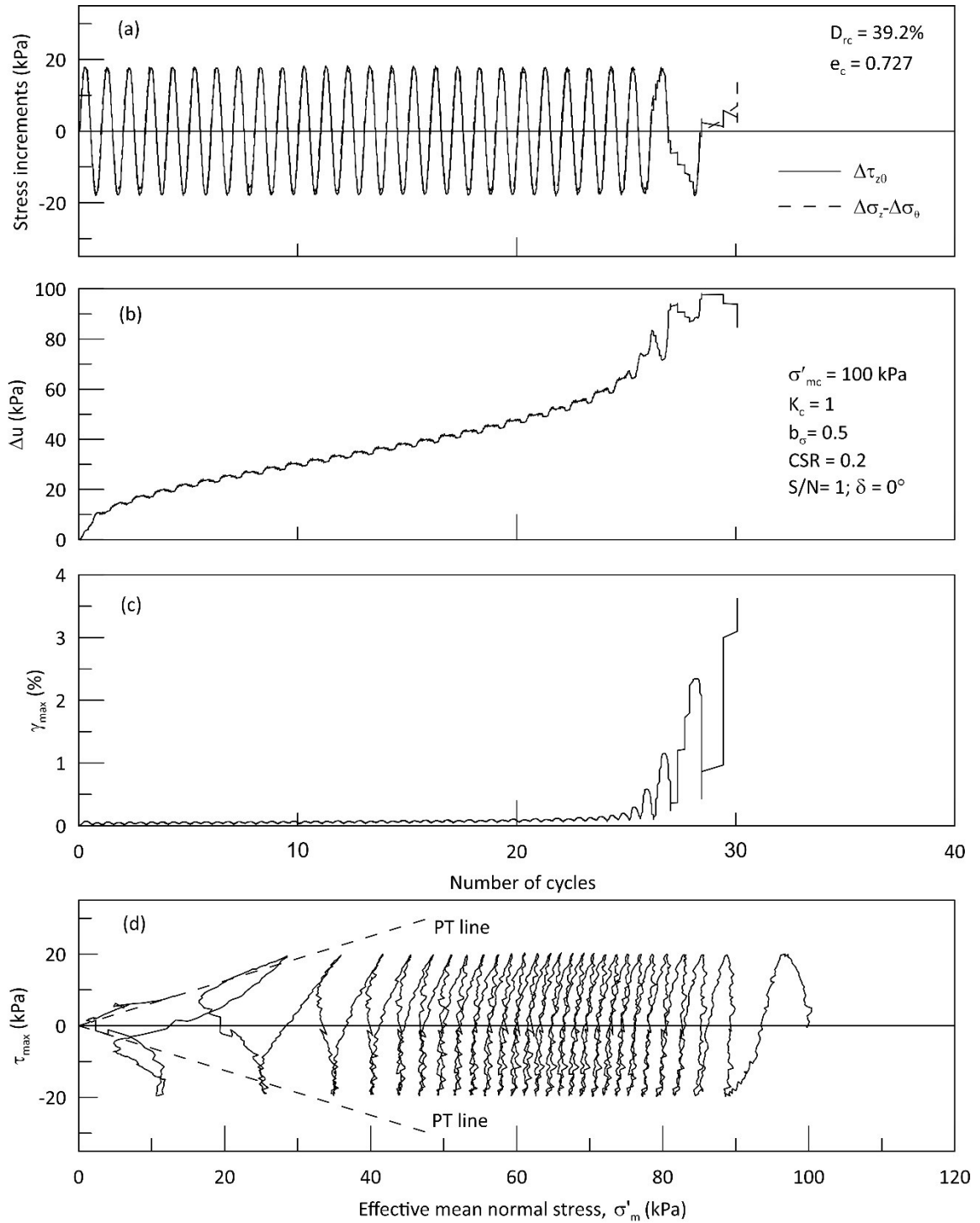


Figure 5.44: Cyclic response of loose Fraser River sand at $CSR = 0.2$ & $S/N = 1$

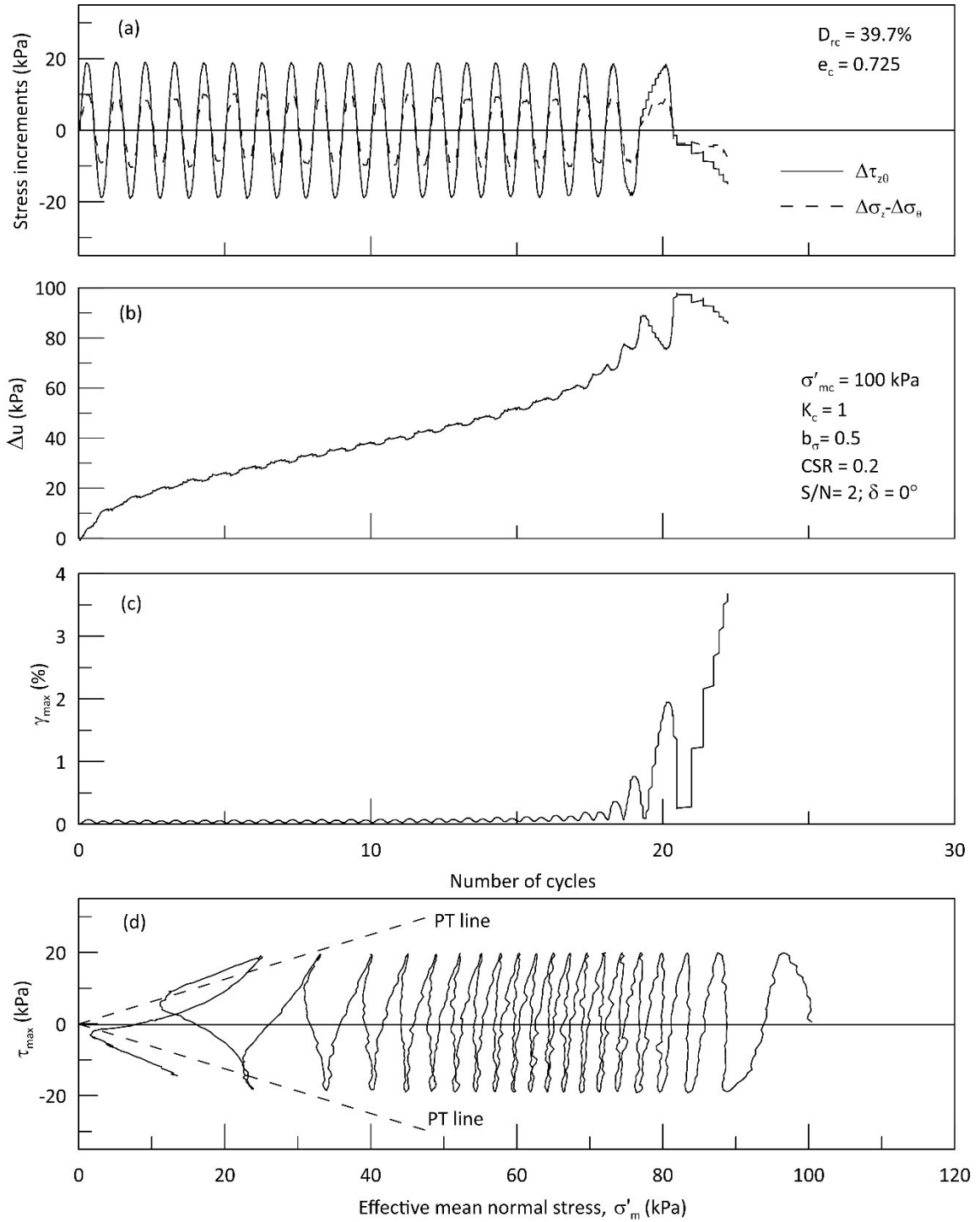


Figure 5.45: Cyclic response of loose Fraser River sand at $CSR = 0.2$ & $S/N = 2$

Figure 5.46 and 5.47 compares the pore pressure and shear strain accumulation of sand subjected to cyclic loading with various S/N at two different CSR s and σ'_{mc} . It can be noticed that there is a steep increase in the rate of pore pressure and shear strain development as the S/N increased from 0.25 to 0.5 and beyond of S/N of 0.5, still the rate of pore pressure and shear strain accumulation increases with S/N but not in a steep rate when compared to the previous case. This similar trend of pore pressure and shear strain accumulation is observed for all the cases considered in this study ($\sigma'_{mc} = 100 \text{ kPa}, 200 \text{ kPa}; CSR = 0.2, 0.225 \text{ and } 0.25$).

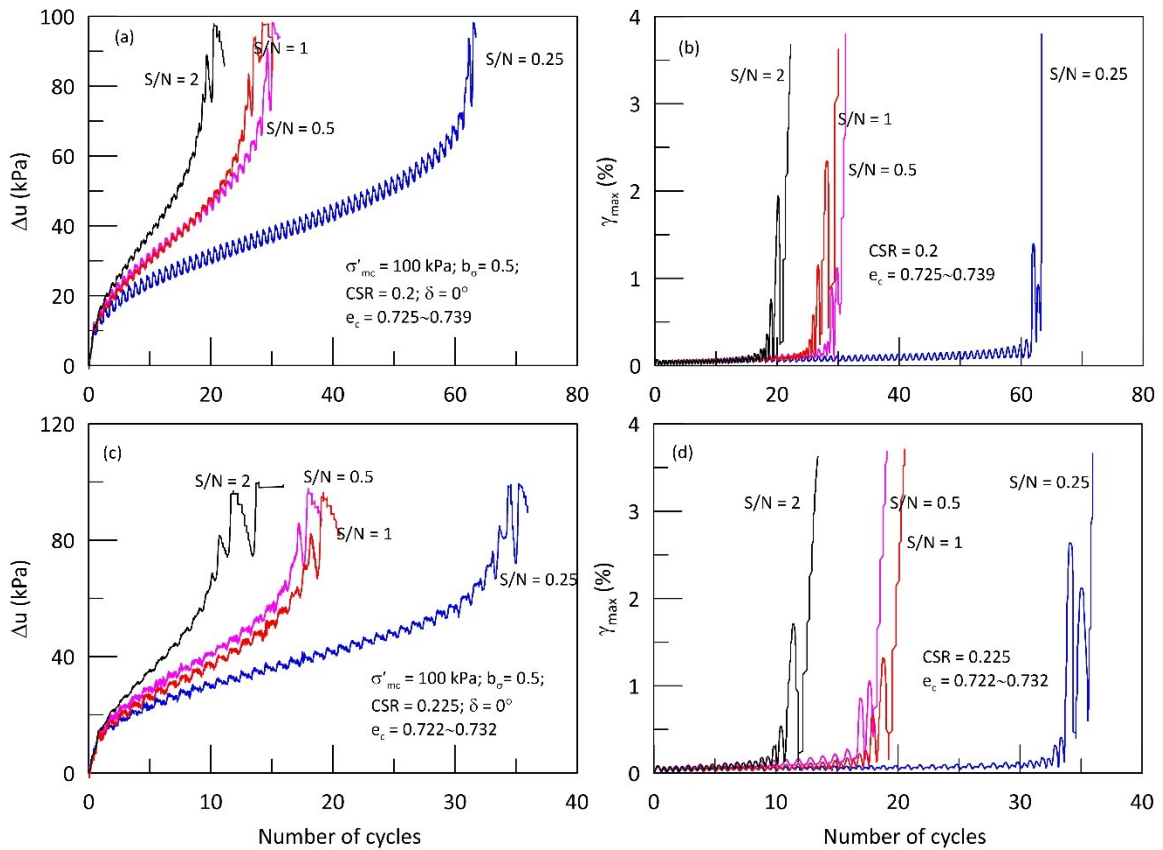


Figure 5.46: Excess pore pressure and shear strain development at various S/N for $\sigma'_{mc} = 100 \text{ kPa}$

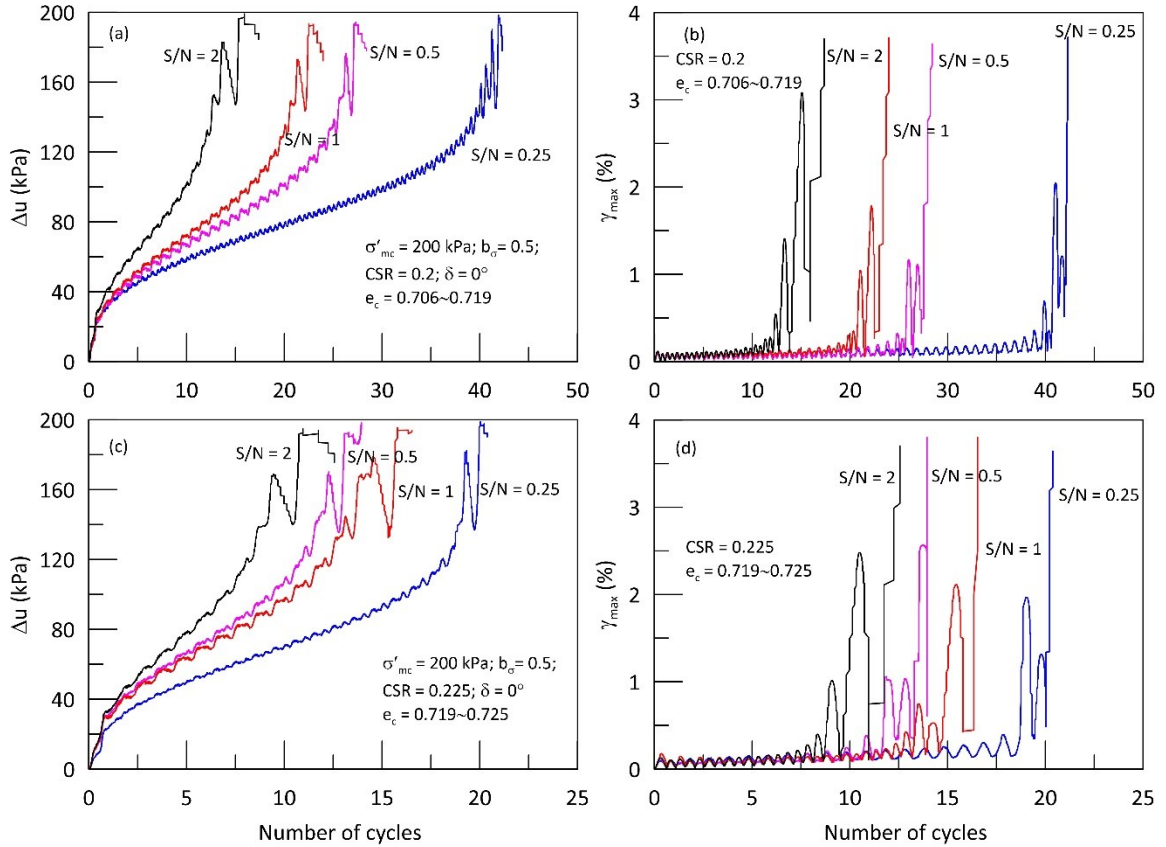


Figure 5.47: Excess pore pressure and shear strain development at various S/N for $\sigma'_{mc} = 200 \text{ kPa}$

Figure 5.48 and 5.49 shows the variation of all normal and shear strain components for coupled loading under different S/N . At $S/N = 0.25$, the contribution of normal strain components ($\epsilon_z, \epsilon_\theta$ and ϵ_r) towards the maximum shear strain (γ_{max}) is more when compared to the shear strain component ($\gamma_{z\theta}$). As the S/N increases, $\gamma_{z\theta}$ contributes more towards γ_{max} when compared with $\epsilon_z, \epsilon_\theta$ and ϵ_r . This observation holds true for all CSR s and initial σ'_{mc} considered in this investigation. This implies that when the individual normal stress increments is greater than the shear stress increment ($|\Delta\tau_{z\theta}| < |\Delta\sigma_z| = |\Delta\sigma_\theta|$), the normal strain components governs the soil liquefaction whereas when shear stress increment greater than or equal to the individual normal stress increment ($|\Delta\tau_{z\theta}| \geq |\Delta\sigma_z| = |\Delta\sigma_\theta|$), the shear strain component is responsible for the development of large

deformations. The accumulation of both normal and shear strain components was limited until the excess pore water pressure generated reaches 65% of the initial σ'_{mc} .

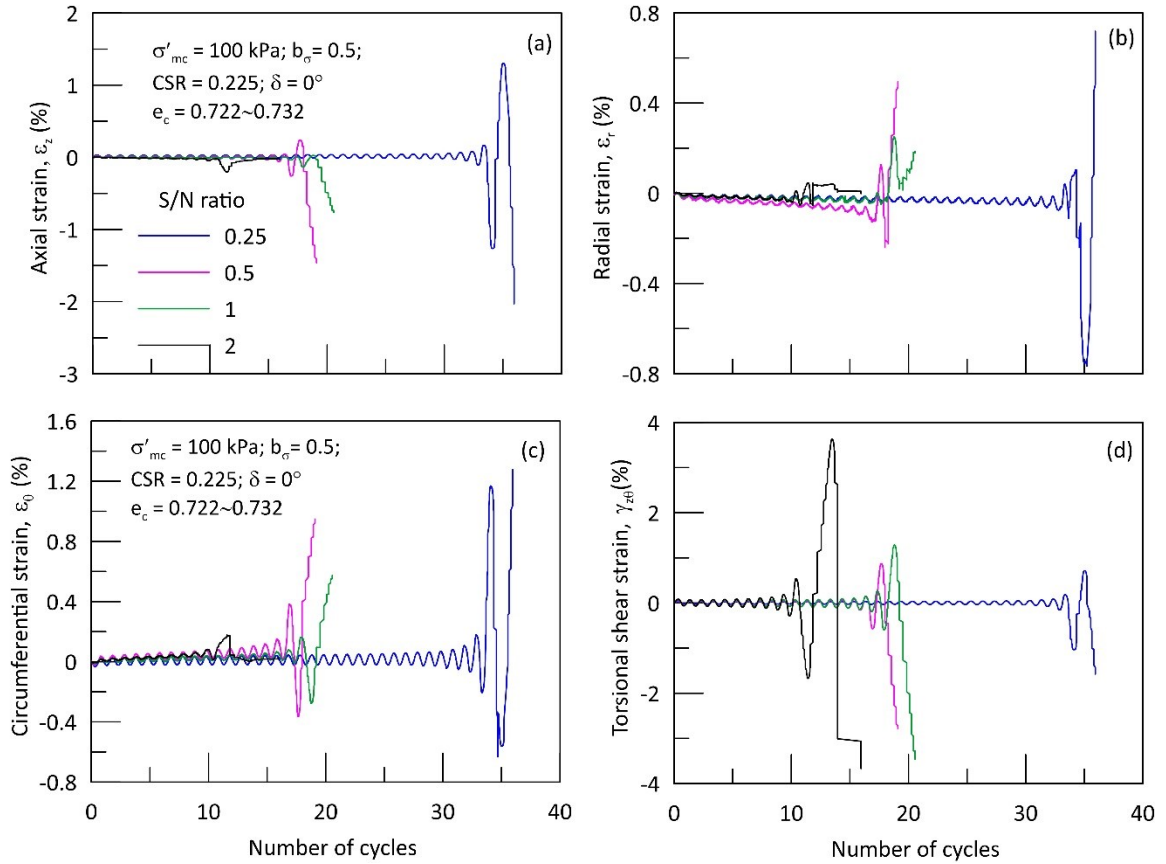


Figure 5.48: Normal and shear strain development at various S/N for $\sigma'_{mc} = 100 \text{ kPa}$

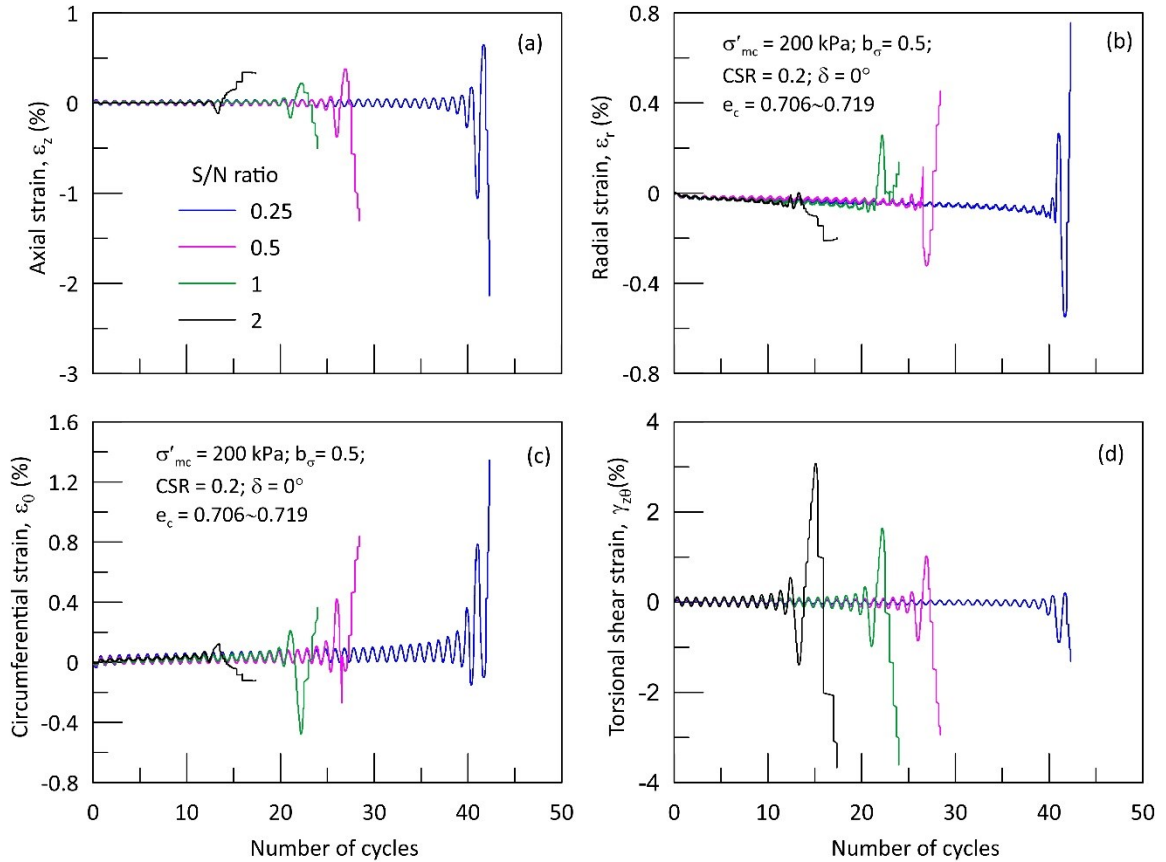


Figure 5.49: Normal and shear strain development at various S/N for $\sigma'_{mc} = 200 \text{ kPa}$.

Figure 5.50 and 5.51 shows the variation of the number of cycles to liquefaction as a function of S/N . In general, at a given CSR , the number of cycles to liquefaction decreases with the increase in S/N . This reduction in liquefaction resistance of sand clearly demonstrates the influence of various degrees of simultaneous propagation of compression and shear waves on the cyclic response of sand. Increasing S/N from 0.25 to 0.5 drastically reduces the cyclic resistance of sand. At lower confining pressure of $\sigma'_{mc} = 100 \text{ kPa}$ there is almost 50% reduction in the cyclic resistance as the S/N increased from 0.25 to 0.5 and almost 35% reduction is noted for $\sigma'_{mc} = 200 \text{ kPa}$. For $S/N > 0.5$, the rate of reduction in the liquefaction resistance decreases with the increase in S/N and the trend of variation tends to be asymptotic with S/N axis for about $S/N > 1.6$. The decrease in the

cyclic resistance of sand with the increase in S/N is primarily due to the coupled action of increase in shear stress on the weak horizontal bedding plane ($\tau_{z\theta}$) and close alignment of τ_{max} axis with the bedding plane. Beyond S/N of 1.6, as the S/N increases, there is insignificant change in both horizontal shear stress and inclination of τ_{max} axis with the bedding plane, which explains the asymptotic change in the liquefaction resistance at larger S/N .

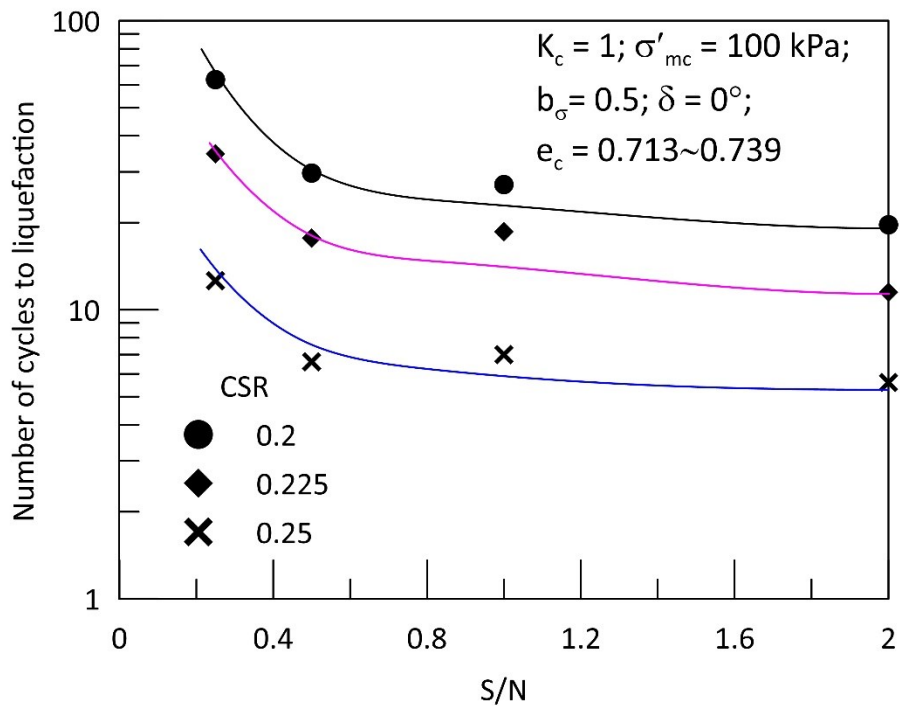


Figure 5.50: Variation of number of cycles to liquefaction with S/N for $\sigma'_{mc} = 100 \text{ kPa}$

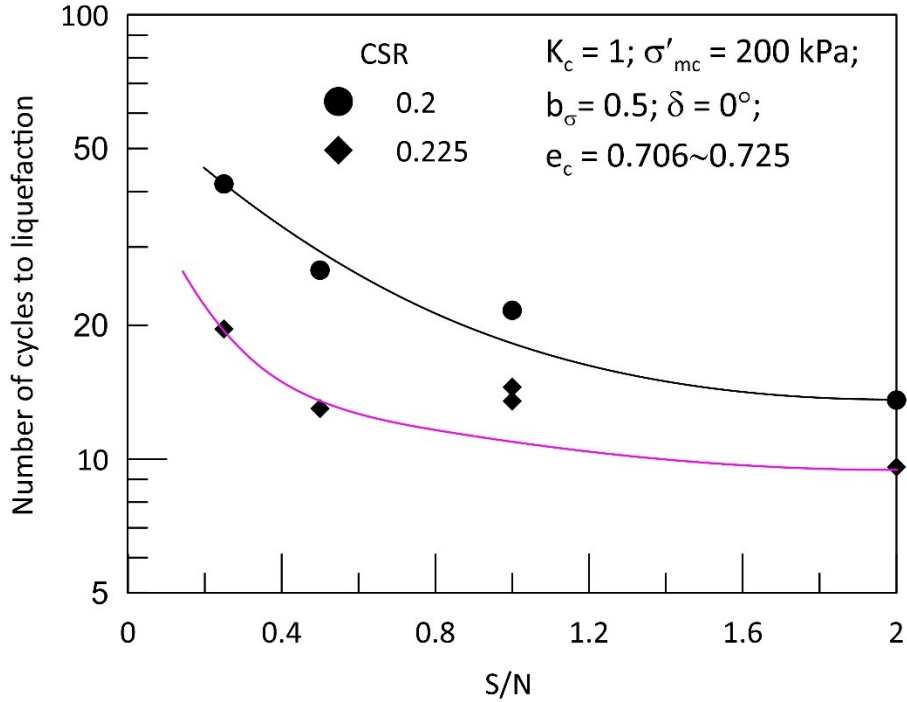


Figure 5.51: Variation of number of cycles to liquefaction with S/N for $\sigma'_{mc} = 200 \text{ kPa}$

The relationship between cyclic stress ratio required to cause liquefaction in 15 cycles versus S/N at two different initial stress levels is shown in Figure 5.52. At a given relative density and confining pressure, CRR decreases with the increase in S/N . For $\sigma'_{mc} = 100 \text{ kPa}$, CRR dropped from 0.25 to about 0.2 for the increase in S/N from 0.25 to 2. This conclusion can be compared with the comparison of liquefaction resistance of Fraser River sand under cyclic triaxial and cyclic simple shear condition reported by Vaid and Sivathayalan (1996a). It is reported that at a given density and confining stress level the cyclic resistance ratio tends to be smaller under simple shear than under triaxial loading condition. Here S/N represents the various degrees of coupled triaxial and simple shear loading condition. Tests with smaller S/N can represent triaxial condition whereas tests with larger S/N can represent simple shear loading condition. Therefore, the reduction in the CRR with respect to the increase in S/N is justifiable. Figure 5.53 shows the variation

of K_σ with the normalized effective mean normal stress for all the cases of S/N . Except at $S/N = 0.25$, the K_σ for all other S/N is just less than about 5 to 7% from unity. Therefore, it can be concluded that regardless of the coupled loading condition, the K_σ stays close to unity for loose sands.

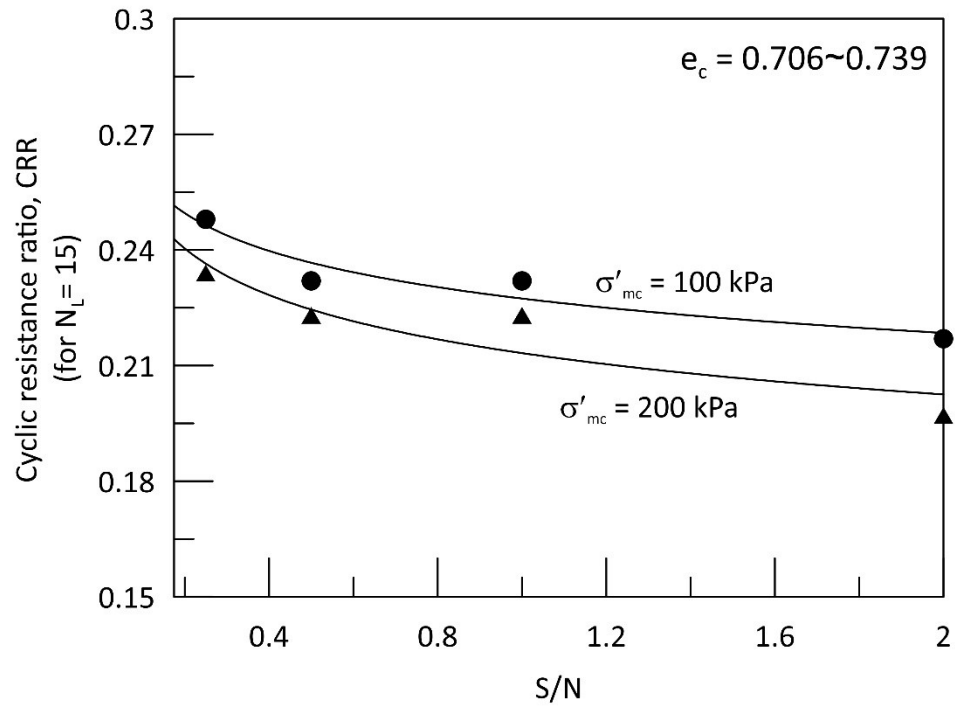


Figure 5.52: Variation of CRR with S/N

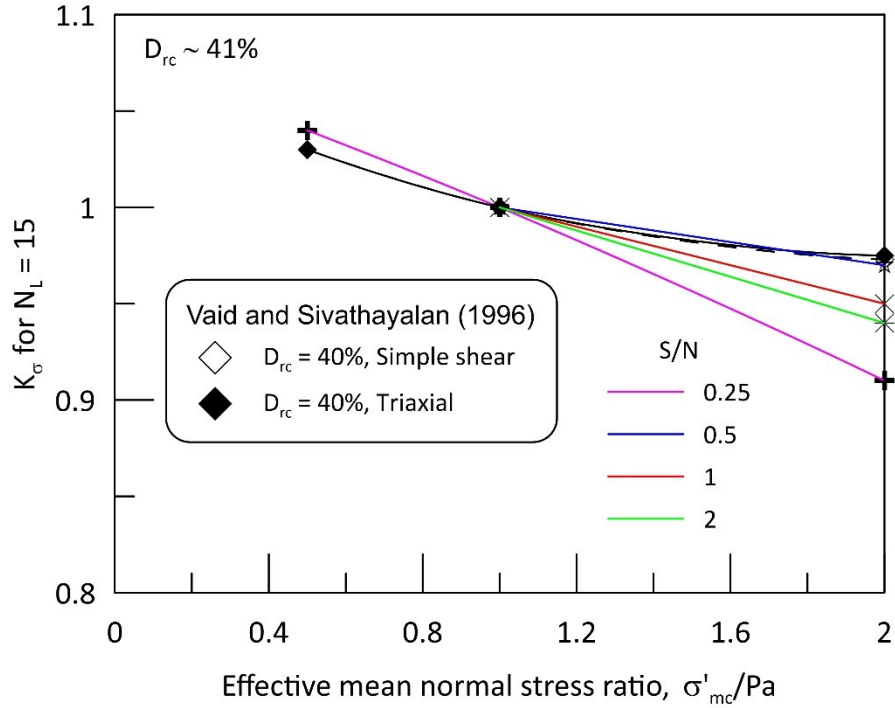


Figure 5.53: Variation of K_σ at different S/N

From this present study it is shown that the coupled loading under an isotropically consolidated stress state results in an unsymmetrical jump rotation of the principal stress axes (α_σ). Logeswaran (2010) and Sivathayalan et al. (2015) performed cyclic tests exclusively to study the effect of symmetrical jump rotation of α_σ on the cyclic resistance of sand. The HSR and S/N from these test series were back calculated and compared with the present study (Figure 5.54). The plot shows that even with symmetrical jump rotation of α_σ the trend of HSR versus S/N is almost identical to the trend adopted in this study. The only difference lies in the method of load application, in this study the normal and shear stress components were varied sinusoidally and α_σ is deduced based on the applied loads whereas in Logeswaran (2010) the normal and shear stresses varied as a one-way sine wave to achieve the targeted changes in the α_σ . The effect of symmetrical jump rotation of α_σ of $\pm 15^\circ$, $\pm 30^\circ$ and $\pm 45^\circ$ on the liquefaction resistance of Fraser River

sand was considered by Logeswaran (2010), and such a symmetrical jump of α_σ may not be possible in the real field scenario.

Figure 5.55 compares the number of cycles to liquefaction versus S/N from the present study and Logeswaran (2010) for cyclic test carried out at a constant CSR of 0.2. Though the comparison shown in the figure was based on cyclic tests with different loading conditions, but it explicitly demonstrates the influence of S/N on the cyclic response. The two important observation to be noted in this figure is the difference in the cyclic resistance of sand at the same level of S/N i.e., at 0.25 and 1. At $S/N \approx 0.25$, higher cyclic resistance is reported by Logeswaran (2010) when compared to the current investigation because in Logeswaran (2010) at this S/N the range of rotation $\alpha_{\sigma,range}$ is only 30° ($-15^\circ \leftrightarrow +15^\circ$) whereas it is 90° ($+13.3^\circ \leftrightarrow -76.7^\circ$) in this study. Moreover, in this study at $S/N = 0.25$, the direction of major principal stress aligns closely with the weak bedding plane in the second half of the loading which reduces the cyclic resistance of the sand. This shows the significance of the range of rotation in the cyclic response of sand. On the other hand, at $S/N = 1$, though the range of rotation is same i.e., $\alpha_{\sigma,range} = 90^\circ$, in both the studies, Logeswaran (2010) exhibited weak resistance even with $b_\sigma = 0$ because here α_σ rotates between ($-45^\circ \leftrightarrow +45^\circ$) against ($+31.7^\circ \leftrightarrow -58.3^\circ$) in this current study. In cyclic test with $\alpha_\sigma = -45^\circ \leftrightarrow +45^\circ$, the plane of maximum shear stress aligns with the bedding plane throughout the cyclic loading which causes the weak liquefaction resistance. This demonstrates the importance of the range of principal stress rotation and degree of rotation in evaluating the liquefaction potential of soil under cyclic shaking which needs to properly be accounted in the design practice.

Therefore, it is evident from these investigations that even within a given CSR , the variation of S/N and α_σ would give a different cyclic response. Hence, the traditional method of defining CSR based on the maximum shear stress will not be applicable in all the cases and it calls for devising a new method of defining cyclic resistance by considering the three-dimensional loading for practical applications.

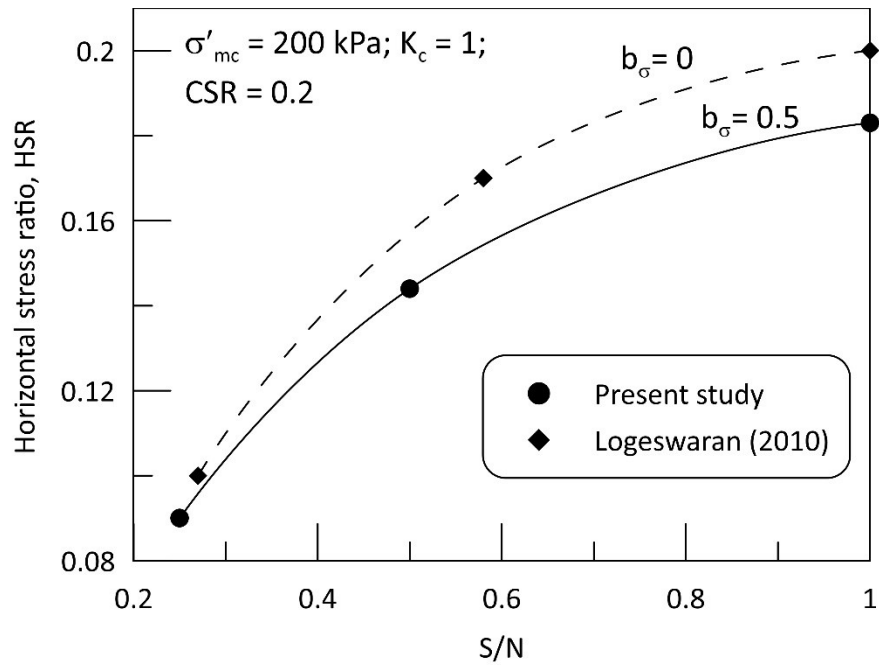


Figure 5.54: Comparison of HSR variation with S/N

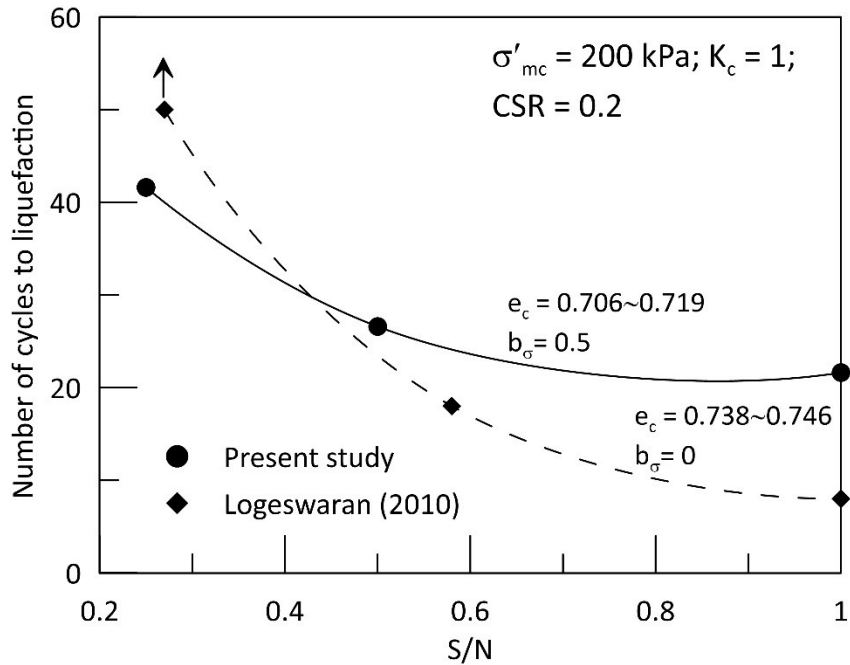


Figure 5.55: Comparison of cyclic resistance variation with S/N

5.8 Energy based method of evaluating the liquefaction potential of soil

5.8.1 Background

Several methods have been proposed in the past to evaluate the liquefaction potential of soil. The stress-based method proposed by Seed et al. (1971) is widely adopted in the current engineering practice. In this method, the liquefaction potential of soil is assessed by comparing the undrained cyclic strength of soil with the shear stress induced during an earthquake. Dobry et al. (1981, 1982) highlighted the disadvantages of stress-based method and proposed an alternate approach based on cyclic shear strain to assess the triggering of liquefaction. In cyclic shear strain approach the threshold shear strain required to trigger soil liquefaction in a specified number of loading cycles is compared with the equivalent shear strain induced by an earthquake. These two methods require the selection of equivalent uniform shear stress or shear strain and equivalent number of loading cycles to

evaluate the liquefaction potential of soil in laboratory. Moreover, these methods mainly focused only on the effect of vertically propagating shear waves and ignores the effect of principal stress rotation. However, in reality, the earthquake waves are so complex which involves the simultaneous propagation of compression and shear waves. As demonstrated earlier this coupled loading condition results in a complex rotation of principal stress axes. Incorporating all these factors on the cyclic strength complicates the simplified procedure and makes it difficult for practical use.

Alternatively, several researchers suggested the use of energy-based methods to evaluate soil liquefaction (Nasser and Shokooh 1979; Davis and Berrill 1982; Berrill and Davis 1985; Towhata and Ishihara 1985; Law et al. 1990; Figueroa et al. 1994; Liang et al. 1995; Dief and Figueroa 2007; Kokusho 2013; Kokusho and Kaneko 2018). Towhata and Ishihara (1985) through a series of undrained cyclic tests on Toyoura sand using a hollow cylinder torsional shear apparatus established that a unique relationship exists between the dissipated strain energy and excess pore water pressure which is independent of the applied shear stress paths. Law et al. (1990) also confirmed the existence of this unique functional relationship between strain energy and pore water pressure through cyclic triaxial and cyclic simple shear testing of Fujian sand. A criterion for defining the liquefaction potential at the site was developed by combining this functional relationship with the energy attenuation equation. Figueroa et al. (1994); Liang et al. (1995); Dief and Figueroa (2007) and Jafarian et al. (2012) proposed empirical equations through a series of torsional shear tests and centrifuge tests to determine the dissipated strain energy per unit volume required to liquefy the soil (W_{liq}). The parameters influencing W_{liq} such as relative density (D_{rc}), effective confining pressure (σ'_c), initial static shear stress, loading amplitude and type of

loading is considered for the analysis. It is found that W_{liq} is proportional to D_{rc} , σ'_c , and initial static shear stress but it is independent of loading amplitude and type of loading (uniform or random loading). The undrained torsional shear tests on sand-silt mixtures by Baziar and Sharafi (2011) and Movahed et al. (2011) showed that W_{liq} is affected by the fines content of the soil and it is independent of loading amplitude and loading frequency. Kokusho (2013) developed an energy-based method to evaluate the liquefaction potential of soil by comparing the strain energy required for liquefaction with the upcoming seismic energy and it is shown that the energy based method unlike stress/strain based method intrinsically considers the irregularities in the input seismic motion. Apart from this, several other studies have demonstrated that there exists a unique relationship between pore pressure ratio ($r_u = \Delta u / \sigma'_c$) and normalized dissipated energy per unit volume (W / W_{liq}) which is independent of relative density, fines content, loading amplitude, type of loading (harmonic or irregular) and method of load application (stress or strain controlled) (Polito et al. 2013; Polito and Moldehaeur 2018, 2019). Pore pressure models were developed based on this unique relationship to predict the excess pore water pressure development during cyclic shearing (Green et al. 2000; Polito et al. 2008; Jafarian et al. 2012).

Hence, these studies have established the uniqueness of dissipated energy per unit volume in evaluating the liquefaction potential of soil and also in predicting the pore pressure response during cyclic loading. Another important aspect of energy-based method is that the dissipated strain energy is a scalar quantity which inherently eliminates the dependency of loading direction. Therefore, this following section aims to verify the applicability of energy principles in assessing soil liquefaction under coupled multidirectional loading involving the simultaneous action of normal and shear stresses.

5.8.2 Energy dissipated during cyclic shearing

During cyclic shearing, the soil deforms by rearrangement of soil particles and hence during this deformation process a certain amount of energy will be dissipated. In drained condition, this deformation leads to the development of volumetric strain whereas in undrained condition, this tendency of volume change is transferred from soil grains to pore water which results in the generation of excess pore water pressure. Therefore, in an undrained condition, generation of excess pore water pressure is proportional to the amount of energy dissipated. Usually, the amount of energy dissipated during cyclic shearing is represented by the area of the hysteresis stress-strain loop. In hollow cylinder torsional shear testing, the incremental energy dissipated per unit volume (ΔW) is given by (Towhata and Ishihara 1985):

$$\Delta W = \sigma'_z d\varepsilon_z + \sigma'_\theta d\varepsilon_\theta + \sigma'_r d\varepsilon_r + \tau_{z\theta} d\gamma_{z\theta} \quad (5.5)$$

Where $\sigma'_z, \sigma'_\theta, \& \sigma'_r$ – effective vertical, circumferential and radial stress,

$\tau_{z\theta}$ – shear stress on the horizontal plane,

$d\varepsilon_z, d\varepsilon_\theta, d\varepsilon_r \& d\gamma_{z\theta}$ – incremental vertical, circumferential, radial and shear strain.

This incremental strain energy (ΔW) is then numerically integrated using the trapezoidal rule to obtain the cumulative dissipated energy per unit volume (W).

The variation of dissipated energy per unit volume (W) with the number of cycles for the coupled loading test on Fraser river sand with $CSR = 0.2$ and $S/N = 0.5$ is plotted in Figure 5.56. The dissipated energy gradually increases as the cyclic loading progresses. The energy stays minimum till the excess pore water pressure (Δu) developed in about 65% of the initial effective confining stress (σ'_{mc}) and beyond that it starts to increase

rapidly with the increasing shear strain as the Δu approaches the initial σ'_{mc} . In other words, the energy dissipation in soil is so rapid when the effective stress path approaches the phase transformation line.

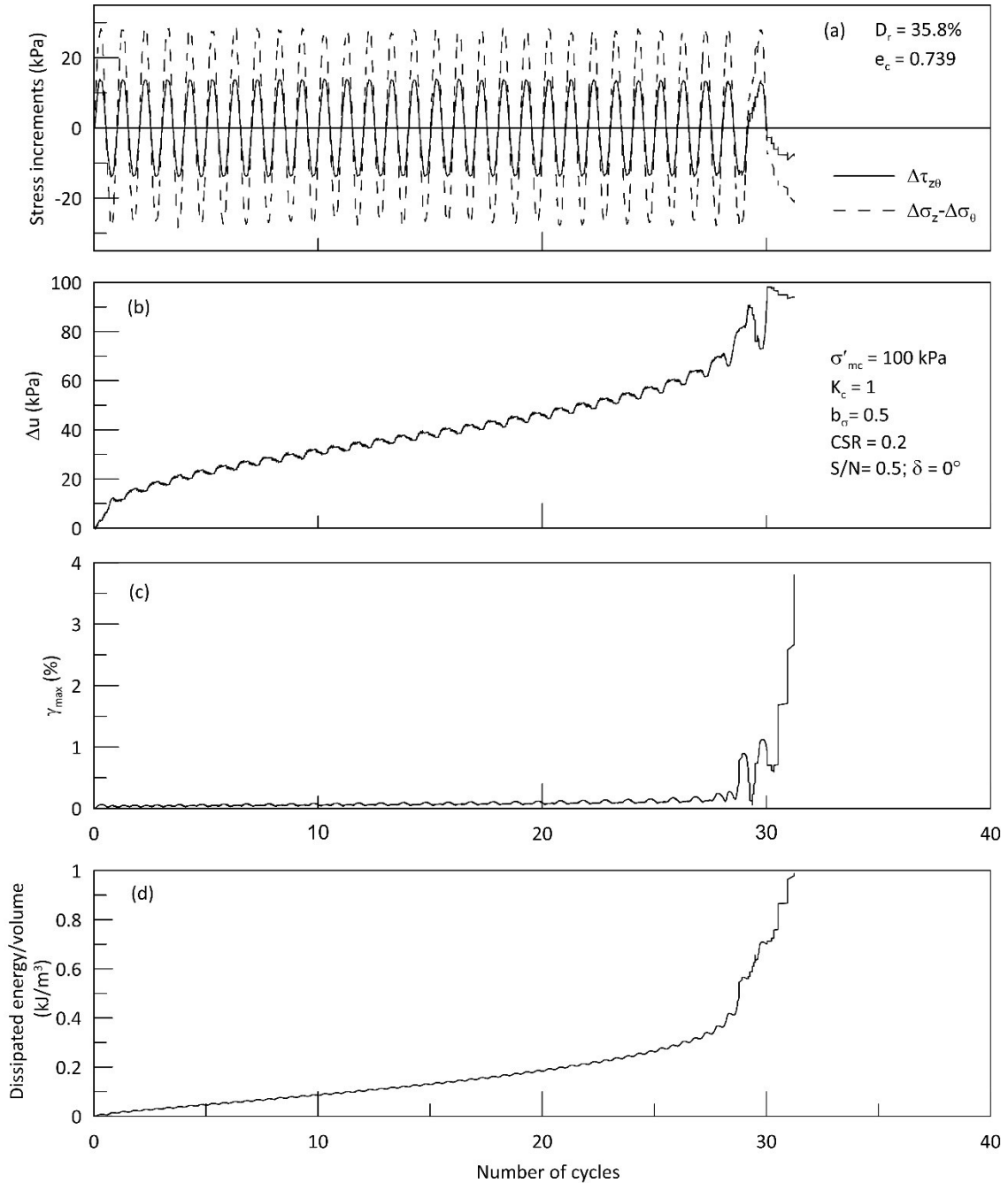


Figure 5.56: Typical variation of dissipated energy per unit volume (W) in a coupled loading test with $CSR = 0.2$ and $S/N = 0.5$

5.8.3 Effects of initial conditions and loading parameters on dissipated energy

The dissipated energy required to cause initial liquefaction (W_{liq}) i.e., W_{liq} required for $r_u = \Delta u / \sigma'_{mc} = 1$ is plotted against initial σ'_{mc} for $CSR = 0.2$ and $S/N = 0.25$ in Figure 5.57. W_{liq} increases almost proportionately with the increase in σ'_{mc} which is consistent with the observation noted by Figueroa et al. (1994) and Dief and Figueroa (2007). The W_{liq} vs σ'_{mc} from this study is also compared with the W_{liq} obtained from the empirical equations proposed by Figueroa et al. (1994), Dief and Figueroa (2007) and Jafarian et al. (2012). These empirical equations for estimating W_{liq} for different types of isotropically consolidated sands are reproduced below:

$$\log_{10} W_{liq} = 2.002 + 0.00477 \sigma'_{mc} + 0.0116 D_{rc}$$

For Reid Bedford sand (Figueroa et al. 1994) (5.6)

$$\log_{10} W_{liq} = 1.371 + 0.005975 \sigma'_{mc} + 0.02067 D_{rc}$$

For Nevada sand (Dief and Figueroa 2007) (5.7)

$$W_{liq} = 136.3 \sigma'_{mc} (D_{rc}/100)^{4.925} + 5.375 \sigma'_{mc}$$

For Toyoura sand (Jafarian et al. 2012) (5.8)

Where W_{liq} in J/m^3 ; D_{rc} in % and σ'_{mc} in kPa.

From Figure 5.57 it can be noticed that W_{liq} obtained from the coupled loading on isotropically consolidated Fraser River sand almost closely matches with the W_{liq} obtained from the empirical equation proposed for Reid Bedford sand. This close agreement is due to the similarity in gradation and mean particle size (D_{50}) of Reid Bedford sand ($D_{50} = 0.26$) considered in Figueroa et al. (1994) with the Fraser River sand ($D_{50} = 0.27$) considered in this study. The comparison of gradation curves between these two sands are presented in Figure 5.58. The trend of W_{liq} vs σ'_{mc} for Nevada sand ($D_{50} = 0.15$) and

Toyoura sand ($D_{50} = 0.20$) shows a considerable deviation from the Fraser River sand because, the mean particle sizes of these sands are quite different from each other. Hence, this clearly demonstrates the influence of mean particle size in affecting the dissipated energy required to cause liquefaction of soils.

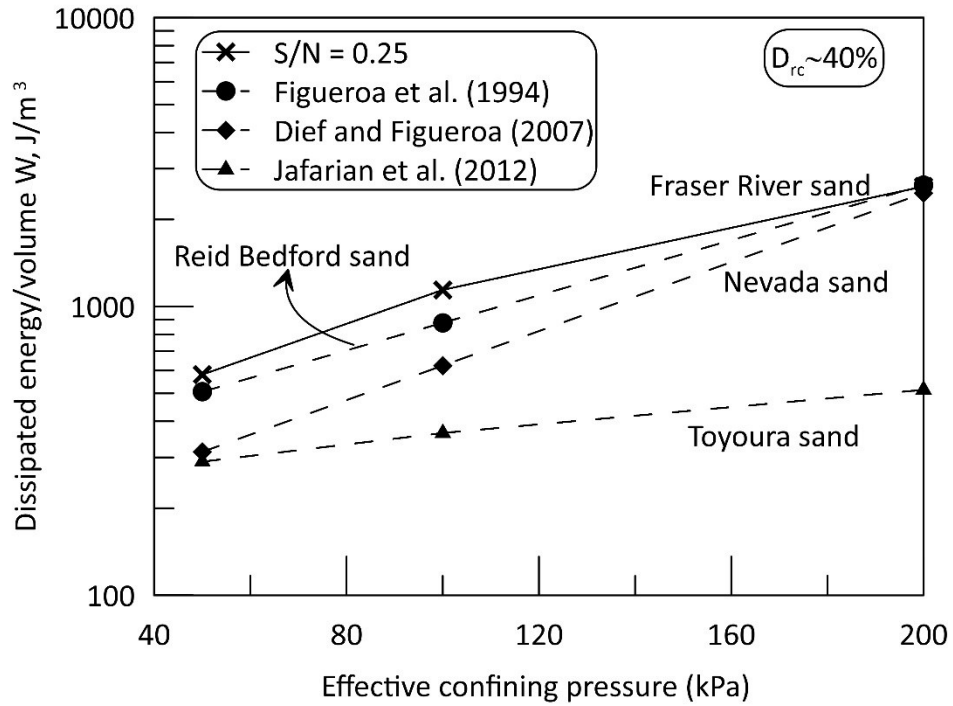


Figure 5.57: Variation of dissipated energy at liquefaction with confining pressure

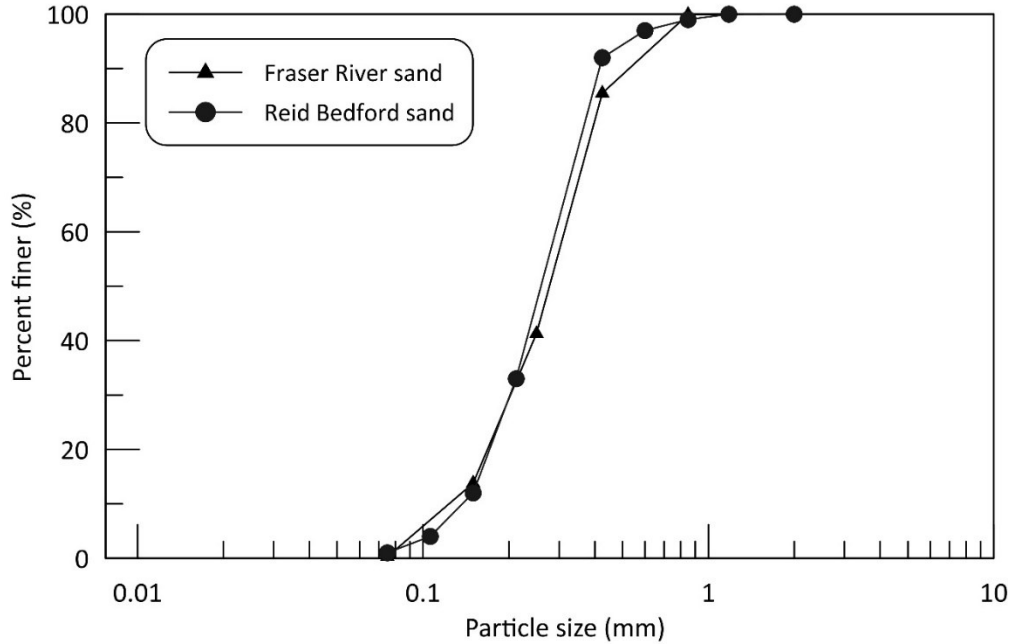


Figure 5.58: Gradation curves of Fraser River sand and Reid Bedford sand

W_{liq} required for $r_u = 1$ and $\gamma_{max} = 3.75\%$ versus cyclic stress ratio, CSR for all σ'_{mc} and $S/N = 0.25$ is plotted in Figure 5.59 and 5.60 respectively. For a given σ'_{mc} and S/N there is no systematic or significant change noted in the variation of W_{liq} with respect to CSR . Kokusho (2013) suggested that for loose sand, the non-systematic variation in dissipated energy with respect to loading amplitude can be judged to be essentially flat. Moreover, several studies reported that a deviation of about $\pm 400 J/m^3$ in W_{liq} can be deemed to be insignificant (Figuroa et al. 1994; Liang et al. 1995; Kokusho 2013). Hence it can be concluded that the W_{liq} is independent of the applied cyclic stress amplitude. This independency of W_{liq} with loading amplitude is consistent with the experimental and numerical findings reported in Figuroa et al. (1994), Baziar and Sharafi (2011), and Olgun and Kamalzare (2017).

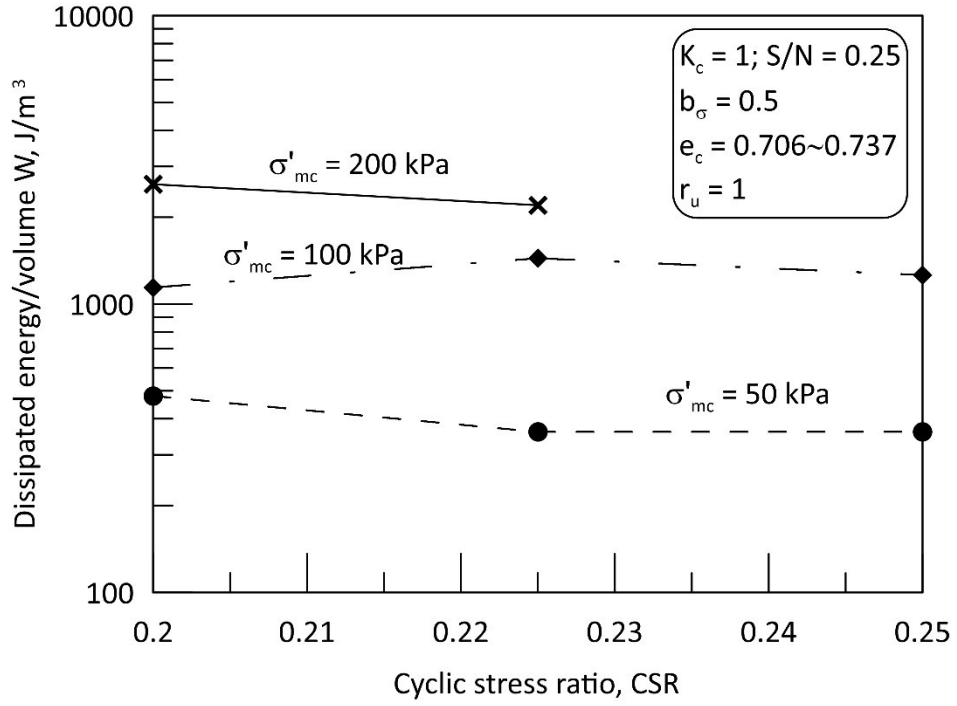


Figure 5.59: Variation of dissipated energy at $r_u = 1$ with CSR

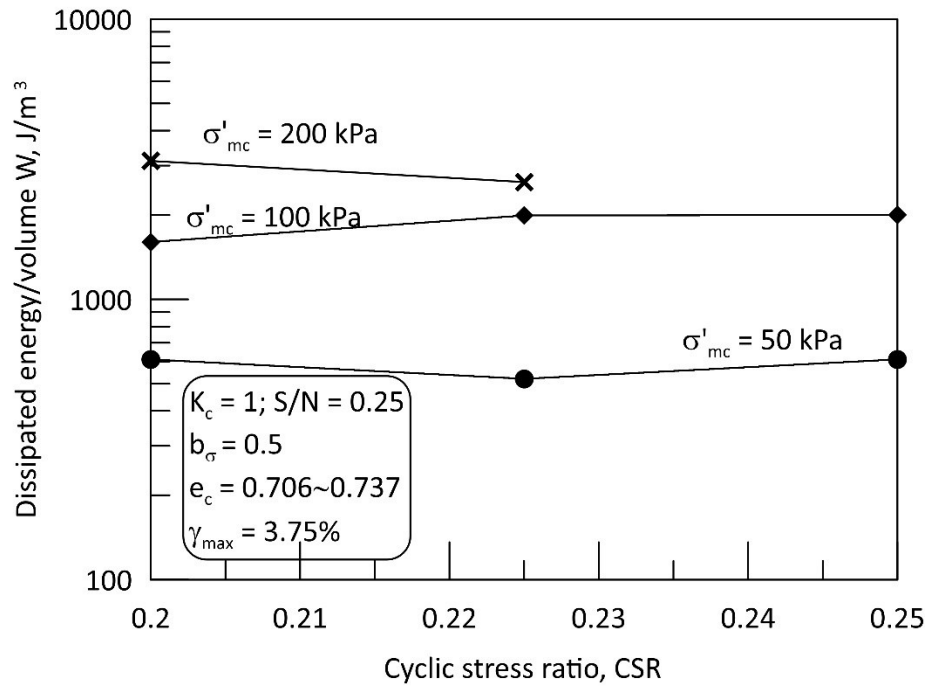


Figure 5.60: Variation of dissipated energy at $\gamma_{max} = 3.75\%$ with CSR

Figure 5.61 shows the variation of W_{liq} required to reach $\gamma_{max} = 3.75\%$ versus S/N for all σ'_{mc} and $CSRs$ considered in this study. It can be noted that irrespective of initial confining stress and CSR , W_{liq} is slightly higher at low S/N of 0.25 and the variation becomes essentially flat for higher values of S/N . Thus, when the magnitude of applied normal stress increments ($|\Delta\sigma_z|, |\Delta\sigma_\theta|$) were higher than the shear stress increments ($|\Delta\tau_{z\theta}|$), higher energy is required to liquefy the soil samples. So far, no studies looked into the aspect of energy variation within a given stress path and given CSR . Therefore, from this study it can be inferred that slightly higher energy will be required to liquefy the soil under triaxial loading mode than the simple shear loading mode since tests with smaller S/N represents triaxial condition and tests with larger S/N represents simple shear loading condition.

Since W_{liq} is shown to increase proportionately with σ'_{mc} (Figure 5.59 to 5.61), the W_{liq} required to reach the liquefying shear strain $\gamma_{max} = 3.75\%$ from the coupled loading tests are normalized with σ'_{mc} and is plotted against S/N in Figure 5.62. This normalized energy ratio (W_{liq}/σ'_{mc}), hereafter referred to as dissipated energy ratio is found to be almost independent of CSR , S/N and σ'_{mc} though a slight increase is noted in $S/N = 0.25$. The S/N also represents change in the degree of principal stress rotation during cyclic shearing. Sinthujan (2013) performed hollow cylinder torsional shear tests on isotropically consolidated Fraser River sand specimens to exclusively study the effect of initial inclination of principal stress axes ($\alpha_{\sigma c}$) and subsequent symmetrical cyclic rotation of principal stress axes ($\alpha_{\sigma, max}$) on the cyclic resistance of sand. The dissipated energy ratio required for $\gamma_{max} = 3.75\%$ is calculated from these tests and it is plotted against amplitude of stress rotation ($\alpha_{\sigma, max}$) in Figure 5.63. It shows that at a given $\alpha_{\sigma c}$, W_{liq}/σ'_{mc}

is almost unaffected by the imposed magnitude of stress rotation ($\alpha_{\sigma,max}$). There is also no systematic change in W_{liq} observed for the change in initial $\alpha_{\sigma c}$ at a given $\alpha_{\sigma,max}$. Though there is some variation noted in the W_{liq} with $\alpha_{\sigma c}$ at lower $\alpha_{\sigma,max}$, which might be attributed to the fluctuation in the relative density of the sample. Therefore, it appears W_{liq} is not significantly affected by the loading amplitude, initial inclination of principal stress axes and magnitude of stress rotation.

Thus, the energy-based method could be a potential alternative to cyclic stress or cyclic strain-based approaches of liquefaction evaluation. Unlike stress-based approach in which the cyclic resistance ratio is affected by S/N , $\alpha_{\sigma c}$ and $\alpha_{\sigma,max}$ (Sinthujan 2013; Sivathayalan et al. 2015), the dissipated energy ratio required for soil liquefaction is almost found to be unique and it is independent of the above mentioned factors. This dissipated energy can be compared with the incoming seismic energy to evaluate the liquefaction potential of soil at a site.

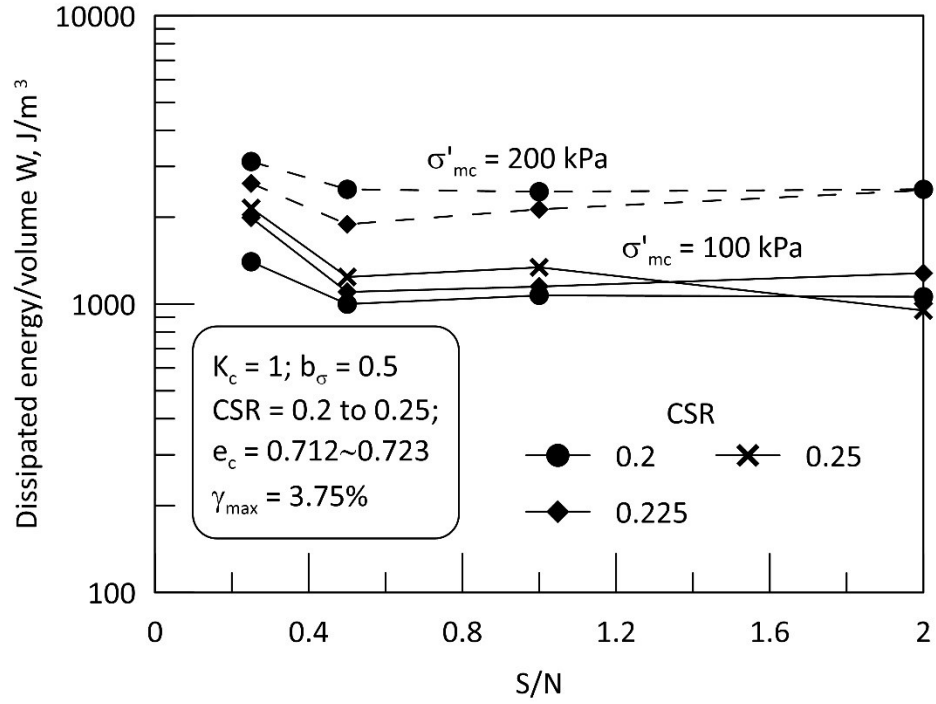


Figure 5.61: Variation of dissipated energy at $\gamma_{max} = 3.75\%$ with S/N

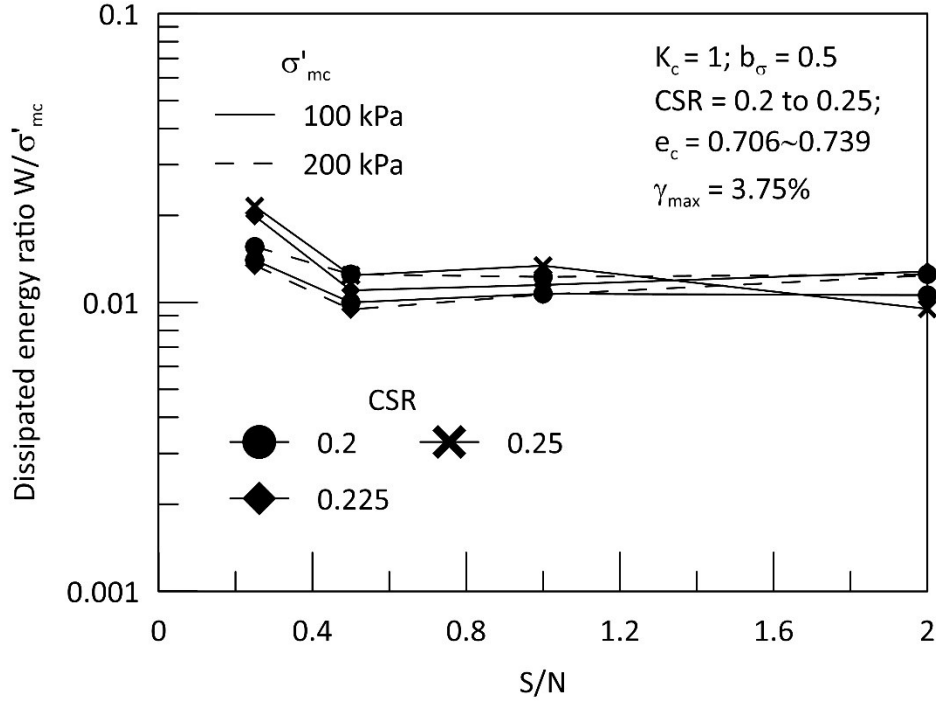


Figure 5.62: Variation of dissipated energy ratio at $\gamma_{max} = 3.75\%$ with S/N

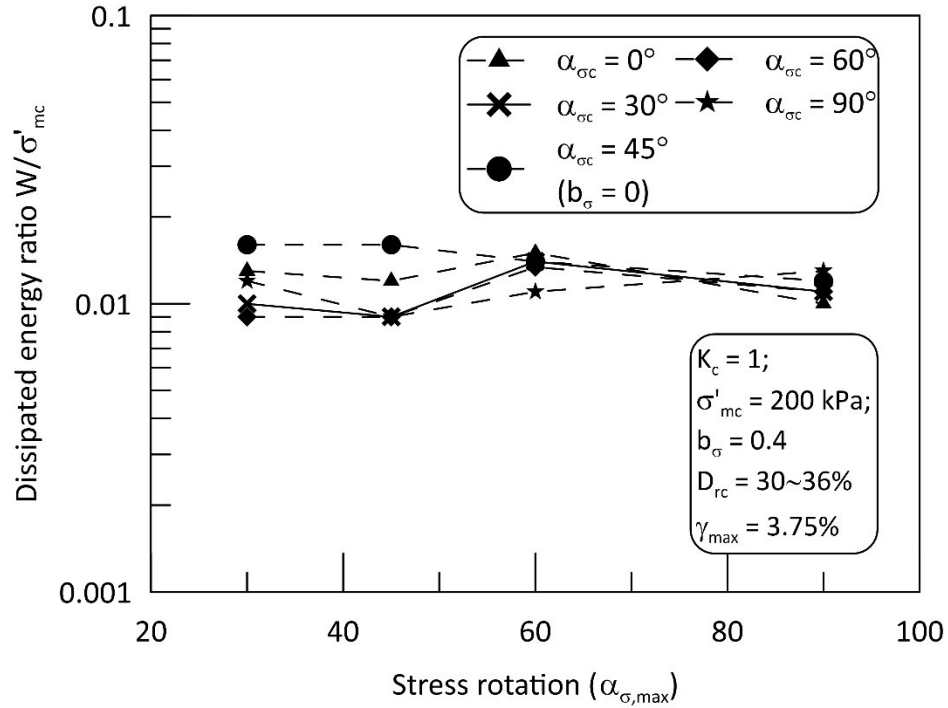


Figure 5.63: Variation of dissipated energy ratio at $\gamma_{max} = 3.75\%$ with different degree of stress rotation.

5.8.4 Pore pressure models

Seed et al. (1976) based on cyclic triaxial and cyclic simple shear tests on different types of sand found that the data of pore pressure ratio (r_u) when plotted against cycle ratio ($r_N = N/N_L$) falls within a narrow band and proposed an empirical correlation to estimate the pore pressure buildup during cyclic shearing for practical design purposes. On a similar note, the pore pressure ratio obtained from the coupled loading tests on isotropically consolidated Fraser River sand is plotted against cycle ratio in Figure 5.63. It can be noticed that irrespective of initial σ'_{mc} , CSR , and S/N , a unique correlation exists between r_u and r_N . The empirical correlation proposed by Seed et al. (1976) to predict excess pore water pressure generation is also plotted in Figure 5.64 and the correlation reported is given below:

$$r_u = 1/2 + 1/\pi \sin^{-1}(2r_N^{1/\alpha} - 1) \quad (5.9)$$

Where α is the calibration parameter.

Even though Eq. (5.9) gives a reasonable estimate of excess porewater pressure, it can be noticed that consistently at lower cycle ratio ($r_N < 0.5$) the average curve from Eq. (5.9) underestimates r_u and at $r_N > 0.5$, it over estimates r_u under generalized loading condition involving principal stress rotation. Hence, in this study based on the average r_u vs r_n curve obtained from the test results a polynomial fit is obtained to predict r_u precisely under generalized cyclic loading. Figure 5.65 presents the polynomial fit obtained from this study along with the upper, average, and lower bound curves obtained from Seed et al. (1976). The obtained polynomial fit is a quintic equation with coefficient of determination $R^2 = 0.9955$ which is given as follows:

$$r_u = 18.5 r_N^5 - 43.4 r_N^4 + 37.6 r_N^3 - 14.7 r_N^2 + 3 r_N + 0.0057 \quad (5.10)$$

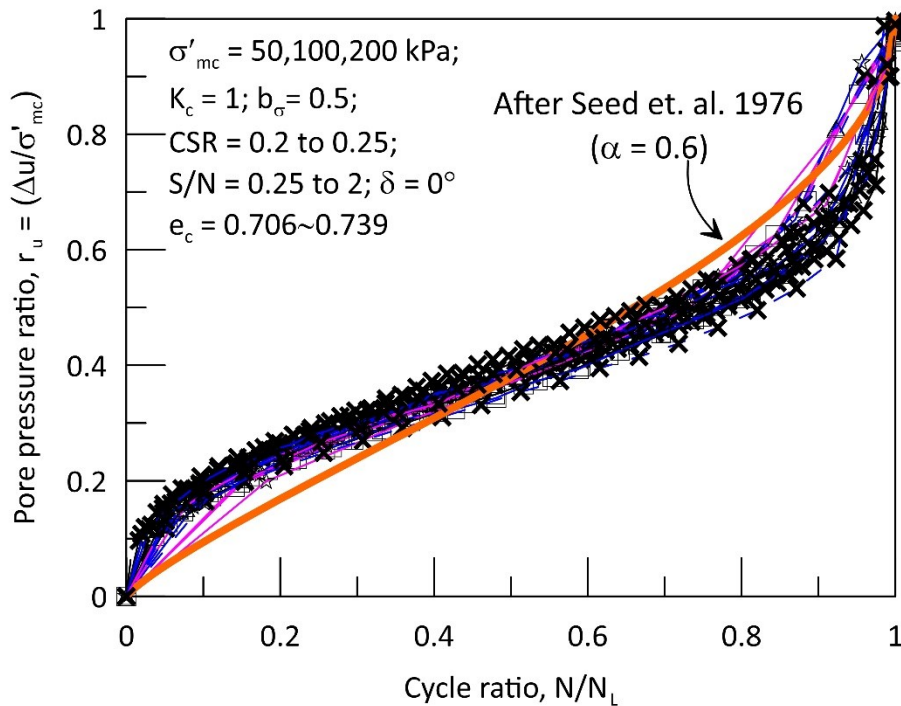


Figure 5.64: Variation of pore pressure ratio with cycle ratio

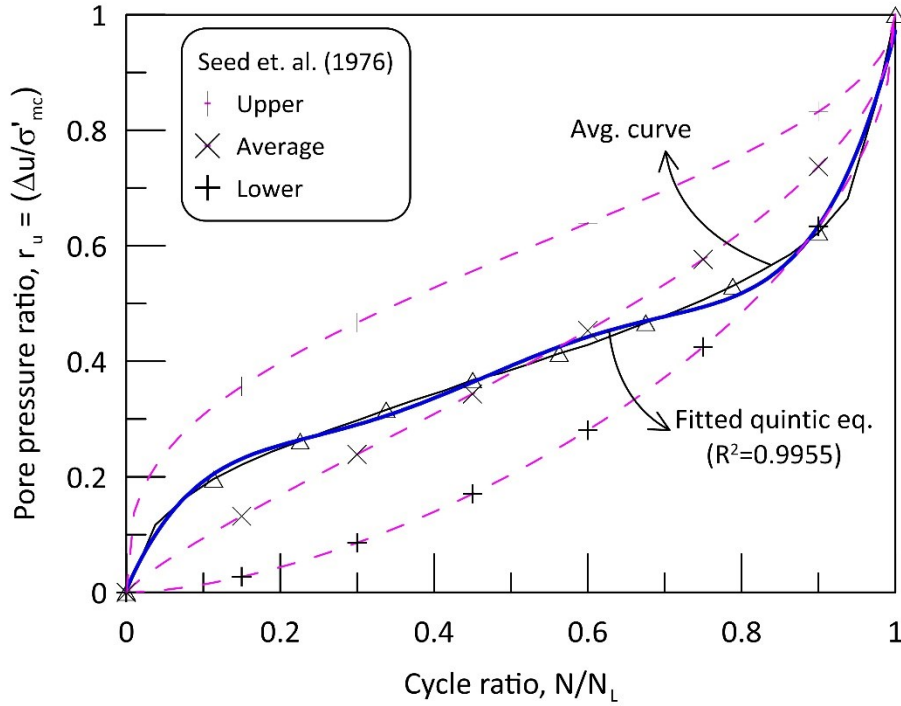


Figure 5.65: Fitted quintic curve to predict r_u

Similar to r_u vs N/N_L , the pore pressure ratio can also be uniquely correlated to the normalized energy ($W_N = W/W_{liq}$). The normalized energy (W_N) here is defined as the ratio of dissipated energy (W) to the dissipated energy required to cause initial liquefaction (W_{liq}). The r_u vs W_N obtained from the coupled loading tests on isotropically consolidated Fraser River sand specimens is plotted in Figure 5.66. Regardless of initial σ'_{mc} , CSR , and S/N , the data falls within a narrow band. This observation is consistent with the findings reported in Towhata and Ishihara (1985), Law et al. (1990), Polito et al. (2013) and Polito and Moldenhauer (2018, 2019). An average curve is obtained from the data and a simple power relationship is proposed to estimate the porewater pressure generated under generalized loading condition. The proposed relationship which has the highest coefficient of determination R^2 is given below:

$$\ln r_u = 0.5073 \ln W_N - 0.0128 \text{ with } R^2 = 0.9991 \quad (5.11)$$

The pore pressure models obtained from r_u vs N/N_L and r_u vs W/W_{liq} are very simplistic in functional form and can be used with the numerical codes to determine the excess pore water pressure generated during cyclic shearing.

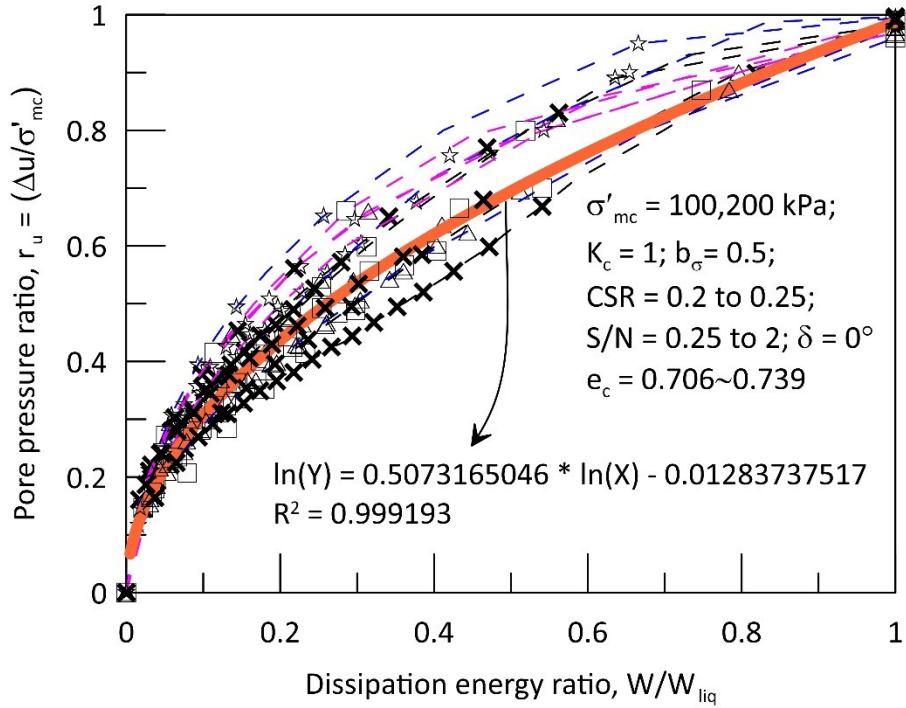


Figure 5.66: Variation of pore pressure ratio with dissipation energy ratio

5.9 Summary and conclusions

In this chapter, it has been demonstrated through numerical simulation using a horizontally layered bedrock and inclined bedrock model that even a slight dip of bedrock could result in a generation of both compression and shear waves during an earthquake. Therefore, during a seismic event, the soil element will be subjected to simultaneous action of both normal and shear stresses. The nature and degree of stress rotation due to this coupled loading condition is also discussed. It is noticed that the nature and degree of stress rotation is significantly influenced by the initial stress state parameters such as K_C , $\alpha_{\sigma C}$ and shearing parameters such as S/N , and δ . The representative values of S/N obtained from the

numerical analysis were used to investigate the cyclic response of Fraser River sand under coupled cyclic loading using the automated hollow cylinder torsional shear apparatus.

Cyclic hollow cylinder torsional shear tests were carried out on isotropically consolidated Fraser River sand to assess the influence of initial effective confining pressure (σ'_{mc}), cyclic stress ratio CSR (τ_{max}/σ'_{mc}) and S/N on the cyclic resistance of sand under the simultaneous action of compression and shear waves. As expected, at a fixed S/N and σ'_{mc} , the number of cycles to liquefaction decreases with the increase in CSR and the rate of reduction is almost fairly consistent with the previous cyclic test data on Fraser River sand reported in the literatures. At a fixed CSR and S/N , the number of cycles to liquefaction decreases with the increase in initial effective confining stress. The K_σ factor which is used to quantify the effect of consolidation stress on cyclic resistance of sand slightly decreases with the increase in σ'_{mc} and it also follows the well-established trend of K_σ variation with σ'_{mc} reported in Vaid and Sivathayalan (1996a) for Fraser delta sand. Thus, from this study it can be concluded that K_σ effect is pronounced even for generalized coupled loading conditions.

At a given CSR and initial σ'_{mc} , the number of cycles to liquefaction decreases with the increase in S/N . This reduction in cyclic resistance clearly demonstrates the influence of various degrees of coupled loading on the cyclic response of sand. There is a drastic reduction in the cyclic resistance with the increase in S/N from 0.25 to 0.5. Beyond S/N of 0.5, the rate of reduction in the liquefaction resistance decreases with the increase in S/N and the trend of variation tends to be asymptotic with S/N axis for about $S/N > 1.6$. This decrease in the cyclic resistance of sand with the increase in S/N is due to the coupled action of increase in shear stress on the weak horizontal bedding plane along with

the close alignment of τ_{max} axis with the bedding plane. Beyond S/N of 1.6, there is no significant change in both horizontal shear stress and inclination of τ_{max} axis with increase in S/N , which explains the asymptotic change in the liquefaction resistance at larger S/N . At smaller S/N , in which the normal stress increments are greater than the shear stress increment, the development of normal strains governs the soil liquefaction whereas when shear stress increment greater than or equal to normal stress increments, the shear strain plays a dominant role in liquefying the soil sample.

At a given relative density and confining pressure, CRR decreases with the increase in S/N . It should be noted here that the tests with smaller S/N represent triaxial condition whereas tests with larger S/N represent simple shear loading condition. Hence the conclusion derived from this test series confirms the conclusion reported by Vaid and Sivathayalan (1996a) that the cyclic resistance ratio tends to be smaller under simple shear than under triaxial loading condition.

Also, the test results obtained from this chapter were analyzed in terms of strain energy dissipated during cyclic shearing. The dissipated energy required to cause liquefaction (W_{liq}) was found to increase proportionately with the increase in σ'_{mc} even under generalized coupled loading condition. W_{liq} required for $r_u = 1$ and $\gamma_{max} = 3.75\%$ is independent of applied cyclic stress amplitude. Irrespective of initial confining stress and CSR , W_{liq} is slightly higher at low S/N of 0.25 and it is almost unaffected at higher values of S/N . This shows that slightly higher energy will be required to liquefy the soil under triaxial loading mode than under simple shear loading mode. This dissipated energy ratio (W_{liq}/σ'_{mc}), is found to be almost independent of CSR , S/N , σ'_{mc} , initial inclination of

principal stress axes and magnitude of stress rotation thus making the energy-based method of liquefaction evaluation a potential alternative to stress and strain based approach.

6. BEHAVIOUR OF SAND UNDER COMPLEX CYCLIC STRESS PATHS

6.1 *Introduction*

The propagation of seismic waves through soil strata subjects the soil element to various multidimensional cyclic loading paths. These loading paths involve the combined action of both cyclic shear stress and cyclic normal stresses, but in different proportions depending on the nature of the earthquake shaking. The dependency of pore pressure and shear strain development on loading paths in saturated soil under undrained shearing is well established (Symes et al. 1984; Miura et al. 1986; Uthayakumar and Vaid 1998; Sivathayalan and Vaid 2002; Georgiannou et al. 2018). The most common laboratory tests such as cyclic triaxial and cyclic simple shear employ simple loading paths to assess the liquefaction characteristics of soil. This may not fully capture the response exhibited under the multidimensional loading encountered in-situ. Several researchers have used bi-directional simple shear apparatus to evaluate the cyclic behavior of soil under multidirectional simple shear condition (Ishihara and Yamazaki 1980; Boulanger and Seed 1995; Kammerer et al. 2002; Matsuda et al. 2004). However, these studies were limited only to shear stresses acting on the horizontal plane. They ignore the shear stress caused by the normal stress variations due to the action of compression waves. Several investigations acknowledge the fact that seismic shaking involves coupling of compression and shear waves (Aggour and Zhang 2006; Gu et al. 2016; Tsaparli et al. 2016). This is also demonstrated in Chapter 5 through the finite difference simulation carried out in FLAC. In the previous chapter, the cyclic behavior of Fraser River sand is

assessed for the coupled action of compression and shear waves which are in phase with each other. As shown earlier in Figure 5.16, when P-waves and S-waves are not in phase with each other, the result is either an elliptical or circular stress path in $\tau_{z\theta} - (\sigma_z - \sigma_\theta)/2$ plane. The elliptical stress path is characterized by simultaneous change in both the magnitude of deviatoric stress and rotation of principal stress axes, whereas the circular loading path is characterized by continuous rotation of principal stress axes without any change in the magnitude of deviatoric stress. Sivathayalan and Vaid (2002) and Sinthujan (2013) investigated the influence of simultaneous change in deviatoric stress and inclination of major principal stress axis to the vertical on the undrained monotonic response of sand using hollow cylinder torsional shear apparatus (HCT). It was demonstrated that the softening tendency of sand increases with an increase in the rate of rotation ($\Delta\alpha_\sigma/\Delta\sigma_d$). Under cyclic loading only very few studies dealt with the effect of elliptical paths or circular loading paths on the undrained cyclic behavior of soil (Ishihara and Towhata 1983; Nakata et al. 1998; Yang et al. 2007; Huang et al. 2015; Wang et al. 2017; Xu et al. 2017). Through undrained cyclic tests on Toyoura sand along circular stress path, Ishihara and Towhata (1983); Nakata et al. (1998) and Yang et al. (2007) demonstrated that continuous rotation of principal stress axes alone without changing the magnitude of maximum shear stress is sufficient to liquefy the sand. Huang et al. (2015) compared the effect of different stress paths (Triaxial, Torsional, Circular, and Elliptical stress paths) on the liquefaction resistance of Fujian standard sand and Qiantang silt, and indicated that the specimens subjected to circular stress path showed lowest liquefaction resistance. Xu et al. (2017) through hollow cylinder torsional shear tests on saturated fine sand showed that the ratio and phase difference between the cyclic

horizontal shear stress and cyclic axial stress significantly influences the liquefaction resistance of sand.

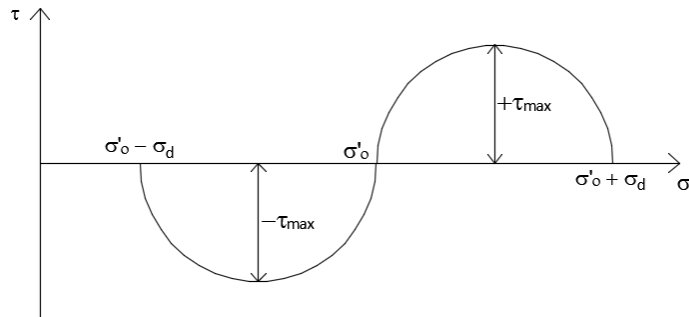
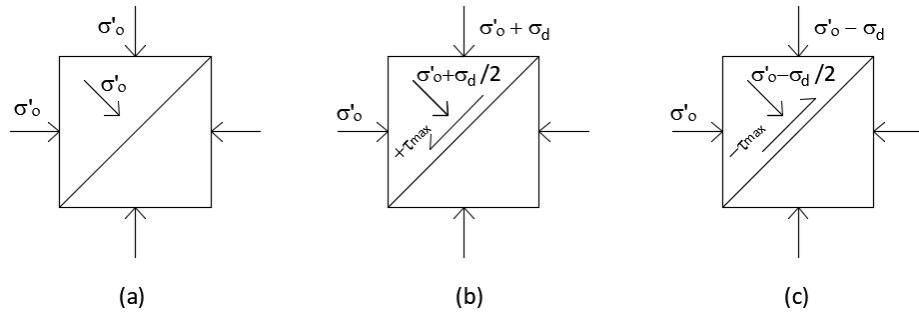
However, only limited investigations related to the effect of phase angle between compression and shear waves on the cyclic resistance of sand are available (Ishihara and Towhata 1983; Huang et al. 2015; Xu et al. 2017). Moreover, most of these studies were carried out under isotropically consolidated initial stress state. The effect of consolidation stress ratio (K_c) on the cyclic behavior of sand under coupled loading is not evaluated so far. Hence, the major objective of this chapter is to investigate the effect of phase angle (δ) and K_c on the liquefaction characteristics of Fraser River sand under coupled compression and shear wave loading during earthquakes. In addition, this chapter explores the effect of simultaneous action of shear wave and one-way compression wave on the cyclic response of sand. This latter case is common in traffic loading, but the loading frequency is usually less than that of the seismic loading (Andersen et al. 2013). Most of the studies on traffic loading stress paths were carried out in soft clay samples in which the testing has been carried out for several hundreds of loading cycles (Grabe and Clayton 2014; Sun et al. 2015; Cai et al. 2017; Wu et al. 2017). Moreover, this one-way cyclic loading is also common in offshore shallow foundations and offshore wind turbine foundations (Andersen 2009; Leblanc et al. 2010; Andersen et al. 2013; Nikitas et al. 2016; Hung et al. 2018). The laboratory tests to characterize the behavior of soil subjected to offshore loadings were carried out under drained condition with frequency of loading ranges between 0.001 to 1 Hz (Nikitas et al. 2017). When these offshore structures are subjected to seismic loading, there is a good possibility of coupled shear loading along with the one-way cyclic loading under undrained condition. To the best of

our knowledge, so far, no studies have addressed this issue. Therefore, this chapter aims to study the evolution of pore pressure and shear strain under these complex loading paths.

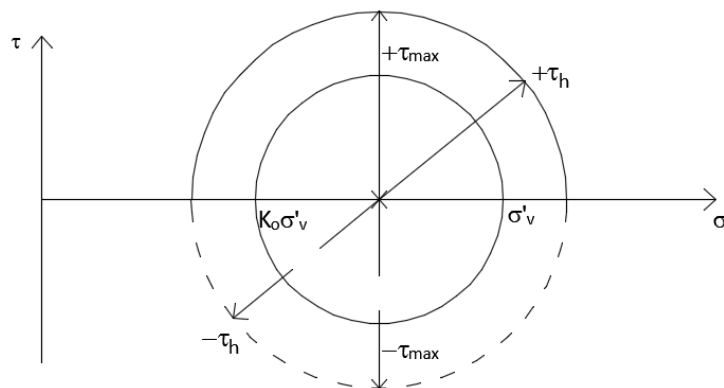
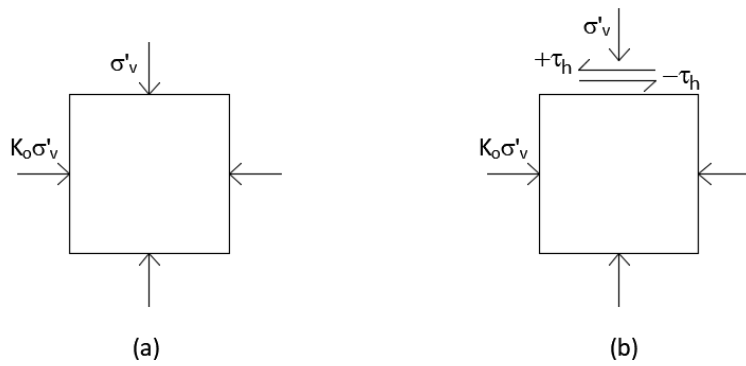
6.2 Definition of Cyclic stress ratio

In the simplified procedure, the liquefaction potential of soil is usually evaluated by comparing the cyclic stress ratio (*CSR*) with the cyclic resistance ratio (*CRR*) of soil. *CSR* represents the intensity of seismic shaking whereas *CRR* represents the capacity of the soil to resist the induced earthquake excitation. *CRR* is defined as the *CSR* required to liquefy soil in a specified number of loading cycles which is usually obtained from laboratory cyclic tests on representative soil samples using cyclic triaxial or cyclic simple shear tests. In cyclic triaxial tests, *CSR* is usually defined as the ratio of maximum shear stress to the effective confining stress ($\sigma_d/2\sigma'_{3c}$) whereas in simple shear it is defined as the ratio of horizontal shear stress to the effective vertical confining stress (τ_h/σ'_v).

Mathematically the sign of maximum shear stress (τ_{max}) stays always positive, since $\sigma_1 > \sigma_3$. But in triaxial and simple shear tests, it is customary to assign a sign convention for τ_{max} based on the direction of loading. Figure 6.1 shows the variation in the direction of τ_{max} for both triaxial and simple shear test conditions. In triaxial, the sign of τ_{max} is taken as positive when $\sigma_v > \sigma_h$, and it is considered negative when $\sigma_h > \sigma_v$ whereas in simple shear, τ_{max} takes the sign of applied τ_h . Hence with sign convention, τ_{max} varies continuously in a smooth sinusoidal manner, which makes the definition of *CSR* straightforward.



(a) Cyclic triaxial



(b) Cyclic simple shear

Figure 6.1: Direction of τ_{max} for both triaxial and simple shear test conditions

Figure 6.2 shows the typical variation of CSR in both triaxial and simple shear tests under different initial conditions. In practice, the maximum amplitude from the initial state or $(maximum - minimum)/2$ is usually defined as *CSR* (Ishihara 1996) as depicted in Figure 6.2.

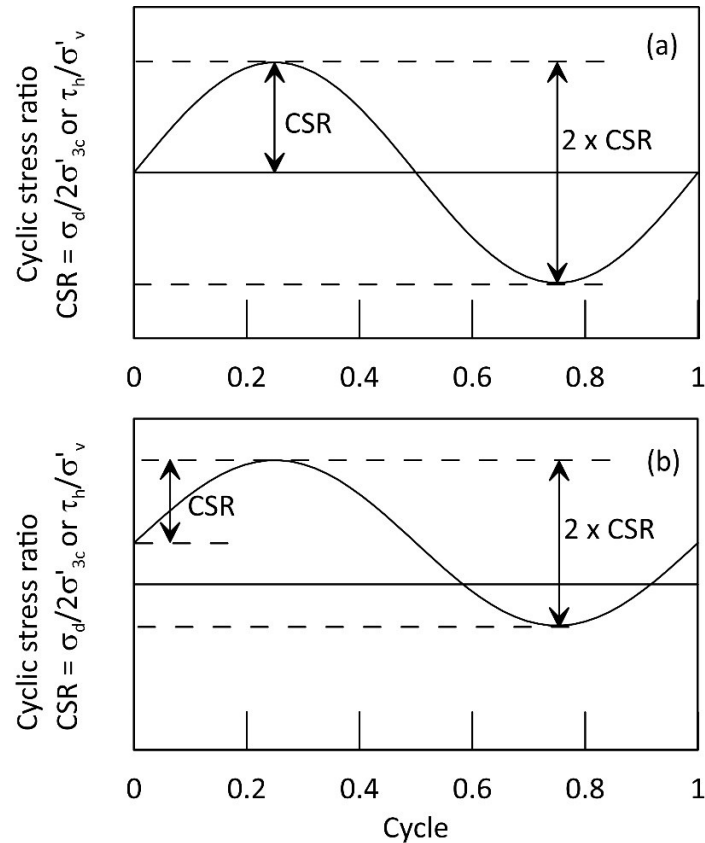
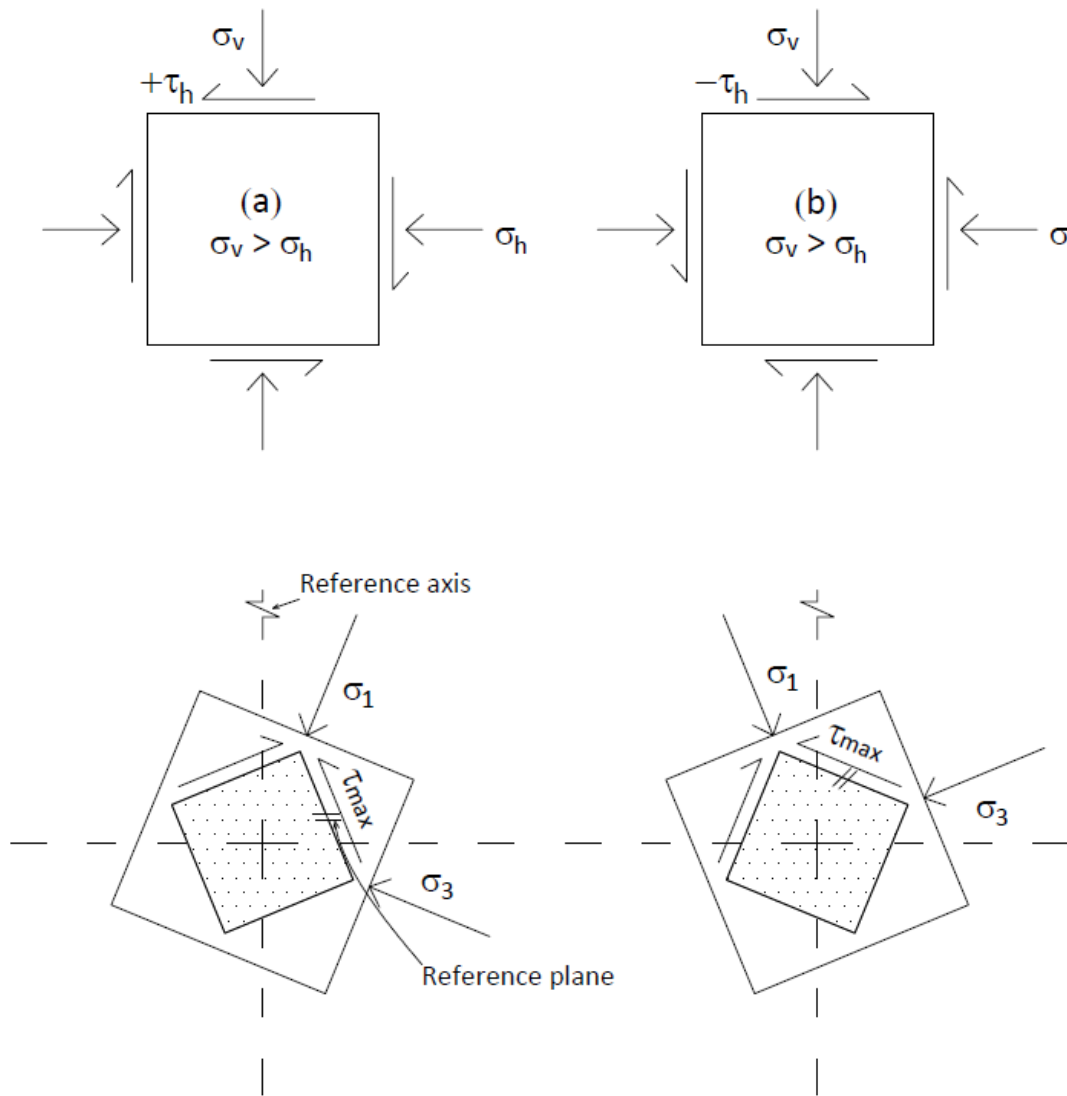


Figure 6.2: Typical variation of cyclic stress ratio in Triaxial and simple shear tests under initial (a) isotropic stress state and (b) anisotropic stress state

In HCT, *CSR* is defined as the ratio of maximum shear stress to the effective mean normal stress ($\sigma_d / 2\sigma'_{mc}$). Here the assignment of sign convention to τ_{max} will be quite straightforward if the loading is unidimensional i.e. either torsional or axial mode. But this will get complicated, if the loading is multidimensional involving coupling of both normal and shear stresses. When an isotropically consolidated soil element is

subjected to coupled loading with waves being in phase with each other, τ_{max} can take either the sign of $\tau_{z\theta}$ or $(\sigma_z - \sigma_\theta)$, since both $\tau_{z\theta}$ and $(\sigma_z - \sigma_\theta)$ changes sign at the same time. Assigning a sign convention for τ_{max} requires careful consideration in the case of more complex loading, such as $(K_c = 1; \delta \neq 0^\circ)$; $(K_c \neq 1; \delta = 0^\circ)$ and $(K_c \neq 1; \delta \neq 0^\circ)$. Therefore, in order to deduce the signage for τ_{max} under these above-mentioned conditions, four different type of stress states acting on a soil element are considered: (i) $\sigma_y > \sigma_x; \tau_{z\theta} > 0$ (ii) $\sigma_y > \sigma_x; \tau_{z\theta} < 0$ (iii) $\sigma_x > \sigma_y; \tau_{z\theta} > 0$ and (iv) $\sigma_x > \sigma_y; \tau_{z\theta} < 0$. Figure 6.3 shows the state of stress acting in a soil element and the corresponding orientation of principal stress and maximum shear stress axes. The variation in the direction of τ_{max} is monitored at a particular reference plane and reference axis which is highlighted in Figure 6.3. It can be observed that the direction of τ_{max} in the reference plane is unchanged and it remains in the same counterclockwise direction irrespective of the loading cases. However, in the reference axis the direction of τ_{max} changes if the direction of $\tau_{z\theta}$ is reversed. The direction of τ_{max} in the reference axis remains unchanged for the reversal of σ_y and σ_x . Therefore, it can be deduced from this discussion that τ_{max} follows the sign convention of $\tau_{z\theta}$ if the reference axis is taken into consideration and τ_{max} is sign independent if reference plane is taken into account. Figure 6.4 shows the definition of *CSR* based on these two references. It can be observed that with sign convention the *CSR* variation is not continuous, and it is not symmetrical with respect to time axis for some cases. Since, it is non-symmetrical, *CSR* can be defined in two possible ways i.e. single amplitude CSR_s (maximum value – initial value) and double amplitude CSR_d (maximum – minimum/2) as shown in Figure 6.4. On the other hand, with sign independency, the *CSR* variation is smooth and continuous, and it is

defined as the difference between the maximum and minimum value (Figure 6.4). The double amplitude CSR_d (maximum – minimum)/2 with sign convention can be treated as equivalent to CSR (Maximum – minimum) with sign independency as depicted in Figure 6.4 a1 and a2.



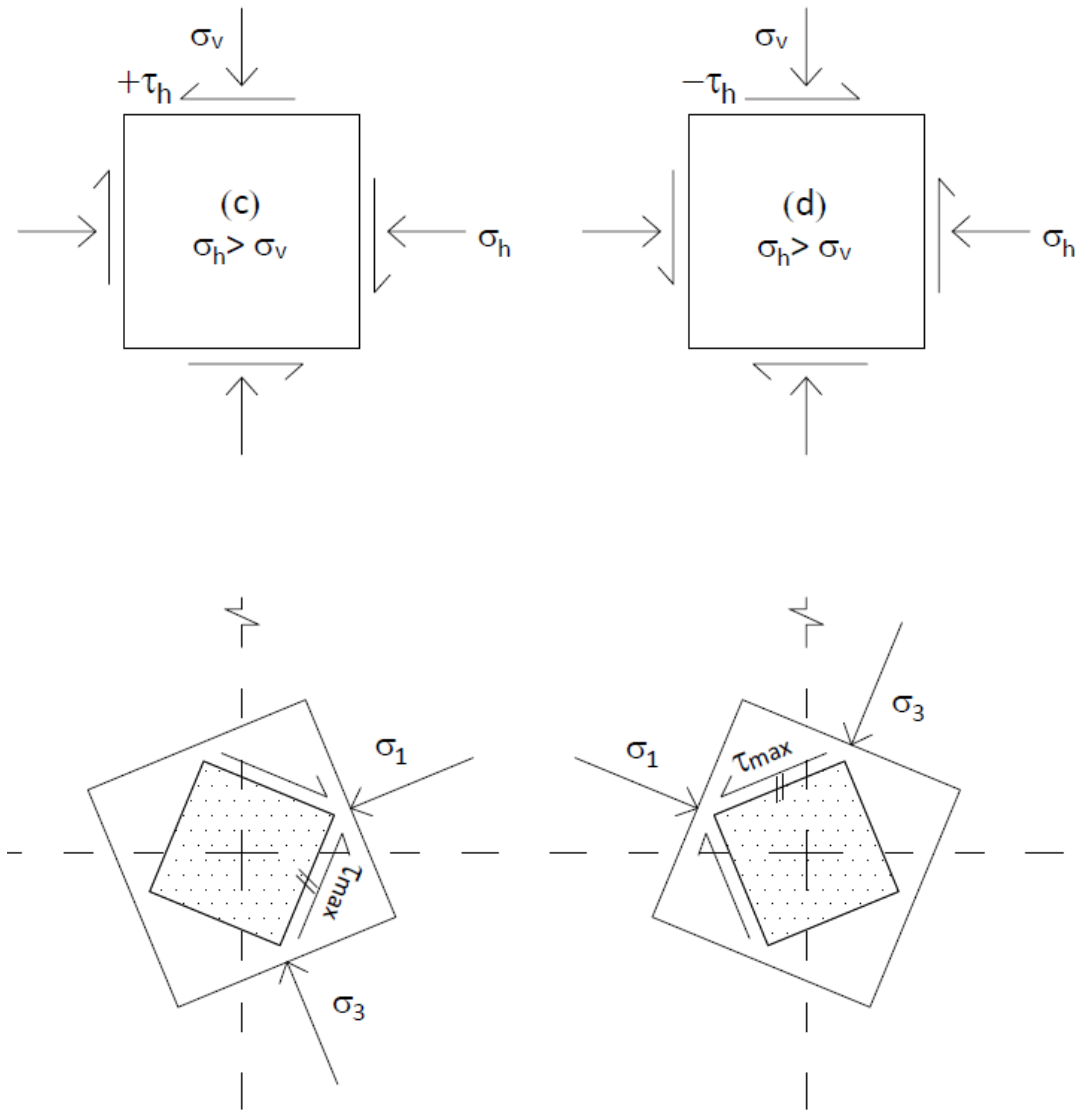


Figure 6.3: Direction of τ_{max} under different stress states

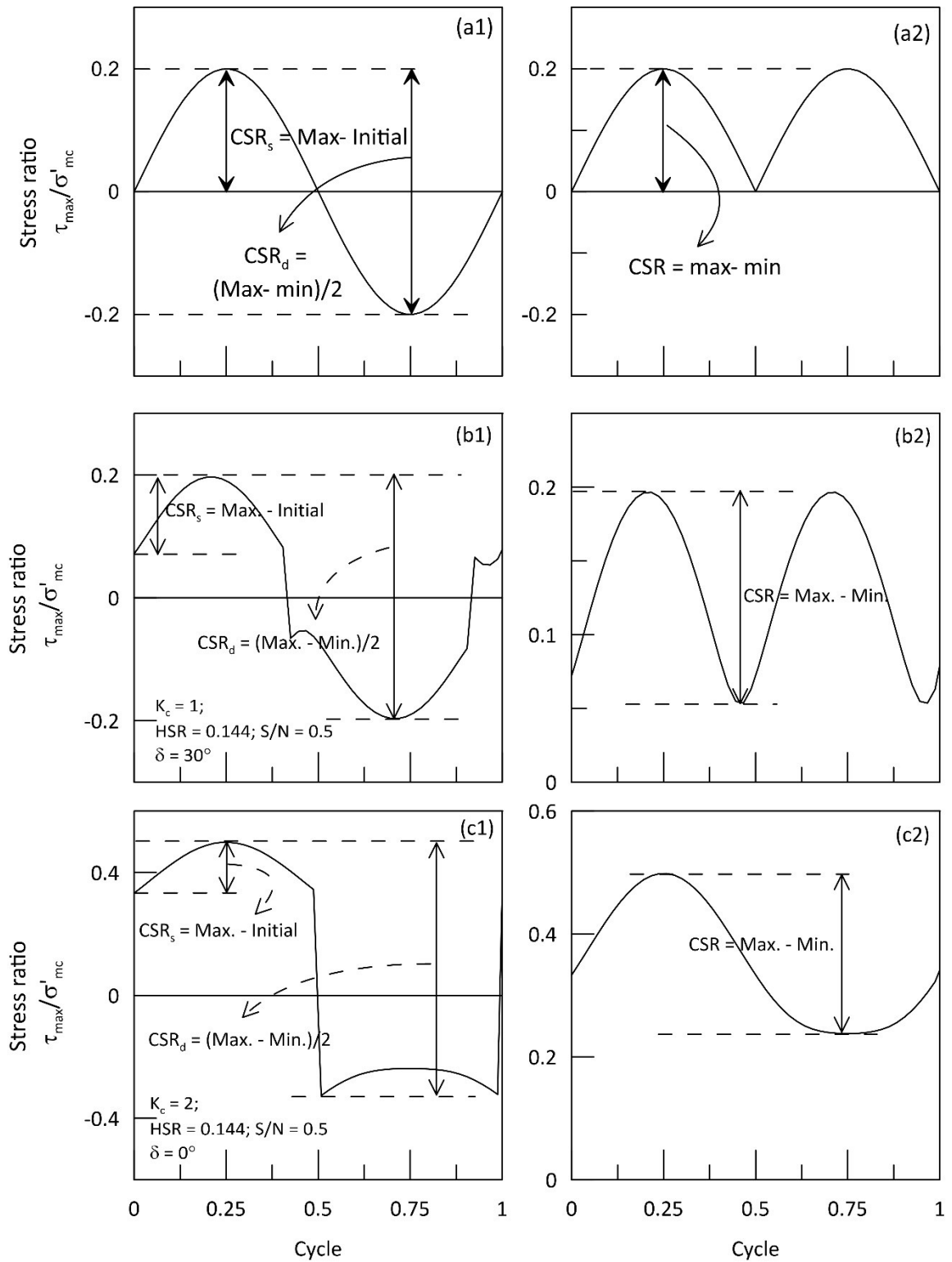


Figure 6.4: Definition of cyclic stress ratio (CSR)

Therefore, in this study, cyclic tests were assessed based on the sign independent definition of *CSR* since it is undergoing a smooth variation. Table 6.1 tabulates the details of cyclic tests carried out for investigating the effects of phase angle δ and consolidation stress ratio K_c on the coupled cyclic loading behavior of loose Fraser River sand. The samples are consolidated to an effective mean normal stress of 100 kPa; and cyclic shearing was carried out under constant total mean normal stress and intermediate principal stress parameter of 0.5.

Table 6.1: Details of initial and cyclic loading parameters with different δ and K_c

<i>Test No</i>	<i>Consolidation stage</i>			<i>Shearing stage</i>				
	<i>Stress state</i>	e_c	D_{rc} (%)	<i>CSR</i>	<i>HSR</i>	<i>S/N</i>	δ (°)	
CEQ27	$\sigma'_{mc} = 100 \text{ kPa};$ $K_c = 1;$ $b_\sigma = 0.5; \alpha_\sigma = 0$	0.737	36.3	0.14	0.144	0.5	30	
CEQ28		0.736	36.5	0.07			60	
CEQ29		0.742	35.0	0			90	
CEQ30		0.727	39.2	0.14			30	
CEQ31		0.729	38.5	0.07			60	
CEQ32		0.738	36.2	0			90	
CEQ35		0.20	0.730	38.4	0.20	0.157	0.5	10
CEQ34			0.733	37.4		0.202		30
CEQ33			0.730	38.2		0.390		60
CEQ38			0.714	42.7		0.098	0.25	10
CEQ39			0.738	36.1		0.098		10
CEQ36			0.740	35.6		0.116		30
CEQ37			0.744	34.3		0.162		60
CEQ43			$\sigma'_{mc} = 100 \text{ kPa};$ $k_c = 1.5;$	0.731		38.0	0.2	0.123
CEQ46	0.716	42.4		0.25	0.07	0.25		

CEQ44	$b_\sigma = 0.5; \alpha_\sigma = 0$	0.737	36.2	0.25	0.162	0.5	
CEQ45		0.733	37.3		0.274	1	
CEQ48	$\sigma'_{mc} = 100 \text{ kPa};$ $k_c = 2; b_\sigma = 0.5;$ $\alpha_\sigma = 0$	0.719	41.4	0.25	0.140	0.5	
CEQ47		0.724	39.9		0.284	1	

6.3 Phase shift between compression and shear waves on the cyclic response

The phase shift between compression and shear waves leads to an elliptical stress path in the $\tau_{z\theta} - (\sigma_z - \sigma_\theta)$ space. Cyclic tests with elliptical stress paths were performed by several researchers using bidirectional simple shear (Ishihara and Yamazaki 1980; Kammerer et al. 2002; Matsuda et al. 2011) and HCT apparatus (Ishihara and Towhata 1983; Huang et al. 2015; Xu et al. 2017), but the specific details about how these stress paths were followed from the initial consolidation stress state were not provided in any of these studies. These elliptical stress paths may be can be approached differently from the initial consolidation state, and it is crucial to investigate how these differences may affect the response. For this purpose, two types of tests are performed with the elliptical path: (a) completely undrained condition from the initial isotropically consolidated stress state to the starting point of the stress path and subsequent undrained cyclic loading (b) Drained pre-shear to the initial starting point of the stress path and followed by undrained cyclic shearing from that point. The objective was to assess the degree of influence caused by the seemingly minor differences in the loading phase.

For this test series, the specimens are isotropically consolidated to σ'_{mc} of 100 kPa and sheared with *HSR* of 0.144, *S/N* of 0.5 and $\delta = 30^\circ$. Figure 6.5 shows the typical variation of applied shear stress ($\Delta\tau_{z\theta}$) and normal stress ($\Delta(\sigma_z - \sigma_\theta)$)

increments for the above-mentioned loading scenarios. Here, the phase shift is applied to the shear stress increment $\Delta\tau_{z\theta}$. In a completely undrained test, an initial shear stress increment $\Delta\tau_{z\theta}$ of 7.2 kPa is applied under undrained condition to reach the starting point of the elliptical path from the consolidation stress state and subsequently coupled cyclic loading is applied to follow the elliptical path in a clockwise manner under undrained condition. In drained pre-shear test, after consolidation, a torsional shear stress of 7.2 kPa is applied under drained condition to reach the initial point of the stress path and sufficient time is allowed for the dissipation of generated excess pore water pressure. A small shear strain of $\gamma_{max} = 0.03\%$ was developed in the sand specimen due to this pre-shear. After this drained pre-shear, cyclic loading was carried out under undrained condition.

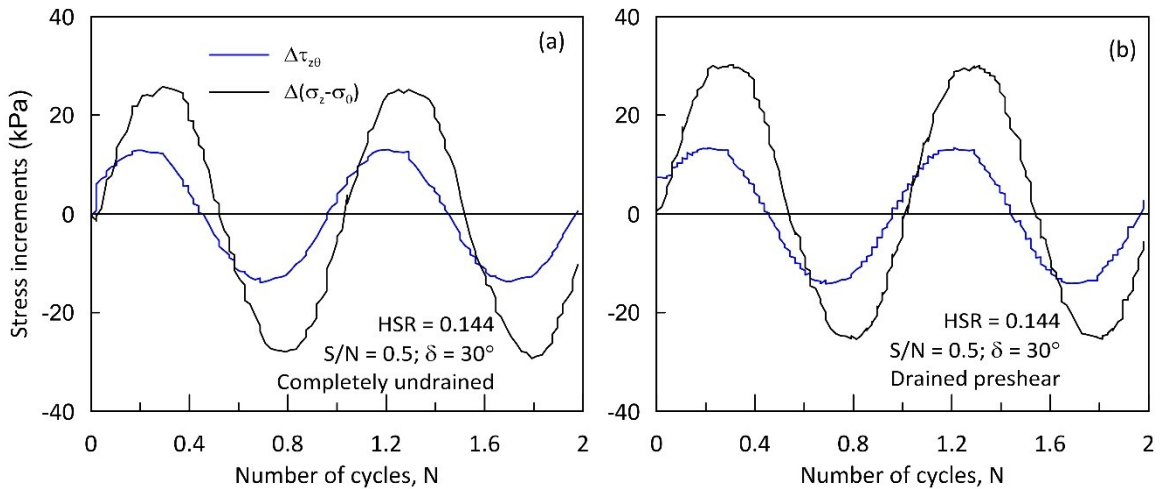


Figure 6.5: Variation of applied shear stress and normal stress increments for $\delta = 30^\circ$

Figure 6.6 compares the applied stress path and effective stress path response of sand subjected to this elliptical path under completely undrained and drained pre-shear condition. In effective stress path plot, τ_{max} is plotted with the sign convention of $\tau_{z\theta}$ where counterclockwise shear is taken as positive. It can be observed that the pore water

pressure rises steadily with the increase in loading cycle and reaches a maximum of about 90% of initial effective confining pressure for both the loading cases but the pattern of rise is quite different in these cases. The cyclic test with drained preshear shows more distinct variation in the peaks and troughs when compared to the cyclic test without preshearing.

The number of loading cycles for the effective stress path to reach the phase transformation state is quite high for the sand subjected to cyclic loading with drained preshear. The sand liquefied in 27 cycles for completely undrained condition and 41 cycles for drained pre-shear condition. This increased cyclic resistance is due to the initial pre-shear and several studies have reported that even a small pre-strain prior to cyclic loading increases the liquefaction resistance of sand (Finn et al. 1970; Ishihara and Okada 1982; Suzuki and Toki 1984; Vaid et al. 1989). The relatively small additional excess pore pressure generated (7 kPa) in the completely undrained test had a cumulative effect that lowered the liquefaction resistance from 41 to 27 cycles. If the reduction in the effective confining stress was considered in defining the intensity of the cyclic stress, the HSR would have been 0.154 instead of 0.144 in this case, but it is not known whether the tests reported in the literature considered these factors. These tests demonstrate that the method of following a complicated stress path such as an elliptical path significantly affects the cyclic response of sand and hence requires careful consideration. All tests reported in this thesis followed the drained mode except for this series of tests conducted to assess the effect of the initial path. The initial state in these tests are analogous to soils with a small amount of static shear prior to cyclic loading.

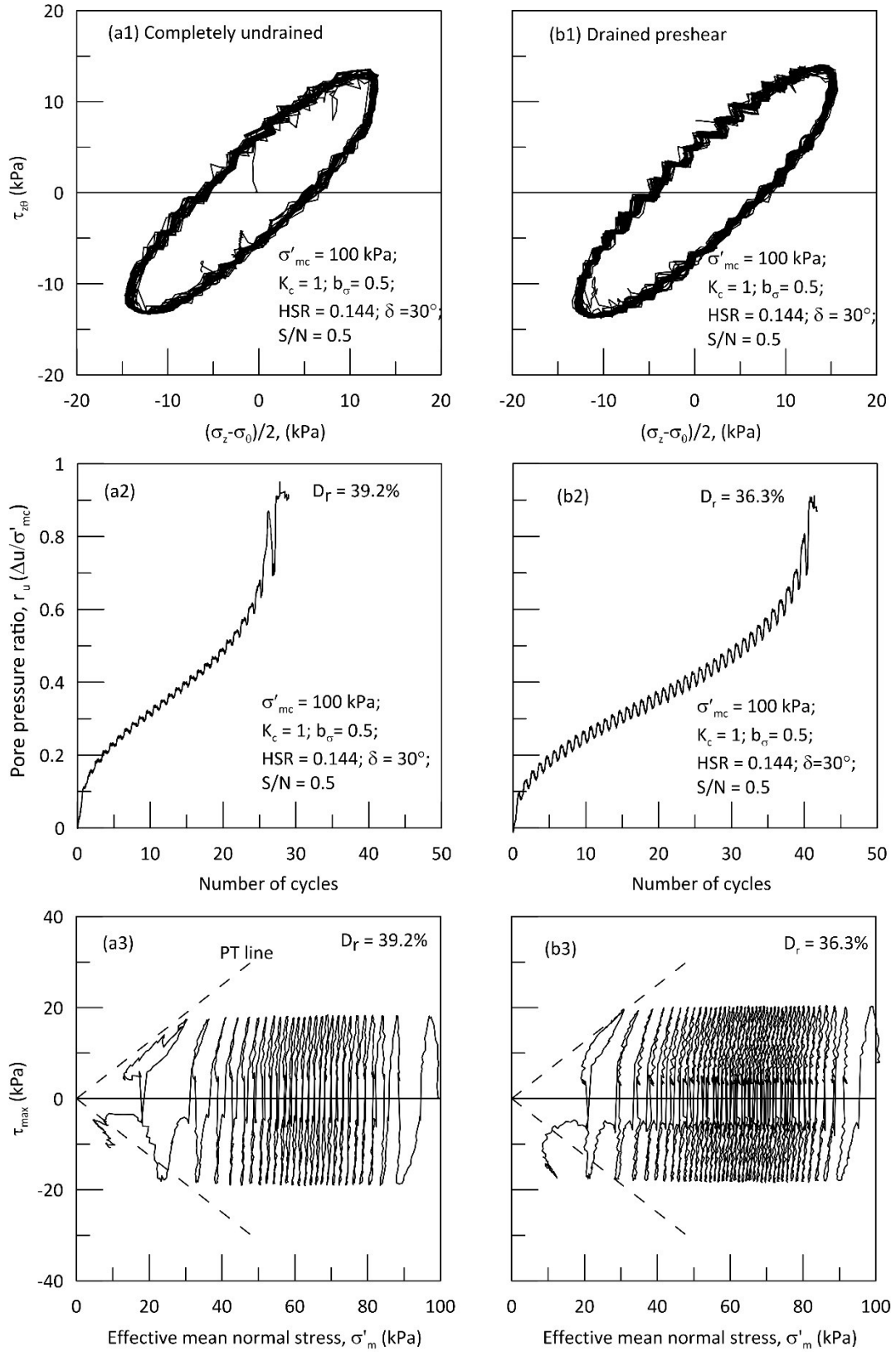


Figure 6.6: Response of sand under elliptical stress path with $\delta = 30^\circ$

6.3.1 Influence of phase angle at constant *HSR* and *S/N*

This test series was carried out to investigate the influence of phase angle (δ) on the cyclic behavior of sand when subjected to coupled loading at a fixed *HSR* and *S/N*. Cyclic tests were carried out on isotropically consolidated Fraser River sand specimen with *HSR* = 0.144; *S/N* = 0.5 and $\delta = 30^\circ, 60^\circ$ & 90° . Both fully undrained and drained preshear loading scenarios were considered for the analysis. At this fixed value of *HSR* and *S/N*, increasing the phase shift from 30° to 90° decreases the *CSR* from 0.14 to 0. At phase shift of 90° , where $|\Delta\tau_{z\theta}| = |\Delta\sigma_z| = |\Delta\sigma_\theta|$, cyclic shearing was carried out under constant deviatoric stress which results in a *CSR* of zero. Figure 6.7 and 6.8 shows the applied stress path and effective stress path response of sand sheared with different phase shifts (δ) under fully undrained and drained preshear condition. It can be observed that the mechanism of liquefaction changes from limited liquefaction to true liquefaction as the phase angle increases from 30° to 90° . The mechanism of strain development during cyclic loading depends upon initial stress state and characteristics of cyclic loading. In this test series, an initial maximum shear stress $\tau_{max,ini}$ was applied to reach the initial point of the elliptical stress path. The applied $\tau_{max,ini}$ increases from 7.21 kPa to 14.4 kPa with the increase in δ from 30° to 90° . This increase in initial $\tau_{max,ini}$ could have exceeded the shear strength of sand at phase transformation and transformed the strain development from limited liquefaction to true liquefaction. At $\delta = 30^\circ$ & 60° sand suffered limited liquefaction which can be identified through the strain development where the accumulation of maximum shear strain is not progressive like in cyclic mobility. At $\delta = 90^\circ$, sand liquefied due to flow liquefaction where large deformation develops before the effective stress path reaches the phase transformation state. This is a

special case because here the cyclic shearing was carried out under a constant deviatoric stress of 28.8 kPa but with continuous rotation of α_σ between $+90^\circ$ and -90° . It can be observed from Figure 6.9 that when the flow deformation is initiated the soil cannot sustain the imposed constant deviatoric stress and flowed with the σ_d lower than the imposed one. This observation is consistent with the observation made by Sivathayalan and Vaid (2002) from the undrained monotonic testing of Fraser River sand under constant deviatoric stress but with continuous rotation of principal stress axes.

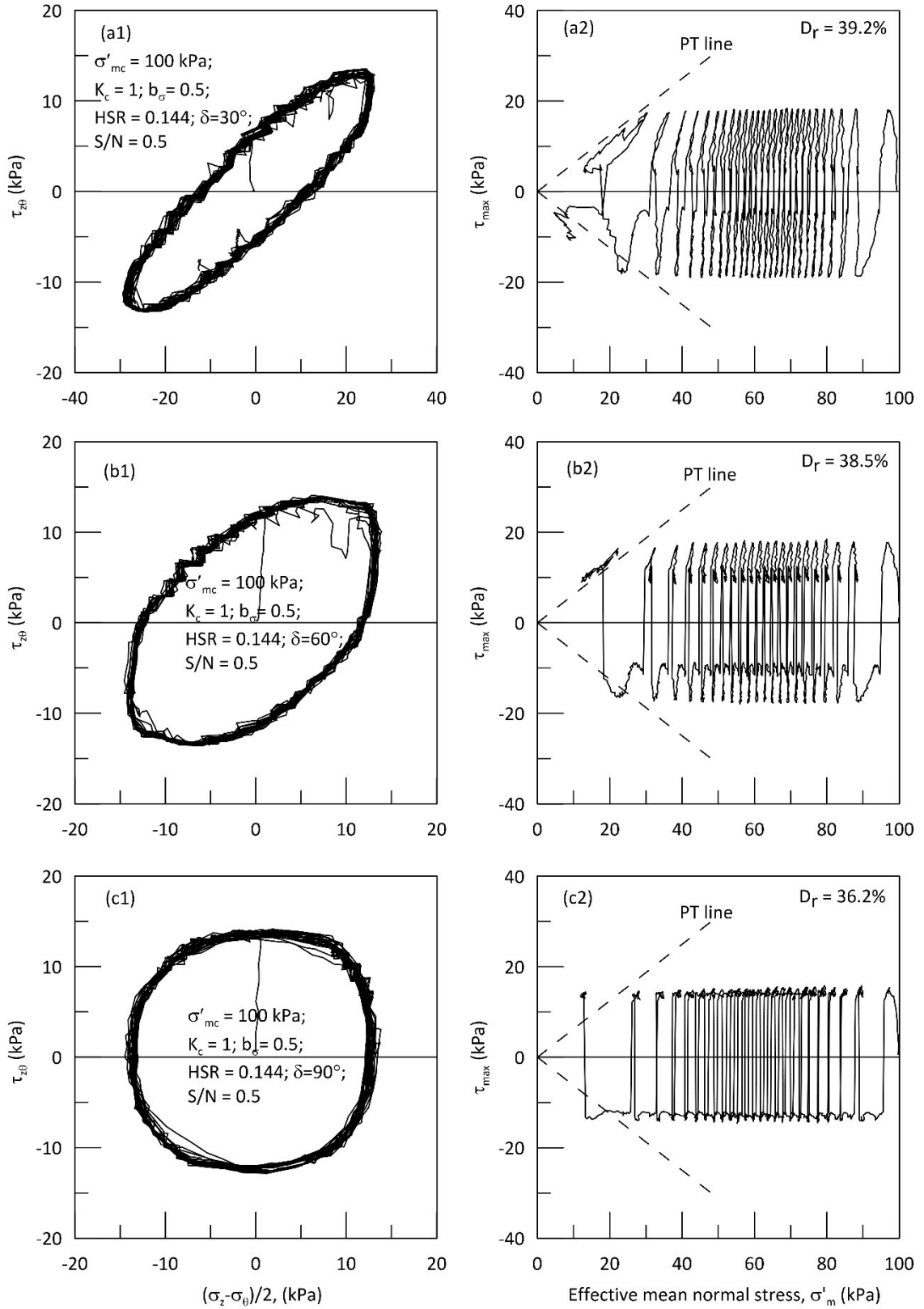


Figure 6.7: Response of sand sheared with different δ under fully undrained condition.

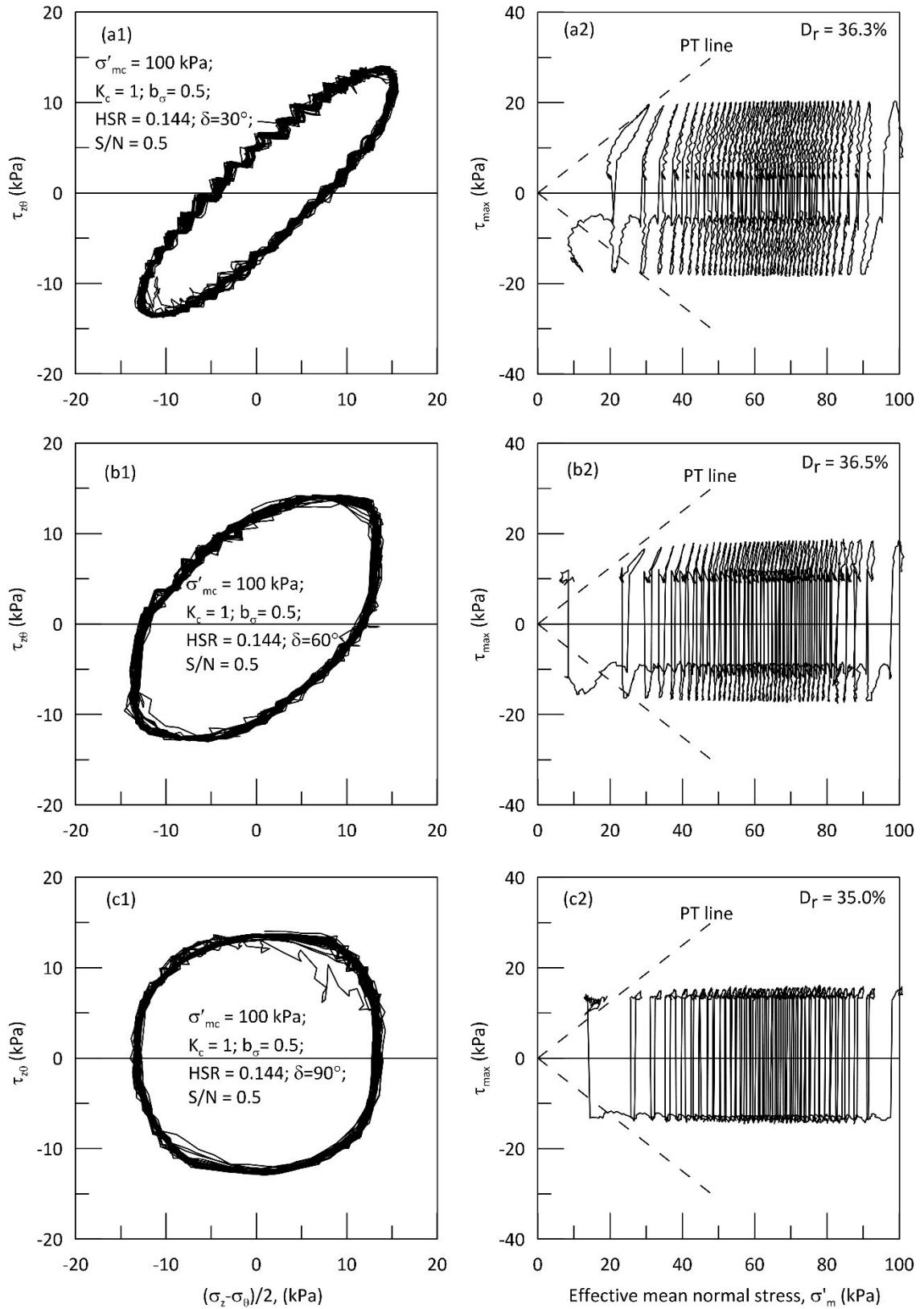


Figure 6.8: Response of sand sheared with different δ under drained preshear condition.

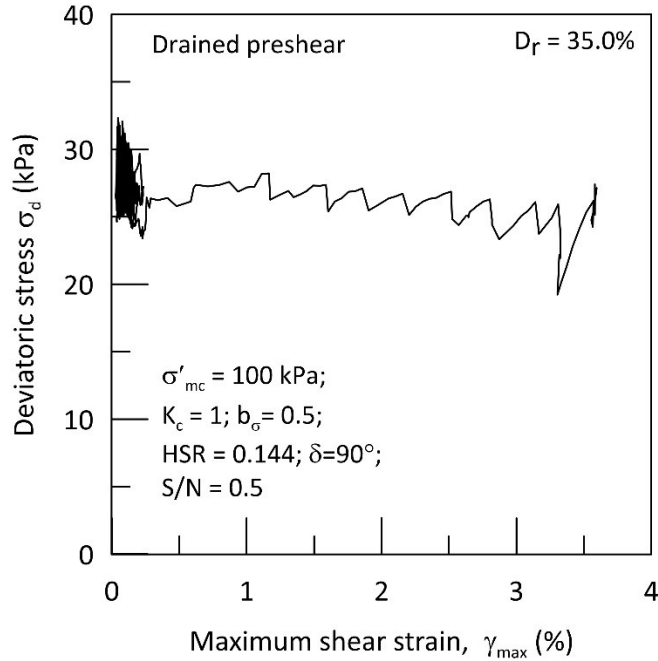


Figure 6.9: Variation of deviatoric stress at $\delta = 90^\circ$ under drained preshear condition

Figure 6.10 shows the pore pressure and shear strain response of sand subjected to different δ but with fixed HSR and S/N . In cyclic tests with preshearing, the rate of pore pressure generation and shear strain accumulation is almost unaffected by the increase in phase angle between the waves. In tests without preshear, the lowest rate of pore pressure accumulation is observed for $\delta = 30^\circ$ and this rate increases for $\delta = 60^\circ$. This increase might be due to the increase in initial $\Delta\tau_{z\theta}$ that is required to reach the beginning point of the elliptical stress path. In $\delta = 30^\circ$, $\Delta\tau_{z\theta}$ of 7.2 kPa is applied instantaneously under undrained condition whereas in $\delta = 60^\circ$, $\Delta\tau_{z\theta}$ of 12.5 kPa is applied to reach the starting point of the stress path. The rate of increase in pore pressure accumulation is not that significant between $\delta = 60^\circ$ and 90° because here the initial $\Delta\tau_{z\theta}$ increases only by 15% i.e., from 12.5 kPa to 14.4 kPa for increase in δ from 60° to 90° . It can also be noted that in all the loading cases the excess pore water pressure accumulated steadily and reached a

maximum value that approximately equals 90% of the initial effective confining stress. The maximum shear strain developed is only about 0.25% before the onset of sudden flow deformation in all three tests.

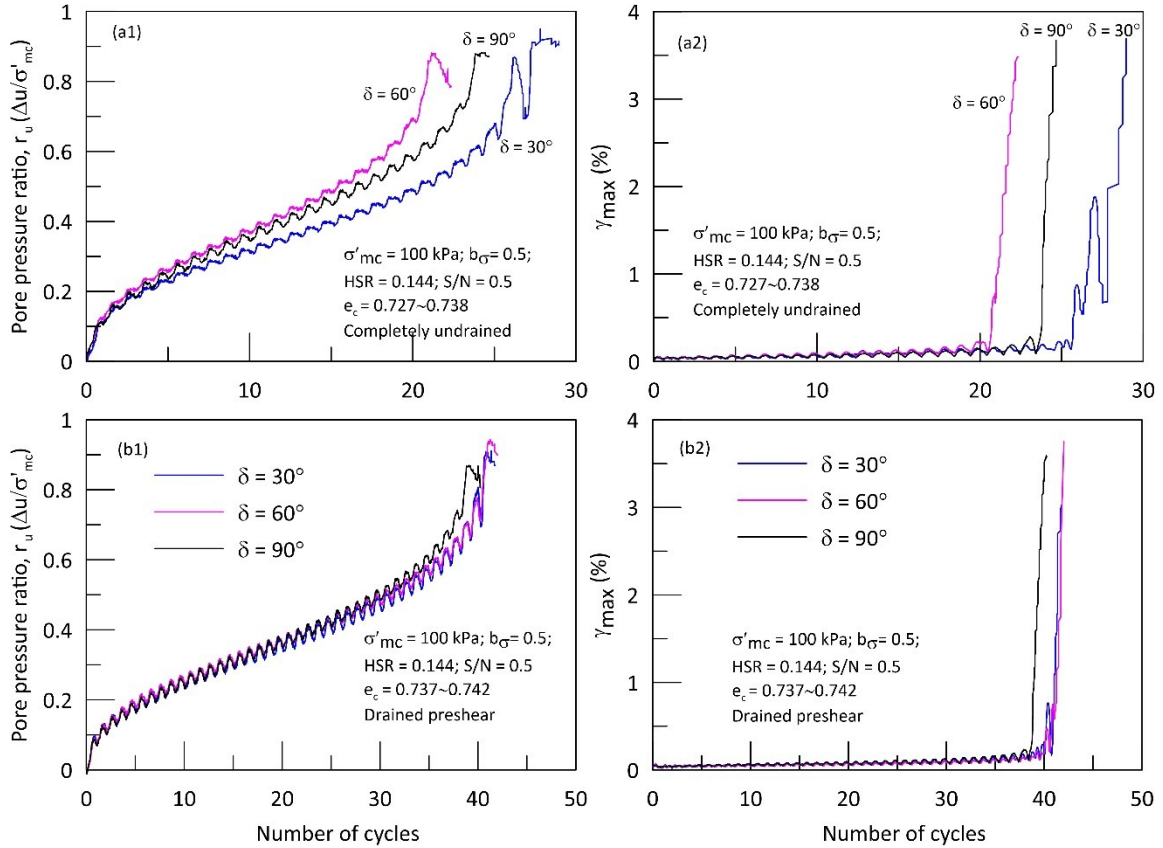


Figure 6.10: Pore pressure and shear strain response of sand at different δ

Figure 6.11 shows the variation in the number of cycles to liquefaction with the phase angle δ . It can be observed that the number of cycles to liquefaction is almost unaffected by the change in δ under drained preshear condition. This might be because that at a fixed *HSR* and *S/N*, the maximum amplitude of shear stress and normal stress applied to the soil specimen remains same for different δ . Under cyclic loading without preshearing, the fluctuation in the number of cycles to liquefaction with δ might be due to the fluctuations in the excess pore water pressure caused by the instantaneous

application of initial $\Delta\tau_{z\theta}$ to reach the starting point of the elliptical stress path. Moreover, at a given HSR , S/N and δ , sand specimens subjected to cyclic loads with preshearing exhibited higher cyclic resistance when compared to the samples subjected to cyclic loads without preshearing. Therefore, this clearly demonstrates the significance of the methods adopted to follow the complex cyclic loading paths on the cyclic response of sand. The method with drained preshearing essentially eliminates the effect of initial $\Delta\tau_{z\theta}$ on the undrained cyclic response of soil. This also indicates that the minor differences in the level of static shear in the specimen on account of the different initial states was not significant to cause a difference in the response. Hence it can be concluded that at a given HSR and S/N , changing the phase shift between compression and shear waves does not significantly affects the liquefaction resistance of soil.

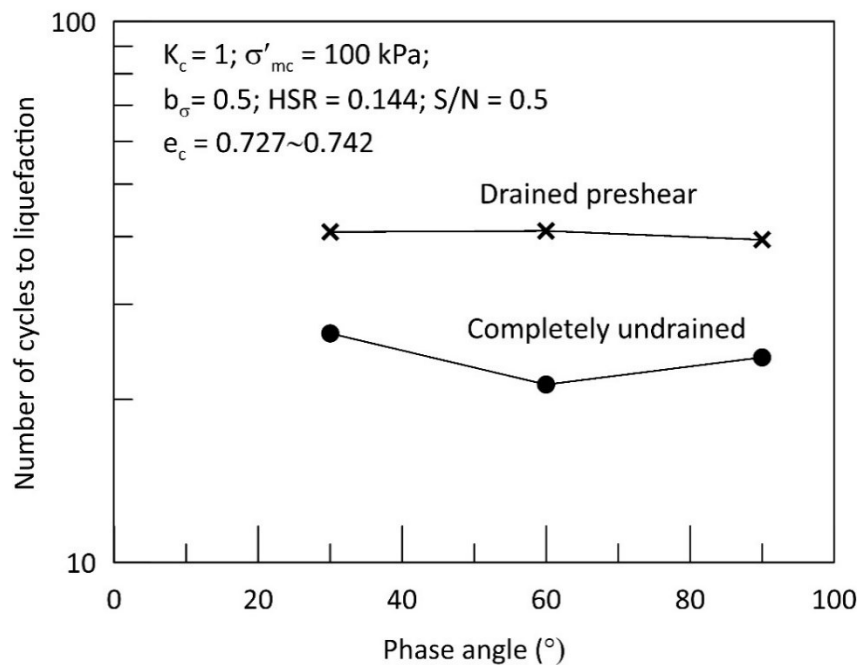


Figure 6.11: Influence of phase angle δ on number of cycles to liquefaction

6.3.2 Influence of phase angle at constant CSR and S/N

This section discusses the effect of phase angle δ on the cyclic response of isotropically consolidated Fraser River sand subjected to coupled loading with the fixed CSR of 0.2. S/N of 0.25 & 0.5 and δ of 10° , 30° & 60° was considered for the analysis. Here for a given S/N and δ , HSR is adjusted to yield a targeted CSR. Figure 6.12 shows the variation of HSR with respect to δ for all the S/N considered in this test series. It can be observed that, to maintain a given CSR of 0.2, HSR increases with an increase in phase shift from 10° to 60° . Figure 6.13 shows the variation of τ_{max} for the imposed HSR , S/N and δ . With the increase in δ from 10° to 60° , peak τ_{max} increases from 22 kPa to 34 kPa for $S/N = 0.25$ and from 22 kPa to 48 kPa for $S/N = 0.5$. Even though with all these variations in the peak value of τ_{max} with δ , the final resulting CSR remains the same for all the loading cases as CSR reflects the change in shear stress and not the absolute shear stress.

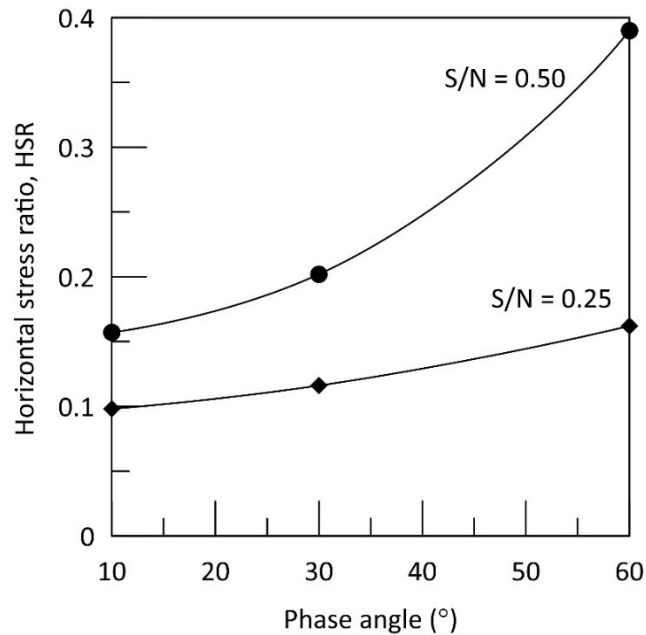


Figure 6.12: Variation of HSR with δ for CSR of 0.2

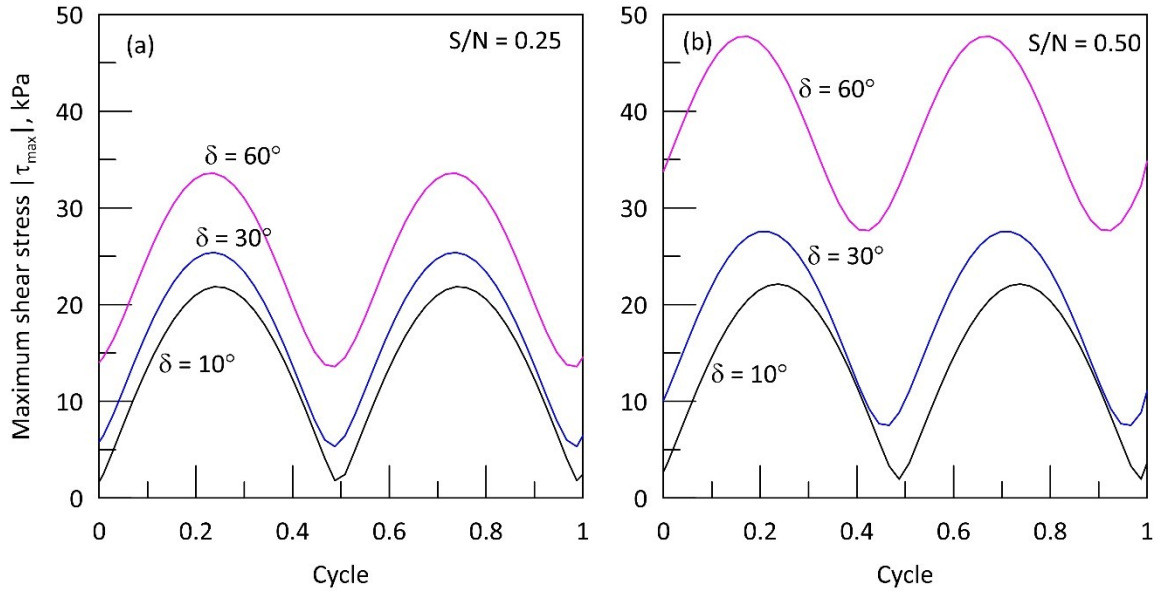


Figure 6.13: Variation of τ_{max} for different δ and CSR of 0.2

In this test series, prior to the application of undrained cyclic loading, preshearing was carried out by applying required torsional shear stress increment $\Delta\tau_{z\theta}$ under drained condition to reach the initial point of the elliptical loading path. Figure 6.14 shows the variation of preshear stress and the associated prestrain for various S/N and δ considered in this test program. For $S/N = 0.25$, the applied initial maximum shear stress $\tau_{max,ini}$ increases from 1.7 kPa to 14 kPa for the change in δ from 10° to 60° , and this $\tau_{max,ini}$ results in a prestrain of 0.01% to 0.06% on the sand specimen. For $S/N = 0.5$, $\tau_{max,ini}$ increases from 2.7 kPa to 33.8 kPa causing a significant prestraining of soil sample with $\gamma_{max,ini}$ varying from 0.01% to 0.28% for the increase in δ from 10° to 60° . After this preshearing, subsequent undrained cyclic loading was carried out under constant σ_m and b_σ of 0.5. If this level of shear stresses were applied undrained, then significant excess pore water pressures would have developed on account of reaching the targeted initial state and made subsequent comparisons not meaningful.

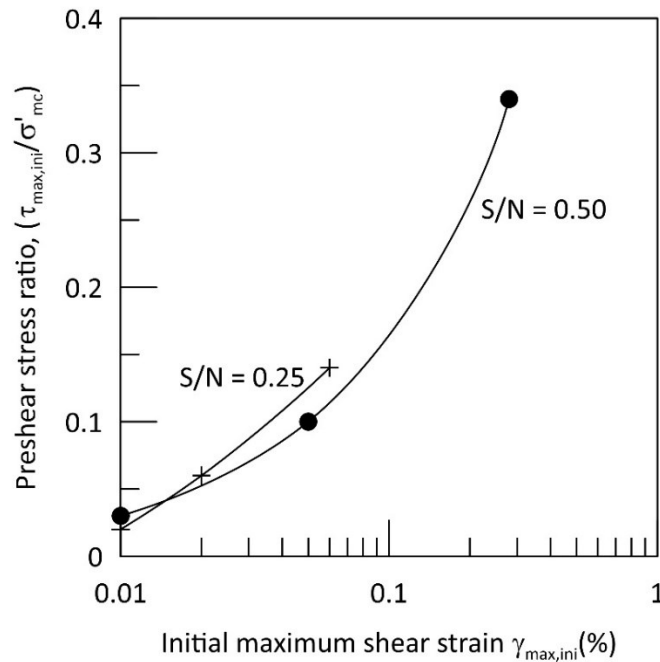


Figure 6.14: Variation of preshear stress and shear strain

Figure 6.15 and 6.16 presents the applied stress path and effective stress path response of sand sheared with CSR of 0.2, S/N of 0.25 & 0.5 and δ of 10° , 30° & 60° . It can be observed that irrespective of S/N , the mechanism of liquefaction changes from cyclic mobility to flow liquefaction with the increase in δ from 10° to 60° . The effective stress path is nonsymmetric about the effective mean normal stress axis because of the unsymmetrical rotation of principal stress directions during the loading cycle. At $\delta = 10^\circ$, liquefaction manifests due to the development of cyclic mobility with excursions through the state of transient zero effective stress. At $\delta = 30^\circ$ & 60° , sand exhibited contractive flow deformation with the sudden development of maximum shear strain. This might be because the imposed shear stress $(\tau_{st} + \tau_{cyc})$ would have exceeded the minimum undrained shear strength of sand at phase transformation (S_{PT}). The dependence of S_{PT} on loading paths is well known and it has been shown that S_{PT} of

water pluviated sand specimens decreases with the increases in α_σ and b_σ (Uthayakumar and Vaid 1998; Sivathayalan and Vaid 2002; Logeswaran 2010; Sivathayalan et al. 2015). Sand exhibits highest S_{pT} during triaxial compression loading mode and weakest during triaxial extension mode. Sivathayalan and Mehrabi Yazdi (2014) reported S_{pT} as low as 9 *KPa* from the triaxial extension test on Fraser River sand isotropically consolidated to 100 kPa. Figure 6.17 shows the rotation of α_σ for $\delta = 30^\circ$ & 60° tests, from which it can be observed that flow deformation is triggered when the α_σ is close to $\pm 90^\circ$ which is the condition of α_σ at extension loading.

Therefore, it is evident from Figure 6.13 that for $\delta = 30^\circ$ & 60° , the applied τ_{max} is well above the S_{pT} of Fraser River sand under triaxial extension condition and hence this triggered the strain softening of sand specimens. This observation of flow failure of water pluviated sand specimens at $\alpha_\sigma = 90^\circ$ is consistent with the findings reported in Vaid et al. (1989); Vaid and Sivathayalan (2000) and Vaid and Thomas (1995).

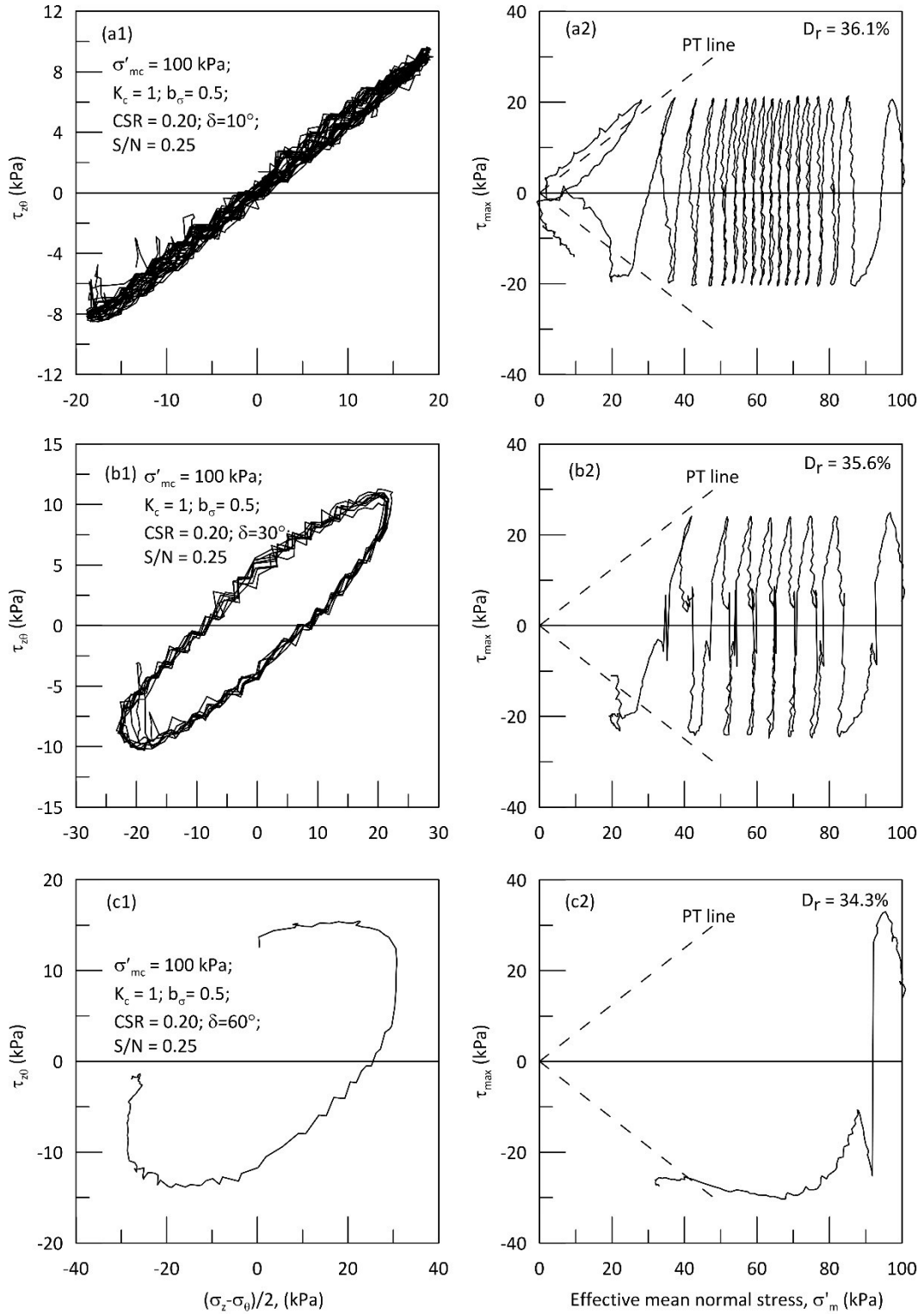


Figure 6.15: Applied stress path and effective stress path response of sand sheared with CSR of 0.2, S/N of 0.25

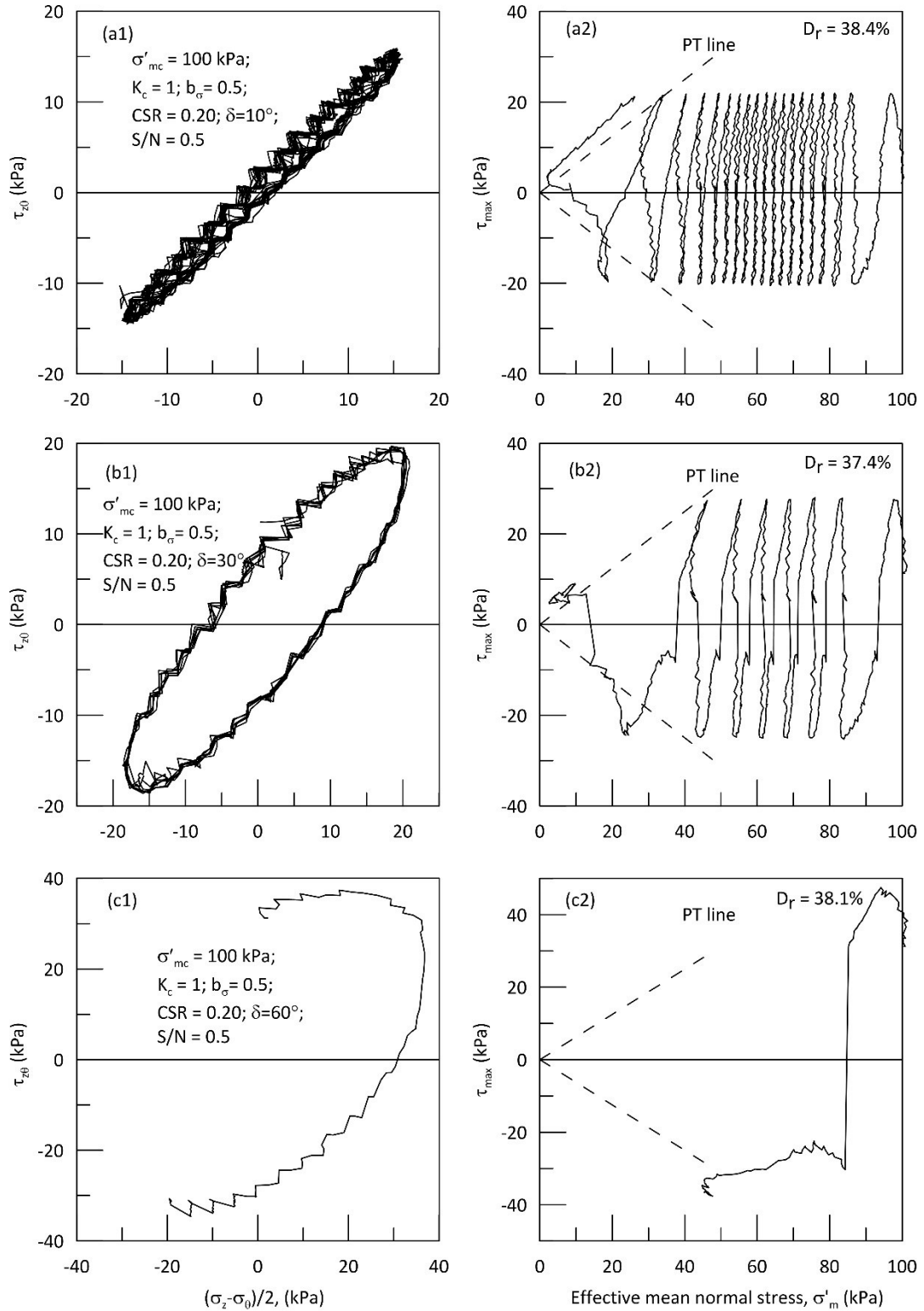


Figure 6.16: Applied stress path and effective stress path response of sand sheared with CSR of 0.2, S/N of 0.5

Figure 6.17 clearly demonstrates the influence of δ at a fixed CSR of 0.2, on the excess pore water pressure and shear strain development of sand. The rate of pore pressure generation is low for $\delta = 10^\circ$ and this rate increases drastically with the increase in δ from 10° to 60° . At $\delta = 60^\circ$, sand liquefied within a loading cycle with the sharp increase in the pore water pressure reaching a maximum of about 60% of initial σ'_{mc} for both the cases of S/N . The γ_{max} development is also so rapid and for all the loading cases the level of γ_{max} is almost less than 0.3% before the triggering of liquefaction.

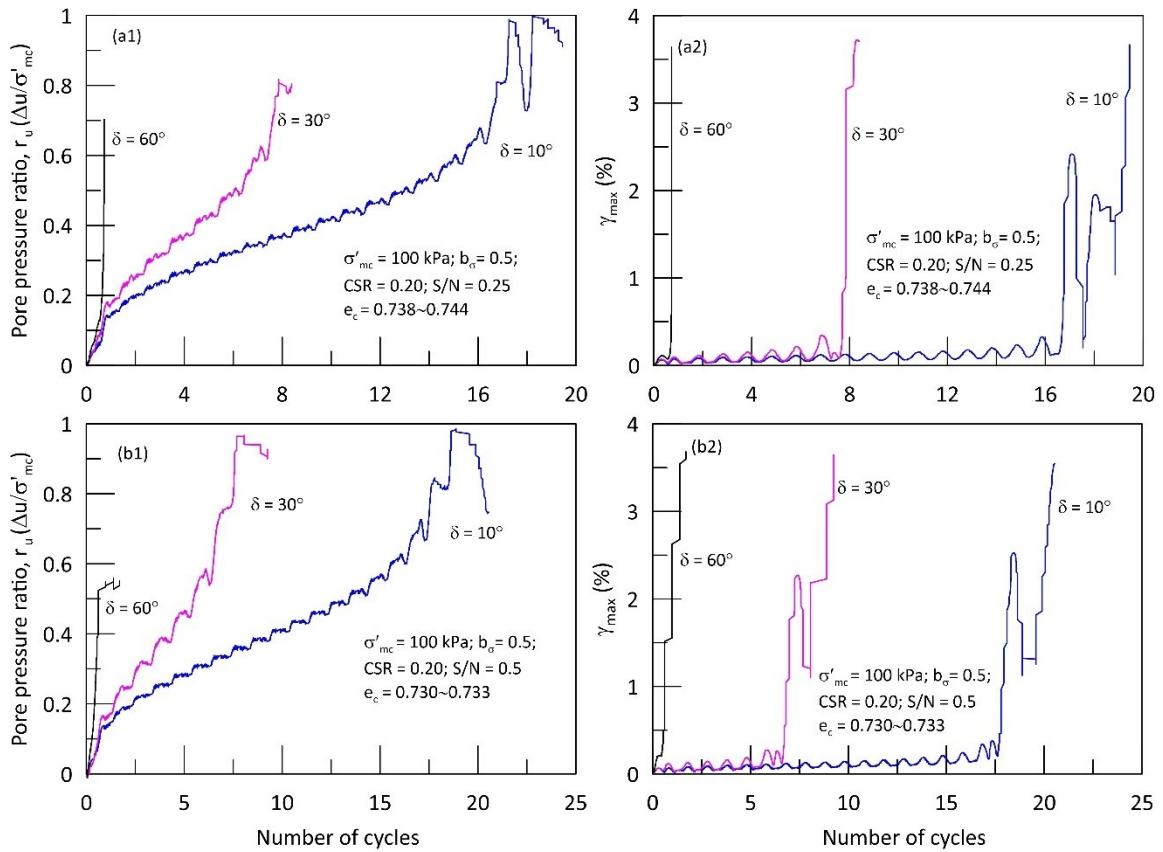


Figure 6.17: Pore pressure and shear strain response of sand at different δ & $CSR = 0.2$

Figure 6.18 shows the variation of number of cycles to liquefaction as a function of δ at two levels of S/N . At a fixed CSR , the number of cycles to liquefaction decreases with the increase in δ and it is also surprising to note that for $\delta \neq 0$, change in S/N does

not affect the liquefaction resistance of sand. This is not consistent with the conclusions deduced from the previous chapter that at $\delta = 0$, the resistance to liquefaction decreases with the increase in S/N . It is to be noted that $\delta = 0$ and $\delta \neq 0$ cases cannot be compared directly because at $\delta = 0$, α_σ undergoes jump rotation and the rotation shifts upwards with the increase in S/N whereas at $\delta \neq 0$ case, α_σ rotates continuously with the magnitude of rotation and the pattern of rotation is almost unaffected by the change in S/N . This is illustrated in Figure 6.19 where α_σ rotates continuously between $\pm 90^\circ$ and the pattern of rotation changes from jump rotation to linear variation in α_σ with the increase in δ . Hence from this investigation it can be concluded that at a fixed CSR , increasing δ reduces the cyclic resistance because increase in δ is accompanied by a decrease in the rate of change in deviatoric stress per degree of rotation ($\Delta\sigma_d/\Delta\alpha_\sigma$). Figure 6.20 shows the variation of number of cycles to liquefaction as a function of $\Delta\sigma_d/\Delta\alpha_\sigma$. As δ increases from 10° to 60° , $\Delta\sigma_d/\Delta\alpha_\sigma$ reduces from 8.3 to 1.95 for $S/N = 0.25$ and from 6.7 to 1.6 for $S/N = 0.5$. Sivathayalan and Vaid (2002) and Sinthujan (2013) showed that the softening tendency of sand increases with the decrease in $\Delta\sigma_d/\Delta\alpha_\sigma$ through undrained monotonic tests on loose Fraser River sand. Therefore, the decrease in $\Delta\sigma_d/\Delta\alpha_\sigma$ due to the increase in δ , increases the strain softening tendency of the sand and thereby reducing its liquefaction resistance. At a given CSR , for $\delta \neq 0$ cases, change in S/N does not affect the liquefaction resistance of sand because the magnitude and pattern of rotation is almost unaffected by the change in S/N .

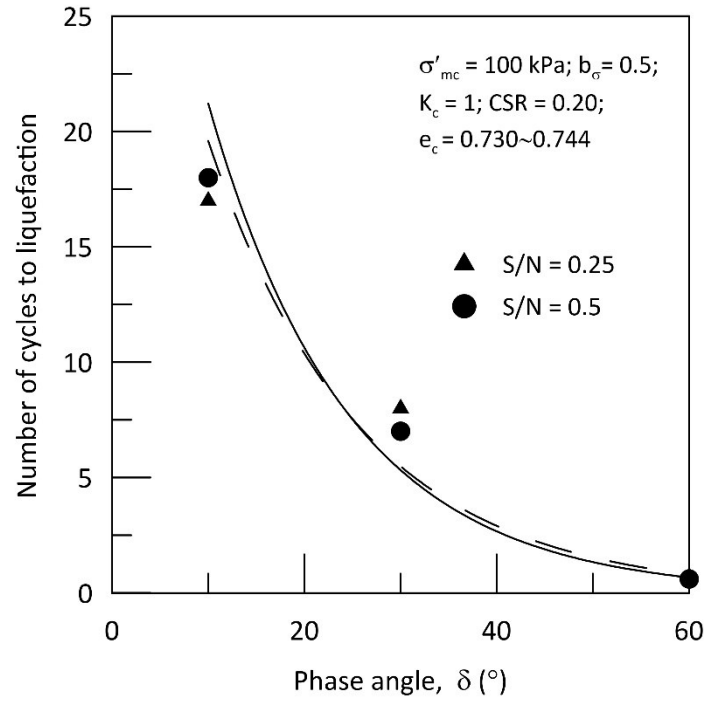


Figure 6.18: Influence of phase angle δ on number of cycles to liquefaction at a fixed $CSR = 0.2$

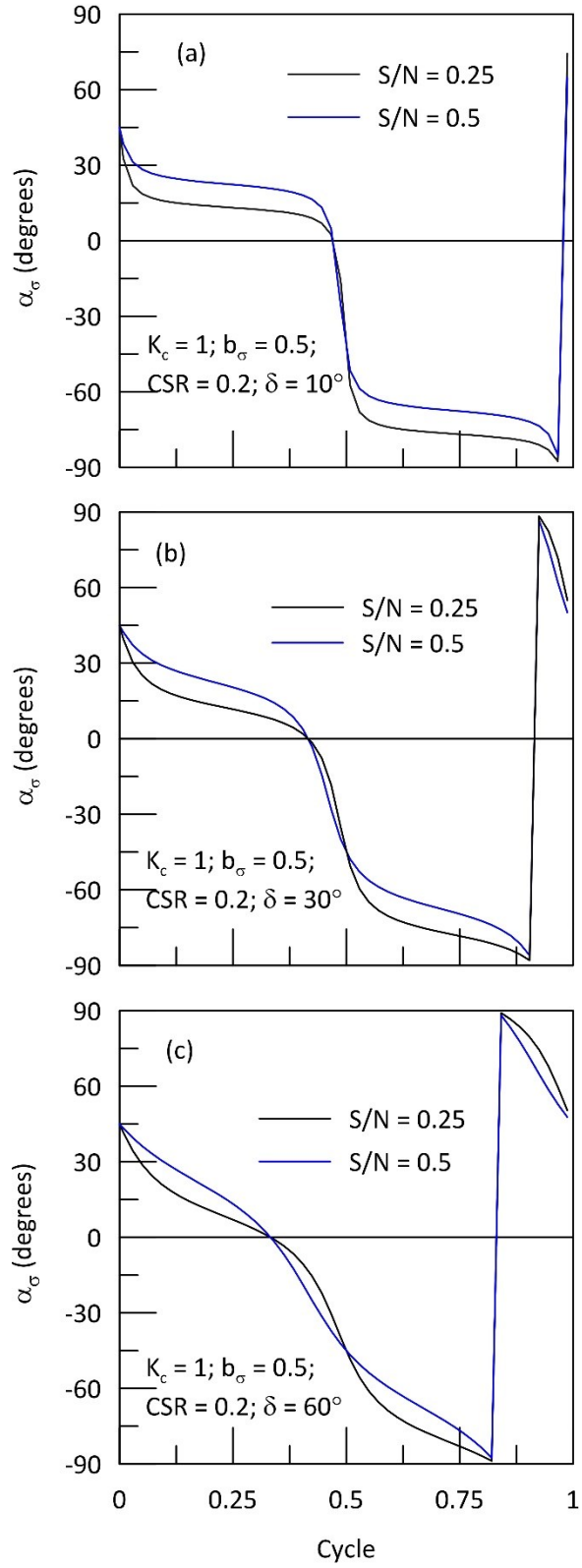


Figure 6.19: Rotation of α_σ for different δ and S/N

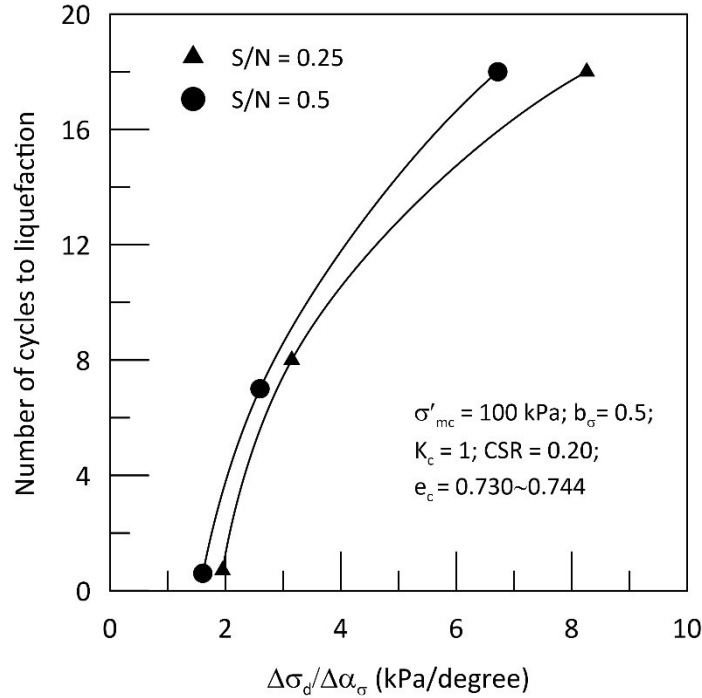


Figure 6.20: Influence of $\Delta\sigma_d/\Delta\alpha_\sigma$ on number of cycles to liquefaction

6.4 Effect of coupled loading on anisotropically consolidated loose sand specimens

This section discusses the cyclic response of anisotropically consolidated Fraser River sand specimens subjected to the simultaneous action of compression and shear waves which are in phase with each other. Loosely deposited sand specimens are consolidated to $\sigma'_{mc} = 100 \text{ kPa}$ with $K_c = \sigma'_{1c}/\sigma'_{3c} = 1.5$ & 2 and subjected to cyclic loading with *CSR* of 0.25, *S/N* of 0.25, 0.5 and 1. The relative density of the specimens at the end of consolidation is about $38 \pm 2\%$. As in the previous case, for a particular *S/N*, *HSR* is modified to yield a targeted *CSR* of 0.25 and the details of these loading parameters are tabulated in Table 6.1. The total mean normal stress σ_m and the intermediate principal stress parameter b_σ was held constant during cyclic shearing.

The results of a typical coupled loading test on anisotropically consolidated (AC) Fraser River sand specimen is shown in Figure 6.21. The sample is anisotropically

consolidated to σ'_{mc} of 100 kPa with $K_c = 1.5$ and this K_c give rise to an initial static shear stress of $\tau_{static} = 20 \text{ kPa}$. The specimen is subjected to a coupled cyclic loading with HSR of 0.162, S/N of 0.5 and $\delta = 0^\circ$. This initial and shearing condition generates an asymmetric sinusoidal rotation of principal stress axes with α_σ rotating between 12.1° and -38.4° . Unlike IC specimen, in AC specimen the accumulated pore water pressure increases rapidly within first few loading cycles and after that the accumulated excess pore water pressure varies only by a small magnitude as the cyclic loading progresses. Unlike IC specimen where the shear strain development is fairly rapid, the shear strain accumulates gradually with the loading cycle and eventually reaches the liquefying shear strain of 3.75% in the AC test. The specimen liquefied in 16 loading cycles but even after reaching the liquefying strain of 3.75% the maximum excess pore water pressure generated is only about 80% of the initial effective confining pressure. The effective stress path once it reaches the phase transformation line gets stabilized and essentially repeats the same pattern. This is due to the fact that the initial static shear is higher than the cyclic shear stress amplitude, and this clearly shows that even under generalized coupled loading condition, the presence of initial static shear stress may significantly alter the pore water pressure and shear strain response of sands. Since the loading is carried out with $\delta = 0^\circ$, the applied stress path varies linearly in $\tau_{z\theta} - (\sigma_z - \sigma_\theta)$ space. For this linear variation in the applied stress path, the developed strain path in $\varepsilon_{z\theta} - (\varepsilon_z - \varepsilon_\theta)$ space almost also follows a linear zig-zag pattern but with increasing magnitude of strains with the loading cycles. This linear zig-zag variation in the developed strain path is also observed in IC specimen till the effective stress path reaches the PT line.

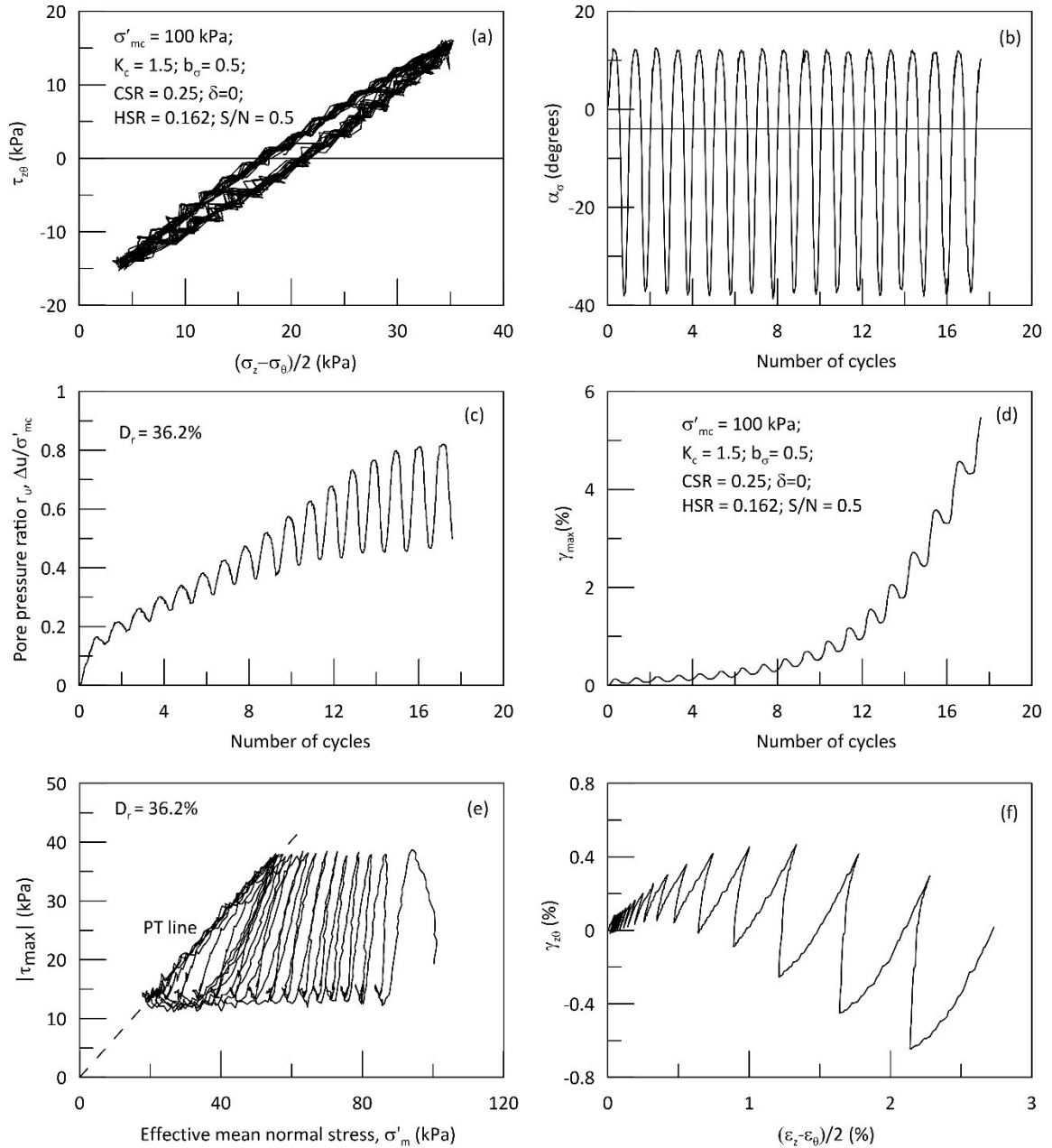


Figure 6.21: Typical response of anisotropically consolidated Fraser River sand specimen subjected to coupled loading.

Figure 6.22 compares the pore pressure and shear strain development of anisotropically consolidated sand subjected to cyclic loading with CSR of 0.25 and S/N varying from 0.25 to 1. The excess pore water pressure accumulated gradually as the loading cycle progresses and the rate of pore pressure generation systematically increases

with the increase in S/N . At $K_c = 1.5$ & $S/N = 0.25$, the sand did not liquefy even after 100 loading cycles. A maximum pore water pressure of about 65% of initial σ'_{mc} and γ_{max} of about 2% was generated at the end of 100 cycles. The sand would have liquefied if the cyclic loading is continued further. However, the stress cycles applied in laboratory cyclic tests correspond to the equivalent number of uniform stress cycles, N_{eq} , proposed by Seed et al. (1975) to represent the shaking during an earthquake. It has been presumed that loading more than hundred N_{eq} is highly unlikely, even during the strongest seismic shaking; thus, cyclic loading was not continued further in these cases. Since the soil did not liquefy even after 100 cycles for this condition, presumably increasing K_c with $S/N = 0.25$ would further increase the cyclic resistance of sand.

Figure 6.23 shows the effect of K_c on the development of pore pressure and maximum shear strain on the cyclic behavior of sand. The rate of pore pressure and shear strain accumulation decreases with the increase in K_c . It can be observed that unlike IC specimens the pore pressure ratio (r_u) never reaches unity for AC specimens even after attaining the liquefying shear strain of 3.75%. The r_u at liquefaction decreases with the increase in K_c . This observation on the reduction in terminal pore water pressure with the increase in K_c is consistent with the findings reported in Vaid and Chern (1983) and Boulanger and Seed (1995).

From Figure 6.22 and 6.23, it can be noted that for anisotropically consolidated specimens, the accumulated maximum shear strain increases steadily with the increase in loading cycle and eventually reaches the failure shear strain. This gradual accumulation of shear strain is a typical feature of liquefaction failure due to cyclic mobility.

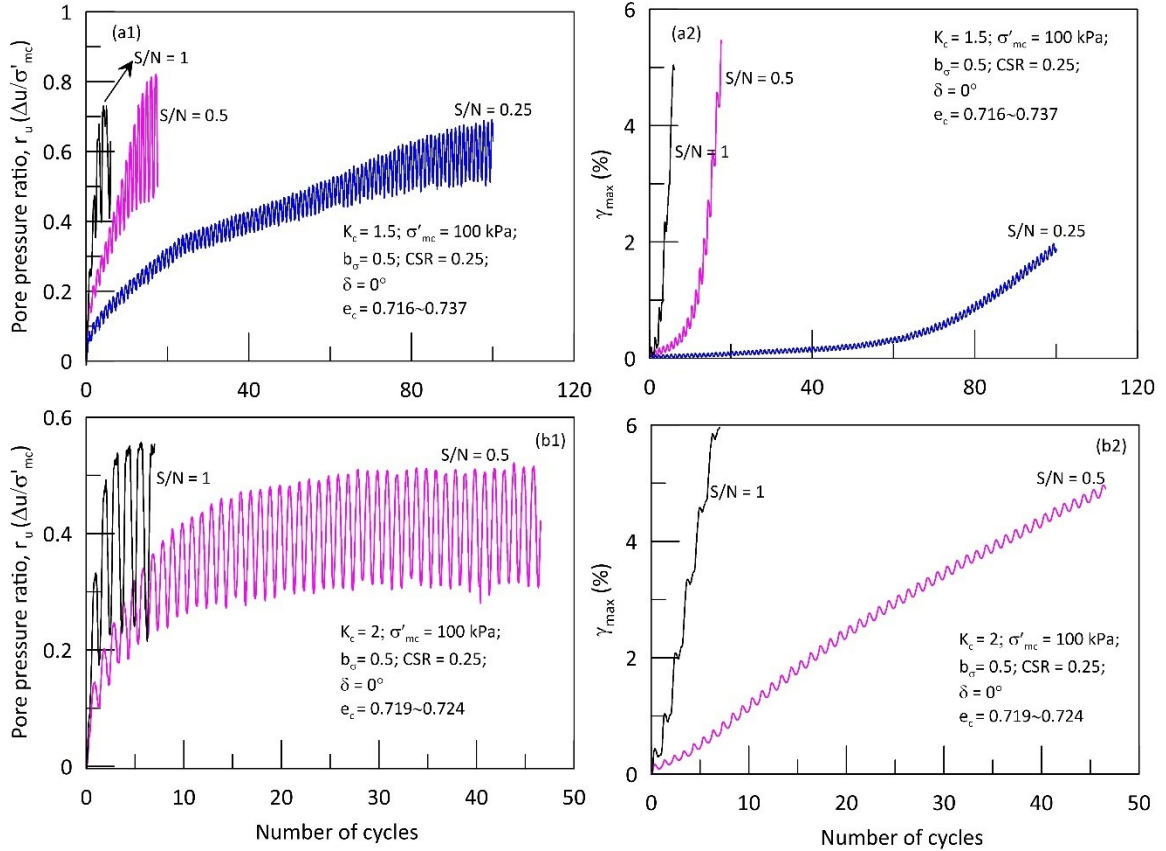


Figure 6.22: Pore pressure and shear strain response of sand different S/N

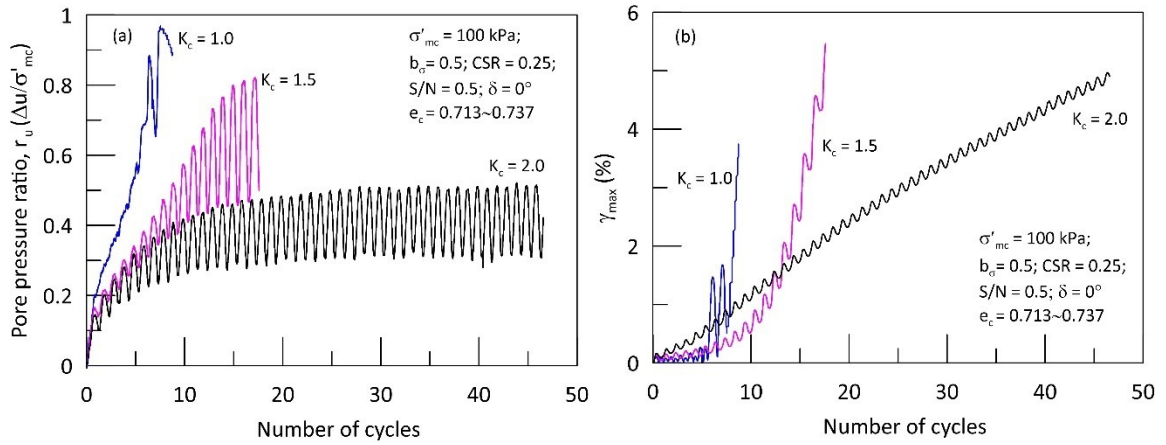


Figure 6.23: Effect of K_c on pore pressure and shear strain response of sand

The variation in the number of cycles to liquefaction (N_L) with S/N at different levels of K_c is illustrated in Figure 6.24. Irrespective of K_c , increasing S/N reduces the cyclic resistance of the sand which is presumably due to the closest alignment of τ_{max}

with the bedding plane along with the increase in shear stress in the horizontal bedding plane with the increase in S/N . Figure 6.25 presents the variation of N_L with respect to initial static shear stress ratio ($\alpha_{st} = (\sigma'_{1c} - \sigma'_{3c})/2\sigma'_{mc}$) for different S/N values. The liquefaction resistance of loose Fraser River sand increases with the increase in α_{st} for $S/N = 0.25$ & 0.5 and the resistance is almost unaffected by the increase in α_{st} for $S/N = 1$. From this it can be concluded that the rate of increase in cyclic resistance with α_{st} decreases with the increase in S/N .

In practice, the influence of initial static shear stress on the cyclic resistance is accounted by the factor K_α which is defined as the ratio of cyclic resistance of the soil with static shear to that without static shear. In addition to initial static shear, K_α depends on different parameters such as relative density, confining pressure, type of sand (contractive or dilative) and degree of stress rotation (Vaid and Chern 1985; Seed and Harder 1990; Harder and Boulanger 1997; Vaid et al. 2001; Sivathayalan and Ha 2011; Sinthujan 2013). Even with many past investigations, still the variation of K_α is contentious and the 2001 NCEER report recommended that non-specialists shall not use the K_α correction factor (Youd et al. 2001). K_α usually accounts for the initial orientation of principal stress but it ignores the effect of subsequent degree of rotation or the effect of loading mode on the cyclic resistance. Sivathayalan and Ha (2011) showed that for semi angular, strain hardening Fraser River sand K_α values almost greater than unity for most of the cases and the K_α obtained from triaxial loading mode is always higher than the one obtained simple shear loading condition (Figure 6.26).

In this present investigation on the coupled loading condition, the ratio S/N represents the various degrees of coupled triaxial and simple shear loading condition

which reproduces the possible nature and degree of stress rotation encountered in-situ. Tests with smaller S/N are closer to the triaxial condition whereas tests with larger S/N approach the simple shear loading condition. Even though only a limited number of cyclic tests were performed on the anisotropically consolidated sand specimens in this study, the observation that the rate of increase in cyclic resistance with α_{st} decreases with the increase in S/N confirms the findings of Sivathayalan and Ha (2011) that for loose sand triaxial loading mode yields higher K_α than the simple shear mode. Therefore, the results from this study adds further confidence to the existing K_α variation with static shear stress under different loading mode for the loose sub angular Fraser River sand.

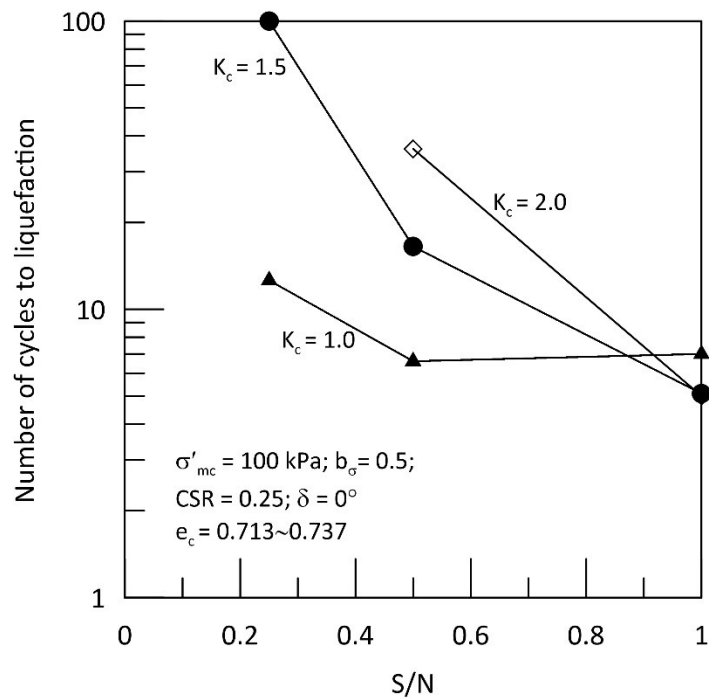


Figure 6.24: Influence of K_c on number of cycles to liquefaction

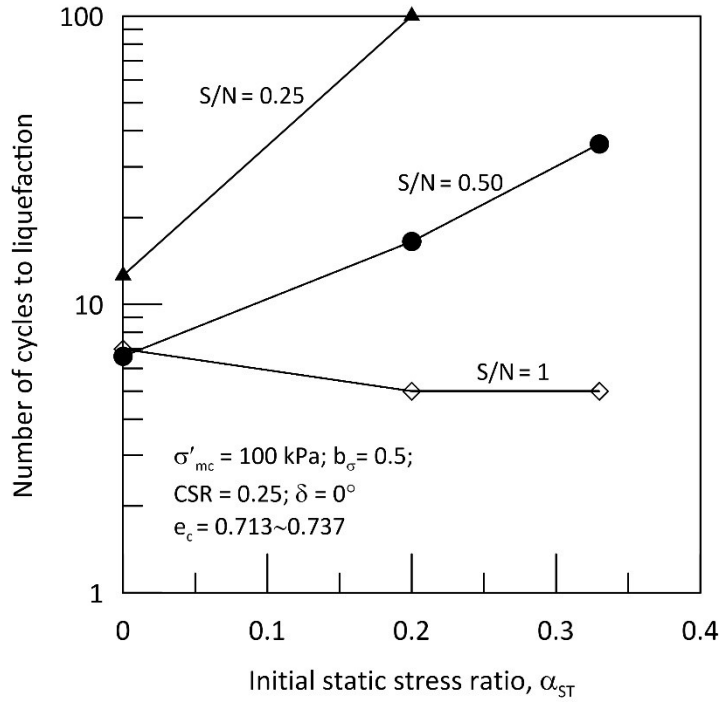


Figure 6.25: variation of N_L with respect to initial static shear stress ratio

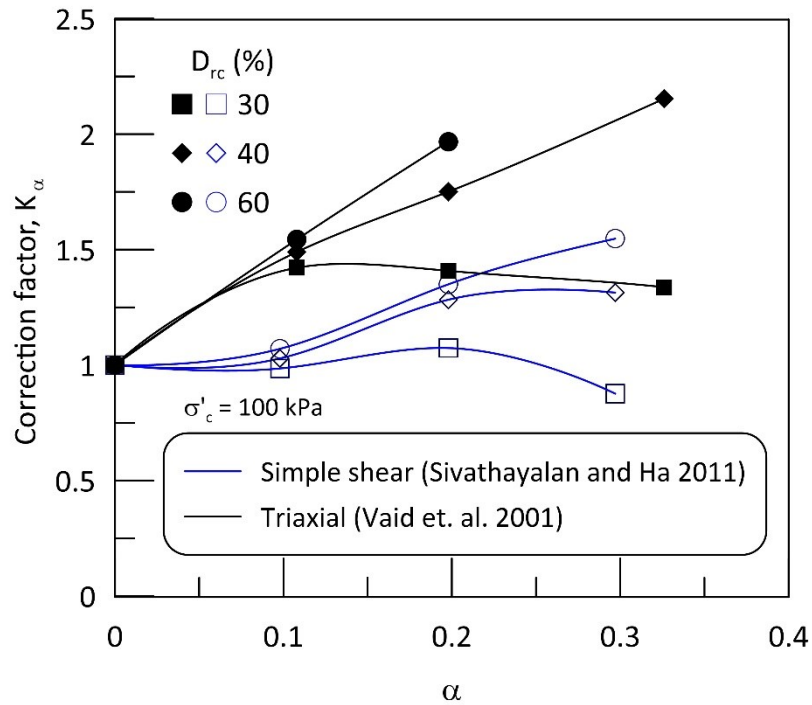


Figure 6.26: K_α under simple shear and triaxial loading mode for Fraser River sand (after Sivathayalan and Ha (2011)).

6.5 Simulation of coupled loading with shear wave and one-way compressional wave

This series of tests were performed to investigate the cyclic behavior of sands under more complicated cyclic loading paths that will be encountered in-situ during various dynamic loading conditions. In the coupled loading cases discussed earlier in Chapter 5, the S/N is maintained constant throughout the cyclic loading. But a constant S/N condition may not necessarily be possible in an actual in-situ loading. Therefore, in order to assess more complex dynamic loading paths, a series of tests where S/N is varied continuously (with normal stress increments in a one-way cyclic pattern and shear stress increment in a two-way cyclic pattern) were conducted. The frequency of applied normal stress increment is twice that of the shear stress increment in this case. In-situ loading always involves seismic waves at different frequencies. But typical liquefaction assessment studies do not consider frequency effect since they only deal with a vertically propagating shear wave, and the effects of frequency have been demonstrated to be not significant in general. However, differences in the frequencies of the P-wave and S-wave components could lead to significantly different loading patterns and peak amplitudes. Therefore, assessment of the issues related to the P- and S- wave frequencies in simultaneous loading is important. The one-way cyclic variation in normal stresses adopted here is also quite common during traffic loading conditions (Brown 1996, Ishihara 1996, Wang et. al. 2017). Further, one-way unsymmetrical cyclic loading is also experienced by soil elements beneath offshore foundations (Randolph and Gourvenac 2011).

Figure 6.27 presents the variation of the applied $\Delta\tau_{z\theta}$ with $\Delta(\sigma_z - \sigma_\theta)$ and its corresponding change in α_σ for different amplitudes of S/N in an isotropically

consolidated stress state. Under this condition, the applied stress path in $\tau_{z\theta} - (\sigma_z - \sigma_\theta)$ space varies parabolically with α_σ undergoing jump rotation, but unlike two-way cyclic waves, α_σ is not constant during the first and second half of the loading cycle. Here α_σ varies in a concave up fashion in the first half of the loading cycle and concave down pattern in second half of the loading cycle. It can also be noticed that the degree of rotation is highly influenced by S/N , with α_σ almost rotates between $\pm 45^\circ$ at larger S/N values.

Figure 6.28 presents the variation of $\Delta\tau_{z\theta}$ and $\Delta(\sigma_z - \sigma_\theta)$ when the phase shift (δ_{SN}) is introduced between $\Delta\tau_{z\theta}$ and S/N . The increase in phase shift between $\Delta\tau_{z\theta}$ and S/N creates a more complicated butterfly shaped loading path in $\tau_{z\theta} - (\sigma_z - \sigma_\theta)$ space. As the δ_{SN} increases from 0° to 90° , the non-reversal variation in normal stress increment changes to a non-symmetrical reversal variation. This butterfly shaped loading path will also be encountered when the frequency is changed between the sinusoidal P-wave and S-wave. From Figure 6.28 c, it can also be observed that the variation of α_σ is continuous in nature but the degree of rotation depends significantly on S/N . For a given S/N , the rotation range is almost unaffected by the increase in δ_{SN} .

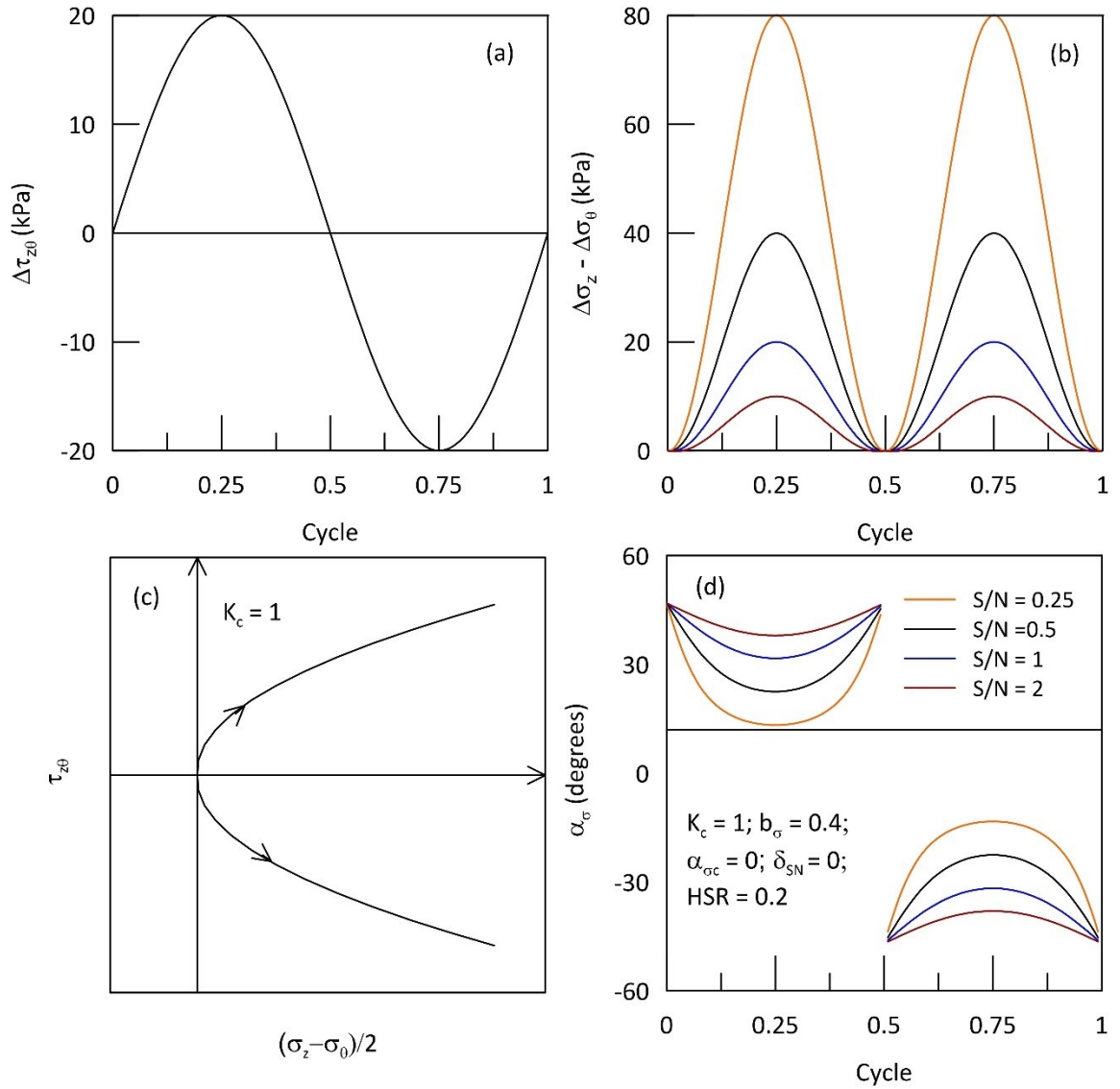


Figure 6.27: Coupled loading with one-way compression wave and its corresponding stress rotation at various S/N .

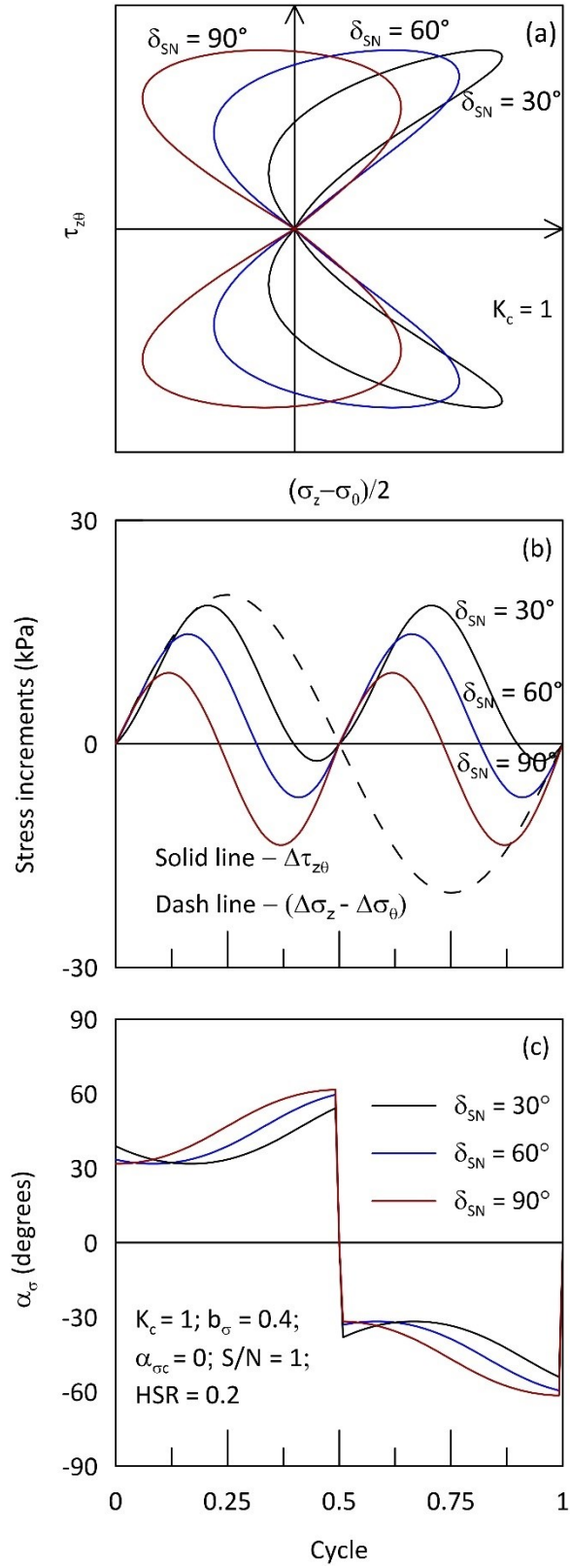


Figure 6.28: Coupled loading with one-way compression wave at different δ_{SN}

In this study, a series of cyclic tests were performed on isotropically consolidated loose Fraser River sand specimens to investigate the effect of cyclic stress ratio CSR (τ_{max}/σ'_{mc}), S/N and phase shift (δ_{SN}) between $\Delta\tau_{z\theta}$ and S/N on the pore pressure and shear strain response of sand. Representative amplitudes of S/N varying from 0.1 to 1.5, CSR ranging from 0.25 to 0.45 and δ_{SN} changing from 0° to 90° were considered for the analysis. Table 6.2 summarizes the details of cyclic tests carried out for this investigation. The cyclic torsional stress increment was applied at a loading rate of 4 minutes per cycle and the loading rate of normal stress increment varies depending on the loading parameters. During cyclic loading, the total mean normal stress (σ_m) and intermediate principal stress parameter ($b_\sigma = 0.4$) were kept constant.

Table 6.2: Initial and cyclic loading parameters for tests with one-way P wave

Test No	Consolidation stage			Shearing stage				
	Stress state	e_c	D_{rc} (%)	CSR	HSR	S/N	$\delta_{SN}(^\circ)$	
EQ02	$\sigma'_{mc} = 100 \text{ kPa};$ $k_c = 1;$ $b_\sigma = 0.4; \alpha_\sigma = 0$	0.732	41.0	0.42	0.2	0.269	0	
EQ03		0.723	40.1	0.32		0.407		
EQ04		0.720	41.1	0.27		0.550		
EQ08		0.724	40.1	0.32	0.083	0.134		
EQ09		0.718	41.7		0.150	0.269		
EQ10		0.713	43.2		0.240	0.55		
EQ11		0.722	40.5		0.273	0.848		
EQ12		0.721	40.9		0.294	1.17		
EQ13		0.731	37.9		0.21	0.437		30
EQ14		0.728	38.9		0.246	0.546		60
EQ15		0.733	37.6		0.292	0.681		90

A typical response of Fraser River sand specimen subjected to coupled one-way cyclic normal stress increment and two-way cyclic shear stress increment is discussed below. The specimen is isotropically consolidated to an effective mean normal stress of 100 kPa and sheared under a constant b_σ of 0.4. The soil specimen is subjected to an HSR of 0.20 and S/N of 0.269 which results in a CSR of 0.42. A maximum shear stress and normal stress increment of 20 kPa and 74.4 kPa was applied to the soil specimen which results in a generation of parabolic loading path. Figure 6.29 presents the suite of data obtained from sand's response to this coupled cyclic loading. Here, the sand liquefied in 5 loading cycles with the generation of maximum porewater pressure ratio of about 0.85. Unlike coupled two-way cyclic loading, here the pore pressure generation shows more distinct variation in the peaks and troughs with even larger pore pressure reversals of about 40% of initial σ'_{mc} after the effective stress path passes the PT line. Here, the liquefaction is predominantly due to cyclic mobility where the shear strain accumulates gradually with the loading cycle and eventually reaches the liquefying shear strain of 3.75% without realizing the transient state of zero effective stress. It is also interesting to note that the developed strain path in $\varepsilon_{z\theta} - (\varepsilon_z - \varepsilon_\theta)$ space almost follows the shape of the applied stress path but the developed parabolic strain path expands with the increasing magnitude of strains.

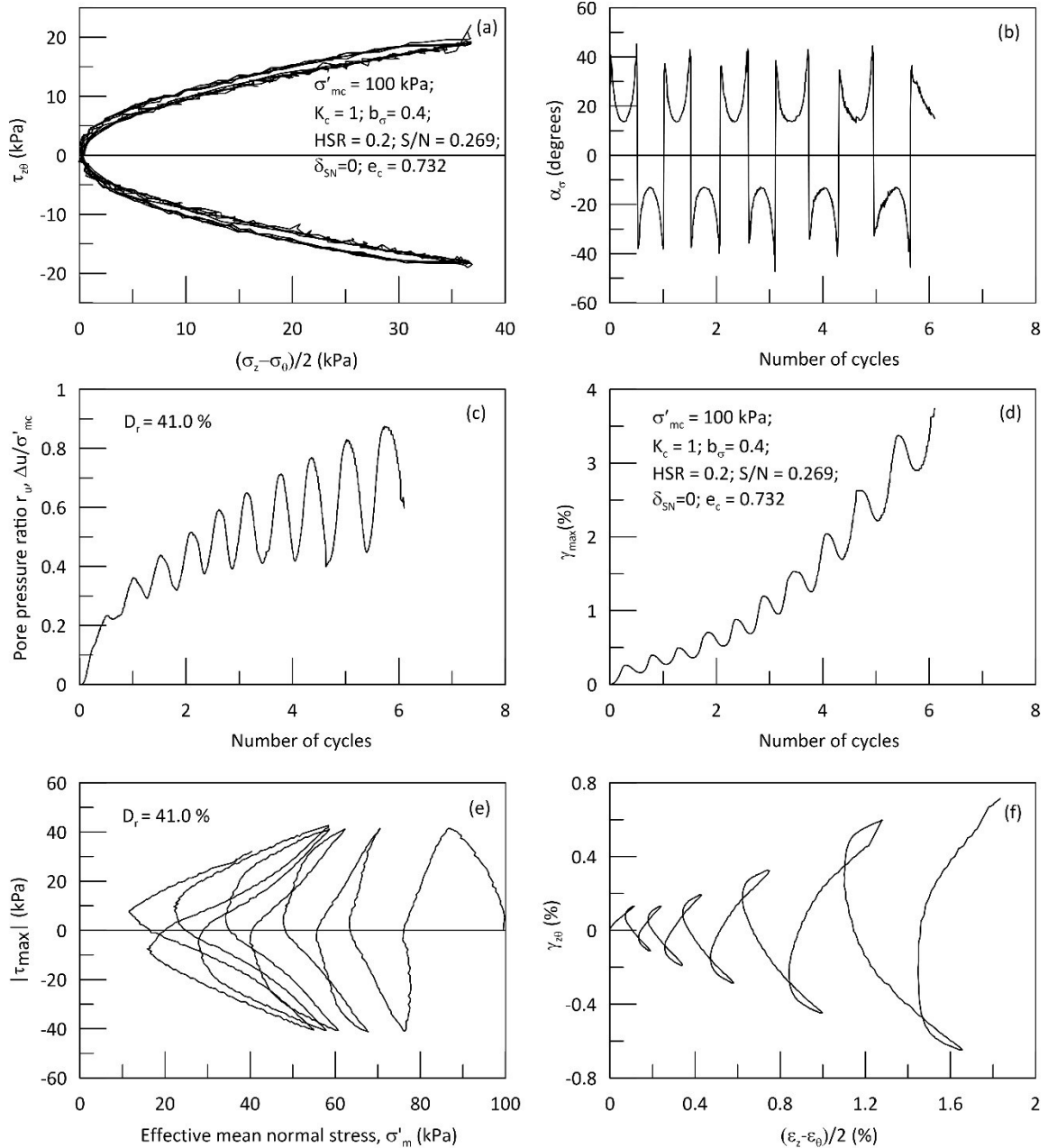


Figure 6.29: Typical response of sand subjected to coupled loading with one-way compression wave

Figure 6.30 illustrates the variation of excess pore water pressure and maximum shear strain induced during this coupled cyclic loading at different levels of cyclic stress ratios. In this test series, the *HSR* is kept constant at 0.2 and *S/N* ratio is altered to give different levels of *CSR*. The change in *CSR* is inversely proportional to the change in

S/N and the range of rotation decreases with increasing S/N . At $S/N = 0.269$, α_σ rotates between 15° to 45° whereas at $S/N = 0.55$, α_σ rotates between 25° to 45° . As an expected behaviour, the cyclic resistance of sand decreases with the increase in CSR . Under this coupled action of one-way cyclic normal stress and two-way cyclic shear stress, the sand liquefied in 21 cycles for CSR of 0.27 and about 5 cycles for CSR of 0.42. Even with the very high CSR of 0.42, in which the applied τ_{max} is almost close to the S_{PT} , there is no sudden development of maximum shear strain or pore water pressure like in flow failure, but the failure is incurred to sand specimens due to the progressive accumulation of shear strains.

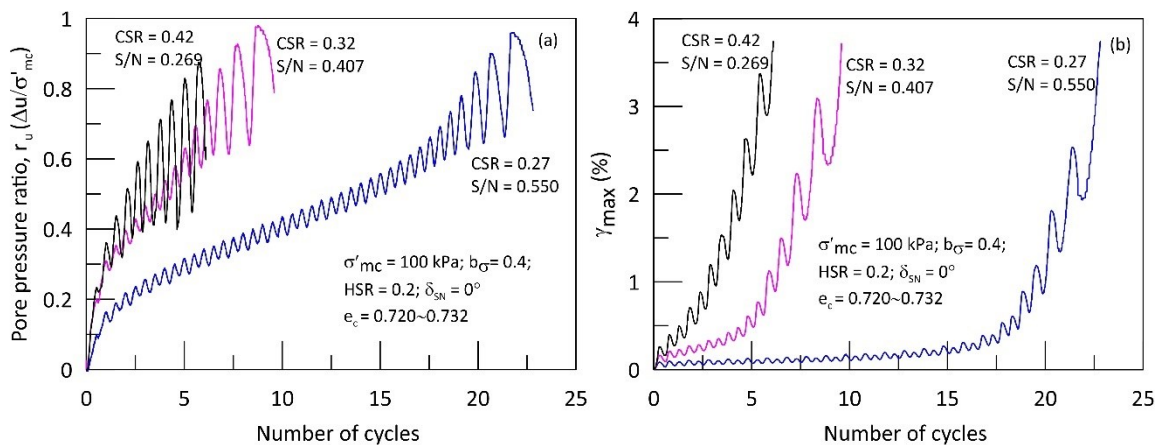


Figure 6.30: Comparison of pore pressure and shear strain response at different CSR

Figure 6.31 compares the cyclic resistance curves obtained from coupled one-way cyclic loading as well as coupled two-way cyclic loading. It can be seen that the cyclic resistance can vary significantly depending on the type of loading waves imposed on the soil samples. Sand specimens tested with one-way loading exhibits higher cyclic strength when compared to the sand specimens tested with two-way loading. Towhata and Ishihara (1985) also made similar observation through the one-way and two-way cyclic triaxial tests on loose Toyoura sand. Figure 6.31 also presents the cyclic resistance curves

obtained from the data reported in the literature from cyclic triaxial (Vaid and Thomas 1995) and cyclic simple shear tests (Vaid and Sivathayalan 1996a) on Fraser River sand to compare the trend of variation in the number of cycles to liquefaction with the cyclic stress ratio. These test results cannot be compared directly because these tests are carried out on different batches of Fraser River sand and subjected to different loading mode involving different b_σ and α_σ rotation. But, the range of variation is an indication of the test conditions, and the effects of stress rotation on the undrained cyclic strength of sands.

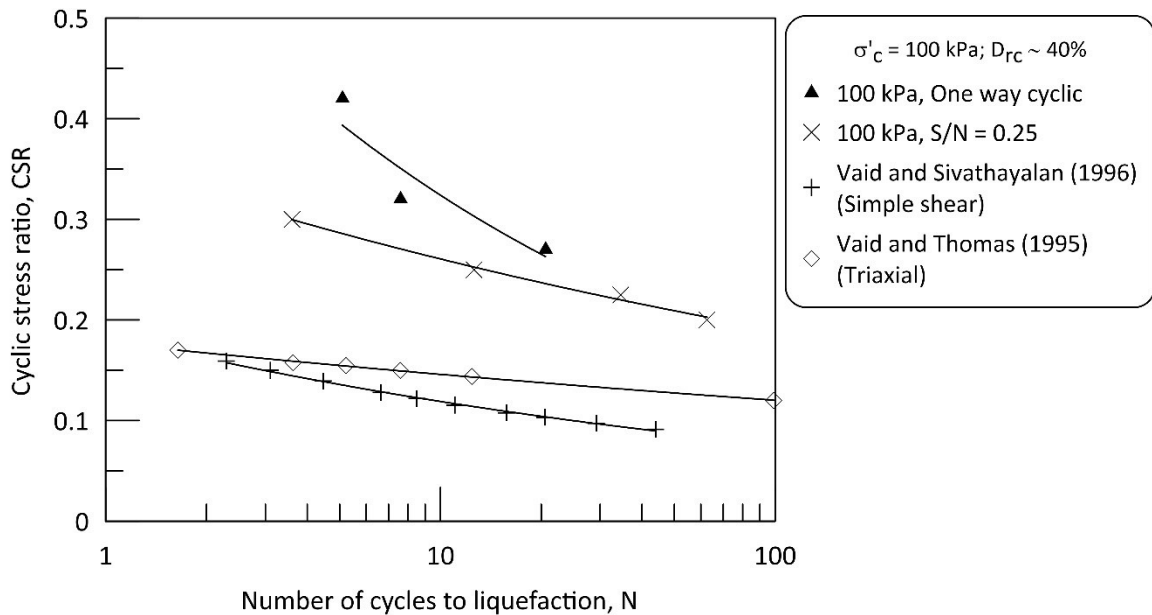


Figure 6.31: Cyclic resistance curves from different loading conditions

6.5.1 Influence of S/N and δ_{SN} on the liquefaction characteristics of Fraser River sand

The objective of this test scheme is to evaluate the cyclic behavior of sand under more complex dynamic loading paths. A series of tests was carried out to assess the effect of different combination of S/N and HSR on the mechanism of liquefaction at a fixed CSR of 0.32 and a fixed parabolic loading path ($\delta_{SN} = 0^\circ$). Figure 6.32 illustrates the variation of HSR with respect to S/N for a given CSR of 0.32 and it can be seen that for

this particular *CSR*, *HSR* increases with the increase in *S/N*. At $S/N < 1$, the amplitude of normal stress increment is greater than the shear stress increment and vice versa for $S/N > 1$. Figure 6.33 shows the variation of principal stresses and the applied torsional and normal stress increments for the typical aforementioned loading cases. This shows that even with these variations in the applied stress increments, the principal stress variations are identical across all the tests due to the fixed *CSR*.

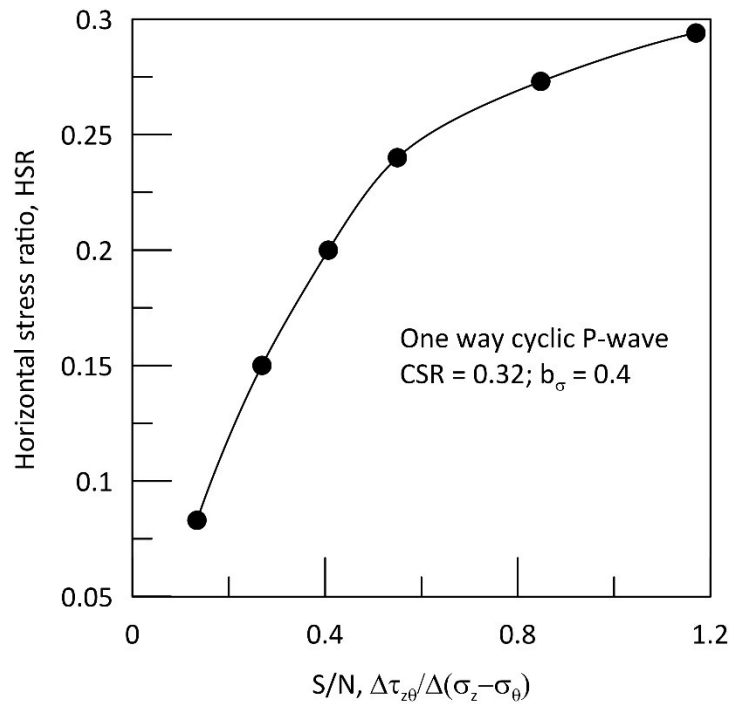


Figure 6.32: Variation of *HSR* with *S/N*

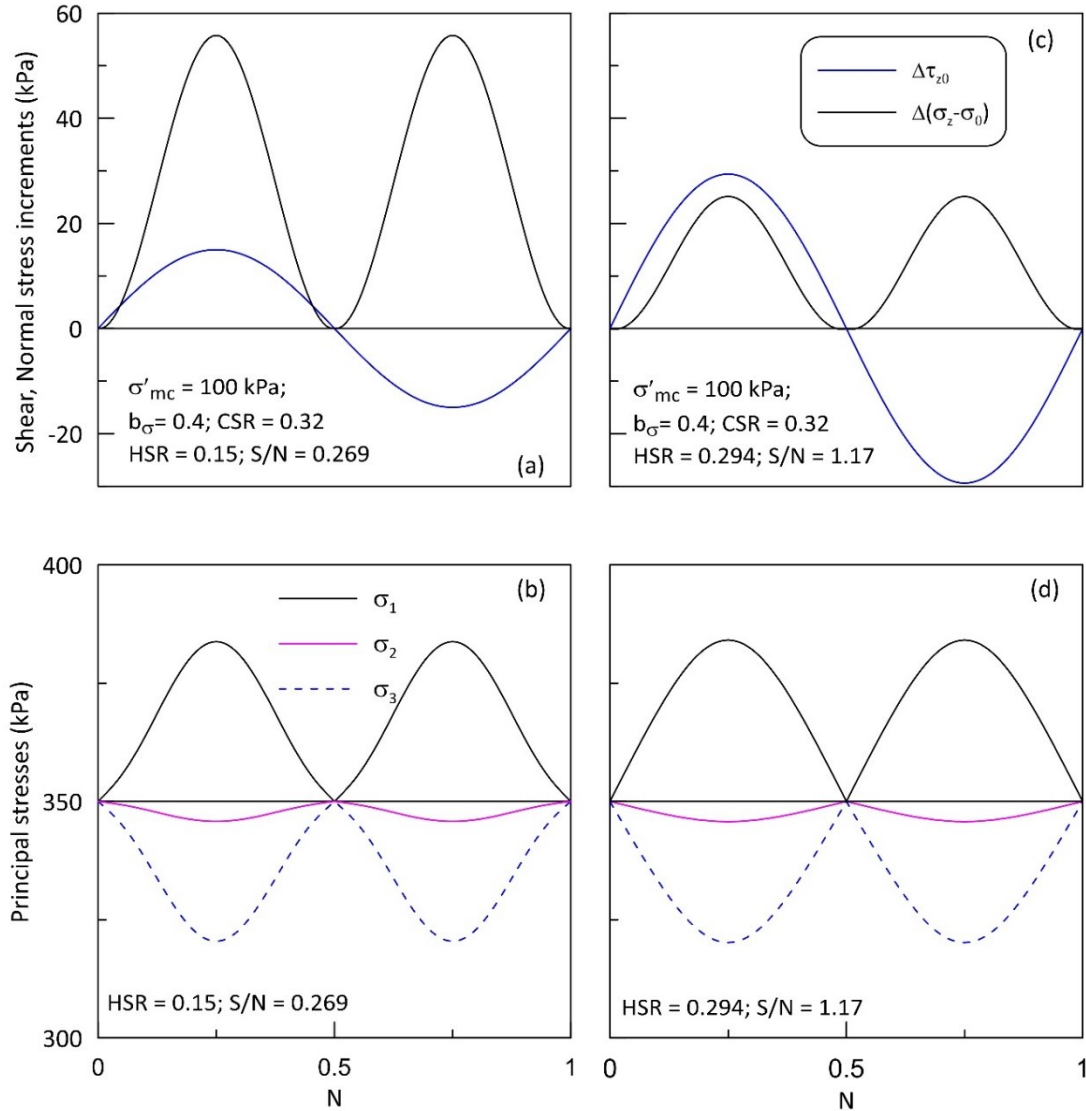


Figure 6.33: Variation of applied stress increments and principal stresses for $S/N = 0.269$ & 1.17

Shown in Figure 6.34 are the effective stress path responses of Fraser River sand subjected to CSR of 0.32 at different levels of S/N . Here the test results are evaluated as a function of S/N . Irrespective of S/N , the liquefaction is incurred to soil samples due to the development of cyclic mobility. Even though the applied τ_{max} might be close to S_{PT} of sand, sand developed cyclic mobility regardless of the cyclic shear stress amplitude. This might be because the one-way normal stress subjects the Fraser River sand to a

stress state predominantly on its compression regime in which the α_σ never gets closer to 90° . It is well known that even in its loosest attainable state, Fraser River exhibits strain hardening response at triaxial compression loading and softening response at extension loading (Vaid and Thomas 1995; Vaid and Sivathayalan 2000 and Sivathayalan and Mehrabi Yazdi 2014) and hence due to this hardening response in the compression region, Fraser River sand exhibited cyclic mobility under coupled one-way loading.

Figure 6.35 compares the pore pressure and shear strain development of sand at different levels of S/N . Regardless of S/N , the excess pore water pressure and shear strain accumulates gradually as the loading cycle progress and the rate of accumulation systematically increases with the increase in S/N . At $S/N = 0.134$, the sand did not liquefy even after 50 loading cycles and the cyclic loading was terminated at the end of 50 cycles because even the strongest earthquakes would not produce an equivalent uniform stress cycles greater than 50 (Seed et al. 1975). A maximum pore water pressure of about 80% of initial σ'_{mc} was generated at the end of 50 cycles.

The relationship between the number of cycles to liquefaction and S/N at a fixed CSR of 0.32 is presented in Figure 6.36. The number of loading cycles required to produce liquefaction decreases with the increase in S/N because at larger S/N the sample is subjected to simple shear loading mode and at smaller S/N the sample is under triaxial loading mode. This observation is consistent with the observation noted in Chapter 5 for the coupled two way cyclic normal and shear stress. Therefore, it can be concluded that irrespective of the waveforms, the cyclic resistance of sand decreases with the closer alignment of τ_{max} with the bedding plane and also due to the increase in shear stress on the weak horizontal bedding plane.

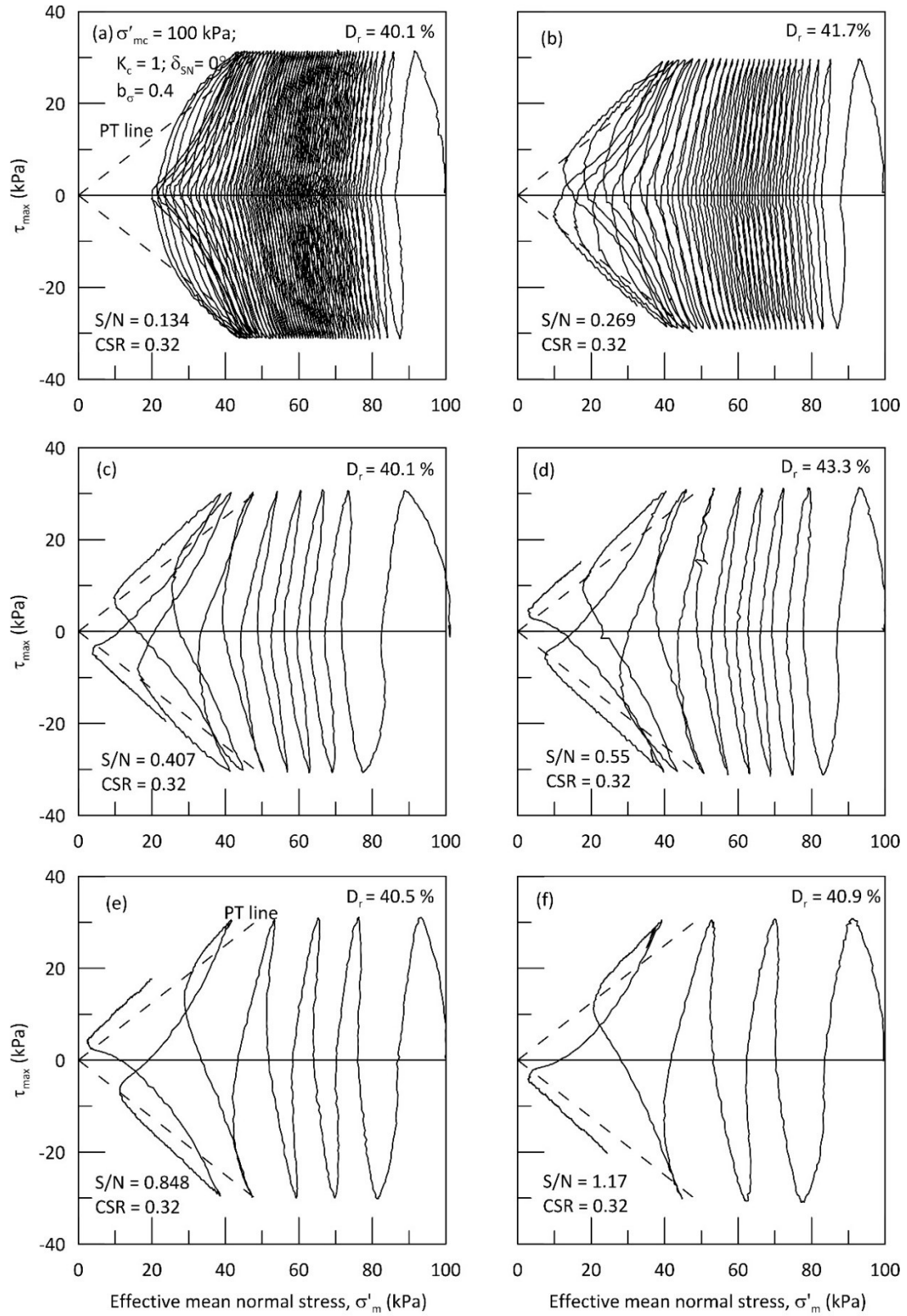


Figure 6.34: Effective stress path responses at various S/N

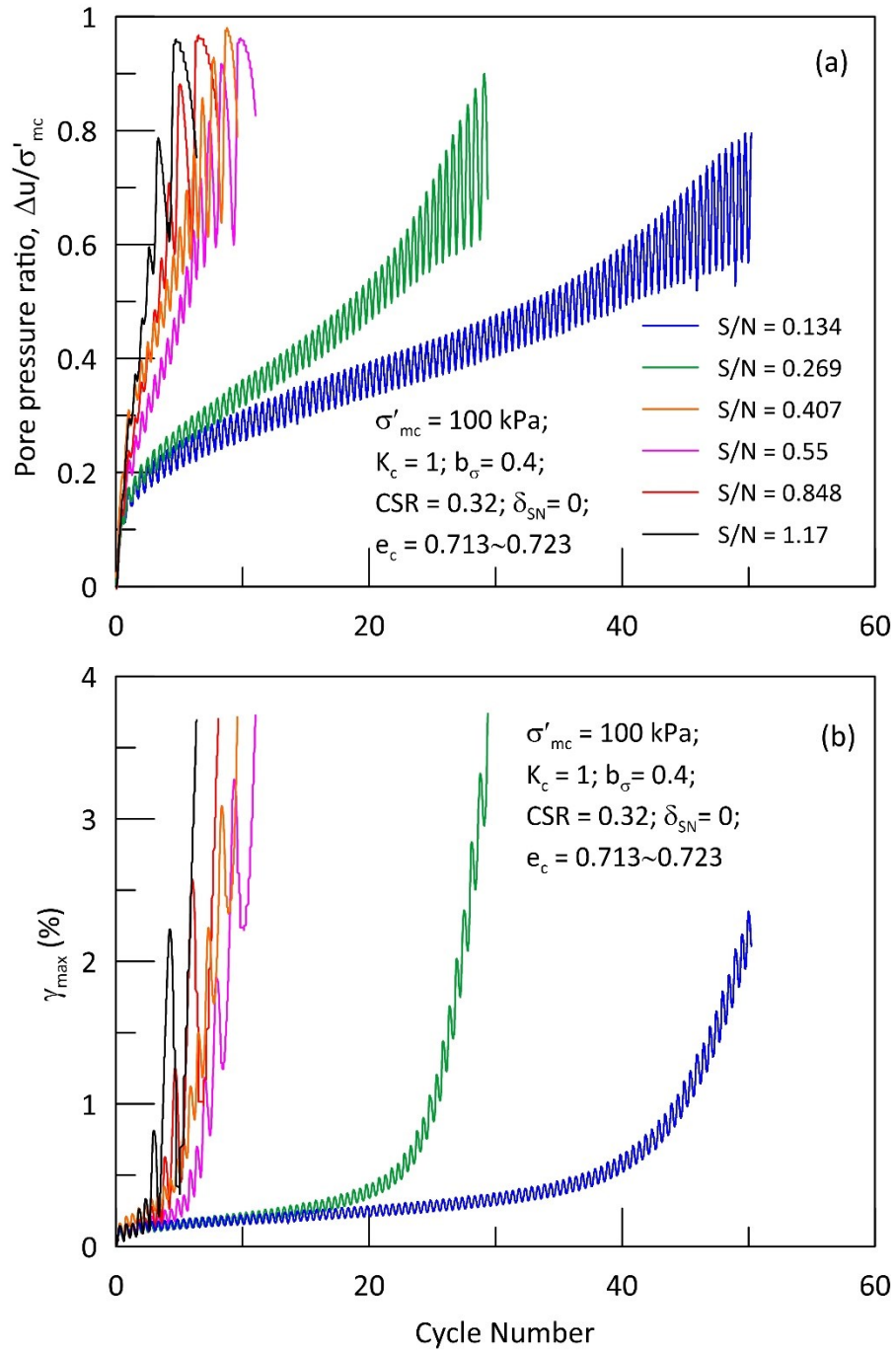


Figure 6.35: Pore pressure and maximum shear strain development at various S/N

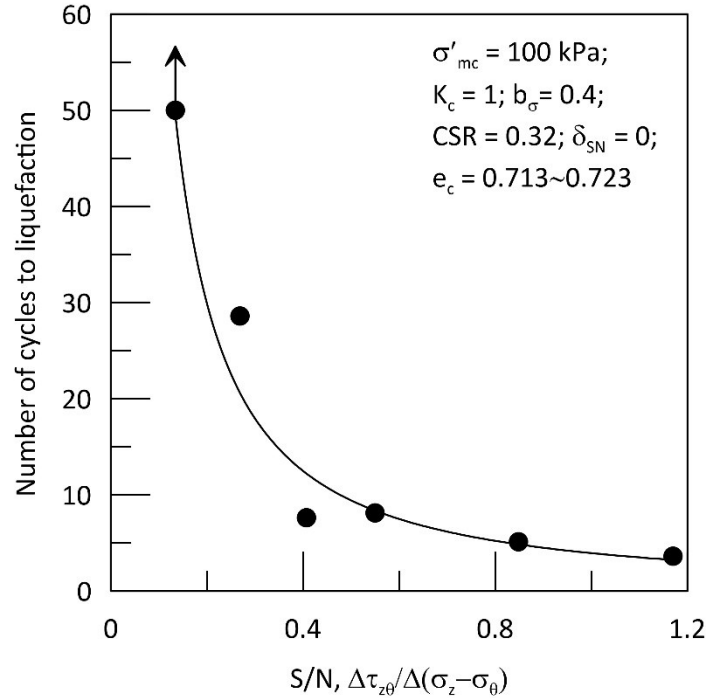


Figure 6.36: Number of cycles to liquefaction with S/N for one-way cyclic P-wave.

Figure 6.37 presents the applied stress path and effective stress path response of sand sheared with a fixed CSR of 0.32, but with different phase shifts ($\delta_{SN} = 30^\circ, 60^\circ$ & 90°). Figure 6.38 shows the variation of applied stress increments, stress rotation and principal stresses for the aforementioned loading cases. This test series demonstrates the ability of CU-HCT to trace fairly complex loading paths with sufficient resolution. It can also be noted that the magnitude of principal stress variation is almost identical in all the loading cases due to the fixed CSR of 0.32. Here δ_{SN} signifies the change in the non-reversal variation in the normal stress increment to reversal variation and also the magnitude of stress reversal increases with the increase in δ_{SN} . The pore water pressure build-up and consequent onset of liquefaction can be observed from the effective stress path plot shown in Figure 6.37. It can be seen that the tendency of cyclic mobility decreases with the increase in δ_{SN} and also the cyclic resistance of sand

decreases with the increase in δ_{SN} . Sand liquefied in 8 cycles for $\delta_{SN} = 30^\circ$ and within 2 cycles for $\delta_{SN} = 90^\circ$. The behavior might be because as the phase δ_{SN} increases, the magnitude of stress reversal increases which brings the α_σ close to 90° and that is responsible for the triggering of strain softening response of loose Fraser River sand.

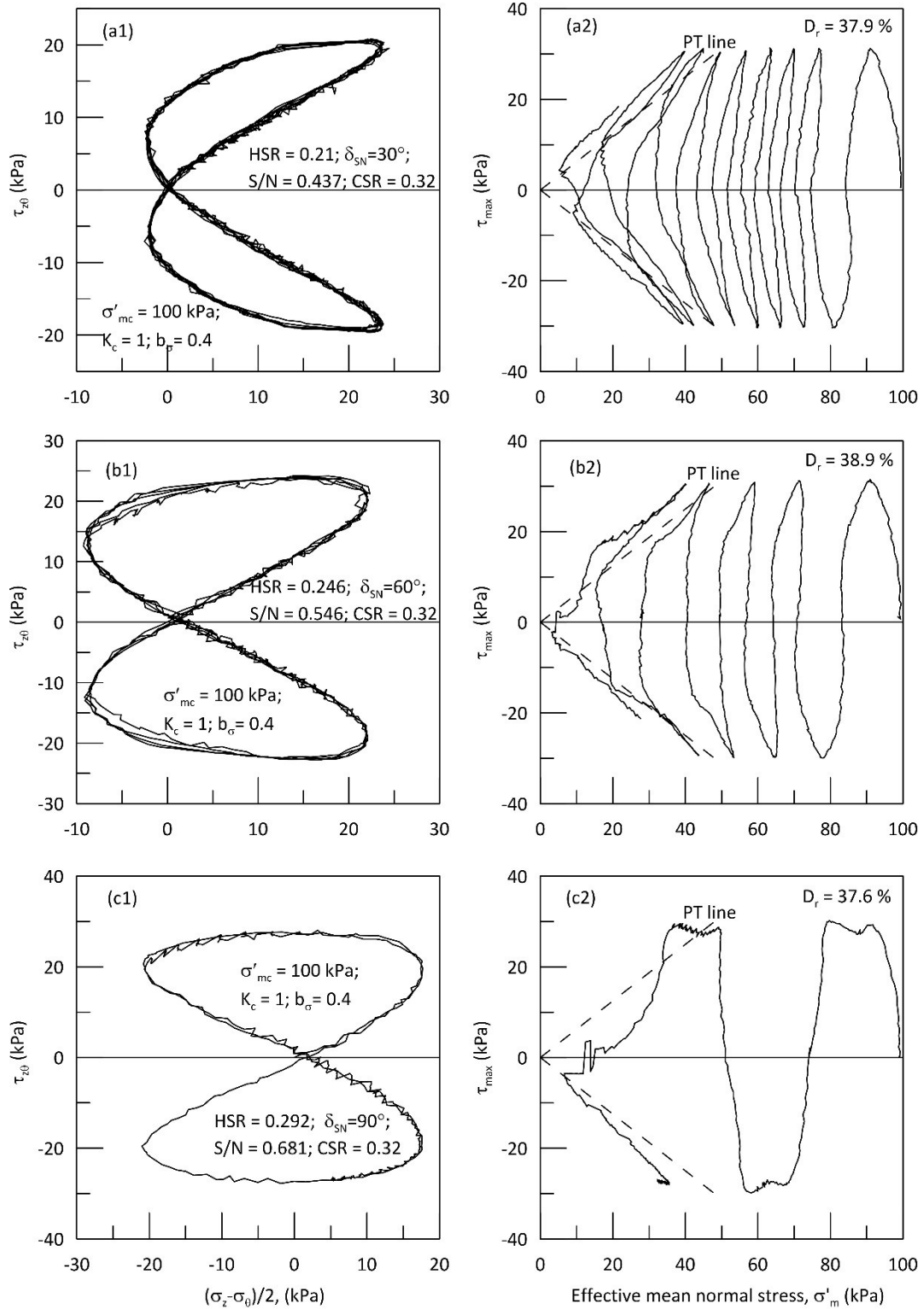


Figure 6.37: Applied stress path and effective stress path response of sand sheared with different δ_{SN}

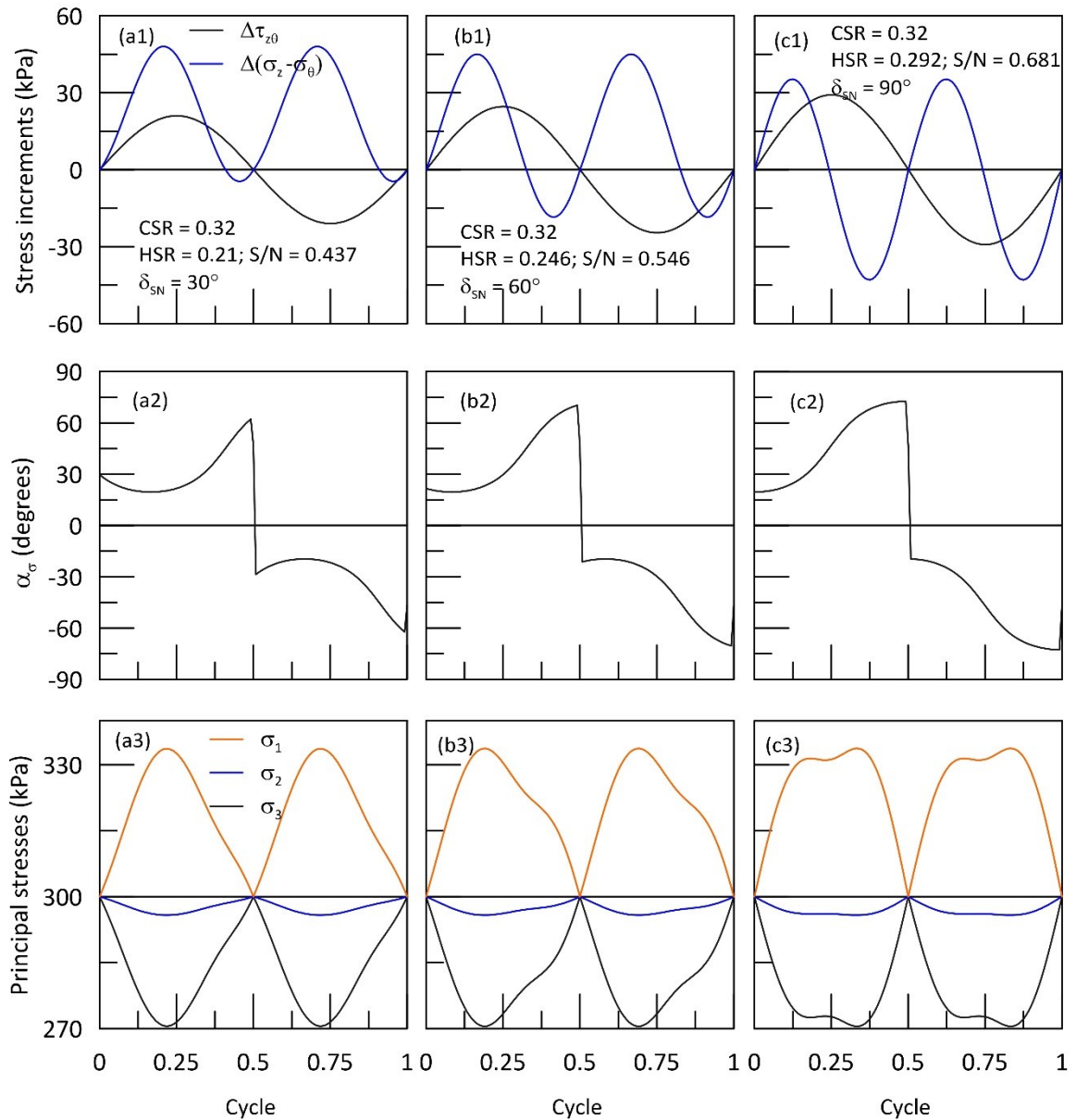


Figure 6.38: Variation of applied stress increments, stress rotation and principal stresses at different δ_{SN} .

6.6 Summary and Conclusions

A series of cyclic hollow cylinder torsional shear tests were carried out to assess the influence of phase angle (δ) between compression and shear waves, consolidation stress ratio (K_c) and the effect of simultaneous action of shear wave and one-way compression wave on the cyclic resistance of sand. In this investigation, due to the uncertainty

associated with the definition of *CSR* based on the sign convention of τ_{max} , the cyclic stress ratio is defined based on the sign independency characteristic of τ_{max} . The following conclusions were drawn based on the coupled cyclic loading tests on loose Fraser River sand:

- Under coupled loading, when the compression and shear waves are not in phase with each other it will result in the generation of elliptical loading path. With these elliptical stress paths, it is critical to examine how these stress paths are followed from the initial consolidation stress state. Two methods were assessed, and the method with drained presharing eliminates the effect of initial $\Delta\tau_{z\theta}$ on the undrained cyclic response of soil and this presharing increases the cyclic resistance of sand.
- With drained presharing and coupled loading at fixed *HSR* and *S/N*, changing the phase shift between compression and shear waves does not significantly affect the liquefaction resistance of the soil. This is possibly because the maximum amplitude of shear stress and normal stress applied to the soil specimen remains same for different δ .
- At a fixed *CSR*, increasing δ reduces the cyclic resistance because increase in δ is accompanied by the decrease in rate of change in deviatoric stress per degree of rotation ($\Delta\sigma_d/\Delta\alpha_\sigma$). At a given *CSR*, for $\delta \neq 0$ cases, change in *S/N* does not affect the liquefaction resistance of sand because the magnitude and pattern of rotation is almost unaffected by the change in *S/N*.
- Consolidation stress ratio K_c , increases the cyclic resistance of sand and it is interesting to note that the rate of increase in cyclic resistance with initial static

shear stress α_{st} decreases with the increase in S/N . This observation on the rate of increase in cyclic resistance with α_{st} decreases with the increase in S/N confirms the findings of Sivathayalan and Ha (2011) that for loose sand triaxial loading mode yields higher K_α than the simple shear mode. The test results from this study adds further confidence to the existing contentious K_α variation with static shear stress under different loading mode for the loose sub angular Fraser River sand.

- The cyclic resistance of sand can vary significantly depending on the type of loading waves imposed on the soil samples. Sand specimens tested with one-way loading exhibits higher cyclic strength when compared to the sand specimens tested with two-way loading.
- Irrespective of the waveforms, the cyclic resistance of sand decreases with the closer alignment of τ_{max} with the bedding plane and also due to the increase in shear stress on the weak horizontal bedding plane.
- The tendency of cyclic mobility decreases with the increase in δ_{SN} and also the cyclic resistance of sand decreases with the increase in δ_{SN} because as the phase δ_{SN} increases, the magnitude of stress reversal increases which brings the α_σ close to 90° and that triggers the strain softening of Fraser River sand.

7. MONOTONIC RESPONSE OF SAND UNDER PARTIALLY DRAINED CONDITION

7.1 Introduction

The strength and deformation characteristics of granular soils are influenced by several factors such as loading mode, drainage condition, soil fabric, confining stress, void ratio, and strain history. In the current design practice, the geotechnical design parameters of soil are derived either from fully undrained tests or fully drained tests because it is presumed that these two drainage conditions represent the extremes of soil response to shearing. Shearing under drained condition represents the state of deformation under constant pore water pressure. Such condition is assumed if the loading rate is slow and the permeability of soil is sufficiently high enough to permit free drainage of water. On the other hand, undrained shearing represents the deformation under constant volume state and this condition is generally assumed if the loading rate is high in a material with low permeability.

The undrained behavior of granular soil is generally assumed while evaluating its liquefaction potential under seismic shaking on account of the time delays associated with pore water pressure dissipation because of the larger area that is loaded, and given the general presumption that that the undrained condition represents the worst-case scenario. The assumption of completely undrained or drained condition is only valid if there is no pore pressure gradient exists within the soil deposit, but this condition is highly unlikely because of the heterogenous nature of the soil deposit. As a result of this heterogeneity in

soil strata, the actual drainage condition in-situ may involve partially drained conditions which can be explained using an example scenario illustrated in Figure 7.1.

Consider a layered soil profile with 5 m thick loose sandy stratum sandwiched between dense silty sand and stiff clay layer as shown in the figure 7.1. The ground water table is 1 m below the ground level and the average unit weight of the soil is taken as 20 kN/m^3 . The variation of total vertical stress, excess pore water pressure and effective vertical stress with depth, before and after a seismic event is illustrated in Figure 7.1. The seismic shaking triggers liquefaction in the loose sandy layer and it is assumed that no excess pore water pressure is generated in the overlying dense sandy stratum. The increase in excess pore water pressure (Δu) due to seismic shaking brings down the effective stress to null and also causes an upward hydraulic gradient (i) of 1 throughout the loose sandy layer. This unit hydraulic gradient is analogous to the piping condition in steady state seepage problem. Therefore, this critical hydraulic gradient causes an upward seepage of water from loose sand stratum to dense silty sand stratum resulting in an increase of excess water pore pressure in the overlying dense layer during or after the earthquake. This might cause liquefaction in the dense silty layer which is otherwise has higher cyclic resistance to seismic shaking if the soil is assumed to be fully undrained.

The upward seepage of water also causes void redistribution in soil deposit which might trigger large deformations and instability in slopes (Whitman 1985; Idriss and Boulanger 2008). The failure mechanisms induced by void redistribution and upward seepage is illustrated in Figure 7.2. In an infinite slope with liquefiable sand layer beneath a less permeable layer, the upward seepage resulting due to the generation of excess pore water pressure loosens the top of the sand layer and densifies the bottom (Figure 7.2a).

This loosened top layer might become unstable and cannot even sustain its static shear stress. The similar phenomenon illustrated in Figure 7.2b shows how the localized pore pressure gradients weakens the overlying soil layers.

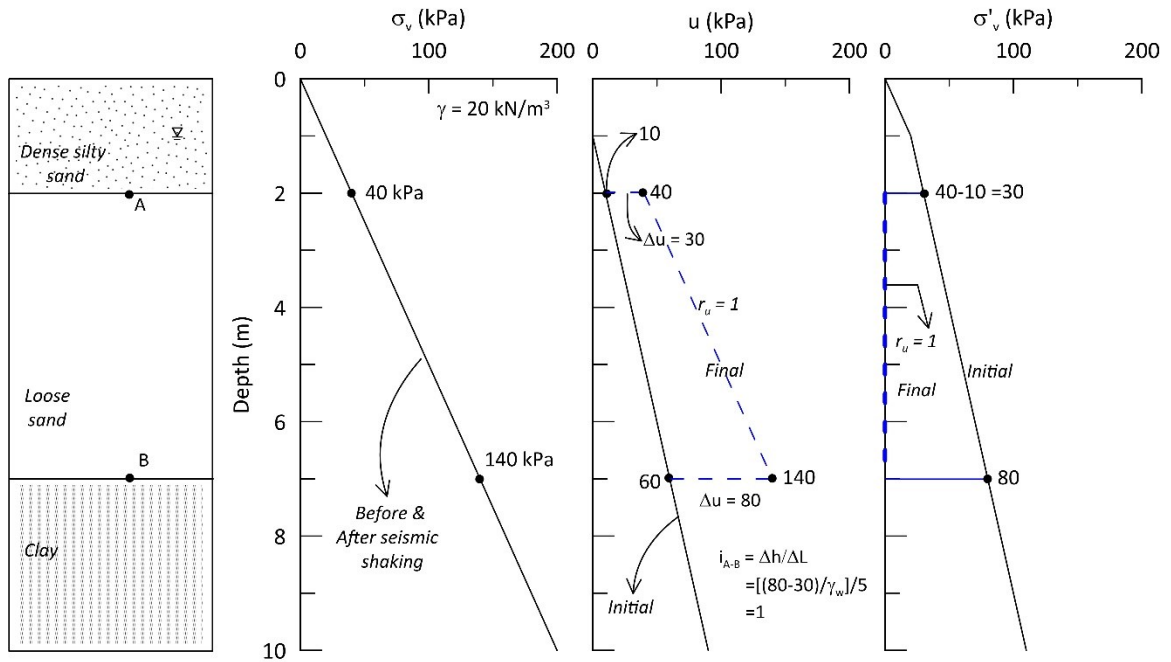


Figure 7.1: Vertical, pore and effective stress in level ground before and after shaking

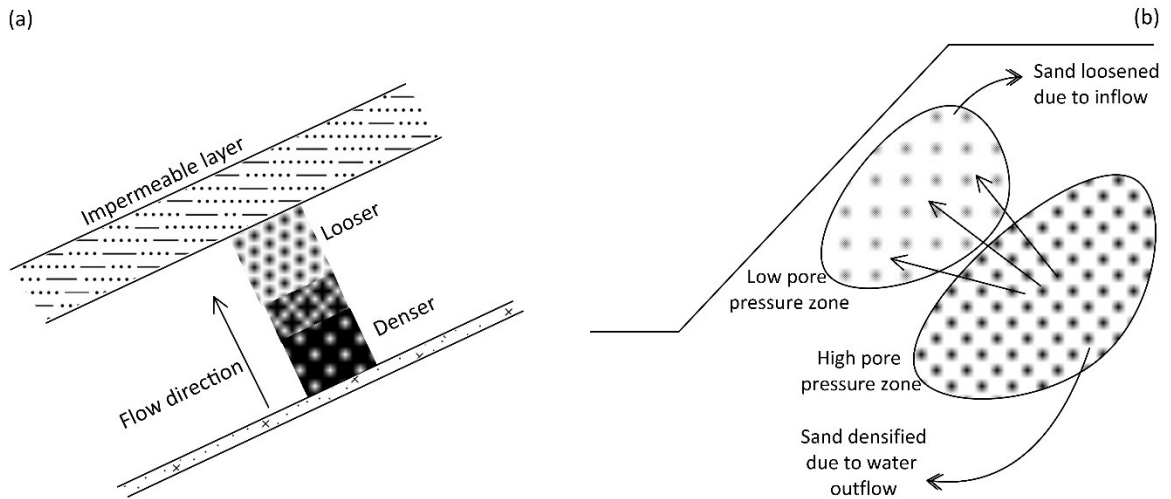


Figure 7.2: Instability due to seepage and void redistribution

The existence of pore pressure gradients and its associated void redistribution is the major reason for delayed failures that occurred after the cessation of earthquakes in several case studies such as the Lower San Fernando dam failure and the Mochikoshi tailing dam failure (Idriss 2004; Okusa et al. 1984). It is evident that due to the existence of pore pressure gradients and the associated void redistribution, the failure of soil element will be caused by simultaneous change in pore pressure and volume. These conditions might be more damaging than the undrained condition which is adopted in the current design practice. Hence a comprehensible understanding of the behavior of sand under simultaneous change in volume and pore pressure is crucial for reliable designs.

Limited laboratory element studies have been carried out to evaluate the “partially drained” behavior of sands under various volumetric strain paths (Chu et al. 1992, 2015; Vaid and Eliadorani 1998, 2000; Lancelot et al. 2004; Sivathayalan and Logeswaran 2007; Lade and Liggio Jr. 2014). The term “partially drained” is used to represent all pore pressure – volume coupled deformation in soil deposits, including those that may yield a higher pore pressure response than undrained, or higher volumetric response than typical drained loading scenarios. It is demonstrated that even a small expansive volumetric deformation can cause instability or strain softening of sand which is otherwise stable or dilative under undrained loading conditions. These laboratory investigations were limited only to linear proportional strain paths in which the rate of volumetric inflow remained constant throughout shearing. Sivathayalan and Logeswaran (2008) recognized that these linear strain paths represent hypothetical loading scenarios because the pore water migration due to the piezometric gradients results in the equalization of pore pressure. Hence, the actual strain paths encountered in-situ will be non-linear with steadily

decreasing rate of volumetric inflow. Sivathayalan and Logeswaran (2008) also evaluated the behavior of loose Fraser River sand subjected to linear strain paths with limiting volumetric strain and non-linear strain paths. It is shown that the rate of volume inflow plays a significant role in affecting the shear strength of the sand. Invariably in all these investigations, the behavior of sand is evaluated under axisymmetric triaxial loading condition in which the directions of principal stresses are confined in the vertical and horizontal directions. The stress path dependent behavior of granular soil under both drained and undrained condition is well established (Symes et al. 1984; Uthayakumar and Vaid 1998; Sivathayalan and Vaid 2002; Miura et al. 1986; Lade et al. 2008; Wijewicreme and Vaid 2008). The major objective of the laboratory element studies is to replicate the in-situ loading condition as closely as possible. Therefore, it is imperative to assess the loading mode dependent behavior of sand under various volumetric strain paths. In order to investigate this aspect, an apparatus which is capable of controlling both stress path and strain paths together is required. CU-HCT is capable of controlling both loading mode and volumetric strain path simultaneously. Logeswaran (2010) examined the anisotropic characteristics of Fraser River sand under various linear volumetric strain path using CU-HCT. Though these linear strain paths are hypothetical, this study is a first step to quantify the effect of expansive volumetric strain under different loading modes. The major objective of the research presented in this chapter is to characterize the behavior of Fraser River sand under generalized loading conditions along with non-linear strain path with limiting volumetric strain.

7.2 *Partially drained behaviour of sand under non-linear strain paths*

The strain path tests were carried out on water pluviated Fraser River sand specimen using Carleton University hollow cylinder torsional shear apparatus (CU-HCT). The co-efficient of permeability (k) is expected to be around $k = 2.112 \times 10^{-2} \text{ cm/s}$ for the D_{10} of 0.13 mm.

After water pluviation, the specimens were saturated by applying a back pressure of about 250 kPa, and complete saturation was ensured by achieving a Skempton's B value of at least 0.99. Then the specimens were isotropically consolidated in stages to an effective mean normal stress of 200 kPa and subsequently sheared according to the target strain paths with fixed α_σ and b_σ . The relative density of the sand specimens at the end of consolidation (D_{rc}) is about $40 \pm 1\%$. Figure 7.3 presents the typical consolidation test data highlighting the hydrostatic variation of applied surface tractions and effective mean normal stress (σ'_{mc}). The σ'_{mc} was increased incrementally with $\Delta\sigma_m = 25 \text{ kPa}$ by simultaneously adjusting the axial, radial and tangential stresses. The variation of normal strains and volumetric strain under this hydrostatic stress increment is presented in Figure 7.3c. The volumetric strain is corrected for the effects of membrane penetration in both consolidation and shearing stages based on the unit membrane penetration resistance (ε_m) obtained from Sivathayalan and Vaid (1998) for Fraser River sand with D_{50} of 0.27 mm. The presence of inherent anisotropy of water pluviated sand specimens can be identified by observing the variation of axial (ε_z), radial (ε_r) and tangential (ε_θ) strains. Figure 7.4 presents the variation of strain increments in Fraser River sand under isotropic stress increments from its initial effective stress state. The observed vertical strain in the depositional direction is much smaller than the radial and tangential strain observed along the bedding plane. This

signifies the existence of cross anisotropic fabric that ensued on water pluviation, and greater stiffness in the depositional plane than the weak bedding plane. Moreover, the identical values of ε_r and ε_θ under hydrostatic stress increments signifies that the sand is isotropic in horizontal bedding plane. Sivathayalan (2000) also made similar observations on Fraser River sand under isotropic stress increments and reported that $\varepsilon_r = 1.9\varepsilon_z$ which is slightly lower than the value reported in this study ($\varepsilon_r = 2.6\varepsilon_z$). This difference is attributed mainly to the different batches of Fraser River sand used for testing purposes.

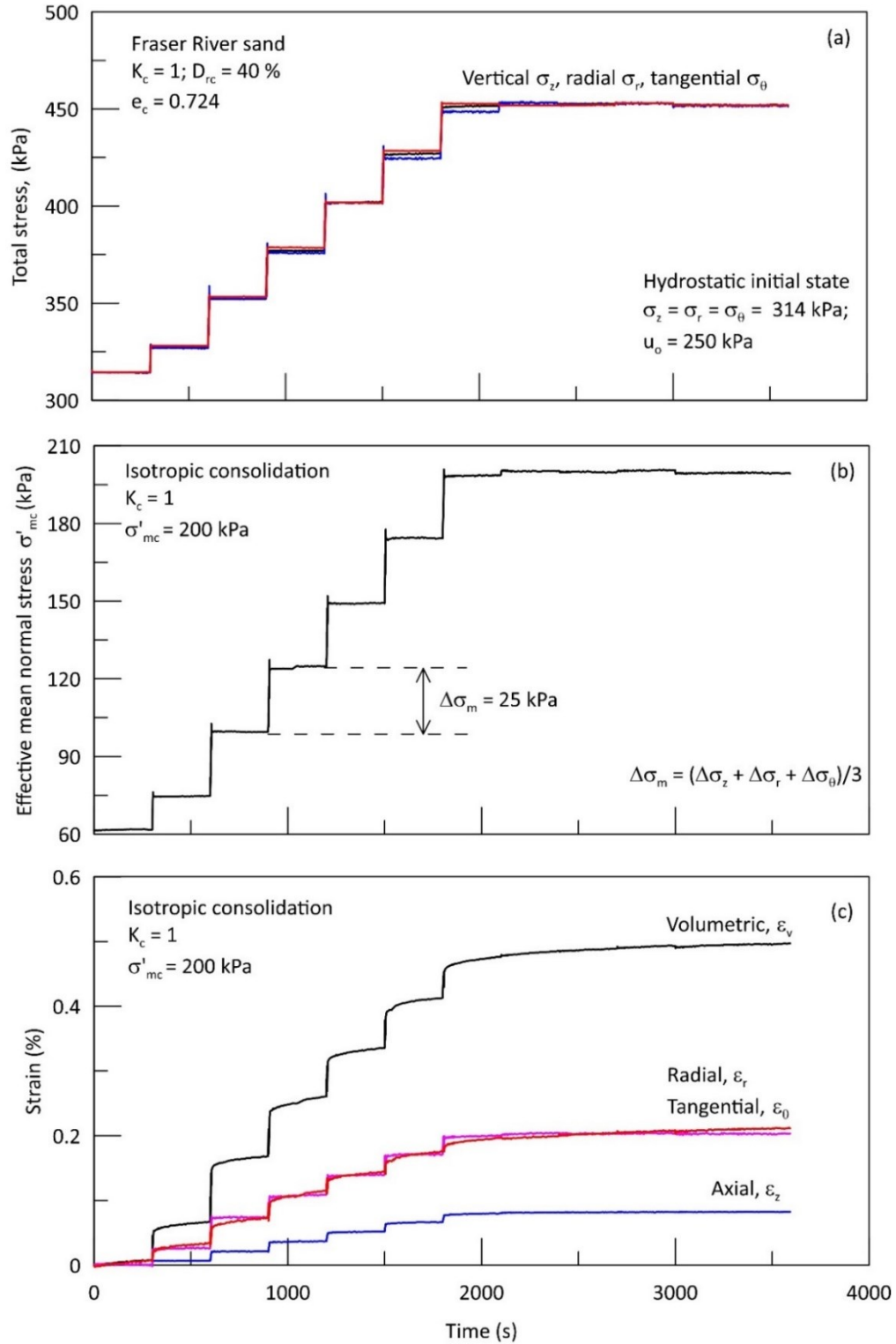


Figure 7.3: Application of isotropic consolidation stresses using CU-HCT: (a) directional stresses; (b) effective mean normal stress; (c) volumetric strain and normal strains

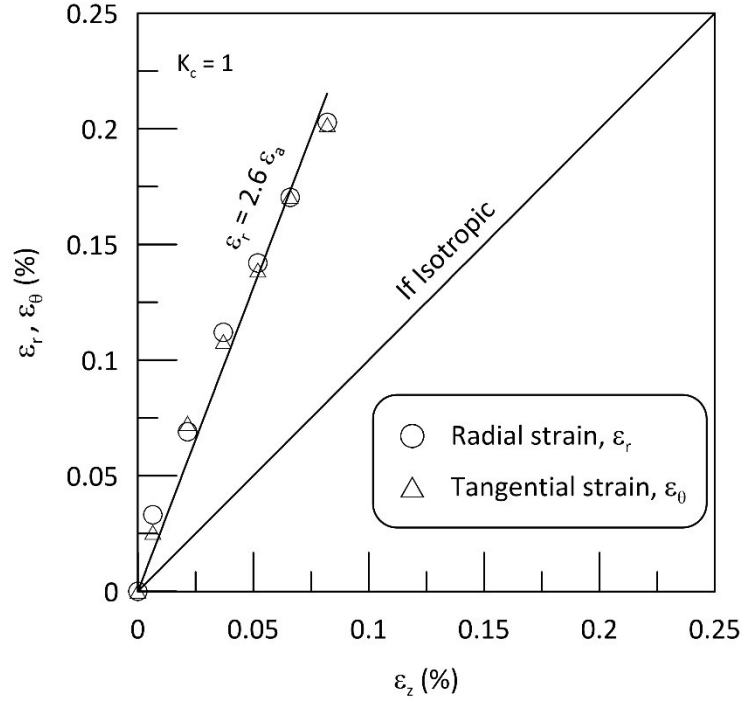


Figure 7.4: Axial, radial and tangential strain increments under hydrostatic stress increment

After consolidating the sand specimens to required effective stress state, the samples were sheared at a constant maximum shear strain rate (γ_{max}) of 3%/hour along the specified volumetric strain paths. This slow rate of loading is adopted to make sure that the velocity head remains insignificant during injection or extraction of water from the soil sample. During shearing the direction of major principal stress axis to vertical (α_σ), intermediate principal stress parameter (b_σ) and total mean normal stress (σ_m) was held constant. The non-linear volumetric strain path imposed on the sand specimen is characterized by strain increment ratio ξ_r , which is defined as the ratio between volumetric strain increment ($\Delta\epsilon_v$) to maximum shear strain increment ($\Delta\gamma_{max}$). The nonlinear strain path used in this study employs an exponential function to define strain increment ratio and its general form is given by;

$$\epsilon_v = m(1 - e^{-R\gamma_{max}}) \quad (7.1)$$

where ε_v and γ_{max} are the volumetric strain and maximum shear strain respectively. The constants m and R represents the nature of the volumetric strain path, in which m defines the maximum volumetric strain imposed to the specimen and R defines the relative rate of volumetric strain increment. Figure 7.5 illustrates the nonlinear strain path adopted in this test program. Here the negative volumetric strain represents volume inflow whereas the positive volumetric strain represents volume outflow. In this test series, the strain increment ratio ξ gradually decreases and move towards zero with maximum shear strain. The limiting volumetric strain ε_{vL} , was reached asymptotically in these nonlinear strain paths. Here the rate of volume flow gradually reduces with time which closely represents the field condition because the pore water migration in in-situ soil deposits gradually decreases the piezometric gradient and eventually equalizes it. In this study, the tests were conducted at a constant R value of 0.75 and m value varies between -0.60% to $+0.3\%$. The actual variation of non-linear strain path in-situ depends on several parameters which makes the quantification of strain path tedious and the exponential strain path adopted in this study is an attempt to replicate the in-situ drainage condition as closely as possible which will helps in the better understanding of anisotropic characteristics of loose Fraser River sand under three dimensional loading with non-linear drainage condition. The details of HCT tests carried out to understand the generalized loading and drainage conditions are tabulated in Table 7.1.

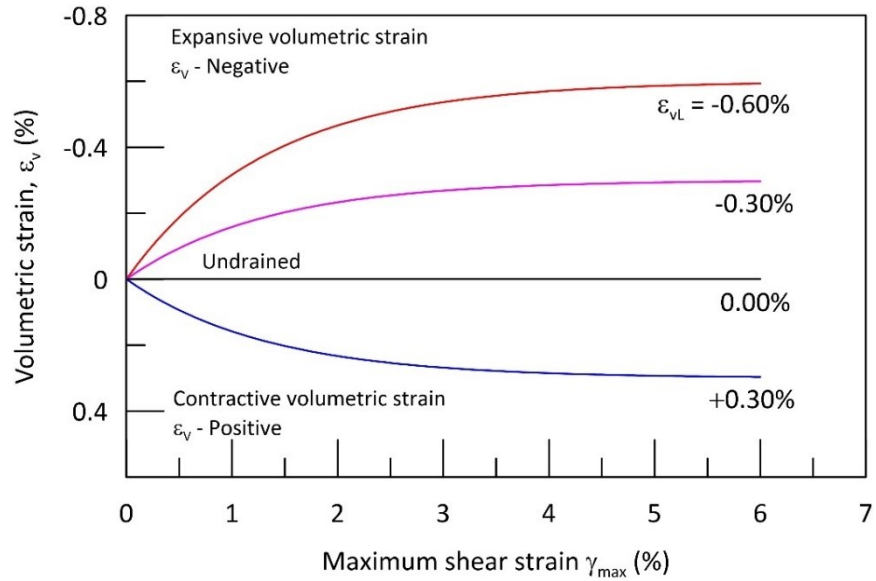


Figure 7.5: Nonlinear strain path imposed on loose Fraser River sand specimens

Table 7.1: Initial and shearing parameters for nonlinear volumetric strain path tests

<i>Test No</i>	<i>Consolidation stage</i>			<i>Shearing stage</i>		
	<i>Stress state</i>	e_c	D_{rc} (%)	b_σ	α_σ (deg)	ϵ_{vL} (%)
PDT01	$\sigma_1 = \sigma_2 = \sigma_3;$ $\sigma'_{mc} = 200$ kPa	0.717	42.0	0.4	45	+0.3
PDT02		0.724	39.9			0
PDT03		0.717	42.0			-0.3
PDT04		0.724	40.1			-0.6
PDT05		0.723	40.2	0	0	-0.6
PDT06		0.710	44.0	1	90	
PDT07		0.725	39.7	0.4	0	
PDT08		0.731	37.9		30	
PDT09		0.725	39.6		60	
PDT10		0.708	44.6		90	

A typical response of Fraser River sand specimen subjected to nonlinear strain path with $\varepsilon_{vL} = -0.60\%$ is shown in Figure 7.6. The hydrostatically consolidated sand specimen was sheared at a constant α_σ of 45° and b_σ of 0.4. Sand exhibits a Quasi Steady State (QSS) response in which the sand strain softens over a limited strain range and strain hardens with subsequent shear deformation. A maximum excess pore pressure of about 167 kPa was developed in the soil sample which corresponds to almost 83.5% of initial σ'_{mc} . Instability or the initiation of strain softening was triggered in the sand specimen once the effective stress path crosses the critical stress ratio (CSR) line. The sand developed instability at a very small maximum shear strain of about 0.26%. This triggering of softening response is associated with an expansive volumetric strain of about 0.1% which increases void ratio merely by 0.0018. Therefore, the triggering of softening response is attributed due to the small volumetric inflow into the sand specimen, and the associated pore pressure response, and not due to the physical loosening of the sand. Figure 7.7 shows the variation of actual parameters with the targeted σ_{mc} , α_σ and b_σ , and it can be noted that the differences are relatively insignificant. This demonstrates that the prescribed stress-strain path is followed closely by the feedback control system.

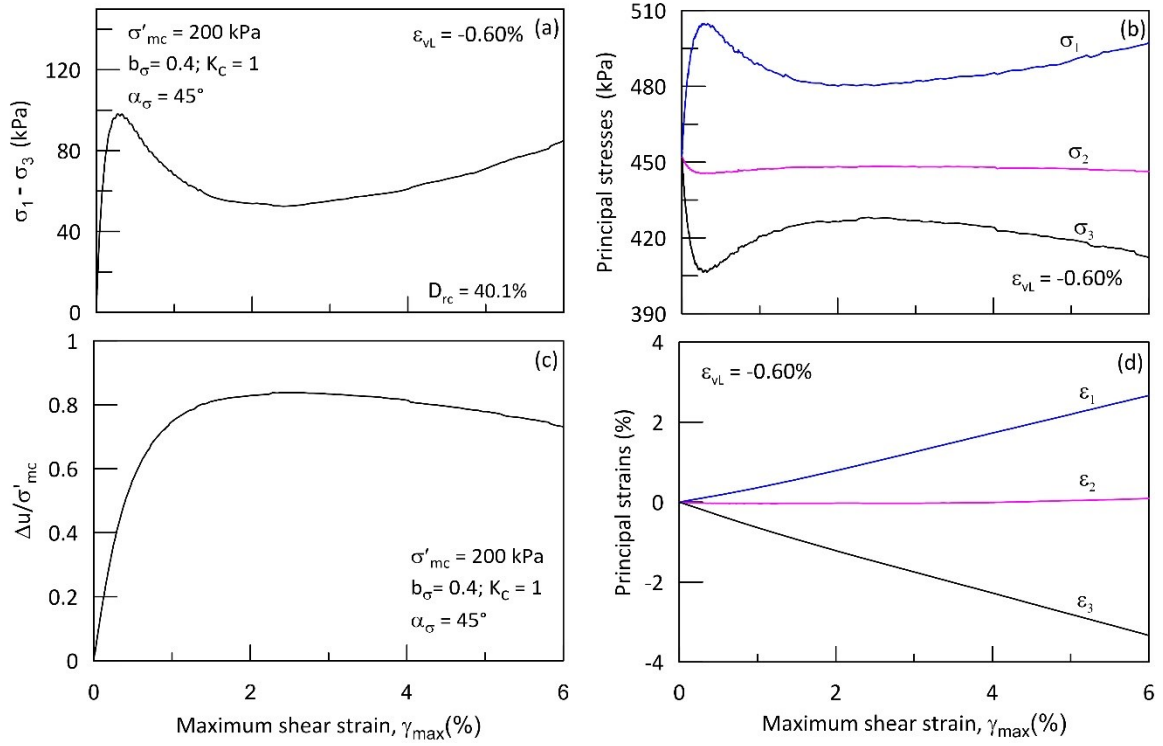


Figure 7.6: Typical response of Fraser River Sand to non-linear volumetric strain path with $\varepsilon_{vL} = -0.60\%$

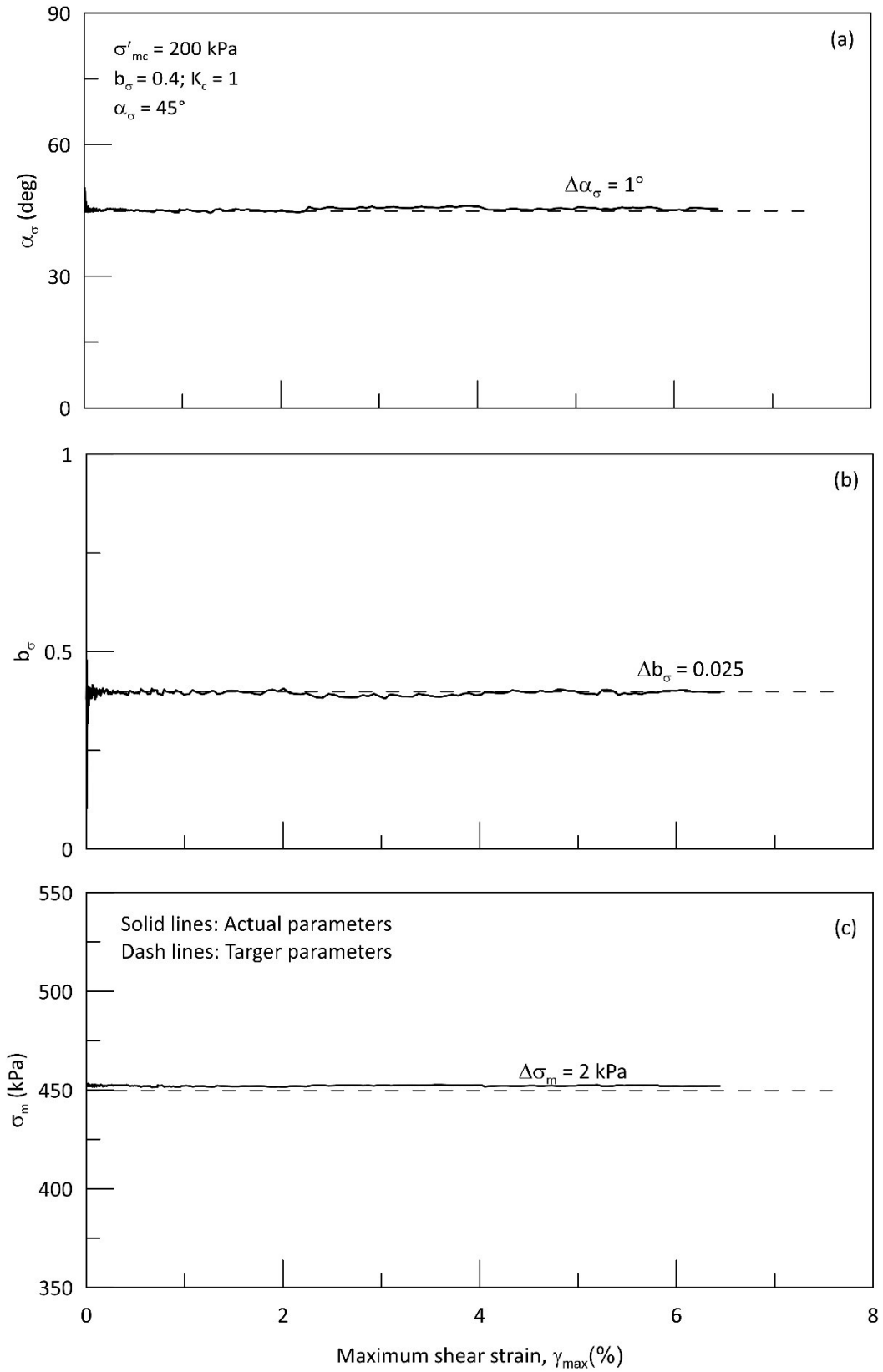


Figure 7.7: Comparison of actual and targeted parameters

7.2.1 Response under fixed α_σ , b_σ but along strain paths with different ε_{vL}

This series of tests were carried out to investigate the influence of non-linear strain paths on the deformation characteristics of water pluviated sand specimens. The non-linear paths adopted in this investigation subjects the sand specimen to different drainage conditions ranging from contractive to expansive drainage as shown in Figure 7.5. The specimens were sheared at a constant α_σ of 45° and b_σ of 0.4. The variations in the imposed surface tractions σ_z , σ_r , σ_θ and $\tau_{z\theta}$ is shown in Figure 7.8. Since the shearing was carried out at a constant α_σ of 45° and b_σ of 0.4, only $\tau_{z\theta}$ and σ_r varies significantly from its initial stress state and the magnitude of normal stresses σ_z and σ_θ remains almost unchanged throughout the shearing. Figure 7.9 presents the variation induced principal strains ($\varepsilon_1, \varepsilon_2, \varepsilon_3$) with respect to γ_{max} . The membrane penetration corrections were properly accounted for while computing the induced principal strains. A systematic variation in the principal strains is observed as the imposed strain path varies from contractive to expansive strain path. Logeswaran (2010) also noted the similar systematic variation in the principal strains with imposed linear strain paths. The magnitude of intermediate principal strain ε_2 is much smaller than the absolute magnitude of major and minor principal strains, which confirms that the plane strain condition is followed closely during shearing under non-linear strain paths. Similar variation in the magnitude of ε_2 is noted for b_σ of 0.4 under undrained shearing by Uthayakumar and Vaid (1998); Yoshimine et al. (1998); Sivathayalan (2000) and shearing under linear strain paths by Logeswaran (2010).

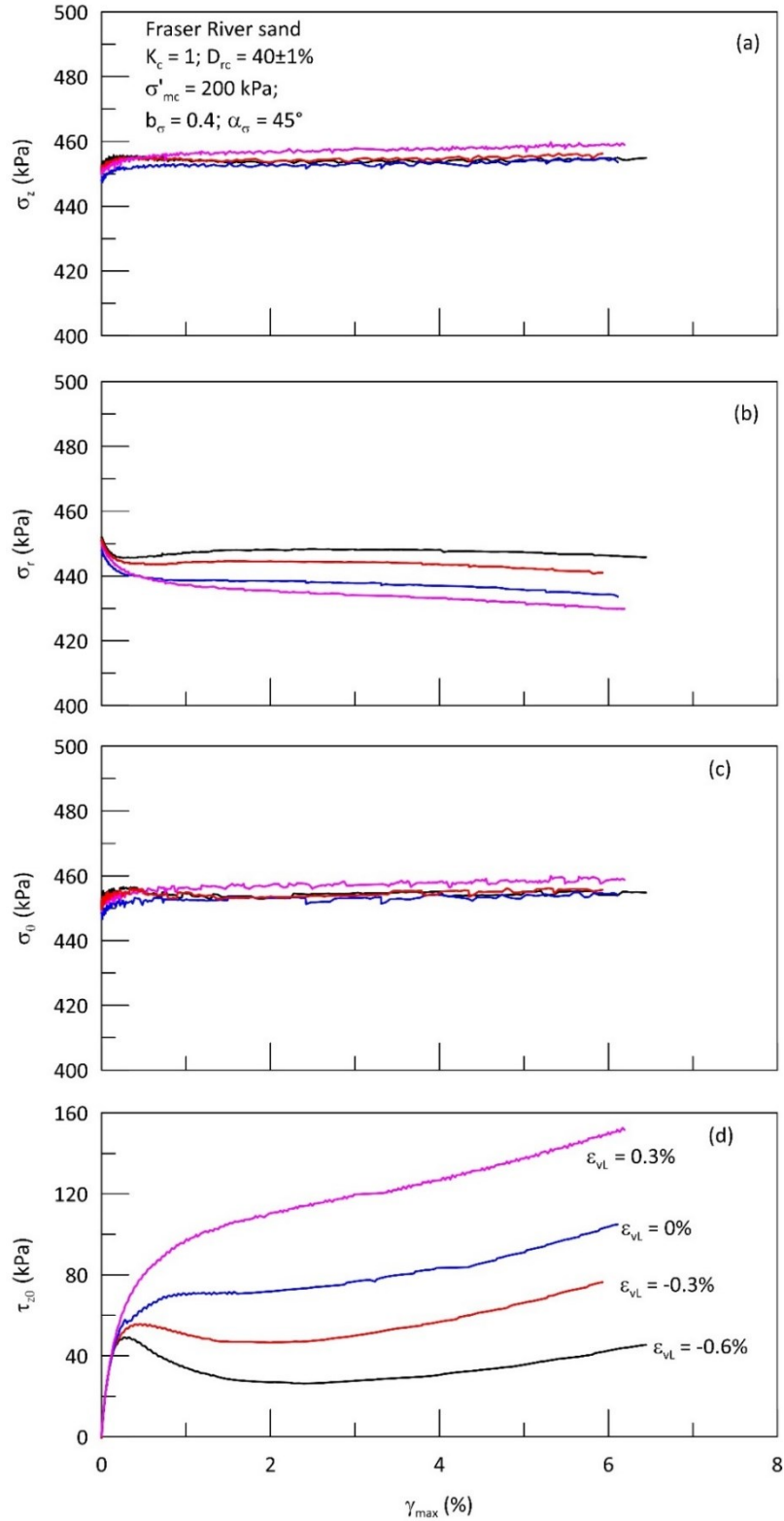


Figure 7.8: Variation of surface tractions for shearing under different non-linear strain paths

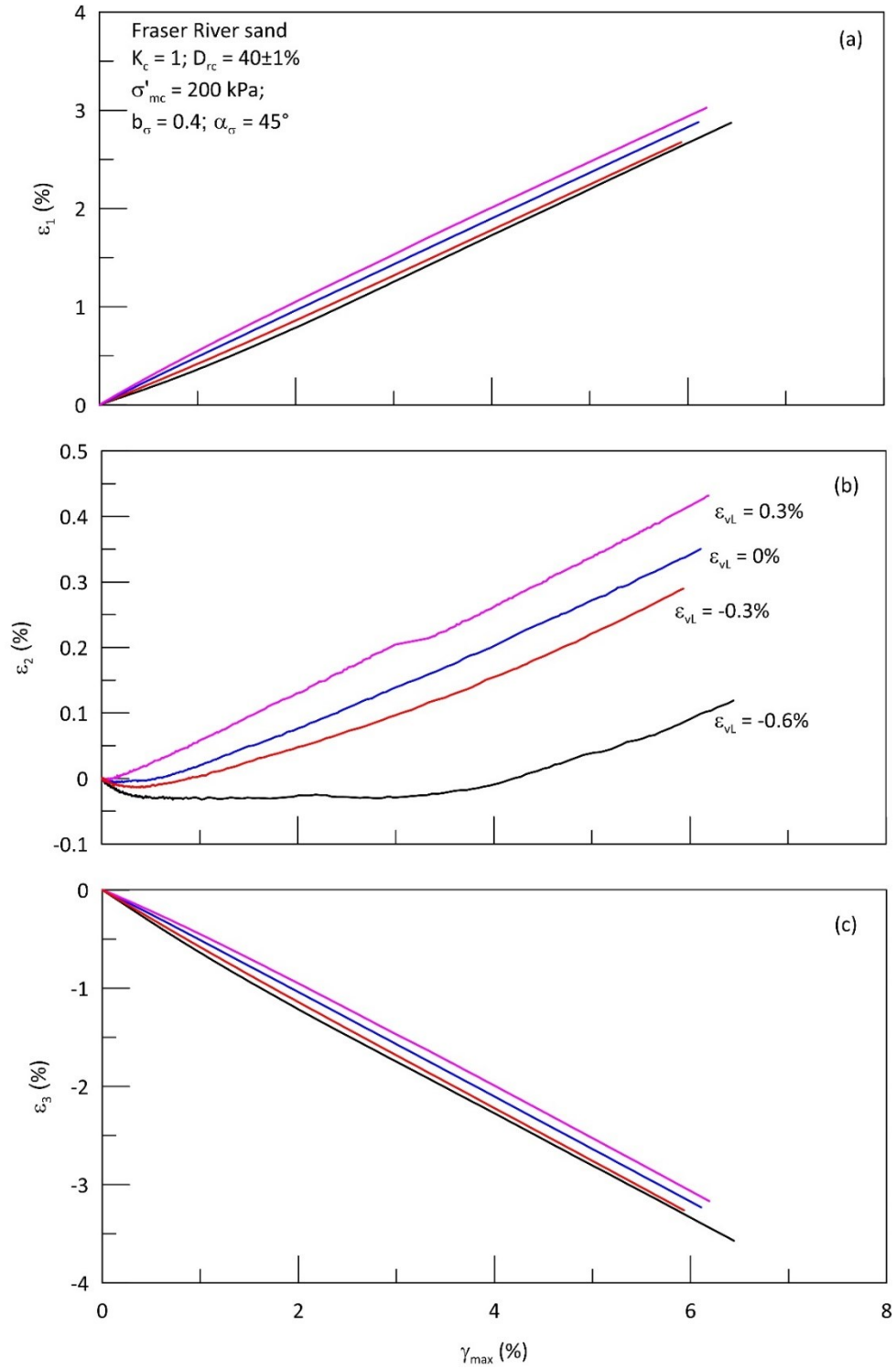


Figure 7.9: Variation of principal strains under different non-linear strain paths

The stress-strain response, variation of excess pore water pressure ratio ($r_u = \Delta u / \sigma'_{mc}$) and effective stress path response of identical Fraser River sand specimens under non-linear strain increment ratio paths as identified in Figure 7.5 is plotted in Figure 7.10. The response of sand systematically changes from strain hardening response to quasi-steady state response as the imposed drainage condition changes from contractive to expansive volumetric deformation. Sand exhibited hardening response for contractive non-linear strain path with limiting volumetric strain (ϵ_{vL}) of +0.3% and for undrained condition (ϵ_{vL} or $\xi_r = 0$). The initial negative pore water pressure noted in test with $\epsilon_{vL} = +0.3\%$ is attributed because the rate of water extracted out of the specimen at $\gamma_{max} < 0.3\%$ might be larger than the rate it would have drained under drained shearing condition. The response of the material becomes progressively softer when increasing levels of expansive volumetric strain is imposed to the sand specimen. In tests under expansive volumetric strain, the peak strength (S_{peak}) nominally reduced from 56 kPa to 49 kPa as expansive strain ϵ_{vL} increased from $\epsilon_{vL} = -0.3\%$ from $\epsilon_{vL} = -0.6\%$. As expected, the developed excess pore water pressure is lower than the undrained case for contractive volumetric strain and higher for expansive volumetric strain. Similar observation of strain hardening for volume outflow and quasi steady state for volume inflow is also noted by Sivathaylan and Logeswaran (2008) under non-linear strain increment ratio tests under triaxial condition.

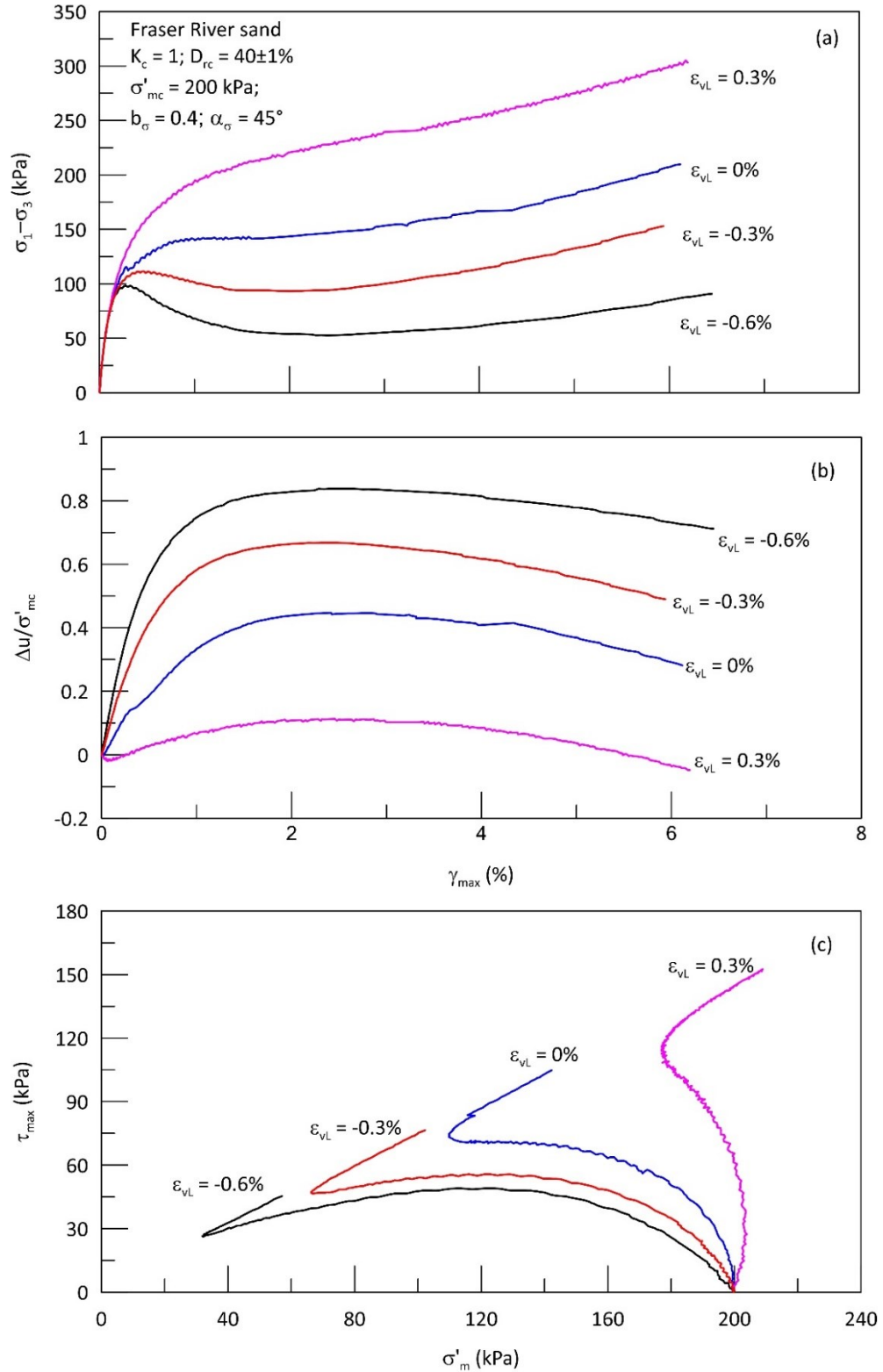


Figure 7.10: Response of Fraser River sand under nonlinear strain paths leading to different limiting volumetric strain.

Figure 7.11 and 7.12 shows the variation of shear strength at phase transformation (S_{PT}) and peak excess pore water pressure (Δu_{peak}) with respect to limiting volumetric strain (ε_{vL}). The shear strength corresponding to peak excess pore water pressure is taken as the shear strength at phase transformation. S_{PT} reduces systematically as the ε_{vL} changes from positive to negative. Here, the S_{PT} under undrained condition is about 73 kPa and which is almost reduced by 65% with the application of non-linear strain path with $\varepsilon_{vL} = -0.60\%$. Figure 7.11 also presents the variation of S_{PT} with ε_{vL} from the data obtained from Sivathayalan and Logeswaran (2008) for Fraser River sand subjected to linear strain path with limiting volumetric strain and similar non-linear strain path adopted in this study. Though there are some differences in sample density and loading condition, similar trend of variation in S_{PT} with ε_{vL} is observed. The potential reason for the similarity is that the specimens tested by Logeswaran were somewhat looser, but were at $\alpha_\sigma = 0$ & $b_\sigma = 0$ whereas these tests were at $\alpha_\sigma = 45^\circ$ & $b_\sigma = 0.4$, both factors lead to weaker response. It appears that the expected stronger response due to about 15% higher relative density was offset by the weakness arising on account of the higher α_σ & b_σ .

The peak excess pore water pressure also shows a systematic variation with ε_{vL} , it increases gradually as the non-linear strain path changes from contractive to expansive deformation (Figure 7.12). The Δu_{peak} developed from shearing under undrained condition reduces by almost 75% with the imposition of contractive strain path with $\varepsilon_{vL} = 0.30\%$ and it increases by about 88% with imposition of expansive strain path with $\varepsilon_{vL} = -0.60\%$.

The effective stress state at the instant of peak excess pore water pressure state for the non-linear strain path tests conducted in this test series are plotted in Figure 7.13.

Regardless of the strain path imposed, the effective stress state at this state lie on a unique straight line which passes through the origin. Therefore, the friction angle mobilized at the state of peak pore pressure (ϕ_{PeakPP}) is essentially a constant and is about 36.9° for this batch of Fraser River sand. The ϕ_{PeakPP} has been given different names depending upon the type of response, such as the friction angle at steady state (ϕ_{SS}), friction angle at quasi-steady state (ϕ_{QSS}) and the friction angle at phase transformation (ϕ_{PT}). Sivathayalan and Logeswaran (2007, 2008) suggested that the uniqueness of mobilized friction angle is related to the instant of peak excess pore water pressure rather than the steady, Quasi steady and phase transformation states. Sinthujan (2013) also reported a similar friction angle ($\phi_{PT} = 36.4^\circ$) for this batch of Fraser River sand through undrained monotonic shearing under different initial condition and loading modes. Hence it can be concluded that ϕ_{PeakPP} is a unique material property and it is independent of initial state, strain path and loading mode.

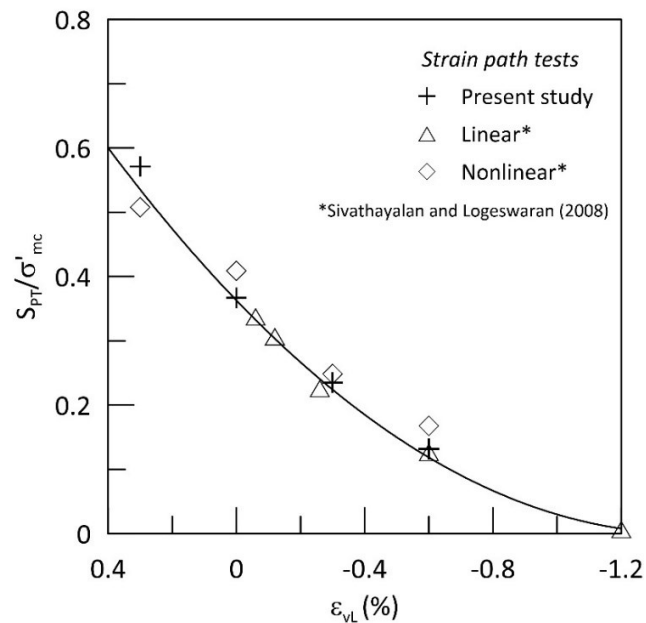


Figure 7.11: Variation of shear strength at phase transformation with magnitude of limiting volumetric strain.

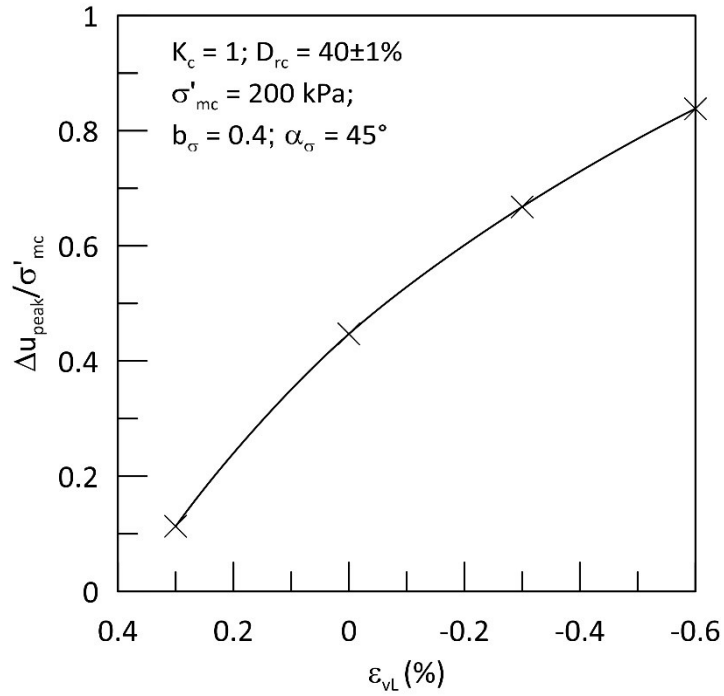


Figure 7.12: Variation of peak excess pore water pressure with magnitude of limiting volumetric strain.

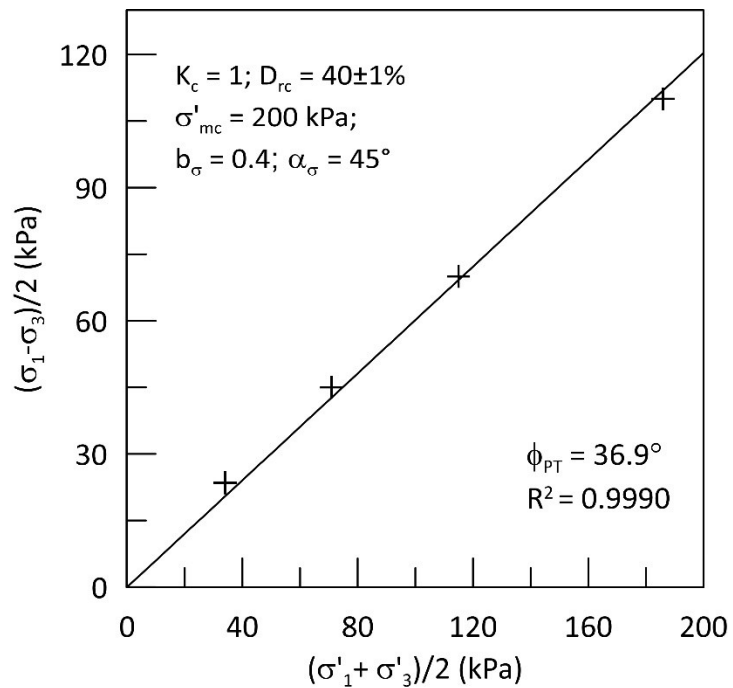


Figure 7.13: Effective stress state at the instant of peak pore water pressure.

7.2.2 Response under fixed ε_{vL} and different α_σ

The objective of this test series is to investigate the influence of direction of major principal stress (α_σ) on the response of Fraser River sand under coupled shear volume loading condition. Non-linear expansive volumetric strain path with $\varepsilon_{vL} = -0.60\%$ was imposed to the sand specimen. The specimens were sheared at a constant α_σ varying from 0° to 90° and b_σ of 0.4. In addition to these tests, specimens were also sheared at triaxial compression ($\alpha_\sigma = 0^\circ$; $b_\sigma = 0$) and triaxial extension ($\alpha_\sigma = 90^\circ$; $b_\sigma = 1$) loading conditions.

The variation of surface tractions ($\sigma'_z, \sigma'_r, \sigma'_\theta, \tau_{z\theta}$) and the corresponding normal strains ($\varepsilon_z, \varepsilon_r, \varepsilon_\theta$) and shear strain ($\gamma_{z\theta}$) induced in an isotropically consolidated sand specimens sheared at different α_σ are illustrated in Figure 7.14 and 7.15. The computed principal stresses and mobilized effective stress ratio, and the induced principal strains for the same test series are plotted in Figure 7.16 and 7.17. These variations are plotted against ε_z because it is one of the independent variables in tests with fixed α_σ . ε_z is an independent variable in $\alpha_\sigma = 0^\circ$ & 90° tests and $\gamma_{z\theta}$ is an independent variable in $\alpha_\sigma = 30^\circ, 45^\circ$ & 90° tests. Plotting the variation of stresses and strains against one of the independent variables can provide a general perspective of applied traction and induced strain variations along different stress paths. ε_z changes gradually from major principal strain to minor principal strain as α_σ changes from 0° to 90° . Since $\alpha_\sigma = 0^\circ$ & 90° tests are controlled only by normal stresses, no change in torsional shear stress and torsional shear strain is observed in these tests. The major and minor principal strains almost showed a linear variation at small strains until a threshold stress ratio is mobilized, whereas the intermediate principal strain varies nonlinearly throughout the shearing. Sivathayalan (2000) and Logeswaran (2010) observed linear variation of ε_2 with ε_z under undrained and

linear expansive volumetric drainage condition respectively. The nonlinear variation of ε_2 observed in this test series might be due to the imposed non-linear strain path to the sand specimens. Identical variation in the magnitude of ε_2 & ε_3 and ε_1 & ε_2 is noted in triaxial compression and triaxial extension test respectively due to the imposed axisymmetric condition of $b_\sigma = 0$ and 1. In tests with b_σ of 0.4, the magnitude of ε_2 is much less than the absolute magnitude of ε_1 and ε_3 signifying the imposition of plane strain deformation during shearing under non-linear expansive volumetric drainage. Similar variation in the magnitude of ε_2 is noted by several researchers under undrained plane strain loading (Uthayakumar and Vaid 1998; Sivathayalan and Vaid 2002; Logeswaran 2010) and plane strain-linear strain path loading (Logeswaran 2010).

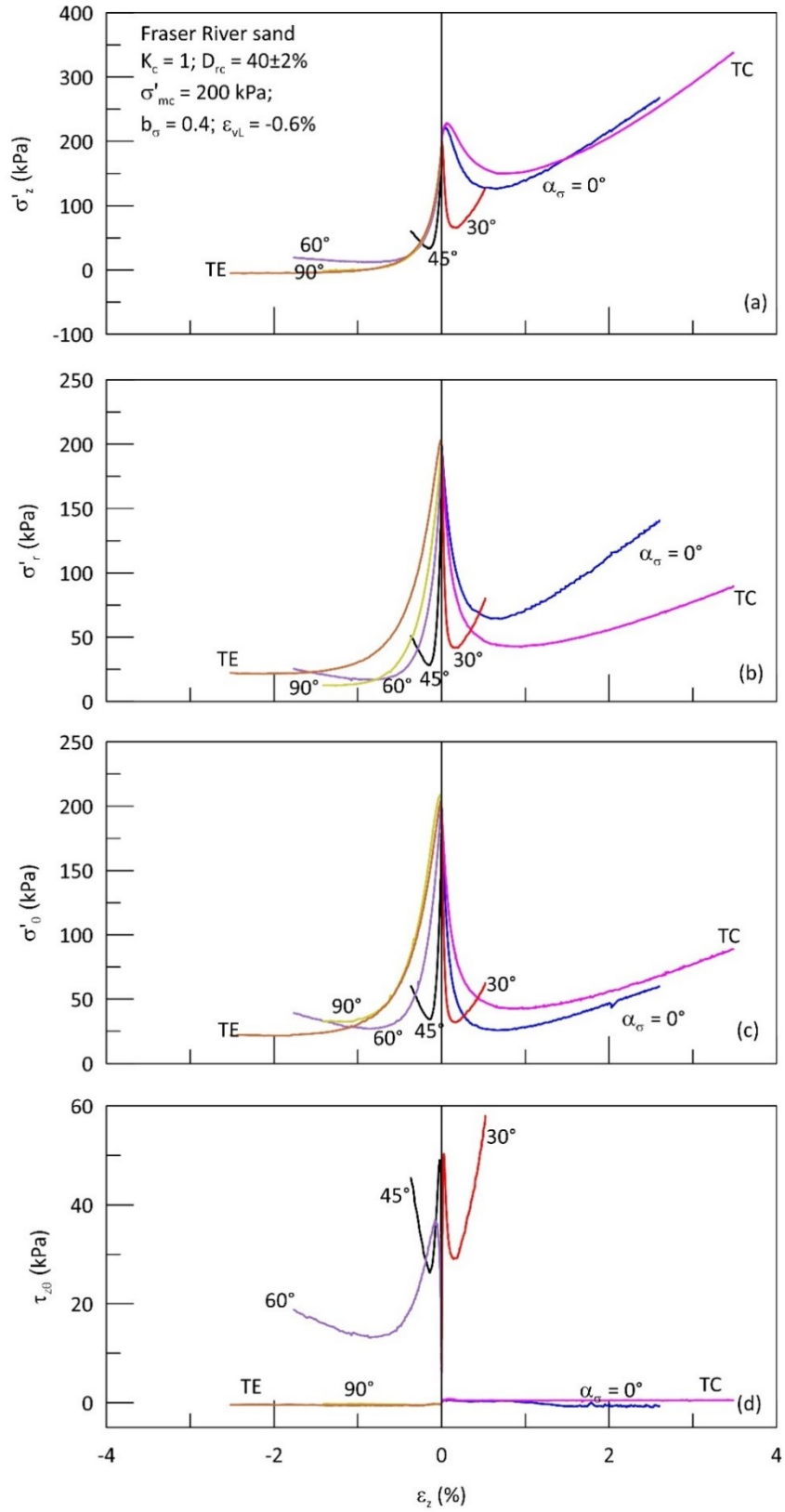


Figure 7.14: Variation of surface tractions during shearing with different fixed α_σ

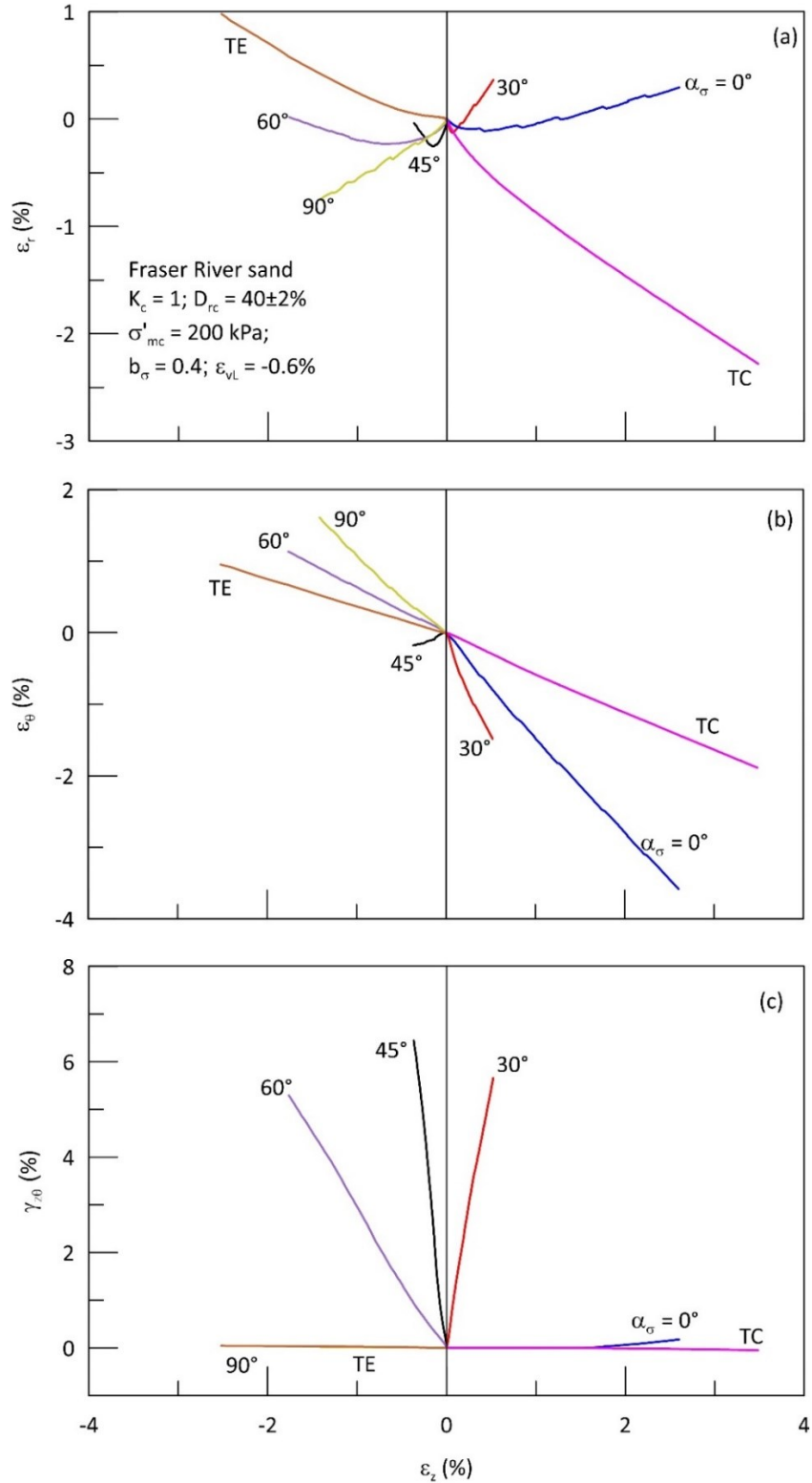


Figure 7.15: Variation of radial, tangential, and torsional shear strain with vertical strain during shearing with different fixed α_σ

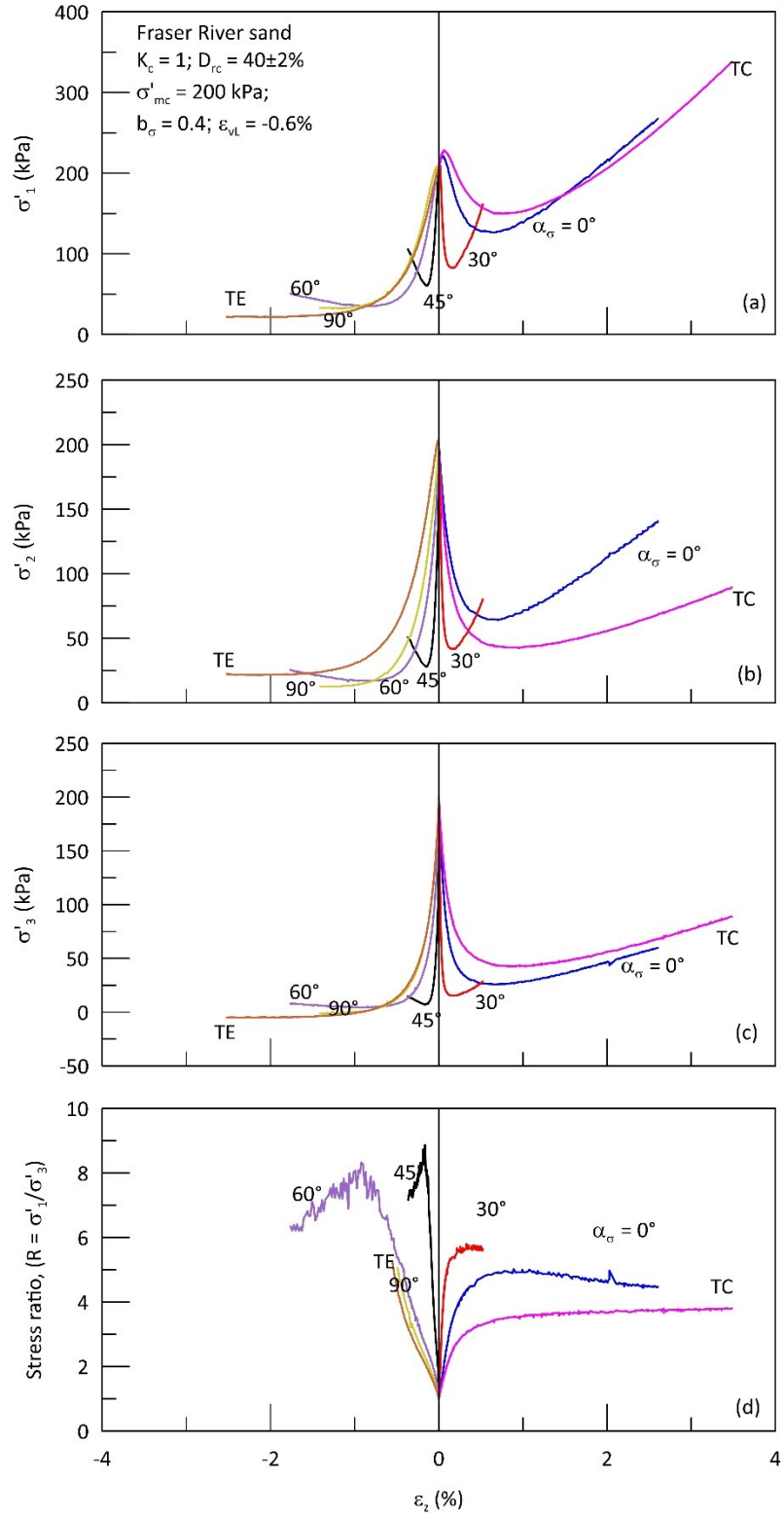


Figure 7.16: Variation of principal stresses and effective stress ratio during shearing with different fixed α_σ

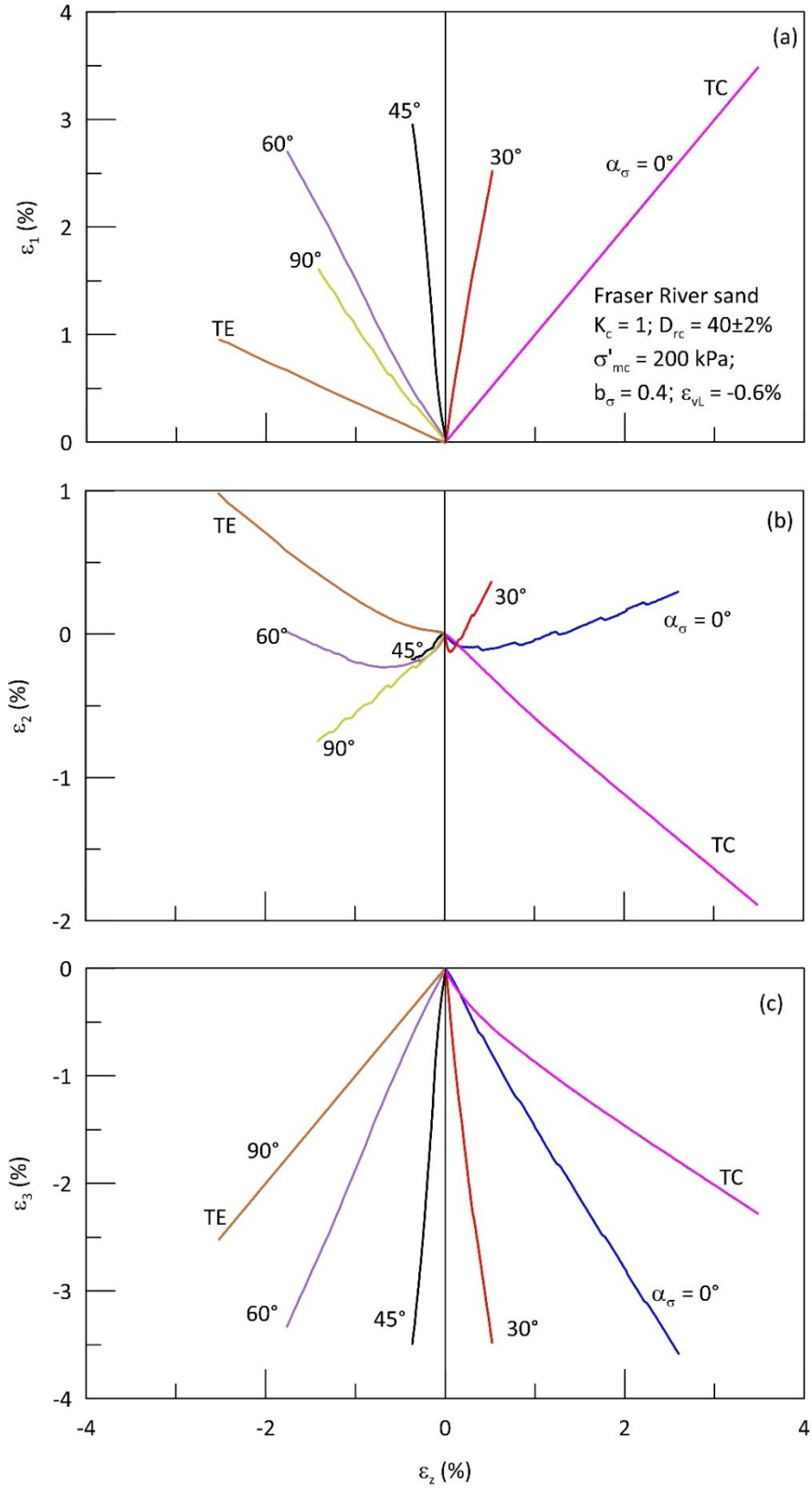


Figure 7.17: Variation of principal strains during shearing with different fixed α_σ

The stress-strain response, variation of excess pore water pressure ratio ($r_u = \Delta u / \sigma'_{mc}$) and effective stress path response of identical Fraser River sand specimens subjected to expansive non-linear strain path with different inclination of principal stress axes is plotted in Figure 7.18. Irrespective of loading mode, all sand specimens exhibit quasi steady state response due to the imposition of expansive volumetric strain, but the specimen becomes progressively softer with the increase in α_σ and finally exhibits a steady state response at $\alpha_\sigma = 90^\circ$.

This systematic softening of sand is due to the development and evolution of anisotropy during the deposition and loading processes. Due to this anisotropic nature, sand exhibits stronger response when direction of major principal stress aligns with the direction of deposition and softer response when the major principal stress axis aligns with the direction of bedding plane. This gradual softening or contractive tendency of pluviated sand specimen with the increase in α_σ from 0° to 90° is consistent with the data reported in the literature (Symes et al. 1985; Sayao 1989; Uthayakumar and Vaid 1998; Sivathayalan and Vaid 2002; Wijewickreme and Vaid 2008; Sivathayalan et al. 2015). All of these investigations were carried out under either undrained or drained drainage condition. Logeswaran (2010) made similar observation on the effect of loading mode through the monotonic shearing of Fraser River sand under linear expansive drainage condition.

It can also be observed that test in triaxial compression mode ($\alpha_\sigma = 0^\circ$; $b_\sigma = 0$) exhibits stronger response when compared to ($\alpha_\sigma = 0^\circ$; $b_\sigma = 0.4$) test and test in triaxial extension mode ($\alpha_\sigma = 90^\circ$; $b_\sigma = 1$) exhibit weaker response when compared to ($\alpha_\sigma = 90^\circ$; $b_\sigma = 0.4$) test. Hence, it can be inferred that increase in b_σ decreases the hardening

tendency of sand. The promotion of softening tendency of sand with increase in b_σ is consistent with the data reported in several investigations.

The degree of strain softening of granular soils can also be characterized by using brittleness index (I_B) (Bishop 1971) which is defined as:

$$I_B = \frac{\sigma_{d(peak)} - \sigma_{d(min)}}{\sigma_{d(peak)}}$$

where $\sigma_{d(peak)}$ and $\sigma_{d(min)}$ are peak deviatoric stress and minimum deviatoric stress respectively. This also serves as an indicator for the flow potential of hydrostatically consolidated contractive sand. Figure 7.19 shows the variation of I_B with α_σ , which increases with the increase in α_σ . This increase in I_B with α_σ signifies the increasing tendency of strain softening of sand with the increase in α_σ .

Figure 7.20 shows the systematic reduction in the peak shear strength (S_{peak}) with increase in α_σ for this level of imposed non-linear strain path to the sand specimen. Since all the test specimens exhibited QSS response, S_{peak} is recognized in all these tests. S_{peak} reduced from about 67 kPa to 44 kPa (about 34% reduction) with the increase in α_σ from 0° to 90°. The effective stress ratio (σ'_1/σ'_3) mobilized at the instant of S_{peak} is called as the critical stress ratio (CSR) since it signifies the initiation of instability or strain softening (Vaid and Chern 1985; Vaid and Eliadorani 1998). The friction angle mobilized at this state ϕ_{CSR} , is not a unique material property, but it is significantly affected by the direction of principal stresses. The variation of ϕ_{CSR} with α_σ is plotted in Figure 7.21 and it can be noted that ϕ_{CSR} showed a systematic reduction with the increase in α_σ . It reduces as low as 19.5° at $\alpha_\sigma = 90^\circ$ from 30.8° at $\alpha_\sigma = 0^\circ$. Similar dependency of ϕ_{CSR} on loading mode for Fraser River sand under different initial stress state and drainage condition is reported

in several investigations (Vaid and Thomas 1995; Vaid and Sivathayalan 1996; Vaid and Sivathayalan 2002; Logeswaran 2010).

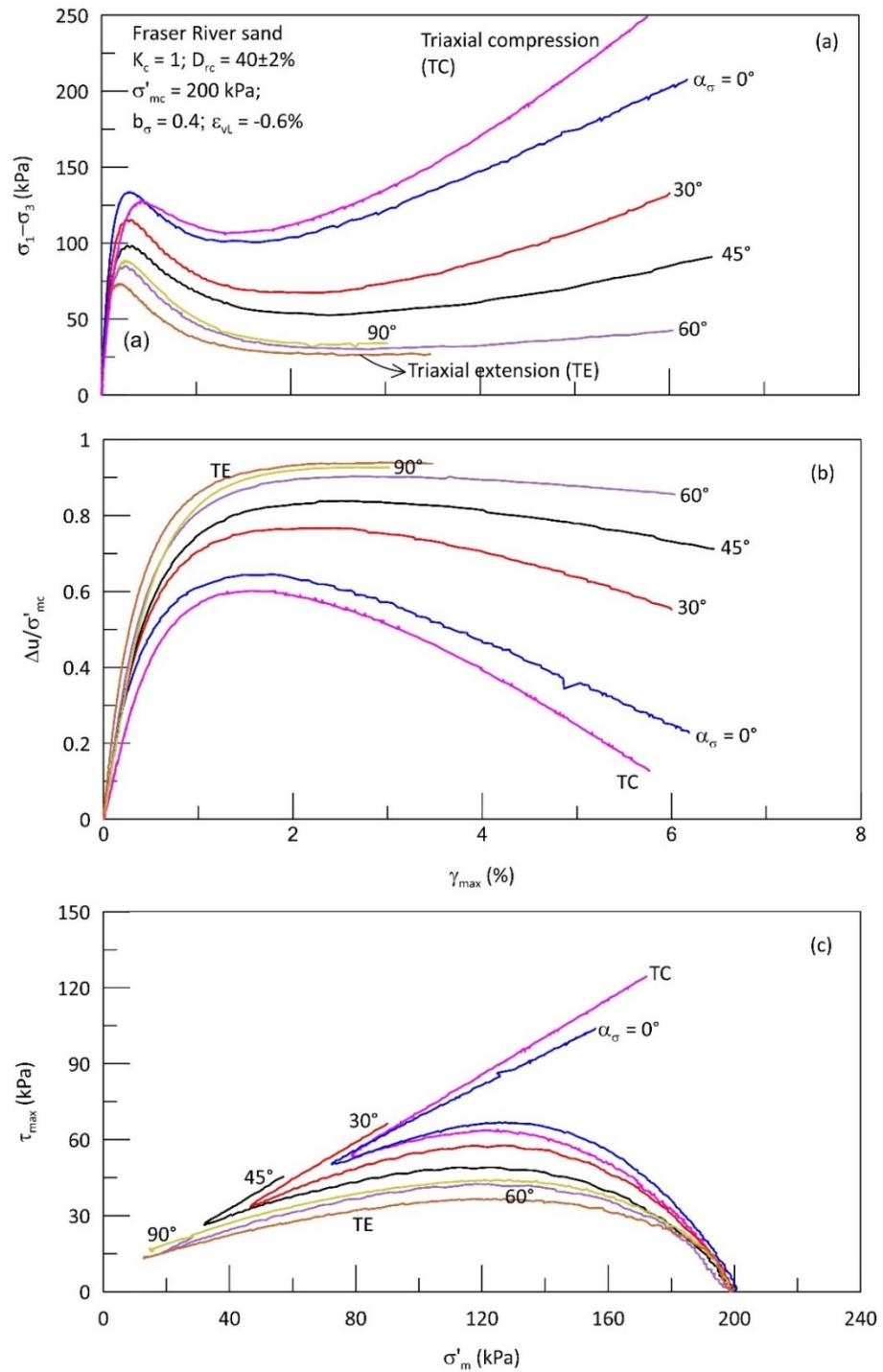


Figure 7.18: Response of Fraser River sand under nonlinear strain path with different fixed

α_σ

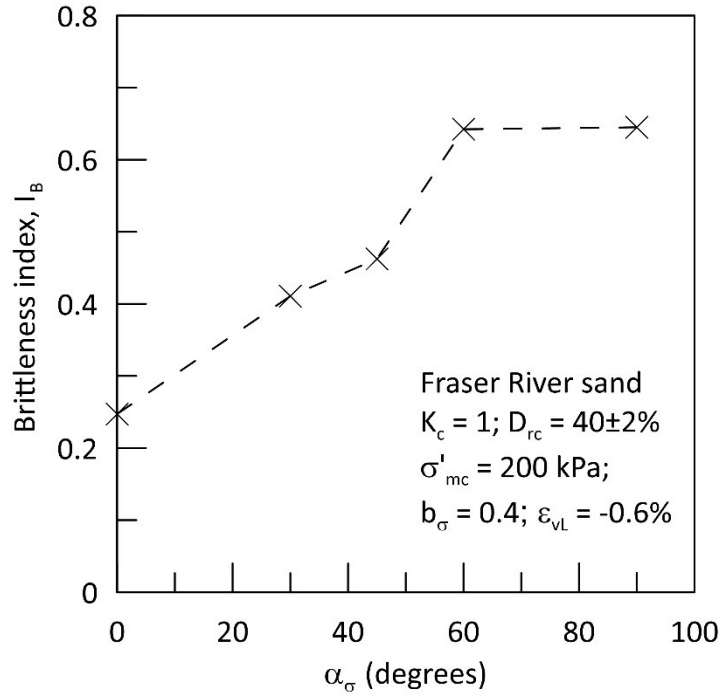


Figure 7.19 Variation of brittleness index with α_σ

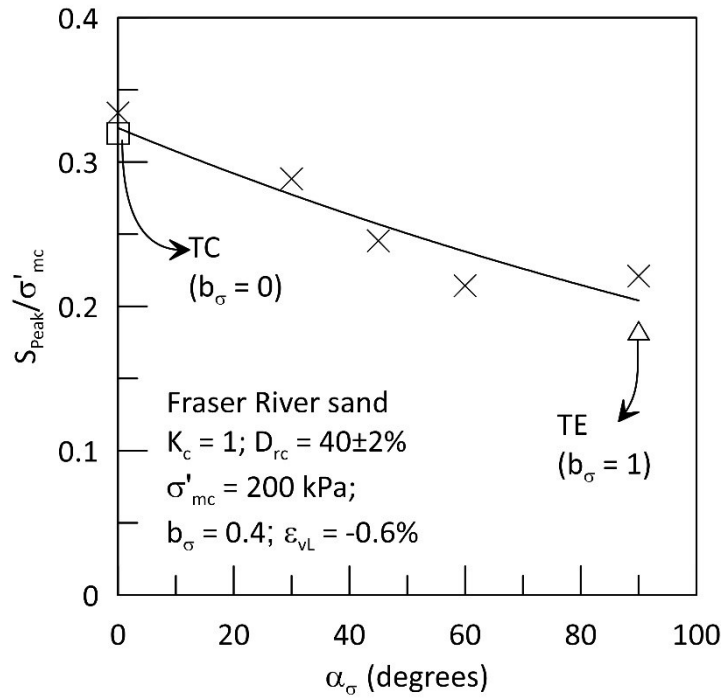


Figure 7.20: Variation of peak shear strength with α_σ

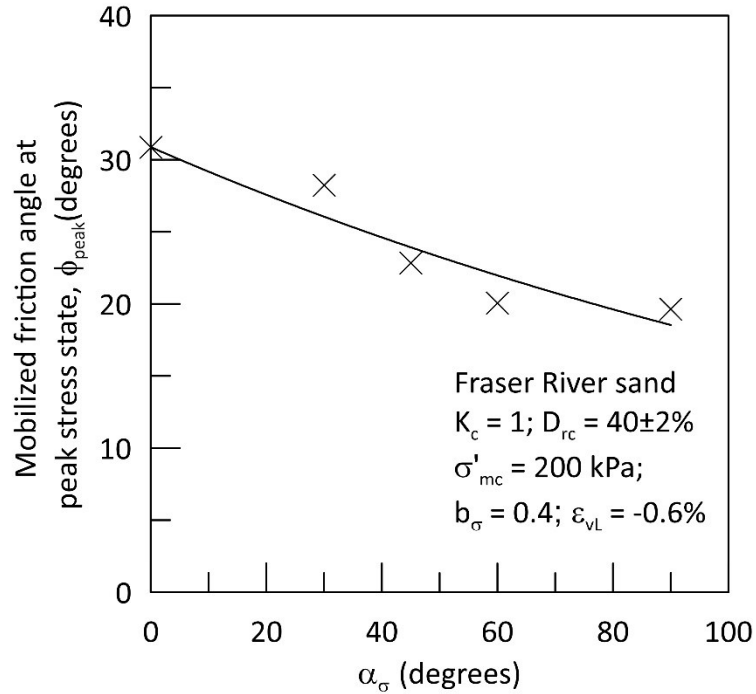


Figure 7.21: Variation of friction angle mobilized at peak shear strength with α_σ

The variation of peak excess pore water pressure (Δu_{peak}) and shear strength at the instant of Δu_{peak} against α_σ is plotted in Figure 7.22 and 7.23. The maximum excess pore pressure was about 130 kPa in $\alpha_\sigma = 0^\circ$ test, and this increases systematically with increasing α_σ and reaches a maximum value of about 185 kPa in the test along $\alpha_\sigma = 90^\circ$. The stress state corresponding to the minimum shear strength following the peak shear strength is termed as Quasi Steady State (QSS) and the stress state corresponding to peak excess pore water pressure is term as the phase transformation state (PT). Irrespective of loading mode, it is observed that QSS and PT stress state almost coincides with each other in this test series. Uthayakumar and Vaid (1998) and Vaid and Sivathayalan (2002) also reported the overlapping of QSS and PT stress state through the undrained testing of Fraser River sand under different α_σ . From Figure 7.23, it can be noted that S_{min} or S_{PT} or S_{QSS} decreases systematically with the increase in α_σ , there is almost 70% reduction in S_{PT} is

observed when the direction of major principal stress axis changes from deposition direction to weak bedding direction.

Figure 7.24 shows the effective stress state corresponding to minimum shear strength or the instant of peak excess pore water pressure state for the range of α_σ considered in this test program. Regardless of α_σ , the data points almost lie along the straight line which passes through the origin. The friction angle mobilized at this effective stress state ($\phi_{PeakPP/QSS/PT}$) is essentially a constant and is about 36.9° for this batch of Fraser River sand. This again confirms that ϕ_{PeakPP} is a unique material property and it is independent of loading mode even under partially drained condition.

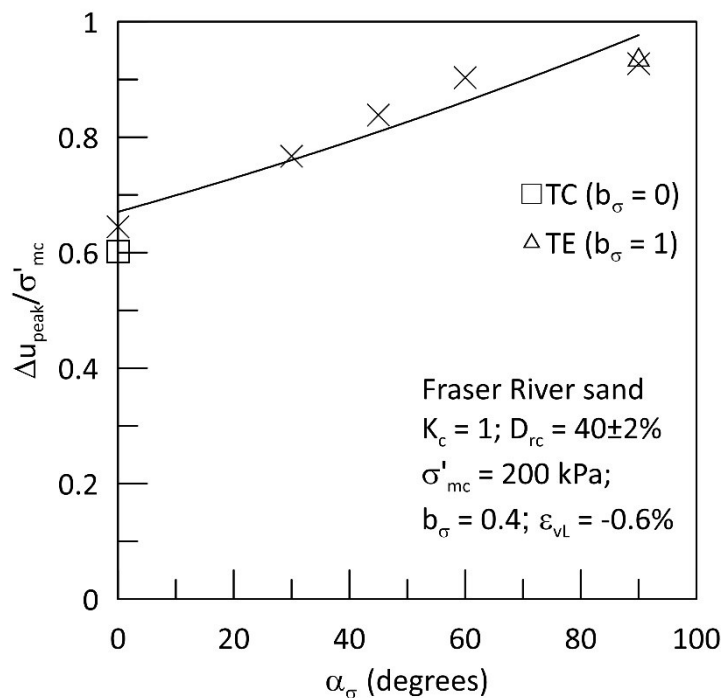


Figure 7.22: Variation of peak excess pore water pressure ratio with α_σ

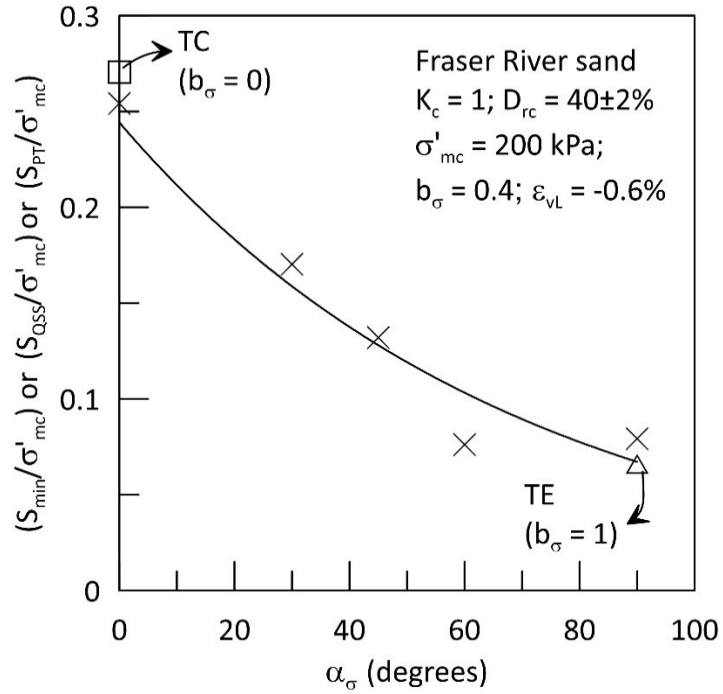


Figure 7.23: Variation of shear strength at phase transformation with α_σ

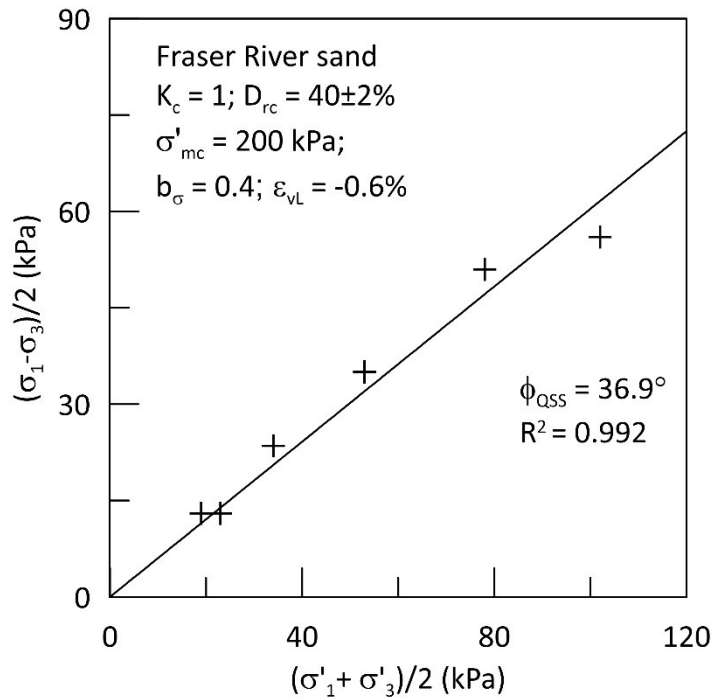


Figure 7.24 Effective stress state at the instant of peak pore water pressure at different loading modes.

7.3 *Summary and conclusions*

An experimental investigation was carried out to evaluate the behaviour of Fraser River sand under different non-linear strain path representing the simultaneous change in pore pressure and pore volume while monotonically shearing with different fixed direction of principal stress axes. At a fixed α_σ and b_σ , a systematic change in the stress-strain response of sand is observed as the imposed volumetric strain changes from contractive to expansive. The strain hardening response of sand at contractive volumetric strain transformed into a quasi-steady state response at expansive volumetric strain. Hence, the strain path with even a small volumetric inflow could transform a strain hardening sand at undrained condition to an unstable softening response. The friction angle at peak pore pressure state which is equivalent to friction angle at phase transformation is independent of the applied imposed drainage condition.

At a given volumetric strain path, due to cross anisotropic nature of water pluviated Fraser River sand, the hardening tendency of sand decreases as the inclination of major principal stress axis changes from direction of deposition to direction of bedding. The sand exhibited steady state flow deformation when the direction of major principal stress axis aligns with the direction of weak horizontal bedding plane. The peak shear strength and shear strength at phase transformation depends significantly on the loading mode. S_{peak} reduced by about 40% and S_{PT} reduced by about 70% with the increase in α_σ from 0° to 90° . The friction angle ϕ_{CSR} , mobilized at peak shear strength state or at the onset of strain softening is not a unique material property, and it is significantly affected by the direction of principal stresses axes during shearing. For this batch of Fraser River sand ϕ_{CSR} reduced from 30.8° at $\alpha_\sigma = 0^\circ$ to about 19.5° at $\alpha_\sigma = 90^\circ$. The friction angle ϕ_{PeakPP} or ϕ_{PT}

mobilized at minimum shear strength or the instant of peak excess pore water pressure state is found to be a unique material property and it is independent of the imposed drainage condition and loading mode.

8. SUMMARY AND CONCLUSIONS

The cyclic behaviour of saturated granular soils are usually evaluated under loading that simulates vertically propagating shear waves. But during seismic shaking, the actual soil element in-situ may be subjected to simultaneous action of both compression and shear waves. Hence firstly, a numerical analysis was carried out using finite difference code FLAC 2D to illustrate the simultaneous propagation of P-waves and S-waves in a soil media. Numerical simulations revealed that even a slight dip of bedrock is sufficient enough to generate both the types of body waves i.e., both compression and shear waves simultaneously from an incoming seismic wave, which in turn will subject the soil element to simultaneous cyclic shear stress and cyclic normal stress changes. Through the numerical simulation carried out with inclined bedrock model with a dip angle of 2.5° , the shear stress increment, normal stress increments and ratio between these stress increments S/N were computed. A wide range of S/N values, as low as 0.05 to as high as 100 were computed from the numerical analysis. This indicates that significantly different loading paths are possible in soil elements subjected to earthquake excitation. Theoretically, $S/N = 0$ corresponds to shear loading due to normal stress changes alone (cyclic triaxial tests) and $S/N = \infty$ corresponds to shear loading due to cyclic shear stresses on the horizontal plane (cyclic simple shear test). The representative values of S/N obtained from the numerical analysis is used as an input for the cyclic hollow cylinder torsional shear tests.

A detailed discussion on the possible nature and degree of stress rotation due to the coupled loading encountered in-situ has been presented. The rotation of major principal

stress axis (α_σ) during shearing plays a significant role in affecting the cyclic resistance of sand. This factor is not considered in the current practice of liquefaction evaluation, even though advanced assessments do consider the effect of the initial direction of the principal stresses using the K_α factor. Thus, a knowledge of the actual stress rotation encountered in-situ during earthquake shaking is crucial to properly analyze the cyclic resistance of soils. The analysis from this study shows that the nature and degree of stress rotation is significantly influenced by the initial consolidation stress ratio K_c , S/N , and phase shift δ between compression and shear waves. In the case of a hydrostatically consolidated specimen ($K_c = 1$) subjected to simultaneous shear loading with compression and shear waves that are in phase with each other ($\delta = 0$), α_σ undergoes jump rotation with degree of rotation changing from triaxial condition at very low S/N to simple shear condition at large S/N . For either initial $K_c \neq 1$ case or $\delta \neq 0$ case, α_σ rotates continuously between -90° to $+90^\circ$.

In order to evaluate the liquefaction characteristics of granular soil deposits under the coupled action of compression and shear waves, an extensive experimental investigation was carried out on water pluviated Fraser River sand specimens using a hollow cylinder torsional shear apparatus. The effects of initial stress state parameters such as effective confining pressure (σ'_{mc}), consolidation stress ratio (K_c) and shearing parameters such as cyclic stress ratio CSR (τ_{max}/σ'_{mc}), S/N , phase angle (δ) between compression and shear waves, and the effect of simultaneous action of shear wave and one-way compression wave on the cyclic resistance of sand were assessed. The following conclusions were drawn from the cyclic test data presented.

- At a fixed S/N and σ'_{mc} , the cyclic resistance of sand decreases with an increase in CSR and the rate of reduction is almost identical to the previous cyclic test data on Fraser River sand reported in the literature.
- At a fixed CSR and S/N , the liquefaction resistance decreases with the increase in initial effective confining stress. The K_σ factor which is used to quantify the effect of consolidation stress on cyclic resistance of sand slightly decreases with the increase in σ'_{mc} thus confirming the presence of K_σ effect even under generalized coupled loading conditions. The range of consolidation stresses used in the experimental study are rather narrow to make firm conclusions in this regard.
- The cyclic resistance of sand is significantly influenced by S/N . For a given CSR and initial σ'_{mc} , the number of cycles to liquefaction decreases with the increase in S/N . The cyclic resistance decreases drastically with the increase in S/N from 0.25 to 0.5. Beyond S/N of 0.5, the rate of reduction in the liquefaction resistance decreases with the increase in S/N and the trend of variation tends to be asymptotic with S/N axis for about $S/N > 1.6$.
- The reduction in the liquefaction resistance with increasing S/N is predominantly due to the coupled action of increase in shear stress on the weak horizontal bedding plane along with the close alignment of τ_{max} axis with the weak horizontal bedding plane. For a given CSR , there is no noticeable change in the magnitude of horizontal shear stress and inclination of τ_{max} axis with increase in S/N further than 1.6 and thus causing the asymptotic change in the cyclic resistance at larger S/N .

- The cyclic resistance ratio CRR is found to decrease with the increase in S/N . This is consistent with the well-established result that cyclic resistance is high under triaxial loading mode than under simple shearing loading mode.
- Test results also revealed that the dissipated energy required to cause liquefaction (W_{liq}) is independent of applied intensity of cyclic loading and it also increases proportionately with the increase in σ'_{mc} even under generalized coupled loading condition.
- Irrespective of initial confining stress and CSR , W_{liq} is slightly higher at low S/N of 0.25 and it is almost unaffected at higher values of S/N . This implies that slightly higher energy will be required to liquefy the soil under triaxial loading mode than under simple shear loading mode.
- This dissipated energy ratio (W_{liq}/σ'_{mc}), is found to be independent of CSR , S/N , σ'_{mc} , initial inclination of principal stress axes and magnitude of stress rotation.
- The pore pressure models proposed from this study relating pore pressure ratio (r_u) vs cycle ratio (N/N_l) and r_u vs (W_{liq}/σ'_{mc}) can reasonably predict the pore pressure under generalized cyclic loading conditions. Moreover, these models are very simplistic in functional forms and can be employed in numerical models to predict the generation of excess pore water pressure under actual seismic loading condition.
- Coupled cyclic loading due to compression and shear waves that are not in phase with each will result in an elliptical loading path. Caution should be exercised in planning the tests while following these non-conventional elliptical or circular

stress paths using the hollow cylinder torsional shear tests. Test results showed that how a given elliptical stress path is initialized from the initial consolidation stress state significantly affects the cyclic response of sand.

- During coupled shear loading at fixed HSR and S/N along with drained preshear to initiate the elliptical stress path, the phase shift between compression and shear waves has little influence on the cyclic resistance of sand. This is because at a fixed HSR and S/N , the amplitude of applied shear stress and normal stresses remains unchanged with the change in phase shift δ .
- At a fixed CSR , increasing the phase shift between the waves reduces the cyclic resistance of sand because increase in δ is accompanied by the decrease in rate of change in deviatoric stress per degree of rotation ($\Delta\sigma_d/\Delta\alpha_\sigma$). Previous investigations from undrained monotonic testing of sands have shown that the softening tendency of the sand increases with the decrease in $\Delta\sigma_d/\Delta\alpha_\sigma$.
- At a fixed CSR , for $\delta \neq 0$ cases, change in S/N does not affect the liquefaction resistance of sand because the magnitude and pattern of stress rotation is almost unaffected by the change in S/N .
- For a fixed CSR , S/N and $\delta = 0$ cases, the tendency of sand to liquefy decreases with the increase in consolidation stress ratio K_c .
- The rate of increase in cyclic resistance with initial static shear stress α_{st} decreases with the increase in S/N which confirms the observation made by Sivathayalan and Ha (2011) that the triaxial loading mode yields higher K_α than the simple shear loading mode. The test data from this investigation adds further confidence to the

existing contentious K_α variation with static shear stress under different loading mode for the loose sub angular Fraser River sand.

- The cyclic resistance of sand is significantly influenced by the wave type that causes the cyclic shear. Sand specimens tested with one-way loading exhibit higher cyclic strength when compared to the sand specimens tested with two-way loading.
- Cyclic test data showed that the tendency of cyclic mobility decreases with the increase in the magnitude of stress reversal because during cyclic shearing increasing magnitude of stress reversal aligns the direction of major principal stress axis closely with the weak bedding plane which promotes the strain softening of sand.

The influence of non-linear strain path representing the simultaneous change in pore pressure and pore volume on the monotonic response of Fraser River sheared along different inclination of principal stress axes was assessed. The following conclusions were derived based on the experimental results presented.

- As noted previously using triaxial tests, the behaviour of water deposited sands systematically transformed from dilative response to softening response as the imposed drainage condition changed from volumetric outflow to volumetric inflow under a fixed generalized loading path.
- Hence, the conventional assumption of undrained drainage condition during seismic shaking may not always represent the critical drainage condition encountered in-situ. Strain paths with even a small volumetric inflow could transform a dilative sand at undrained condition to an unstable contractive sand.

- At a given drainage condition, as a result of cross-anisotropic soil fabric, the strain hardening tendency of the water deposited sand specimens systematically reduces as the direction of major principal stress changes from direction of deposition ($\alpha_\sigma = 0^\circ$) to the direction of bedding ($\alpha_\sigma = 90^\circ$). The sand exhibited unlimited flow deformation when the major principal stress direction aligns with the horizontal bedding plane during shearing.
- The loading mode substantially influences the peak shear strength S_{peak} and minimum shear strength or shear strength at phase transformation S_{PT} of the sand. Both S_{peak} and S_{PT} systematically decreases with the increase in α_σ from 0° to 90° . The friction angle ϕ_{CSR} , mobilized at the onset of strain softening is decreased from 30.8° at $\alpha_\sigma = 0^\circ$ to about 19.5° at $\alpha_\sigma = 90^\circ$.
- The friction angle ϕ_{PeakPP} or ϕ_{PT} mobilized at the instant of peak excess pore water pressure state is not influenced by the imposed volumetric strain path and principal stress rotation, and appears to be a unique property of the sand.

This research study emphasized the importance of assessing the liquefaction potential of soil to the actual seismic loading condition encountered in-situ. The test data presented herein demonstrates the influence of various initial stress state parameters such as effective confining pressure, consolidation stress ratio and shearing parameters such as ratio between compression and shear waves and phase shift between the waves on the coupled cyclic loading response of water deposited sands. Also, high quality experimental data pertaining to the effect of coupled shear-volume deformation under generalized stress state is also presented. Hence, it is believed that this research shed some light into the grey areas in evaluating the liquefaction potential and shear strength of soil under different drainage

condition and also opened up the possibility of revisiting the current design practices based on the conventional approaches.

8.1 Recommendations for future research

This thesis highlighted the importance of evaluating the cyclic behaviour of soil under simultaneous action of both compression and shear waves. The application of both compression and shear waves simultaneously under different combinations has a profound influence on the pore pressure and shear strain development of the sand. And also, the stress-strain behaviour of granular soils are found to be greatly affected by the imposed drainage conditions and loading modes. Hence, the findings reported herein has serious practical implications and thus further research in the following topics are needed to complement the conclusions reported here.

- Extend investigations on coupled cyclic loading behaviour of soils to initial anisotropically consolidated stress state with various initial inclination of principal stress axis. The current simplified procedure of liquefaction evaluation implicitly considers the effect of initial inclination of principal stress direction through the factor K_α but it did not consider the subsequent nature and degree of stress rotation on the cyclic resistance of soil.
- The research reported here on the cyclic behaviour and partially drained behaviour of granular soil was conducted at specific conditions, and a more comprehensive study considering the effect of density, fabric, and anisotropic consolidation is required to generalize the conclusions for practical applications.

- The investigations on the cyclic behaviour of soils can be further extended by considering the various drainage condition encountered in-situ during seismic shaking due to the existence of pore pressure gradients within the soil deposit.
- A comprehensive analysis of the data to evaluate the variations of the principal stress increment directions and the strain increment direction to assess the nature of plastic deformations, and their dependence on stage of deformation and loading path.

REFERENCES

- Aggour, M. S., and Zhang, J. X. (2006). "Degradation of sands due to combined sinusoidal loading." *Journal of Geotechnical and Geoenvironmental Engineering*, 132(12), 1628–1632.
- Aki, K., and Richards, P.G. (1980). *Quantitative seismology*. University Science Books, Sausalito, California.
- Alarcon-Guzman, A., Leonards, G. ., and Chameau, J.L. (1988). "Undrained Monotonic and Cyclic Strength of Sands." *Journal of Geotechnical Engineering*, American Society of Civil Engineers, 114(10), 1089–1109.
- Ampadu, S. I. K. (1991). "Undrained behavior of kaolin in torsional simple shear", PhD thesis, The University of Tokyo, Japan.
- Andersen, K. H. (2009). "Bearing capacity under cyclic loading -offshore, along the coast, and on land. The 21st Bjerrum Lecture presented in Oslo, 23 November 2007." *Canadian Geotechnical Journal*, 46(5), 513–535.
- Andersen, K. H., Puech, A., and Jardine, R. J. (2013). "Cyclic resistant geotechnical design and parameter selection for offshore engineering and other applications." *Design for Cyclic Loading: Piles and Other Foundations. Proceedings of TC 209 Workshop, 18th ICSMGE - Paris, 4 September 2013*, 9-44
- Ansal, A.M., and Erken, A. (1996). "Post correction procedure for membrane compliance effects on pore pressure." *Journal of Geotechnical Engineering, ASCE*, 122(1), 27–38.
- Arthur, J. R. F., Chua, K. S., and Dunstan, T. (1977). "Induced anisotropy in a sand." *Géotechnique*, 27(1), 13–30.
- Arthur, J.R.F., Chua, K.S., Dunstan, T., and Rodriguez del, C.J.I. (1980). "Principal stress rotation: a missing parameter." *Journal of the Geotechnical Engineering Division*, 106(4), 419–433.
- Arthur, J. R. F., and Menzies, B. K. (1972). "Inherent Anisotropy in a sand." *Géotechnique*, 22(1), 115–128.

- Arthur, J.R.F. (1988). "Cubical Devices: Verstality and Constraints", *Advanced triaxial testing of soil and rock, STP977*, R. T. Donaghe, R. C. Chaney, and M. L. Silver, eds., ASTM, West Conshohocken, PA, 743-765.
- ASTM (2014a). "Standard Test Methods for Specific Gravity of Soil Solids by Water Pycnometer." *D854*, West Conshohocken, PA.
- ASTM. (2014b). "Standard test methods for maximum index density and unit weight of soils using a vibratory table." *D4253*, West Conshohocken, PA.
- ASTM. (2014c). "Standard test methods for minimum index density and unit weight of soils and calculation of relative density." *D4254*, West Conshohocken, PA
- Baziar, M. H., and Sharafi, H. (2011). "Assessment of silty sand liquefaction potential using hollow torsional tests-An energy approach." *Soil Dynamics and Earthquake Engineering*, Elsevier, 31(7), 857–865.
- Been, K., Jefferies, M. G., and Hachey, J. (1991). "The critical state of sands." *Géotechnique*, 41(3), 365–381.
- Berrill, J. B., and Davis, R. O. (1985). "Energy Dissipation and Seismic Liquefaction of Sands: Revised Model." *Soils and Foundations*, 25(2), 106–118.
- Bernardie, S., Foerster, E., and Modaressi, H. (2006). "Non-linear site response simulations in Chang-Hwa region during the 1999 Chi-Chi earthquake, Taiwan." *Soil Dynamics and Earthquake Engineering*, 26(11), 1038–1048.
- Bishop, A.W. (1971). "Shear strength parameters for undisturbed and remoulded soil specimens." *Proceedings of the Roscoe Memorial Symposium*, Cambridge University, Cambridge, Mass., 3–58.
- Blanc, M., Di Benedetto, H., and Tiouajni, S. (2011). "Deformation characteristics of dry Hostun sand with principal stress axes rotation." *Soils and foundations*, 51(4), 749–760.
- Bolt, B.A., (1999). *Earthquakes*. W.H. Freeman and Company, New York, NY, USA
- Boulanger, R.W., (2003). "Relating K_{α} to relative state parameter index." *Journal of Geotechnical and Geoenvironmental Engineering*, 129(8), 770–773.
- Boulanger, R.W., and Idriss, I.M. (2007). "Evaluation of cyclic softening in silts and clays." *Journal of Geotechnical and Geoenvironmental Engineering*, 133(6), 641–652.

- Boulanger, R. W., and Seed, R. B. (1995). "Liquefaction Of Sand under Bidirectional Monotonic and Cyclic Loading." *Journal of Geotechnical Engineering*, American Society of Civil Engineers, 121(12), 870–878.
- Brosse, A. M. (2012). "Study of the anisotropy of three British mudrocks using a Hollow Cylinder Apparatus." Ph.D thesis, Imperial College London.
- Brosse, A., Hosseini Kamal, R., Jardine, R. J., and Coop, M. R. (2016). "The shear stiffness characteristics of four Eocene-to-Jurassic UK stiff clays." *Géotechnique*, 67(3), 242–259.
- Brosse, A. M., Jardine, R. J., and Nishimura, S. (2017). "Undrained stiffness anisotropy from Hollow Cylinder experiments on four Eocene-to-Jurassic UK stiff clays." *Canadian Geotechnical Journal*, 54(October 2016), 313–332.
- Brown, S.F. (1996). "Soil mechanics in pavement engineering." *Géotechnique*, 46(3): 383–426.
- Cai, Y., Sun, Q., Guo, L., Juang, C. H., and Wang, J. (2015). "Permanent deformation characteristics of saturated sand under cyclic loading." *Canadian Geotechnical Journal*, 52(6), 795–807.
- Cai, Y. Q., Guo, L., Jardine, R. J., Yang, Z. X., and Wang, J. (2017). "Stress–strain response of soft clay to traffic loading." *Géotechnique*, 67(5), 446–451.
- Casagrande, A. (1975). "Liquefaction and cyclic deformation of sands: a critical review." *Proceedings of the Pan-American Conference on Soil Mechanics and Foundation Engineering*, Buenos Aires, Argentina, Vol. 5, 79–133.
- Casagrande, A., and Carillo, N. (1944). "Shear failure of anisotropic materials." *J. Boston Soc. Civil Eng.*, 31(4), 122–135.
- Castro, G. (1969). "Liquefaction of sands." Ph.D. thesis, Harvard University, Cambridge, Mass.
- Castro, G. (1975). "Liquefaction and cyclic mobility of saturated sands.", *Journal of Geotechnical Engineering Division*, ASCE, 101(6), 551-569.
- Castro, G., and Poulos, S.J. (1977). "Factors affecting liquefaction and cyclic mobility.", *Journal of Geotechnical Engineering Division*, ASCE, 103(6), 501-516.
- Chern, J. C. (1985). "Undrained Response of Saturated Sands with emphasis on Liquefaction and Cyclic Mobility." Ph.D thesis, University of British Columbia.

- Chiaro, G. (2010). "Deformation properties of sand with initial static shear in undrained cyclic torsional shear tests and their modeling." Ph.D thesis, University of Tokyo.
- Chiaro, G., Koseki, J., and Sato, T. (2012). "Effects of initial static shear on liquefaction and large deformation properties of loose saturated Toyoura sand in undrained cyclic torsional shear tests." *Soils and Foundations*, Elsevier, 52(3), 498–510.
- Chu, J., Lo, S.C.R., and Lee, I.K. (1992). "Strain softening behaviour of granular soils under strain path testing." *Journal of Geotechnical Engineering*, 118(2), 191-208.
- Chu, J., Wanatowski, D., Loke, W. L., & Leong, W. K. (2015). "Pre-failure instability of sand under dilatancy rate controlled conditions." *Soils and Foundations*, 55(2), 414–424.
- Davis, R.O. and Berrill, J.B., (1982). "Energy dissipation and seismic liquefaction of sands," *Earthquake Engineering and Structural Dynamics*, 10, 59-68.
- Dief, H. M., and Figueroa, J. L. (2007). "Liquefaction assessment by the unit energy concept through centrifuge and torsional shear tests." *Canadian Geotechnical Journal*, 44(11), 1286–1297.
- Dobry, R., Stokoe II, K.H., Ladd, R.S., and Youd, T.L. (1981). "Liquefaction Susceptibility from S-wave Velocity," *Proceedings ASCE Nat. Convention, In Situ Tests to Evaluate Liquefaction Susceptibility*, ASCE, New York.
- Dobry, R., Ladd, R.S., Yokel, F.Y., Chung, R.M., and Powell, D. (1982). "Prediction of Pore Water Pressure Buildup and Liquefaction of Sands During Earthquakes by the Cyclic Strain Method," *NBS Build. Sci. Ser. 138*, National Bureau of Standards, Gaithersburg, Maryland.
- Elnashai, A.S., and Sarno, L.D. (2008). *Fundamentals of earthquake engineering*. John Wiley & Sons Ltd, UK.
- Fauzi, U. J. (2015). "Local Deformation and Repeated Liquefaction Properties of Segregated Sand Specimen in Hollow Cylindrical Torsional Shear Tests." Ph.D thesis, University of Tokyo.
- Finn W.D.L., Bransby P.L., and Pickering D.J., "Effects of strain history on liquefaction of sands." *Journal of Soil Mechanics and Foundation Engineering Division*, 96(6), 1917–34

- Finn, W.D.L., Vaid, Y.P., and Bhatia, S.K. (1978). "Constant volume simple shear testing." *Proceedings of the 2nd International Conference on Microzonation for Safer Construction Research and Application*, San Francisco, Calif., 26 November – 1 December 1978. Vol. 2, 839–851.
- Figueroa, J. L., Saada, A. S., Liang, L., and Dahisaria, N. M. (1994). "Evaluation of Soil Liquefaction by Energy Principles." *Journal of Geotechnical Engineering*, American Society of Civil Engineers, 120(9), 1554–1569.
- Foundoukos, M. (2006). "Investigation of soil anisotropy using a hollow cylinder apparatus and numerical analysis." Ph.D. thesis, Imperial College London.
- Frydman, S., Talesnick, M., and Puzrin, A. (1995). "Colinearity of stresses, strains, and strain increments during shearing of soft clay." *Journal of Geotechnical Engineering - ASCE*, 121(2), 174–184.
- Georgiannou, V. N., and Konstadinou, M. (2014). "Effects of density on cyclic behaviour of anisotropically consolidated Ottawa sand under undrained torsional loading." *Géotechnique*, 64(4), 287–302.
- Georgiannou, V. N., Konstadinou, M., and Triantafyllos, P. (2018). "Sand Behavior under Stress States Involving Principal Stress Rotation." *Journal of Geotechnical and Geoenvironmental Engineering*, 144(6), 1–14.
- Gräbe, P. J., and Clayton, C. R. (2014). "Effects of Principal Stress Rotation on Permanent Deformation in Rail Track Foundations." *Journal of Geotechnical and Geoenvironmental Engineering*, 140(2), 1–10.
- Green, R.A., Mitchell, J.K. and Polito, C.P., (2000). "An Energy-Based Pore Pressure Generation Model for Cohesionless Soils," *In the Proceedings of the John Booker Memorial Symposium – Developments in Theoretical Geomechanics*, November 16-17, 2000, Balkema, Rotterdam, Netherlands, pp. 383-390.
- Gu, C., Gu, Z., Cai, Y., Wang, J., and Ling, D. (2016). "Dynamic modulus characteristics of saturated clays under variable confining pressure." *Canadian Geotechnical Journal*, 7(December), 1–7.
- Gu, C., Wang, J., Cai, Y., Yang, Z., and Gao, Y. (2012). "Undrained cyclic triaxial behavior of saturated clays under variable confining pressure." *Soil Dynamics and Earthquake Engineering*, Elsevier, 40, 118–128.

- Gutierrez, M., and Ishihara, K. (2000). "Non-coaxiality and energy dissipation in granular materials." *Soils and Foundations*, 40(2), 49–59.
- Guo, L., Cai, Y., Jardine, R. J., Yang, Z., and Wang, J. (2018). "Undrained behaviour of intact soft clay under cyclic paths that match vehicle loading conditions." *Canadian Geotechnical Journal*, 55(1), 90–106.
- Guo, L., Chen, J., Wang, J., Cai, Y., and Deng, P. (2016). "Influences of stress magnitude and loading frequency on cyclic behavior of K₀-consolidated marine clay involving principal stress rotation." *Soil Dynamics and Earthquake Engineering*, Elsevier, 84, 94–107.
- Guoxing, C., Zhenglong, Z., Hua, P., Tian, S., and Xiaojun, L. (2016). "The influence of undrained cyclic loading patterns and consolidation states on the deformation features of saturated fine sand over a wide strain range." *Engineering Geology*, Elsevier B.V., 204, 77–93.
- Harder, L.F., and Boulanger, R.W., (1997), "Application of K_σ and K_α correction factors", *Report No. NCEER-97-0022*, NCEER, Buffalo, NY.
- Hight, D., Gens, A., and Symes, M. . (1983). "The development of a new hollow cylinder apparatus for investigating the effects of principal stress rotation in soils." *Geotechnique*, 33(4), 355–383.
- Hong, W. P., and Lade, P. V. (1989a). "Elasto-Plastic Behaviour of K₀-Consolidated Clay in Torsion Shear Tests." *Soils and Foundations*, 29(2), 127–140.
- Hong, W. P., and Lade, P. V. (1989b). "Strain Increment and Stress Directions in Torsion Shear Tests." *Journal of Geotechnical Engineering*, 115(10), 1388–1401.
- Huang, B., Chen, X., and Zhao, Y. (2015). "A new index for evaluating liquefaction resistance of soil under combined cyclic shear stresses." *Engineering Geology*, Elsevier B.V., 199, 125–139.
- Hung, L. C., Lee, S. H., Vicent, S., and Kim, S. R. (2018). "An experimental investigation of the cyclic response of bucket foundations in soft clay under one-way cyclic horizontal loads." *Applied Ocean Research*, Elsevier B.V., 71, 59–68.
- Idriss, I.M. (2004). "Resolved and unresolved issues in soil liquefaction." *Keynote lecture. International Conference on Cyclic Behaviour of Soils and Liquefaction Phenomena*, 31 March – 2 April 2004, Ruhr University, Bochum, Germany

- Idriss, I.M., and Boulanger, R.W. (2008). "Soil liquefaction during earthquakes", Monograph MNO-12, Earthquake Engineering Research Institute, California.
- Inam, A., Ishikawa, T., and Miura, S. (2012). "Effect of principal stress axis rotation on cyclic plastic deformation characteristics of unsaturated base course material." *Soils and Foundations*, Elsevier, 52(3), 465–480.
- Ishihara, K. (1982). "Evaluation of soil properties for use in earthquake response analysis." *Proceedings of the International symposium on Numerical Models in Geomechanics*, Zurich, 13-17 September, 237-259.
- Ishihara, K. (1993). "Liquefaction and flow failure during earthquakes." *Géotechnique*, 43(3), 351–451.
- Ishihara, K. (1996). *Soil behaviour in earthquake geotechnics*. Oxford University Press, New York.
- Ishihara, K., and Okada, S. (1982). "Effects of large preshearing on cyclic behaviour of sand." *Soils and foundations*, 22(3), 109–125.
- Ishihara, K., and Towhata, I. (1983). "Sand Response to Cyclic Rotation of Principal Stress Directions as Induced by Wave Loads." *Soils and Foundations*, 23(4), 11–26.
- Ishihara, K., and Yamazaki, F. (1980). "Cyclic Simple Shear Tests on Saturated Sand in Multi-Directional Loading." *Soils and Foundations*, 20(1), 45–59.
- Ishihara, K., Tatsuoka, F., and Yasuda, S. (1975). "Undrained deformation and liquefaction of sand under cyclic stresses." *Soils and Foundations*, 15(1), 29–44.
- Itasca Consulting Group. (2016). *FLAC - Fast Lagrangian Analysis of Continua - dynamic analysis, FLAC Version 8*. Minneapolis, Itasca.
- Jafarian, Y., Towhata, I., Baziar, M. H., Noorzad, A., and Bahmanpour, A. (2012). "Strain energy-based evaluation of liquefaction and residual pore water pressure in sands using cyclic torsional shear experiments." *Soil Dynamics and Earthquake Engineering*, 35(2012), 13–28.
- Jefferies, M., Shuttle, D., and Been, K. (2015). "Principal stress rotation as cause of cyclic mobility." *Geotechnical Research*, 2(2), 66–94.
- Jiang, M., Shen, Z., and Li, L. (2016). "Noncoaxial Behavior of a Highly Angular Granular Material Subjected to Stress Variations in Simple Vertical Excavation." *International Journal of Geomechanics*, 16(2), 1–12.

- Kamai, R., and Boulanger, R. W. (2012). "Single-element simulations of partial-drainage effects under monotonic and cyclic loading." *Soil Dynamics and Earthquake Engineering*, Elsevier, 35, 29–40.
- Kammerer, A. M., Pestana, J. M., and Seed, R. B. (2002). "Undrained response of Monterey 0/30 sand under multidirectional cyclic simple shear loading conditions", *Report No. UCB/GT/02-02*, University of California, Berkeley, Calif.
- Kasgin, K. B., (2010). "Site Response Analysis and Seismic Surveying of High Contrast Soil Profiles for the City of Ottawa" Ph.D thesis, Carleton University.
- Kokusho, T. (2013). "Liquefaction potential evaluations: energy-based method versus stress-based method." *Canadian Geotechnical Journal*, 50, 1088–1099.
- Kokusho, T., and Kaneko, Y. (2018). "Energy evaluation for liquefaction-induced strain of loose sands by harmonic and irregular loading tests." *Soil Dynamics and Earthquake Engineering*. 114(August), 362–377.
- Konstadinou, M., and Georgiannou, V. N. (2013). "Cyclic behaviour of loose anisotropically consolidated Ottawa sand under undrained torsional loading." *Geotechnique*, 63(13), 1144–1158.
- Koseki, J., Yoshida, T., and Sato, T. (2005). "Liquefaction Properties of Toyoura Sand in Cyclic Torsional Shear Tests Under Low Confining Stress." *Soils and Foundations*, 45(5), 103–113.
- Kramer, S.L., and Sivaneswaran, N. (1989). "Stress-path-dependent correction for membrane penetration." *Journal of Geotechnical Engineering, ASCE*, 115(12), 1787–1804.
- Kuerbis, R. H., and Vaid, Y. P. (1990). "Corrections for membrane strength in the triaxial test." *Geotechnical Testing Journal*, 13(4), 361–369.
- Lade, P. V., and Kirkgard, M. M. (2000). "Effects of stress rotation and changes of b-values on cross-anisotropic behavior of natural, K_0 -consolidated soft clay." *Soils and Foundations*, 40(6), 93–105.
- Lade, P.V., and Liggio Jr, C.D. (2014). " Stability and Instability of Granular Materials under Imposed Volume Changes: Experiments and Predictions." *International Journal of Geomechanics*, 14(5), 04014020.

- Lade, P. V., and Wasif, U. (1988). "Effects of height-to-diameter ratio in triaxial specimens on the behavior of cross-anisotropic sand." *Advanced triaxial testing of soil and rock, STP977*, R. T. Donaghe, R. C. Chaney, and M. L. Silver, eds., ASTM, West Conshohocken, PA, 706–714.
- Lade, P. V., Nam, J., and Hong, W. P. (2008). "Shear banding and cross-anisotropic behavior observed in laboratory sand tests with stress rotation." *Canadian Geotechnical Journal*, 45, 74–84.
- Lade, P. V., Nam, J., and Hong, W. P. (2009). "Interpretation of strains in torsion shear tests." *Computers and Geotechnics*, Elsevier Ltd, 36, 211–225.
- Lade, P. V., Rodriguez, N. M., and Van Dyck, E. J. (2013). "Effects of Principal Stress Directions on 3D Failure Conditions in Cross-Anisotropic Sand." *Journal of Geotechnical and Geoenvironmental Engineering*, 140(2), 1–12.
- Lade, P. V., Van Dyck, E., and Rodriguez, N. M. (2014). "Shear banding in torsion shear tests on cross-anisotropic deposits of fine Nevada sand." *Soils and Foundations*, Elsevier, 54(6), 1081–1093.
- Lancelot, L., Shahrour, I., and Al Mahmoud, M. (2004). "Instability and static liquefaction on proportional strain paths for sand at low stresses." *Journal of Engineering Mechanics*, 130(11), 1365-1372.
- Law, K. T., Cao, Y. L., and He, G. N. (1990). "An energy approach for assessing seismic liquefaction potential." *Canadian Geotechnical Journal*, 27(3), 320–329.
- Lee, K.L., and Seed, H.B. (1967). "Cyclic stress condition causing liquefaction of sand." *Journal of the Soil Mechanics and Foundations division., ASCE*, 93(1), 47–70.
- LeBlanc, C., Houlsby, G. T., and Byrne, B. W. (2010). "Response of stiff piles in sand to long-term cyclic lateral loading." *Geotechnique*, 60(2), 79–90.
- Leroueil, S., and Hight, D.W. (2003). "Behaviour and properties of natural soils and soft rocks." *Characterization and Engineering Properties of Natural Soils: Proceedings of the International Workshop*. Edited by T.S. Tan, K.K. Phoon, D.W. Hight, and S. Leroueil. A.A. Balkema, Rotterdam, The Netherlands. Vol. 1, 29–254.
- Liang, B. L., Figueroa, L., and Saada, A. S. (1995). "Liquefaction under random loading: Unit energy approach." *Journal of Geotechnical Engineering*, 121(11), 776–781.
- Lin, M. L., Wang, K. L., and Chen, T. . (2009). "Tsaoling landslide in Taiwan during the

- 1999 Chi-Chi earthquake.” *Earthquake geotechnical case histories for performance-based design*. Ed by Kokusho. Taylor and Francis group, London. 273–287.
- Liu, H., and Qiao, T. (1984). “Liquefaction potential of saturated sand deposits underlying foundation of structure.” *8th World Conference on Earthquake Engineering*, Vol. III, San Francisco, California.
- Logeswaran, P. (2010). “Behaviour of Sands under Generalized Loading and Drainage Conditions.” Ph.D. thesis, Carleton University.
- Logeswaran, P., and Sivathayalan, S. (2014). “A new hollow cylinder torsional shear device for stress/strain path controlled loading.” *Geotechnical Testing Journal*, 37(1), 0–12.
- Mahmood, A., and Mitchell, J. K. (1974). “Fabric-property relationships in fine granular materials.” *Clays and Clay Minerals*, 22(5–6), 397–408.
- Mangal, J. K. (1999). “Partially-Drained Loading of Shallow Foundations on Sand.” Ph.D. thesis, University of Oxford.
- Manmatharajan, V., and Sivathayalan, S. (2011). “Effect of overconsolidation on cyclic resistance correction factors K_{σ} and K_{α} .” *Proc., Fourteenth Pan-American Conference on Soil Mechanics and Geotechnical Engineering and the Sixty-Fourth Canadian Geotechnical Conference*, Ontario, Canada.
- Matsuda, H., Shinozaki, H., Okada, N., Takamiya, K., and Shinyama, K. (2004). “Effects of multi-directional cyclic shear on the postearthquake settlement of ground”. *13th World Conf. on Earthquake Engr., Proceedings*, Vancouver, B.C., Canada, Paper No. 2890.
- Menkiti, C.O. (1995). “Behaviour of clay and clayey-sand, with particular reference to principal stress rotation.” Msc. thesis, Imperial College London.
- Minh, N. A. (2006). “An investigation of the anisotropic stress-strain-strength characteristics of an Eocene clay.” Ph.D. thesis, Imperial College London.
- Miura, K., Miura, S., and Toki, S. (1986). “Deformation behavior of anisotropic dense sand under principal stress axes rotation.” *Soils and Foundations*, 26(1), 36–52.
- Miura, S., and Toki, S. (1982). “A sample preparation method and its effect on static and cyclic deformation-strength properties of sand.” *Soils and Foundations*, 22(1), 61–77.
- Montgomery, J., Boulanger, R. W., and Harder, L. F. (2014). “Examination of the K_{σ}

- overburden correction factor on liquefaction resistance.” *Journal of Geotechnical and Geoenvironmental Engineering*, 140(12), 1–11.
- Movahed, V., Sharafi, H., Baziar, M. H., and Shahnazari, H. (2020). “Comparison of Strain Controlled and Stress Controlled Tests in Evaluation of Fines Content Effect on Liquefaction of Sands-An Energy Approach.” *Geo-Frontiers 2011*, Proceedings.
- Nakata, Y., Hyodo, M., Murata, H., and Yasufuku, N. (1998). “Flow Deformation of Sands Subjected to Principal Stress Rotation.” *Soils and Foundations*, 38(2), 115–128.
- Nemat-Nasser, S., and Shokoh, A. (1979). “A unified approach to densification and liquefaction of cohesionless sand in cyclic shearing.” *Canadian Geotechnical Journal*, 16(4), 659–678.
- Nicholson, P.G., Seed, R.B., and Anwar, H.A. (1993a). “Elimination of membrane compliance in undrained triaxial testing. I. Measurement and evaluation.” *Canadian Geotechnical Journal*, 30(5), 727–738.
- Nicholson, P.G., Seed, R.B., and Anwar, H.A. (1993b). “Elimination of membrane compliance in undrained triaxial testing. II. Mitigation by injection compensation.” *Canadian Geotechnical Journal*, 30(5), 739–746.
- Nikitas, G., Vimalan, N. J., and Bhattacharya, S. (2016). “An innovative cyclic loading device to study long term performance of offshore wind turbines.” *Soil Dynamics and Earthquake Engineering*, 82(March), 154–160.
- Nikitas, G., Arany, L., Aingaran, S., Vimalan, J. N., and Bhattacharya, S. (2017). “Predicting long term performance of offshore wind turbines using cyclic simple shear apparatus.” *Soil Dynamics and Earthquake Engineering*, Elsevier, 92(September 2016), 678–683.
- Nishimura, S. (2005). “Laboratory Study on Anisotropy of Natural London Clay.” *Imperial College London*, Ph.D thesis, Imperial College London.
- Nishimura, S., Jardine, R. J., and Minh, N. a. (2007). “Shear strength anisotropy of natural London Clay.” *Géotechnique*, 57(1), 49–62.
- NRC. (1985). “Liquefaction of soils during earthquakes.” *Report of the Committee on Earthquake Engineering*, National Research Council, National Academy Press, Washington, DC.
- Ochiai, H., and Lade, P. V. (1983). “Three-Dimensional Behavior of Sand with Anisotropic

- Fabric.” *Journal of Geotechnical Engineering*, 109(10), 1313–1328.
- Oda, M. (1972). “Initial Fabrics and Their Relations to Mechanical Properties of Granular Material.” *Soils and Foundations*, 12(1), 17–36.
- Oda, M., and Iwashita, K. (1999). *Mechanics of granular materials: an introduction*, Balkema, Rotterdam, Netherlands
- Oda, M., Koishikawa, I., and Higuchi, T. (1978). “Experimental study of anisotropic shear strength of sand by plane strain test.” *Soils and Foundations*, 18(1), 25–38.
- Oda, M., Nasser, N., and Konishi, J. (1985). “Stress-induced anisotropy in granular masses.” *Soils and Foundations*, 25(3), 85–97.
- Okusa, S., Anma, S., and Maikuma, M. (1984). "The propagation of liquefaction pressure and delayed failure of a tailings dam dike in the 1978 Izu–Oshima–Kinkai earthquake." *In Proceedings of the 8th World Conference on Earthquake Engineering*, 21–28 July 1984, San Francisco, California. Vol. 8. pp. 389–396.
- Olgun, C. G., and Kamalzare, S. (2020). “Energy Dissipation in Soil Structures during Uniform Cyclic Loading.” *Geotechnical Frontiers 2017*, Proceedings.
- Phillips, A.B., and May, P.H. (1967), "A Form of Anisotropy in Granular Media", *Special Task Report*, Dept. of Civil and Municipal Engineering, University College, London
- Polito, C., and Moldenhauer, H. (2018). “Pore Pressure Generation and Dissipated Energy Ratio in Cohesionless Soils.” *Geotechnical Earthquake Engineering and Soil Dynamics V*, GSP 293, 336-344.
- Polito, C., and Moldenhauer, H. (2018). “Energy Dissipation and Pore Pressure Generation in Stress- and Strain-Controlled Cyclic Triaxial Tests.” *Geotechnical Testing Journal*, ASTM International, West Conshohocken, PA, 42(4), 1083–1089.
- Polito, C., Green, R. A., and Lee, J. (2008). “Pore Pressure Generation Models for Sands and Silty Soils Subjected to Cyclic Loading.” *Journal of Geotechnical and Geoenvironmental Engineering*, American Society of Civil Engineers, 134(10), 1490–1500.
- Polito, C., Green, R. A., Dillon, E., and Sohn, C. (2013). “Effect of load shape on relationship between dissipated energy and residual excess pore pressure generation in cyclic triaxial tests.” *Canadian Geotechnical Journal*, 50(October 2012), 1118–1128.

- Prasanna, R., Sinthujan, N., and Sivathayalan, S. (2018). "Effect of Cyclic Rotation of Principal Stresses on Liquefaction Resistance of Sands." *Geotechnical Earthquake Engineering and Soil Dynamics V*.
- Ramana, K.V., and Raju, V.S. (1982). "Membrane penetration in triaxial tests." *Journal of Geotechnical Engineering, ASCE*, 108(2), 305–310.
- Randolph, M., and Gourvenac, S. (2011). *Offshore Geotechnical Engineering*. Spoon Press. Oxon Ox.
- Rodriguez, N. M., and Lade, P. V. (2014). "Non-coaxiality of strain increment and stress directions in cross-anisotropic sand." *International Journal of Solids and Structures*, Elsevier Ltd, 51(5), 1103–1114.
- Rolo, R. (2003). "The anisotropic stress–strain–strength behaviour of brittle sediments." Ph.D thesis, Imperial College London.
- Roscoe, K. H., Schofield, A. N., and Wroth, C. P. (1958). "On The Yielding of Soils." *Géotechnique*, 8(1), 22–53.
- Rothernburg, L., and Bathurst, R. J. (1989). "Analytical study of induced anisotropy granular materials." *Geotechnique*, 39(4), 601–614.
- Saada, A. S. (1970). "Testing of anisotropic clay soils." *J. Soil Mech. and Found. Div.*, 96(5), 1847–1852.
- Sayao, A. S. F. . (1989). "Behaviour of sand under general stress paths in the hollow cylinder torsional device." Ph.D thesis, University of British Columbia.
- Sayao, A., and Vaid, Y. P. (1991). "A critical assessment of stress nonuniformities in hollow cylinder test specimens." *Soils and Foundations*, 31(1), 60–72.
- Schnabel, P.B., Lysmer, J. & Seed, H.B., (1972). "SHAKE: a computer program for earthquake response analysis of horizontally layered sites" *Report EERC-71-12*, University of California, Berkeley: Earthquake Engineering Research Center (EERC).
- Seed, H.B. (1979). "Soil Liquefaction and Cyclic Mobility Evaluation for Level Ground during Earthquakes.", *Journal of Geotechnical Engineering Division.*, ASCE, 105(2), 201-225.
- Seed, H.B. (1983). "Earthquake-resistant design of earth dams." *In Proceedings of the Symposium on Seismic Design of Earth Dams and Caverns*, Philadelphia, Pa., 16–20 May 1983. Edited by T.R. Howard. American Society of Civil Engineers, New York.

pp. 41–64.

- Seed, H.B. (1987). “Design Problems in Soil Liquefaction.” *Journal of Geotechnical Engineering*, American Society of Civil Engineers, 113(8), 827–845.
- Seed, R.B., and Harder, L.F. (1990). “SPT-based analysis of cyclic pore pressure generation and undrained residual strength”. In *Proceedings of H.B. Seed Memorial Symposium*, University of California Berkeley, Berkeley, Calif. Edited by J.M. Duncan. BiTech Publishers, Vancouver, B.C. Vol. 2, pp. 351–376.
- Seed, H.B., and Idriss, I.M. (1971). “Simplified procedure for evaluating soil liquefaction potential”. *Journal of the Soil Mechanics and Foundations Engineering Division*, ASCE, 97(9), 1249–1274.
- Seed, H.B., and Lee, K.L. (1966). “Liquefaction of saturated sands during cyclic loading.” *Journal of the Soil Mechanics and Foundations division.*, ASCE, 92(6), 105–134.
- Seed, H.B. and Sun, J.H., (1989). “Implication of site effects in the Mexico City earthquake of September 19, 1985 for earthquake-resistance-design criteria in the San Francisco Bay Area of California”. *Report No. UCB/EERC-89/03*, University of California, Berkeley, California.
- Seed, R. B., Anwar, H. A., and Nicholson, P. G. (1989). “Elimination of membrane compliance effect in undrained testing.” *Twelfth International Conference on Soil Mechanics and Foundation Engineering*, Vol. 1, 111-114.
- Seed, H. B., Idriss, I. M., Makdisi, F., and Banerjee, N. (1975). “Representation of, irregular stress time histories by equivalent uniform stress series in liquefaction analysis.” *Rep. No. EERC 75-29*, Earthquake Engineering Research Center, College of Engineering, Univ. of California, Berkeley, Calif.
- Seed, H.B, Lysmer, J., Martin, PP. (1976). "Pore water pressure change during soil liquefaction." *Journal of Geotechnical Engineering Division*, ASCE, 102(4), 323-346
- Seismosignal (2016). *Seismosignal's help system*, Seismosoft Ltd.
- Sento, N., Kazama, M., Uzuoka, R., Ohmura, H., and Ishimaru, M. (2004). “Possibility of Postliquefaction Flow Failure due to Seepage.” *Journal of Geotechnical and Geoenvironmental Engineering*, 130(7), 707–716.
- Shaw, R., McMahan, G., and Davey, K.. (2018). “Types of seismic waves”. Figshare. <https://doi.org/10.17028/rd.lboro.7309127.v1> Accessed on 6th May 2020.

- Shibuya, S., and Hight, D. . (1987). “A Bounding Surface for Granular Materials.” *Soils and Foundations*, 27(4), 123–136.
- Sinthujan, N. (2013). “Pore pressure parameters and cyclic resistance under generalized loading.” Carleton University.
- Sivathayalan, S. (2000). “Fabric, Initial State and Stress Path Effects on Liquefaction Susceptibility of Sands.” Ph.D thesis, University of British Columbia.
- Sivathayalan, S., and Ha, D. (2011). “Effect of static shear stress on the cyclic resistance of sands in simple shear loading.” *Canadian Geotechnical Journal*, 48, 1471–1484.
- Sivathayalan, S., and Logeswaran, P. (2007). “Behavior of Sands under Generalized Drainage Boundary Conditions.” *Canadian Geotechnical Journal*, 44(2), 138–150.
- Sivathayalan, S., and Logeswaran, P. (2008). “Experimental assessment of the response of sands under shear–volume coupled deformation.” *Canadian Geotechnical Journal*, 45(9), 1310–1323.
- Sivathayalan, S., and Mehrabi, Y. A. (2014). “Influence of Strain History on Postliquefaction Deformation Characteristics of Sands.” *Journal of Geotechnical and Geoenvironmental Engineering*, American Society of Civil Engineers, 140(3), 4013019.
- Sivathayalan, S., Logeswaran, P., and Manmatharajan, V. (2015). “Cyclic Resistance of a Loose Sand Subjected to Rotation of Principal Stresses.” *Journal of Geotechnical and Geoenvironmental Engineering*, 141(3), 1–13.
- Sivathayalan, S., and Vaid, Y. P. (1998). “Truly undrained response of granular soils with no membrane-penetration effects.” *Canadian Geotechnical Journal*, 35(5), 730–739.
- Sivathayalan, S., and Vaid, Y. P. (2002). “Influence of generalized initial state and principal stress rotation on the undrained response of sands.” *Canadian Geotechnical Journal*, 39(1), 63–76.
- Soralump, S., and Prasomsri, J. (2016). “Cyclic Pore Water Pressure Generation and Stiffness Degradation in Compacted Clays.” *Journal of Geotechnical and Geoenvironmental Engineering*, 142(1), 1–13.
- Strenk, P.M., and Wartman, J., (2011). “Comparison of dynamic response of equivalent-linear and cyclic non-linear models of hysteretic soil behavior” *Proceedings of the 2nd International FLAC/DEM Symposium*. February 2011, Melbourne, Australia,

Paper: 09-01 .

- Sun, L., Gu, C., and Wang, P. (2015). “Effects of cyclic confining pressure on the deformation characteristics of natural soft clay.” *Soil Dynamics and Earthquake Engineering*, Elsevier, 78, 99–109.
- Suzuki, T., and Toki, S. (1984). “Effects of preshearing on liquefaction characteristics of saturated sand subjected to cyclic loading.” *Soils and Foundations*, 24(2), 16–28.
- Symes, M., Gens, A., and Hight, D. W. (1984). “Undrained anisotropy and principal in saturated sand.” *Geotechnique*, 34(1), 11–27.
- Tatsuoka, F., and Ishihara, K. (1974). “Drained deformation of sand under cyclic stresses reversing direction.” *Soils and Foundations*, 14(3), 51.
- Tatsuoka, F., Sonoda, S., Hara, K., Fukushima, S., and Pradhan, T. B. . (1986). “Failure and deformation of sand in torsional shear.” *Soils and Foundations*, 26(4), 79–97.
- Timoshenko, S., and Goodier, J. . (1951). *Theory of Elasticity*. McGraw Hill Book Company Inc.
- Tokimatsu, K., and Nakamura, K. (1987). “A simplified correction for membrane compliance in liquefaction tests.” *Soils and Foundations*, 27(4), 111–122.
- Tong, Z.-X., Zhang, J.-M., Yu, Y.-L., and Zhang, G. (2010). “Drained Deformation Behavior of Anisotropic Sands during Cyclic Rotation of Principal Stress Axes.” *Journal of Geotechnical and Geoenvironmental Engineering*, 136(11), 1509–1518.
- Towhata, I., and Ishihara, K. (1985). “Shear work and pore water pressure in undrained shear.” *Soils and foundations*, 25(3), 73–84.
- Tsaparli, V., Kontoe, S., Taborda, D. M. G., and Potts, D. M. (2016). “Vertical ground motion and its effects on liquefaction resistance of fully saturated sand deposits.” *Proceedings of the Royal Society A: Mathematical, Physical and Engineering Science*, 472(2192), 20160434.
- Tsaparli, V., Kontoe, S., Taborda, D. M. G., and Potts, D. M. (2017). “An energy-based interpretation of sand liquefaction due to vertical ground motion.” *Computers and Geotechnics*, The Authors, 90, 1–13.
- Tsaparli, V., Kontoe, S., Taborda, D. M. G., and Potts, D. M. (2018). “Liquefaction triggering due to compressional waves: validation through field records.” *16th European Conference on Earthquake Engineering*, 1–12.

- Tsutsumi, S., and Hashiguchi, K. (2005). "General non-proportional loading behavior of soils." *International Journal of Plasticity*, 21(10), 1941-1969.
- Umehara, Y., Zen, K., and Hamada, K. (1985). "Evaluation of soil liquefaction potentials in partially drained conditions." *Soils and foundations*, 25(2), 57–72.
- Uthayakumar, M., and Vaid, Y. P. (1998). "Static liquefaction of sands under multiaxial loading." *Canadian Geotechnical Journal*, 35(2), 273–283.
- Vaid, Y.P., and Chern, J.C. (1983). "Effect of static shear on resistance to liquefaction." *Soils and Foundations*, 23(1), 47–60.
- Vaid, Y.P., and Chern, J.C. (1985). "Cyclic and monotonic undrained response of sands.", *Proceedings Advances in the Art of Testing Soils under Cyclic Loading Conditions*, Detroit, 120-147.
- Vaid, Y. P., and Eliadorani, A. (1998). "Instability and liquefaction of granular soils under undrained and partially drained states." *Canadian Geotechnical Journal*, 35(6), 1053–1062.
- Vaid, Y. P., and Eliadorani, A. (2000). "Undrained and drained (?) stress-strain response." *Canadian Geotechnical Journal*, 37(5), 1126–1130.
- Vaid, Y. P., and Negussey, D. (1984). "A critical assessment of membrane penetration in the triaxial test." *Geotechnical Testing Journal, ASTM*, 7(2), 70–76.
- Vaid, Y. P., Chung, E. K. F., and Kuerbis, R. H. (1989). "Preshearing and undrained response of sand." *Soils and Foundations*, 29(4), 49–61.
- Vaid, Y. P., Sayao, A., Hou, E., and Negussey, D. (1990). "Generalized stress-path-dependent soil behaviour with a new hollow cylinder torsional apparatus." *Canadian Geotechnical Journal*, 27, 601–616.
- Vaid, Y. P., Stedman, J. D., and Sivathayalan, S. (2001). "Confining stress and static shear effects in cyclic liquefaction." *Canadian Geotechnical Journal*, 38(3), 580–591.
- Vaid, Y. P., and Sivathayalan, S. (1996a). "Static and cyclic liquefaction potential of Fraser Delta sand in simple shear and triaxial tests." *Canadian Geotechnical Journal*, 33, 281–289.
- Vaid, Y. P., and Sivathayalan, S. (1996b). "Errors in estimates of void ratio of laboratory sand specimens." *Canadian Geotechnical Journal*, 33(6), 1017–1020.
- Vaid, Y. P., and Sivathayalan, S. (2000). "Fundamental factors affecting liquefaction

- susceptibility of sands.” *Canadian Geotechnical Journal*, 37, 592–606.
- Vaid, Y. P., Sivathayalan, S., and Stedman, D. (1999). “Influence of Specimen-Reconstituting Method on the Undrained Response of Sand.” *Geotechnical Testing Journal*, 22(3), 187–195.
- Vaid, Y. P., and Thomas, J. (1995). “Liquefaction and Postliquefaction Behavior of Sand.” *Journal of Geotechnical Engineering*, American Society of Civil Engineers, 121(2), 163–173.
- Wang, Y., Gao, Y., Guo, L., Cai, Y., Li, B., Qiu, Y., and Mahfouz, A. H. (2017). “Cyclic response of natural soft marine clay under principal stress rotation as induced by wave loads.” *Ocean Engineering*, Elsevier, 129(November 2015), 191–202.
- Whitman, R.V. (1985). “On liquefaction.” *11th International Conference on Soil Mechanics and Foundation Engineering*, San Francisco, 12-16 August 1985, Vol. 3, 1923–1926.
- Wijewickreme, D., and Vaid, Y. P. (1991). “Stress Nonuniformities in Hollow Cylinder Torsional Specimens.” *Geotechnical Testing Journal*, 14(4), 349–362.
- Wijewickreme, D., and Vaid, Y. P. (2008). “Experimental observations on the response of loose sand under simultaneous increase in stress ratio and rotation of principal stresses.” *Canadian Geotechnical Journal*, 45(5), 597–610.
- Wong, R. K. ., and Arthur, J. R. F. (1985). “Induced and inherent anisotropy in sand.” *Geotechnique*, 35(4), 471–481.
- Wu, T., Cai, Y., Guo, L., Ling, D., and Wang, J. (2017). “Influence of shear stress level on cyclic deformation behaviour of intact Wenzhou soft clay under traffic loading.” *Engineering Geology*, Elsevier, 228(January), 61–70.
- Xu, B., Nakai, K., Noda, T., and Takaine, T. (2013). “A three-dimensional soil–water coupled FE analysis of hollow cylinder test concerning non-uniform deformation.” *Soils and Foundations*, Elsevier, 53(6), 923–936.
- Xu, C., Jia, J., Sun, Y., Du, X., and Gao, Y. (2017). “Cyclic strength of saturated sand under bi-directional cyclic loading.” *Engineering Geology*, Elsevier B.V., 227, 23–31.
- Yamada, Y., and Ishihara, K. (1979). “Anisotropic Deformation Characteriscs of Sand under Three Dimensional Stress Conditions.” *Soils and Foundations*, 19(2), 79–94.

- Yamamoto, Y., Hyodo, M., and Orense, R. P. (2009). "Liquefaction Resistance of Sandy Soils under Partially Drained Condition." *Journal of Geotechnical and Geoenvironmental Engineering, ASCE*, 135(8), 1032–1043.
- Yang, Z. X., Li, X. S., and Yang, J. (2007). "Undrained anisotropy and rotational shear in granular soil." *Géotechnique*, 57(4), 371–384.
- Yang, L. (2013). "Experimental study of soil anisotropy using hollow cylinder testing." Ph.D thesis, The University of Nottingham.
- Ye, B., Lu, J., and Ye, G. (2015). "Pre-shear effect on liquefaction resistance of a Fujian sand." *Soil Dynamics and Earthquake Engineering*, Elsevier, 77, 15–23.
- Yoshimine, M., Ishihara, K., and Vargas, W. (1998). "Effects of principal stress direction and intermediate principal stress on undrained shear behavior of sand." *Soils and Foundations*, 38(3), 179–188.
- Youd, T.L., Idriss, I.M., Andrus, R.D., Arango, I., Castro, G., Christian, J.T., et al. (2001). "Liquefaction resistance of soils: summary report from the 1996 NCEER and 1998 NCEER/NSF Workshops on Evaluation of Liquefaction Resistance of Soils." *Journal of Geotechnical and Geoenvironmental Engineering*, 127 (10), 817–833.
- Zdravković, L., Potts, D. M., and Hight, D. W. (2002). "The effect of strength anisotropy on the behaviour of embankments on soft ground." *Géotechnique*, 52(6), 447–457.